Max-Planck-Institut für Metallforschung
Stuttgart

Mechanics of Soft Polymer Indentation

Julia Deuschle

Dissertation
an der
Universität Stuttgart

Bericht Nr. 214
Februar 2008

Mechanics of Soft Polymer Indentation

Von der Fakultät Chemie der Universität Stuttgart
zur Erlangung der Würde eines
Doktors der Naturwissenschaften (Dr. rer. nat.)
genehmigte Abhandlung

Vorgelegt von

Dipl.-Ing. Julia Deuschle

aus Stuttgart

Hauptberichter:	Prof. Dr. Eduard Arzt
Mitberichter:	Prof. Dr. Fritz Aldinger
Tag der mündlichen Prüfung:	28.2.2008

Max-Planck-Institut für Metallforschung Stuttgart
und
Institut für Metallkunde der Universität Stuttgart

Stuttgart, Februar 2008

Julia Deuschle

Mechanics of Soft Polymer Indentation

189 pages, 67 figures, 8 tables

Abstract

Nanoindentation has become a fast and reliable technique for the mechanical characterization of engineering materials. The applicability of this technique to small or confined volumes and the sub- µN and sub- nm resolution of the instruments are unique features in the field of mechanical testing and make nanoindentation a promising, yet not fully accepted tool for the investigation of soft materials. Since these materials are of high importance for technological and biomedical purposes, a strong interest in the application of nanoindentation to this class of materials exists. The present work deals with nanoindentation studies on various polymers in order to address the two crucial factors for testing of soft materials, which are surface detection and contact area determination. An improved surface detection criterion was established, which allows testing of materials with elastic moduli below 1 MPa, whereas before only materials stiffer than several GPa could be tested. The advances in the surface identification are based on the usage of dynamically acquired instead of quasi-static quantities, which exhibit a much better signal-to-noise ratio, thus allow a more accurate surface detection. The improvements of this method were successfully demonstrated for polymers ranging over 4 orders of magnitude in modulus. For a quantitative determination of the contact area, comparative finite element simulations, in-situ indentation tests and tensile tests were performed. Several factors like viscoelasticity and adhesion can influence the contact area of polymeric materials; thus they must be taken into consideration, which is not done in the widely used Oliver & Pharr method for contact area determination. Through this comparative approach, individual sources of error were identified and their contributions quantified. The Oliver & Pharr method was found to underestimate the contact area for shallow indentations, because the contact increase due to adhesive forces is neglected. For high penetrations, the sink-in effect is underestimated slightly. This leads to the conclusion that common indentation techniques are not applicable to soft polymeric materials without modifications. A methodology with alterations necessary for achieving accurate indentation results is provided in the present study. Thus, nanoindentation is confirmed as a usable tool for the mechanical characterization of materials with elastic moduli below 1 MPa.

Julia Deuschle

Mechanik der Indentation von weichen Polymeren

189 Seiten, 67 Abbildungen, 8 Tabellen

Kurzzusammenfassung

Nanoindentation als Methode zur Bestimmung mechanischer Kenngrößen wird heute in verschiedensten Bereichen angewendet. Vorteilhaft gegenüber konventionellen Prüfmethoden sind dabei die hohe Kraft- und Wegauflösung und die kleinen Probenvolumina, die zur Messung ausreichen. Diese Eigenschaften haben, bedingt durch die rasche Entwicklung von Medizin- und Biotechnologie, ein starkes Interesse an der Anwendung von Nanoindentation auf weiche Materialien hervorgerufen. In der vorliegenden Arbeit wurden systematische Untersuchungen an Polymeren durchgeführt. Es zeigte sich, dass die Oberflächenfindung und die Kontaktflächenbestimmung die beiden entscheidenden Faktoren für eine verlässliche Bestimmung der mechanischen Eigenschaften weicher Materialien darstellen. Zunächst konnte die Oberflächendetektion wesentlich verbessert werden, wodurch die Basis für die Untersuchung von Proben mit E-Moduli unter 1 MPa geschaffen wurde. Im Vergleich dazu konnten vorher nur Proben mit E-Moduli von einigen GPa getestet werden. Die neue Methode verwendet die dynamische Kontaktsteifigkeit, die im Gegensatz zur sonst verwendeten statischen Kontaktsteifigkeit ein deutlich geringeres Rauschen aufweist und somit eine sensiblere Oberflächendetektion ermöglicht. Die weiteren Arbeiten konzentrierten sich auf eine quantitative Ermittlung der Kontaktfläche und eine Quantifizierung der Effekte, die die Kontaktfläche verändern können. Bei Polymeren sind hier vor allem Viskoelastizität und Adhäsionseffekte zu nennen. Durch Vergleiche zwischen Nanoindentation, In-Situ Indentation, Finite Elemente Simulationen und Zugversuchen konnte herausgefunden werden, dass die Kontaktflächen, die üblicherweise mittels der Oliver & Pharr Methode bestimmt werden, deutlich von den tatsächlichen Werten abweichen. Für geringe Eindringtiefen werden adhäsive Kräfte vernachlässigt, daher sind die Kontaktflächen bis zu 40 % zu klein; bei Eindringtiefen oberhalb einiger µm ergeben sich um ca. 5 % zu große Kontaktflächen. Diese Abweichungen sind zurückzuführen auf das Deformationsverhalten der Elastomere, das sich klar von der Verformung elastisch-plastischer Materialien unterscheidet. Diese im Rahmen der vorliegenden Arbeit erzielten Erkenntnisse erlauben nun eine geeignete Wahl der Indentationsmethodik für Polymere und biologischen Materialien und bestätigen somit, dass eine adäquate mechanische Charakterisierung solcher Materialien mittels Nanoindentation möglich ist.

Danksagung

Die vorliegende Arbeit wurde in der Zeit von Dezember 2004 bis Oktober 2007 am Max-Planck-Institut für Metallforschung in Stuttgart angefertigt. An dieser Stelle möchte ich denjenigen von Herzen danken, die mich bei dieser großen Aufgabe begleitet und unterstützt haben und am Gelingen dieser Arbeit beteiligt waren:

An erster Stelle danke ich Herrn Prof. Eduard Arzt ich für die Aufnahme in seine Arbeitsgruppe und die Möglichkeit, diese Arbeit in seiner Abteilung durchführen zu können.

Herrn Prof. Fritz Aldinger gilt mein Dank, da er sich freundlicherweise bereit erklärt hat, den Mitbericht zu übernehmen.

Ein riesengroßes, von Herzen kommendes Dankeschön geht an meine Betreuerin Frau Dr. Susan Enders. Durch ihre stete Unterstützung und Ermutigung über alle Entfernungsskalen hinweg und nicht zuletzt durch ihr großes Fachwissen hat sie wesentlich zum Gelingen dieser Arbeit beigetragen. Es war mir ein Vergnügen mit ihr zusammen zu arbeiten.

Diese Arbeit ohne PDMS ist schwer vorstellbar. Ohne Herrn Dr. Emerson de Souza, die unerschöpfliche Quelle für PDMS-Proben und den Überfluss seiner Ideen wäre diese Arbeit sicher nicht das geworden, was sie jetzt ist. Dafür bin ich ihm zu großem Dank verpflichtet.

Herrn Prof. Bernd Kröplin möchte ich meinen Dank aussprechen für die Möglichkeit, die FEM-Erfahrung am ISD zu nutzen und meine Simulationen dort durchführen zu können. Bei allen ISD-lern möchte ich mich für die freundliche Aufnahme und die angenehme Arbeitsatmosphäre bedanken.

Während meiner Aufenthalte in Thun durfte ich erfahren, dass die EMPA nicht nur grandiose Ausblicke auf die Natur, sondern auch sehr aufschlussreiche Einblicke „in die Natur“ zu bieten hat! Ganz herzlichen Dank an Herrn Gerhard Bürki für die unzähligen Versuche und Videos, die er für mich gemacht hat. Herrn Dr. Johann Michler danke für die fruchtbare Zusammenarbeit und sein Interesse an meiner Arbeit.

Für hilfreiche Diskussionen, nützliche Tipps im Umgang mit MTS-Geräten und die Unterstützung beim Fortgang meiner Arbeit möchte ich mich bei den Herren Ryan O'Hagan, Michel Fajfrowski, Pierre Morel und Jerry Anderson bedanken. Zu Dank verpflichtet bin ich auch Herrn Dr. Holger Pfaff, der mir stets mit Rat und Tat zur Seite stand und vor allem als „Ersthelfer" für krankende Indenter und strapazierte Nerven wertvolle Dienste geleistet hat.

Frau Dr. Nicole Rauch gilt mein Dank für die Durchführung der Rheometermessungen in Kooperation mit dem IDM der Universität Ulm und das Interesse, mit der sie meine Arbeit begleitet hat. Frau Dr. Zaklina Burghard hat für mich einige Messungen am Hysitron-Indenter gemacht. Vielen Dank dafür!

Für die Konstruktion und Fertigung des In-situ-Messaufbaus für das Bionix-System bedanke ich mich bei Herrn Frank Thiele und Herrn Hubert Knebel.

Dank sagen möchte ich Herrn Prof. Al Crosby, der als Polymer-Spezialist durch seine Kommentare zum 5. Kapitel sehr zur Verbesserung dieses Teils beigetragen hat.

Allen Kollegen der Abteilung Arzt möchte ich für das angenehme Arbeitsklima danken. Im Besonderen geht mein Dank an unsere Sekretärin Frau Jutta Heß, sowie an Herrn Dr. Stanislav Gorb, Frau Dr. Camilla Mohrdieck und Frau Dr. Ulrike Wegst, die mir durch ihre Hilfe und in vielen Diskussionen oft zu neuen Ideen verholfen und mir wesentliche Dinge aufgezeigt haben. Bei Frau Dr. Viola Küstner bedanke ich mich für die Hilfe bei der Fertigstellung der Arbeit.

Für ihre Freundschaft und ihr offenes Ohr für kleinere und größere Probleme aller Art möchte ich mich bei Frau Ellen Wohlfart bedanken.

Mein Mann Matthias war durch die Hilfe bei den FE-Simulationen für diese Arbeit fachlich eine tragende Stütze. Ohne seine Unterstützung im Privaten wäre diese Arbeit kaum möglich gewesen. Für seinen Rückhalt, sein Vertrauen und seine Geduld mit mir danke ich ihm aus tiefstem Herzen.

List of Contents

List of symbols and abbreviations

Symbols

α	Face opening angle of indenter tip	[°]
a_c	Contact radius	[m]
A	Tip area function	[-]
A_c	Contact area	[m^2]
β	Geometry correction parameter	[-]
B	Fitting parameter in the Oliver & Pharr method	[-]
γ	Shear deformation	[-]
C_{10}	Neo-Hooke parameter	[Pa]
δ	Phase angle	[°]
D	Damping	[N/m]
D_1	Neo-Hooke parameter	[Pa]
D_i	Damping of the indenter head	[N/m]
D_s	Damping of the sample	[N/m]
ε	Strain	[-]
ε	Tip geometry parameter	[-]
E	Elasticity modulus	[Pa]
E*	Complex modulus	[Pa]
E’	Storage modulus	[Pa]
E’’	Loss modulus	[Pa]
E_r	Reduced modulus	[Pa]
ϕ	Half included angle of indenter tip	[°]
F	Harmonic force	[N]
F_0	Amplitude of harmonic force	[N]
h	Tip displacement	[m]
h_c	Contact depth	[m]
h_f	Final depth after indentation	[m]
h_{max}	Maximum displacement	[m]
h_s	Surface displacement	[m]
H	Hardness	[Pa]

I	Strain tensor invariant	[-]
J_{el}	Elastic volume ratio	[-]
K	Bulk modulus	[Pa]
K	Stiffness	[N/m]
K_0	Initial bulk modulus	[Pa]
K_f	Load frame stiffness	[N/m]
K_s	Support spring stiffness	[N/m]
λ	Principal stretch	[-]
l	Length	[m]
l_0	Initial length	[m]
μ	Shear modulus	[Pa]
μ_0	Initial shear modulus	[Pa]
m	Mass	[g]
m	Fitting parameter in the Oliver & Pharr method	[-]
ν	Poisson's ratio	[-]
N_v	Number of network chains per unit volume	[1/m^3]
P	Load	[N]
P_{max}	Maximum load	[N]
R_a	Root mean square roughness	[m]
σ	Stress	[Pa]
S	Contact stiffness	[N/m]
S_{unl}	Unloading stiffness	[N/m]
t	Time	[s]
T_g	Glass transition temperature	[K]
ω	Angular frequency	[°]
z	Harmonic displacement	[m]
z_0	Amplitude of harmonic displacement	[m]

Abbreviations

AC	Alternating current
AFM	Atomic force microscopy
CCD	Charge coupled device
CSM	Continuous stiffness measurement
DC	Direct current
DMA	Dynamic mechanical analysis
DSI	Depth sensing indentation
3D	Three-dimensional
FEA	Finite element analysis
FEM	Finite Elemente Methode
Gew %	Gewichtsprozent
HDPE	High density polyethylene
IRHD-SS	International rubber hardness degree-super soft
JKR	Johnson-Kendall-Roberts
LT	Lead term of area function
MD	Molecular dynamics
O&P	Oliver and Pharr method
PC	Polycarbonate
PDMS	Polydimethylsiloxane
PE	Polyethylene
PMMA	Polymethylmethacrylate
PS	Polystyrene
PU	Polyurethane
REM	Rasterelektronenmikroskop
RMS	Root mean square
SEM	Scanning electron microscopy
TEM	Transmission electron microscopy
UHMWPE	Ultra-high molecular weight polyethylene
wt %	Weight %

1 Introduction and motivation

The determination of mechanical properties of materials such as elastic modulus and hardness by means of nanoindentation has become more and more popular in recent years [1]. Testing equipment and methods underwent a continuous improvement. This technique, also termed depth-sensing indentation (DSI), is used widely to study the behavior of metallic or ceramic engineering materials. It also offers a favorable means for the investigation of the mechanical behavior of thin films and coatings, which is essential for many technical applications, e.g. for microelectronic devices and protective coatings. Due to the limited dimensions and reduced materials volumes of thin films, it is not possible to measure the properties with classical methods like tensile or bend testing. Thus, the capability of DSI to probe mechanical properties in confined volumes and with sub-micron spatial resolution is a unique feature in the field of mechanical testing. For the same reason, DSI is not only a useful technique for the investigation of hard films but can also be beneficial for mechanical characterization of very compliant materials, e.g. polymeric materials or biological tissues.

Polymers with moduli of several GPa are more and more used as wear-and scratch-resisting coatings, electrically insulating or optically functional coatings, softer polymeric materials (modulus < GPa) are intended to be used as artificial tissue substitutes for medical applications. The use of polymeric material in reduced dimensions, however, requires methods for investigating the mechanical properties that can, on one hand, account for the time-dependent viscoelastic behavior of polymers and, on the other, are capable of measuring forces below the µN-range, which are associated with mechanical testing of such compliant materials. Several studies reported in the literature [2-8] indicate that nanoindentation can be successfully applied to measure mechanical properties of polymers, but there is still some uncertainty associated with the accuracy of these measurements.

Also in the biological field more and more knowledge is gained about processes, which are strongly dependent on the mechanical properties of the related tissues/materials. For many diseases, ranging from caries to cancer, it was found that their development is accompanied or presumably even caused by changes in mechanical properties of the tissues involved. Thus, the understanding and investigation of the properties of such materials is of great importance for medical and clinical purposes. Again, this underlines the need for the development of techniques, which are capable of determining mechanical properties of materials with elastic moduli down to the kPa-range. Nanoindentation is one of the most promising techniques for the application in mechanical testing of soft materials and also small volumes, because the instrumentations possess many of the features, which are needed in this respect. Yet, the nanoindentation instruments still are designed for the use on hard and stiff materials, so their usage on soft samples makes it very difficult to obtain accurate results and poses questions that are still to answer. Since most of the approaches discussed in the literature are dedicated to modeling and correcting the experimentally obtained load-displacement data to account for undesired effects *after* the experiment is done, the objective of this work is to contribute to the development of more adequate nanoindentation testing methods that are especially designed for the characterization of different types of compliant materials, i.e. polymeric *and* biological materials.

The present work focuses on nanoindentation studies on various polymers. For this study only polymeric materials were chosen, because their properties are reproducible, which facilitates the analysis and evaluation of nanoindentation data. The selection was done in a way that the polymer properties cover a certain range of stiffnesses from the kPa- up to the GPa-regime. The first step in this work was the development of an improved testing method, which allows a more accurate surface detection for polymers and to verify the results obtained by the new method. This improved method was used to investigate the crosslinking and curing kinetics of Polydimethylsiloxane (PDMS) specimens. In order to deepen the general understanding of the indentation process and respective deformation mechanisms in polymeric materials, comparative finite element simulations and in-situ testing methods were applied. These techniques allowed a detailed investigation of the contact area evolution during indentation testing and hence a quantitative analysis of the surface detection errors, the influences of viscoelasticity and adhesion effects on the accuracy of indentation results for polymeric materials.

2 Literature review

In this section, a brief outline of current nanoindentation applications and the most common approaches to apply this testing method to the mechanical characterization of polymeric materials will be given. A more detailed literature review on specific issues related to the topics of the individual chapters can be found at the beginning of each chapter.

2.1 Current applications of nanoindentation

The accurate determination of mechanical properties of materials is essential to a lot of applications. In many cases the mechanical behavior is the determining factor for the performance and life time, not only in the construction of load bearing or structural components, but also for the application of materials as functional components and even for the biological function of body parts [9-11]. The conventional techniques for mechanical testing are uniaxial tests in tension or compression, bend tests or cyclic testing, which all have the following features in common: Specimens of macroscopic dimensions (sizes of several mm and g-quantities) are needed, the load resolution is in mN-range and they are time consuming due to little test automation. Contrary to this the ongoing trend in industrial and research development is towards miniaturization and automation, which requires for adequate methods to mechanically characterize structures in the sub-µm range [12].

A generally accepted and widely used technique, which accounts for these demands, is depth-sensing indentation, which was presented in its most popular form by Oliver and Pharr [12] in 1992. This technique was developed according to the principles of macroscopic hardness measurements of the Vickers or Brinell type, in DSI, however, the load and displacement data are recorded continuously during an experiment. The theoretical background of indentation relies on classical work in contact mechanics by Hertz [13], Boussinesq [14], and Sneddon [15]. Although the instrumentations were originally developed for stiff/hard bulk materials like metals or ceramics, the load and displacement resolutions of today's commercially available instruments are typically below one nN and one nm [16]. Thus, these instruments offer the possibility to test specimens apart from engineering materials like thin films [17-19].

The application of nanoindentation testing to biological tissues often is motivated by medical interests, since many diseases are associated with altered or altering mechanical properties of the respective biological tissues [20]. Thus, the investigation of tissue properties can help in preventing and healing of diseases. One example for the relations between mechanical properties and diseases is the formation of caries. In different studies [10, 11, 21] it was possible to correlate areas of reduced mineral content in the human dental enamel with decreased modulus and hardness values. These regions of lower mineral content and reduced properties were exactly the positions, where lesion and cavity formation occurred later on. Another important aspect for medical/clinical applications is the probing of materials used as artificial restorations for body parts and tissues in the human body. In order to properly fulfill their purpose in the human body, these materials need to have comparable properties and a similar behavior as the original biological tissue. For hard tissues like dental enamel or bone, ceramics or metals may be used [21]. For softer tissues like cartilage or skin, however, softer materials, i.e. polymeric materials are suitable [22]. The mechanical characterization of these very soft materials is a very challenging issue, since they are very damageable, have to be kept hydrated and are available only in small quantities. One possible approach to account for this is AFM–based nanoindentation, as it has been shown by Berger et al. [20].

2.2 Testing of polymers

In recent years a growing interest in mechanical testing of “soft” materials with moduli below 1 GPa for medical purposes and also for industrial and technological reasons can been seen, indicated e.g. by the elaboration of a new DIN testing standard for macroscopic hardness measurement of “supersoft” polymers (International Rubber Hardness Degree Super Soft IRHD-SS) [1]. Also in the field of polymer research much work dealing with nanoindentation testing of polymeric materials and its challenges was carried out [2-8, 23-30]. The most difficult and challenging features are the time-dependent viscoelastic behavior and the low forces and stiffness values respectively in the µN- and MPa-range or below. Various approaches to account for the low stiffnesses and the viscoelasticity will be discussed more detailed in the following.

The high compliance of polymers in comparison to metals or ceramics leads to very low forces during the indentation experiment. The forces that typically occur during an indent on a polymer sample are in the hundreds of µN for the maximum applied force and in the nN-range for the initial tip-sample contact force [2, 4, 6]. First of all, these forces have to be measured accurately, which requires a sufficient load resolution of the instrument and the stability of the surrounding conditions in the laboratory [23]. For most commercially available nanoindentation instruments, the theoretical load resolution is below 1 nN, they are thus theoretically capable of detecting the initial contact; in practice, however, the achievable load resolution is no better than 100 nN [2, 16]. This is due to noise in the measured force data caused by vibrations and thermal drift. Therefore it is common to position the instruments in laboratories with temperature control and to run measurements over night.

As mentioned above, a critical issue concerning the low forces is the detection of the initial point of contact between the tip and the specimen, so to speak of “finding” the specimen surface and setting the measured indentation depth as well as the contact area to zero. In many instruments a certain amount of pre-loading (~ 1 µN) is used for identifying the surface regardless of the specimen stiffness, which can correspond to a considerable indentation for softer materials with the measured contact depth and area being in error [2-4, 23, 24]. As the contact area is directly used for the calculation of the hardness and modulus values [12, 31], an incorrect surface detection leads to erroneous results. In general, it can be assumed that the softer the material, the larger the under-estimation of the contact area will be with the respective modulus and hardness values being too large. This is in agreement with experimental findings [2, 6], where nanoindentation results are higher than results obtained from other techniques such as dynamic mechanical analysis (DMA).

Although the surface detection should be the most important source of error, several other factors influence the determination of the contact area and must be considered as well. Despite its limited importance for the testing of softer materials, but for the sake of completeness the load frame compliance is mentioned. It was found by Van Landingham et al. [2] that the calibration procedure for the load frame compliance is influenced by the reference sample used. The load frame compliance values diverged by a factor of two when the indents were performed one time on a fused silica and the other on a tungsten specimen. This influence, however, decreases for higher ratios of load frame to specimen compliance, which is the case for polymeric samples. Another unforeseen but critical feature is the calibration of the tip area function itself when performed according to the Oliver & Pharr method on a fused silica standard [12, 31]. The intention of this procedure is to determine the tip area function, i.e. the appropriate function to convert the measured indentation depths into the projected contact area and to account for tip imperfections such as tip rounding, opening angle deviations or misalignment. Because of the high stiffness of silica the indentation depths that can be reached at maximum load of the instrumentation and thus the depths that can be calculated correctly, are several hundreds of nm, whereas indentations into polymeric materials far exceed this depth [2, 4, 6, 23]. So it is not possible to account for any deviation of the ideal geometric area function in the biggest part of indentation depth range, which may also lead to erroneous contact areas.

An interesting finding regarding the influence of adhesion forces between the tip and the sample on the contact area was made by Grunlan et al [32]. They carried out indentation experiments with diamond and tungsten tips on PS and PE samples and the comparison of results yielded significantly higher values for the diamond tip than for the tungsten tip. This is attributed to a stronger adhesion between diamond and the polymeric materials, which leads to some kind of pile-up effect and the contact area is underestimated by the area function. The original intention of this investigation was to verify the usage of tungsten tip for indentation of polymeric materials, because the fabrication of conical tungsten tips by electrochemical etching is relatively easy, fast and cheap compared to the complex fabrication of diamond tips. Several other studies on the influence of adhesive forces on the results of indentation tests have been conducted [33-36] and it was found that the contribution of adhesive forces is considerable and has to be taken into account, especially for shallow depths. These studies [33-35] present different approaches to correct the contact area for the adhesive portion in the framework of the Johnson-Kendall-Roberts (JKR) theory [37] for adhesive elastic contacts.

The properties of fused silica are well-known and stable and therefore it is commonly used as reference material for most of the calibration procedures and as standard material to control the well-functioning of the instrumentations. For testing of polymers with a considerably lower modulus, however, it would be favorable to use a polymeric material with similar modulus as a reference at least for the tip shape calibration [2]. One approach to overcome this uncertainty has been presented by Odegard et al. [4]. In this study DMA and nano-indentation testing results of several polymers were compared. The tip shape calibration was done on one of the test materials, and modulus from DMA was used to calculate the area function of the tip. Since in this case the value obtained from DMA might be the most accurate one available, this is an acceptable procedure. But generally the accuracy of this procedure is doubtable, because it is implemented here that the DMA measurements yield a proper modulus value and are free of error, which is certainly not the case. Anyway, the use of a nanoindentation method that can only be calibrated with the help of another technique for the determination of elastic moduli is more than questionable, especially if it is intended to verify the more convenient nanoindentation technique as an absolute technique. Although the need for a polymeric standard is certainly given, choosing a suitable material is tricky, because the material must possess constant and stable properties for a reasonable time frame and under a certain range of conditions. Considering inherent features associated with polymers like the glass transition and various degrees of crystallinity and their effects on the mechanical behavior [2], it is clear that it is almost impossible to select a polymer and to define one specific state of a certain hardness and modulus that matches the reproducibility and reliability needed for a standard.

Another very typical feature of polymers is their viscoelasticity, which results in a time–dependent deformation behavior. Under an applied load viscoelastic materials show a delayed deformation response in contrast to purely elastic materials, which reveal instantaneous deformation. In order to model the different types of behaviors in a phenomenological way elements like springs and dashpots and combinations of them are used. The classical representations and their reaction to the application of a stress can be seen in figure 1.

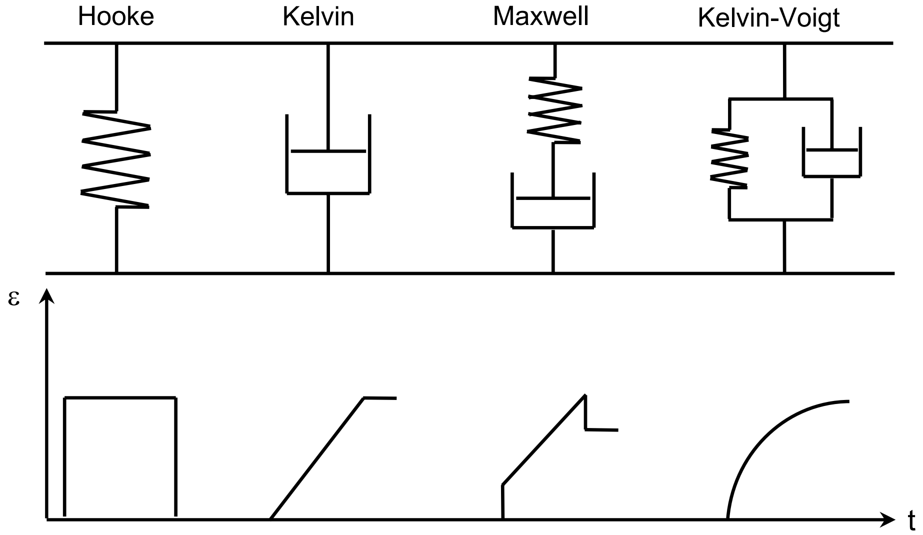

Figure 1: Classical elements used for modeling of elastic solids, viscous fluids, viscoelastic fluid-like behavior associated with stress relaxation as well as permanent deformation, and viscoelastic solid-like behavior showing retarded but reversible deformation [38].

The combined models in figure 1 (Maxwell and Kelvin-Voigt) can be connected to features occurring during indentation experiments of polymeric materials. Both, the occurrence of stress relaxation under constant deformation as well as retarded permanent deformation under constant load, which is referred to as creep, strongly influence the results of indentation experiments. It has to be carefully considered which quantity is extracted out of load-displacement data obtained from viscoelastic materials. Especially for quasi-static loading the effects of rate- dependency and relaxation time frames have to be taken into account, which makes quasi-static indentation of viscoelastic polymers a difficult issue.

In figure 2 a quasi-static indentation load-displacement curve for an elastic (figure 2a) and for a viscoelastic material (figure 2b) is shown. For the elastic material the upper portion of the unloading curve can be approximated linearly, whereas the curve for the viscoelastic material shows the typical nose-formation during unloading. This nose is caused by the delayed deformation, i.e. the displacement still increases during the peak load holding and even in the initial unloading stage although the load is already decreasing again. The increasing displacement during the constant load period is referred to as nanoindentation creep.

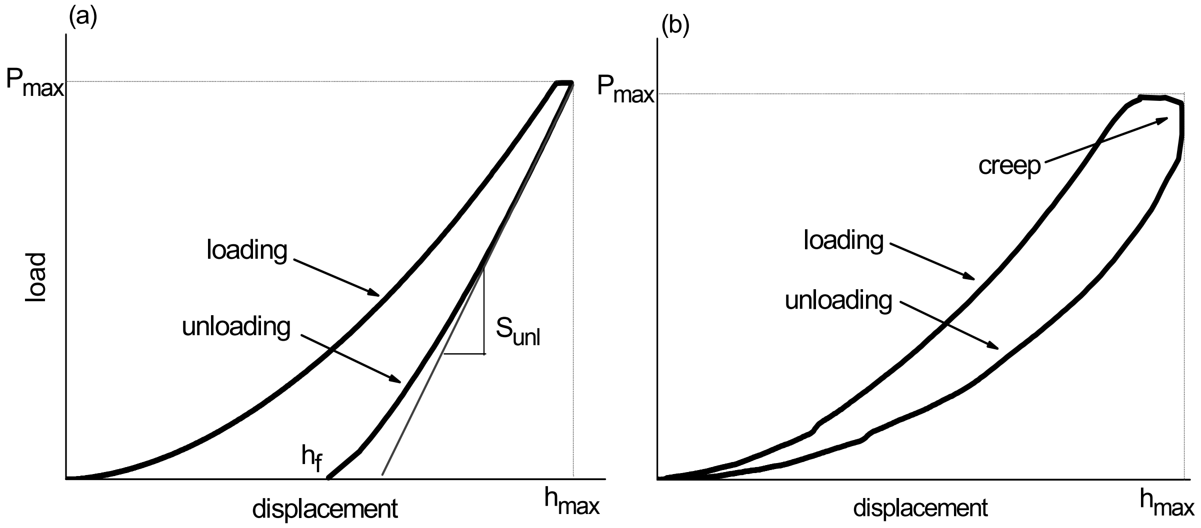

Figure 2: Typical load-displacement curves for an elastic (a) and a viscoelastic material (b). The unloading curve of the elastic material can be approximated linearly, whereas the unloading curve of the viscoelastic material shows a so-called nose. This nose is caused by creep and leads to trouble in the fitting procedure for analysis, because one and the same displacement value occurs at two different loads during the unloading stage.

In the conventional analysis of unloading data from indentation experiments according to the Oliver & Pharr method [12, 31] it is assumed that the initial part of the unloading curve corresponds to elastic recovery of the material and therefore is linear. The slope dP/dh of this linear part of the unloading curve is termed contact stiffness S and is used for the calculation of the modulus. As it can be seen from figure 2(b), the assumption of linearity does not apply for viscoelastic materials. Due to the delayed deformation the slope of the unloading curve appears steeper than it would be without viscoelastic effects, which brings about an overestimation of the modulus. In extreme cases the nose-effect can cause a negative slope and hence negative stiffness and modulus values [27]. The easiest way to overcome these difficulties is to adjust the testing parameters. It is generally acknowledged that longer peak load holding times and faster unloading rates are helpful in avoiding the occurrence of the nose [22, 23, 24]. The peak load holding times have to be longer than the characteristic relaxation time of the specimen in order to allow all the viscoelastic effects and relaxation to complete, thus elastic unloading can be achieved. In contrast, the unloading rate has to be sufficiently fast, i.e. quicker than the characteristic time, to suppress viscoelastic effects. Several investigators have carried out experiments with different unloading rates and found that for high enough unloading rates the curves converge to one single curve, which is assumed to represent the purely elastic reaction of the material [25, 27]. Tang and Ngan [27] have proposed formulas to correct for the creep effects in the measured contact depth and unloading stiffness calculation. These corrections were implemented in the Oliver & Pharr method. They simply assume that the total displacement is the sum of elastic, plastic and viscoelastic contributions and that the viscoelastic displacement only occurs in the peak load holding period for sufficient high loading and unloading rates.

Phenomenological modeling on the basis of the spring/dashpot elements in figure 1 is also used in literature to describe viscoelastic effects. For this purpose the elements are first put together to a certain combination, second a constitutive equation for the system behavior is derived and third the solutions of the constitutive equations are fitted to experimental indentation data by adjusting the parameters. As the adjustable parameters in these models correspond to the mechanical quantities elastic modulus and viscosity, they are yielded from modeling by the fitting procedure. Models used to describe the viscoelasticity of polymers are e.g. the generalized Kelvin-model, which is a spring, a dashpot and an user-defined number of Kelvin-Voigt elements in series applied to PC, PMMA, PS, PET and Epoxy specimens [26] or a 4-element combination of one Kelvin-Voigt and one Maxwell element in series applied to an 1 µm-thick Al film, fused silica and a polyurethane/acrylic copolymer film [29]. Considering the approaches used in [26, 29] it has to be noted, that the formulations are for linear viscoelasticity and therefore only hold for infinitesimal deformations [2, 6, 39]. For indentation experiments using a sharp pyramidal tip, however, the strains induced under the indenter tip are about 8 – 10 % [40], which requires non-linear viscoelastic treatment and subsequently the use of quadratic elements, as done by modeling the behavior of PMMA, PC, HDPE, PU and PDMS with a series of quadratic spring, quadratic dashpot and quadratic slider [30].

The most common approach to circumvent the difficulties of quasi-static testing is dynamic testing according to figure 3, where a sinusoidal load is applied and the resulting deformation is measured. For linear-viscoelastic materials the answer-function has the same angular frequency ω as the applied load function, but lags behind by a phase angle δ. The definition of a complex modulus E* according to

$$E^* = E' + iE'' = E^* \cdot \cos\delta + i \cdot E^* \cdot \sin\delta \qquad (1)$$

yields the storage modulus E' as the real part, thus the in-phase component, and the loss modulus E'' as the imaginary part, thus the out-of-phase component. The storage and the loss modulus of a material are considered as a measure for the capability of reversible energy storage and the heat losses due to internal friction.

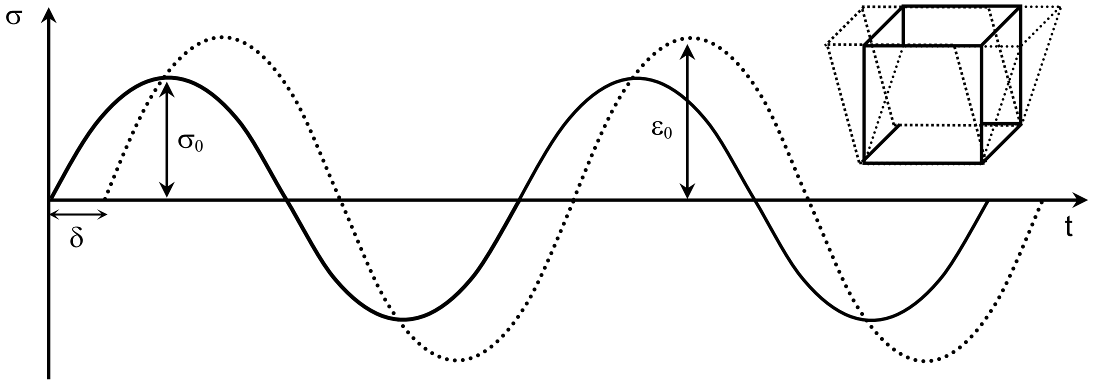

Figure 3: Dynamic testing of viscoelastic materials: the application of a sinusoidal load function of an amplitude σ_0 leads to an answer function of the same frequency with an amplitude ε_0, but shifted by a phase angle δ [41].

The determination of storage and loss modulus as a characterization of viscoelasticity by means of dynamic indentation testing is accomplished by exciting the tip to a sinusoidal oscillation in the **C**ontinuous **S**tiffness **M**easurement (CSM) mode [12, 31]. Recently, dynamic indentation techniques have been applied to facilitate the treatment of viscoelasticity in indentation testing [2, 4, 6, 23, 42]. Through the relatively high frequencies of tip oscillation, the retarded viscoelastic displacements should be suppressed and elastic responses should be obtained. Two straight forward applications of CSM are presented by Loubet et al. [7, 8] where natural rubber and LDPE were investigated and results were favorably compared with literature data.

In other studies, the results from dynamic indentation were compared with results obtained from DMA and good agreement between both techniques has been found [4, 6]. In both cases the dependence of the storage and loss modulus on the oscillation frequency was measured and only a slight but not significant increase with higher frequencies occurred in accordance with the DMA measurements. The amplitude of the tip oscillation has also been varied and in one case no effect has been seen [4], whereas in the other case a slight decrease in the moduli for amplitudes below 10nm was found. Fischer-Cripps introduced an alternative to CSM, namely multiple-frequency dynamic indentation testing [42], where a random force signal is applied to the indenter including a certain frequency range. The measured response is then deconvoluted into single frequency components by using a Fourier transformation. This is a favorable method since the frequency dependence of viscoelastic properties can be accessed by one single indent and thus may be time-saving, but computationally intensive.

For mechanical investigation of very soft or hydrated materials with stiffnesses below 1 MPa an atomic force microscope (AFM) can be used as an indentation tool as well. Hereby the specimen is mounted on a piezoelectric positioning stage and then pushed against the tip that is fixed to a cantilever. While the tip penetrates into the surface the cantilever deflection is measured with the help of a laser/photodiode system. For the conversion of the measured deflection into forces and to obtain the displacement into the specimen surface a reference curve is used, which is measured on a rigid material with no penetration of the tip into the surface. In this case the deflection of the cantilever can be directly coupled with the movement of the piezoelectric scanner and thus be subtracted from the curves measured on compliant specimens. But there are still several technical problems that limit the accuracy of results and have to be addressed when performing AFM indentation experiments [28]. First of all, the selection of the initial contact point has a clear influence on the results obtained [20]. Second, the alignment of the tip to the sample surface should be perpendicular, during indentation; however, the orientation of the tip to the specimen may change due to the cantilever deflection. Third the piezoelectric stage can show a hysteresis between movements in opposite directions (+/- z-direction). Last, the cantilever stiffness has to be known with some accuracy. Despite all these uncertainties the results presented in [28] agreed well with DMA measurements.

2.3 Simulation of nanoindentation

Complementary to experimental work simulation of nanoindentation, e.g. by finite element analysis (FEA), can be a useful and valuable tool, since it allows the investigation of problems, which require complicated or time-consuming experimental work or may even surpass the experimental scope. Further, simulation offers the possibility to vary the indentation parameters or other experimental conditions in a systematic and controlled way, thus their influence can be studied in more detail. In the literature studies on the effects e.g. of surface roughness [39], indenter geometry [43, 44], and sink-in/pile-up effects [45] have been presented.

One of the common aims of simulating the indentation process is to gain information on the deformation behavior and the stress and strain distributions which are developing under the indenter tip during loading [46-48]. A detailed finite element analysis of Berkovich indentation for elastic and elastic-plastic materials was performed in [46] and work on a broad spectrum of material behaviors was presented by Bucaille and coworkers [47, 48], who simulated not only indentation but also scratching. Covering the scope of elastically to plastically dominated deformation is done by varying the rheological factor, i.e. the ratio of elastic and plastic contributions in the overall deformation. These studies addressed not only the determination of stress/strain fields under the indenter but also the contact evolution (inside the contact area as well as in the contact periphery) and how this is influenced by the material behavior.

FEA provides not only information about sizes of the plastic zones but also on interactions of different components in a material system such as substrate effects for thin film testing, which is helpful for improving experimental work. Thus, it was confirmed [49, 50], that a maximum indentation depth of 10% of the film thickness should not be exceeded to avoid effects of the substrate in indentation experiments using a Berkovich tip. Further, it has been shown that for a hard film on a softer substrate the size of the plastic zone reaches or even can exceed the film thickness at an indentation depth of about 10-15 % of the film thickness.

The determination of the contact area from simulations [40, 45, 51, 52] is another very important issue, since the contact area is a crucial parameter in the calculation of mechanical properties from indentation data, but cannot be measured. For this purpose, the number of surface nodes in contact with the indenter tip can be taken according to [40]. This study [40] also included the simulation of viscoelastic material behavior and dynamic measurements (CSM) as well as the effects of loading/unloading profiles on the results from quasi-static testing. Chen and Ke [53] also worked on a more accurate determination of the contact area, which included sink-in and pile-up effects, but this time molecular dynamics simulations were performed instead of finite element analysis.

In general, molecular dynamics simulations (MD) can be performed in order to study small-scale or surface effects and effects related to atomistic mechanisms [53-58]. One example for the applications of MD simulations is the investigation of anisotropy in Al single crystals, where indentation followed by scratching was modeled for different crystallographic orientations and parallel to various slip systems [54]. For modeling of dislocation behavior MD simulations are a suitable tool, since analysis on the atomic level [55-57] can be used in order to study e.g. interactions of dislocations and grain boundaries or dislocation creation under an indenter tip. But also investigations focusing on polymeric materials and accounting for the typical macromolecular features like chain rotation and intermolecular forces have been done [57, 58]. According to the limits set by computational power, Päzold et al. simulated indentation tests where the maximum dimension of the sample did not exceed 120 Å, forces of 2 nN and chain lengths of 60 repetition elements [58]. In [59] the samples were cubic polyethylene blocks of 30 nm edge length. Here, the deformation mechanisms associated with indentation of differently oriented PE crystals and amorphous PE were investigated.

Although simulations can be helpful in many cases, it still has to be closely observed whether the conditions used in the simulation model allow conclusions that are directly transferable to experimental work. These models often use simplifying conditions for the sake of reducing computational power and time. One example for this is that the normal approach for simulating indentation experiments using pyramidal tips is modeling 2-dimensional or axis symmetric conical indenter representations instead of 3D representations [43, 44, 50, 60]. In some cases, however, these simplified models may not behave in the same way. Several studies [43, 44, 60] investigated the equivalency of indentation results from conical and Berkovich tips and noticeable discrepancies were found [44, 60]. In the work in [43] Cu indentations were simulated and a reasonable agreement between cone and 3D pyramidal results was obtained for Berkovich and Vickers tips, whereas the Knoop indenter could not be replaced by a cone successfully. Therefore, model simplifications have to be validated carefully to assure that the modeling mirrors the real problem and trustable results are obtained.

3 Experimental

The following section is intended to give an overview about the theory of instrumented indentation and the Continuous Stiffness Measurement (CSM), which will be described together with the nanoindenter setup. Further, the relevant properties of the polymeric materials, which have been used in this study, are illustrated briefly.

3.1 Instrumentation

In principle, nanoindentation can be considered as hardness testing at the nanometer scale. To test a sample an indenter tip of a certain shape is driven into the surface, while the applied force and the resulting penetration are continuously monitored. The set of load-displacement data obtained from such an indentation test can be used for the determination of mechanical properties of the specimen. A Nano Indenter SA2® from MTS Nano Instruments (Oak Ridge, TN, USA) equipped with CSM was used for the performance of the indentation testing. The setup of the instrument is shown in figure 4.

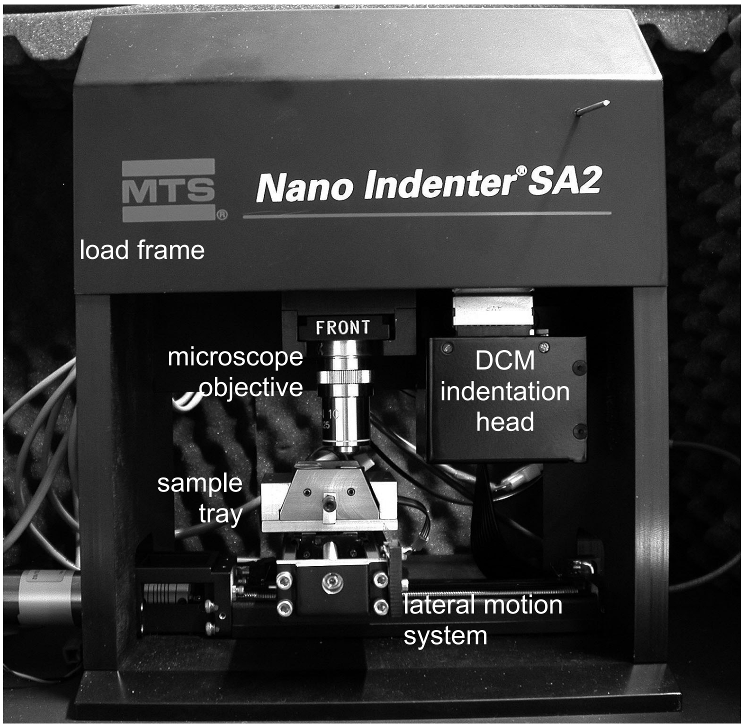

Figure 4: Nano Indenter SA2® with Dynamic Contact Module (DCM) head [61]. For the performance of experiments the system is placed on a vibration isolation table to reduce external vibrations and then put into an isolating cabinet for maintaining thermal stability.

A deeper insight in the construction of the actual indentation head/indenting system is provided by the schematic drawing in figure 5. As can be seen the load application is accomplished electromagnetically by passing a current through a coil-magnet assembly. The theoretical load resolution of the system is 50 nN. For quasi-static loading a DC voltage is applied to a maximum load of approximately 20 mN, for dynamic testing with the CSM technique a sinusoidal AC voltage is superimposed. The acquisition of the indenter shaft movement, which is, by construction, the same as the displacement of the indenter tip, is performed by a three-plate-capacitive gage. Two plates, the upper and the lower one are fixed to the head and have a hole to let the indenter shaft pass through. The middle plate is fixed to the indenter shaft and moves up and down together with the tip when the system is loaded or unloaded. The position of the center plate within the outer plates can be obtained by measuring the voltage between the center plate and both of the outer plates. This displacement sensing system allows a theoretical displacement resolution of 0.01 nm. The total displacement range accessible is determined by the gap between the two outer plates and is about 40 µm for this instrument. Further the indenter shaft is supported by two springs that possesses a stiffness of ~ 80 N/m in the z-direction, i.e. the direction of the shaft up and down movement. It has to be noted that these springs also have to be deflected during loading, which requires a certain amount of force.

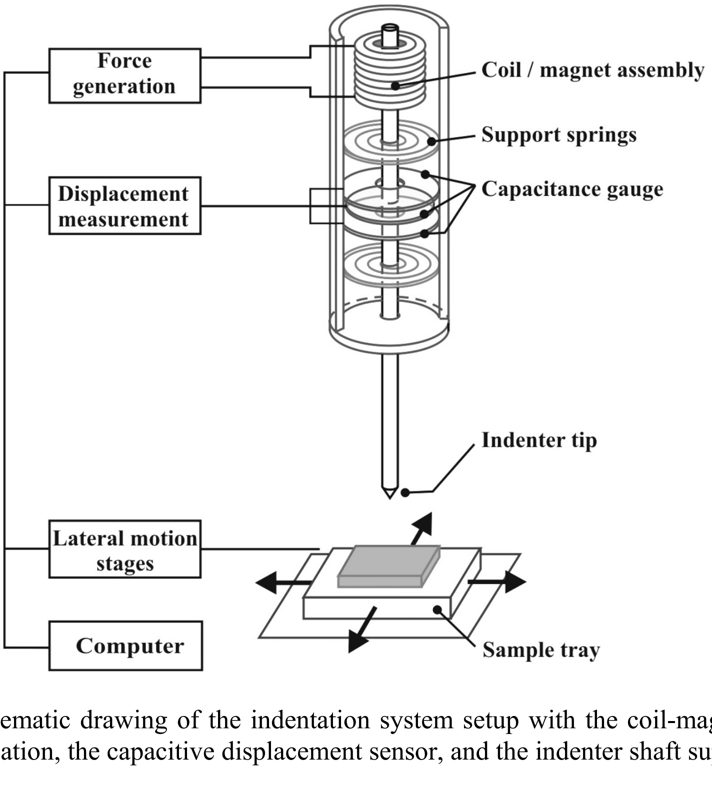

Figure 5: Schematic drawing of the indentation system setup with the coil-magnet assembly for load application, the capacitive displacement sensor, and the indenter shaft support springs.

3.2 Theory of nanoindentation

3.2.1 Quasi-static indentation analysis according to the Oliver & Pharr method

Nanoindentation experiments can be conducted in a quasi-static way to measure the elastic modulus and the hardness or in a dynamic way to determine the storage and the loss modulus of a material. During a quasi-static test a continuously increasing force is applied to the indenter tip until a certain load level (i.e. in load-control) or penetration depth (i.e. displacement control) is reached, and then the indenter is unloaded again. During the loading segment a hardness impression is formed as a result of elastic and/or plastic deformation occurring under the indenter tip. Upon the withdrawal of the tip the elastic portion of the deformation recovers and thus allows the elastic modulus of the material to be quantified. The amount of plastic deformation in the specimen can be identified from the permanent hardness impression. In contrast to conventional hardness testing the hardness value from nano-indentation is not yielded from the size of the permanent impression. Here, the hardness H is defined as the mean pressure under the indenter tip and is calculated according to:

$$H = \frac{P_{\max}}{A_{\max}} \tag{2}$$

where $P_{\max}$ is the maximum load applied and $A_{\max}$ is the contact area at maximum load. For the calculation of the elastic modulus from the unloading curve two equations are needed:

$$E_r = \frac{\sqrt{\pi} \cdot S}{2\beta\sqrt{A_c}} \tag{3}$$

In equation (3), S is the unloading contact stiffness, A_c the contact area, β is a constant depending on the indenter geometry and E_r is the reduced modulus. The reduced modulus E_r is an effective modulus combining the moduli of the tip material and the specimen according to:

$$E_r = \frac{1-\nu_s^2}{E_s} + \frac{1-\nu_i^2}{E_i} \tag{4}$$

Here E is the Young's modulus and ν the Poisson's ratio for the specimen (denoted by subscript s) and for the indenter (denoted by subscript i), respectively.

In order to gain the elastic modulus from equation (3) the determination of the unloading contact stiffness and the contact area are necessary first. Therefore the unloading curve is fitted to a power-law relation proposed by Oliver and Pharr [12, 31]:

$$P = B \cdot (h - h_f)^m \tag{5}$$

where P is the applied load, h is the resulting penetration, h_f is the depth of the residual impression and B and m are fitting parameters. The analytical differentiation of equation (5) delivers the slope of the unloading curve dP/dh, which is equivalent to the unloading stiffness S when evaluated at the maximum penetration h_{max}:

$$S = \left.\frac{dP}{dh}\right|_{h=h_{\max}} = Bm(h - h_f)^{m-1} \tag{6}$$

As can be seen from equations (2) and (3) the determination of the contact area is important for achieving exact results from indentation testing. The area function A(h), which is used to compute the contact area A_c, geometrically relates the projected, i.e. the cross-sectional area of the indenter tip to the distance from its apex. Thus, with a known area function, the measurement of indentation depth h is sufficient to obtain hardness and elastic modulus, when applying the load-displacement relationship (7) and the equation for the surface displacement h_s (8) deduced by Sneddon [15]:

$$h - h_f = 2\frac{P}{S} \tag{7}$$

The term (h-h_f) in equation (7) corresponds to the displacement caused by elastic deformation only. For the displacement of the surface the following equation is given:

$$h_s = \frac{\pi - 2}{\pi} \cdot (h - h_f) \tag{8}$$

The overall displacement of the indenter is the sum of the contact depth and the surface displacement, which can be seen from the schematic sketch in figure 6, where all the quantities used in the analysis are illustrated. The relationship for the contact depth can now be established by taking equations (7) and (8) into account:

$$h_c = h_{\max} - h_s = h_{\max} - \varepsilon \frac{P}{S} \tag{9}$$

with ε being a geometric constant with a value of 0.72 for a conical indenter tip, 0.75 for a paraboloid of revolution and 1 for a flat punch. Once the contact depth has been determined for an indentation, the contact area is simply the value of the area function at the contact depth A (h_c). The area function A (h) itself is calibrated for each tip individually by indenting a fused silica standard of known modulus and calculating the contact area from equation (3). For three-sided pyramidal indenter tips A (h) is given by:

$$A(h) = LT \cdot h_c^2 + \sum_{i=0}^{7} C_i \cdot h_c^{1/2^i} \tag{10}$$

$$= LT \cdot h_c^2 + C_0 h_c + C_1 h_c^{1/2} + C_2 h_c^{1/4} + C_3 h_c^{1/8} + C_4 h_c^{1/16} + C_5 h_c^{1/32} + C_6 h_c^{1/64} + C_7 h_c^{1/128}$$

The actual shape of the pyramidal tip is determined by the lead term *LT* in equation (10), which is 24.56 for a perfectly sharp Berkovich tip and 2.57 for a perfect cube corner tip. The constants C_i are derived from curve fitting and are necessary to account for tip imperfections.

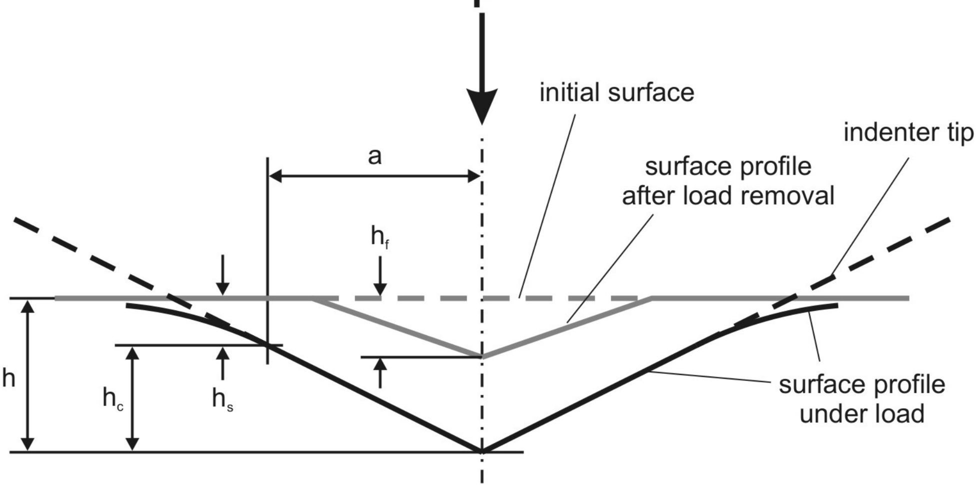

Figure 6: Cross-section of an indentation with the parameters h (indenter displacement), h_s (surface displacement), h_c (contact depth), h_f (final impression depth), and a (radius of contact circle), which are used in the Oliver & Pharr method.

3.2.2 Continuous Stiffness Measurement (CSM)

The CSM technique offers a means of performing dynamic nanoindentation testing, thus allowing viscoelastic quantities like storage and loss modulus to be determined as well as hardness and modulus to be measured as a continuous function of penetration depth. Further, the detection of the initial contact point is facilitated [12; 31]. For the purpose of dynamic testing the indenter is loaded in the same way as it is done during the quasi-static test but additionally to this load a small sinusoidal load signal is superimposed to excite the tip and forcing it to oscillate. In figure 7 the overall loading during a CSM indentation is illustrated.

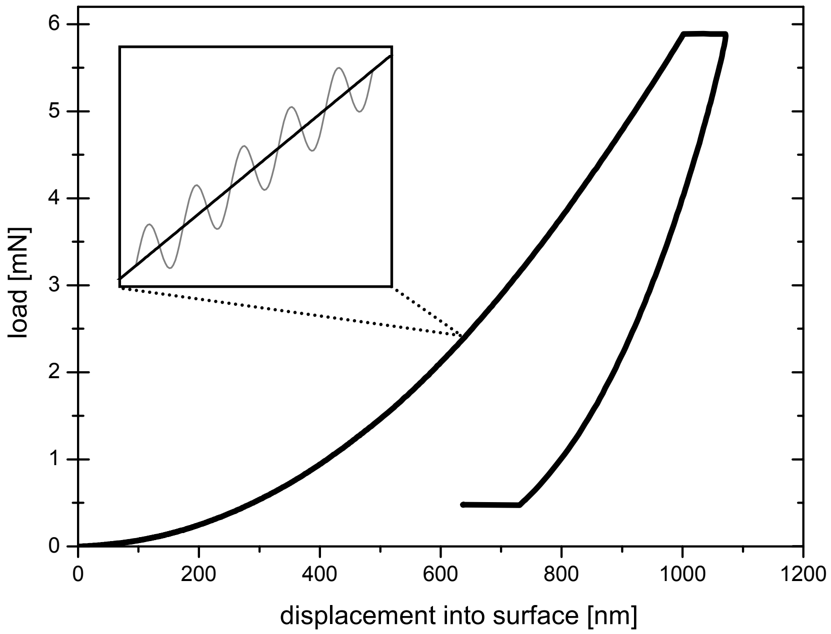

Figure 7: Quasi-static loading, load holding and unloading during an indentation are represented by the black curve; the dotted sinusoidal curve in the inset illustrates the superimposed dynamic loading.

In order to figure out the dynamic behavior of the specimen, one first has to consider the overall dynamic behavior of the system and find a way to separate the responses attributed to the instrument and the ones coming from the specimen. To accomplish this issue, the behavior of the whole system under dynamic conditions is treated as a harmonic oscillator and modeled in the way shown in figure 8 [50].

When the sinusoidal force signal with an angular frequency ω and amplitude F_0 is applied to the system according to

$$F(t) = F_0 \cdot e^{i\omega t} \tag{11}$$

the resulting displacement z(t) has the same frequency but lags behind by a phase angle δ :

$$z(t) = z_0 \cdot e^{i\omega t+\delta} \tag{12}$$

where z_0 is the displacement amplitude resulting from the excitation F (t).

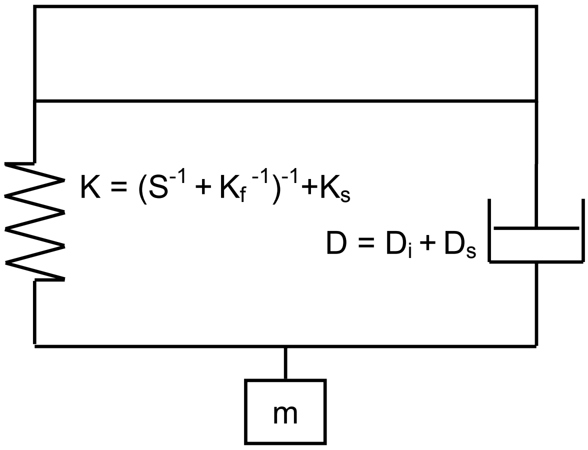

Figure 8: Model of a harmonic oscillator used to describe the dynamic behavior of the overall system through the parameters of effective stiffness K, effective damping D and the mass m of the indenter shaft; including instrument and specimen contributions to stiffness and damping [62].

The differential equation of motion that holds for a harmonic oscillator is given by:

$$F(t) = m\ddot{z} + D\dot{z} + Kz \tag{13}$$

where F (t) is the force, m is the mass, D is the effective damping, K is the effective stiffness, and z represents the displacement and its derivatives with respect to time. As already indicated in figure 8 the effective stiffness and effective damping can be separated into its components according to the model presented in figure 9. The effective stiffness K thus can be written:

$$K = K_s + \left(\frac{1}{S} + \frac{1}{K_f}\right)^{-1} \tag{14}$$

with K_s being the support spring stiffness, K_f the load frame stiffness, and S the contact stiffness. The effective damping D also can be rewritten as:

$$D = D_i + D_s \tag{15}$$

Here D_i is the damping of the capacitive gage in the head and D_s is the damping of the contact.

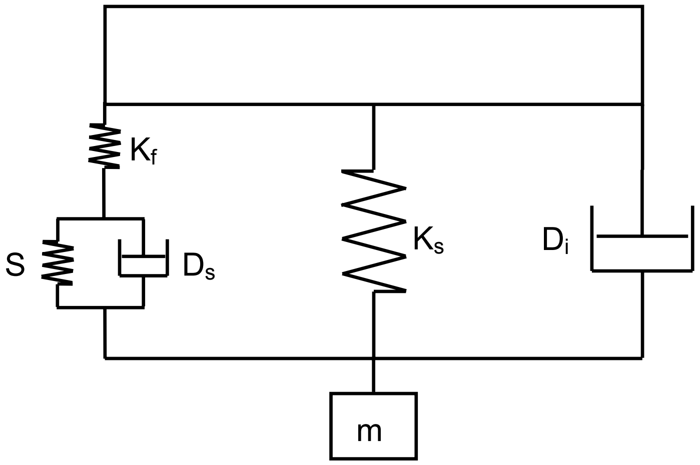

Figure 9: Model used to describe the dynamic responses of the indentation head (D_i), load frame (K_f), support springs (K_s), and the tip/sample contact (S) [61, 62].

After considering the overall behavior of the system and dividing it into individual contributions, the quantities of interest, namely contact stiffness and contact damping, can be calculated. Substituting equations (14) and (15) into equation (13) and applying it to its particular solution (12) the following relationships can be obtained for the contact stiffness:

$$S = \left(\frac{1}{\frac{F_0}{z_0} \cdot \cos\delta - (K_s - m\omega^2)} - \frac{1}{K_f} \right)^{-1} \tag{16}$$

and for the contact damping:

$$D_s \cdot \omega = \frac{F_0}{z_0} \cdot \sin\delta - D_i \cdot \omega \tag{17}$$

The viscoelastic properties storage E’ and loss modulus E’’ are related to the quantities given in equations (16) and (17) by the contact area A as follows:

$$E' = S \cdot \frac{\sqrt{\pi}}{2\sqrt{A}} \tag{18}$$

$$E'' = D_s \omega \cdot \frac{\sqrt{\pi}}{2\sqrt{A}} \tag{19}$$

The ratio of the loss and the storage modulus is referred to as the loss tangent, which is usually taken as a measure for heat losses in a material:

$$\tan\delta = \frac{E''}{E'} \tag{20}$$

The storage and the loss modulus can be determined with the CSM technique using equations (16) and (17), since all the values needed are available from the CSM data. During an indentation the angular frequency is set, the force and displacement amplitudes F_0 and z_0 are measured continuously along with the phase angle δ. The other terms referring to the instrument behavior are evaluated by calibration procedures with the indenter hanging free in the air for acquiring m, K_s, and D_i and indenting the fused silica standard for determining the load frame compliance. The phase angle is determined with the help of a lock-in amplifier.

As an additional advantage of CSM it has to be mentioned that through this technique the surface finding, i.e. the detection of the initial point of contact between the indenter tip and the specimen, is simplified and more accurate, because the behavior of the system with the indenter hanging in the air and the system in contact with the sample can be monitored and the transition between both stages can be associated with the contact formation. This contact formation should be identifiable in the stiffness values, the damping values, the quantities related to the dynamic loading F(t) and in the phase angle.

3.3 Materials

The polymeric materials that where used for this investigation are an epoxy based photo resist SU8, two types of polyethylene, **l**ow **d**ensity LDPE and **u**ltra **h**igh **m**olecular **w**eight UHMWPE (Goodfellow) as well as **P**oly**D**i**M**ethyl**S**iloxane PDMS (Dow Corning). These materials were selected in order to cover a wide range of stiffnesses reaching from elastic moduli of several GPa down to moduli of several MPa. For SU8 and the PE materials the elastic modulus is well characterized, thus these materials were used as reference materials to verify the results obtained from our measurements in chapter 4. The chemical structure of the SU8 epoxy is given in figure 10. This material has a Young's modulus of 4.4 GPa and a Poisson's ratio of 0.22. The SU8 specimen was a spin-coated layer on a silicon substrate, approximately 5µm thick. The LDPE and UHMWPE were provided in form of sheets and cut into rectangular pieces. Due to the high surface roughness of the sheets the specimens were mechanically polished down to 1 µm diamond paste. The LDPE is semi-crystalline with a density of 0.92 g/cm^3 and has a modulus between 100 and 300 MPa. The UHWMPE is semi-crystalline as well, has a density of 0.94 g/cm^3 and a modulus between 0.2 and 1.2 GPa. Both PE materials have a Poisson's ratio of 0.46. For further information, the properties of these reference materials, as provided by the manufacturers [64, 65], are summarized in appendix A (see pages 175-177).

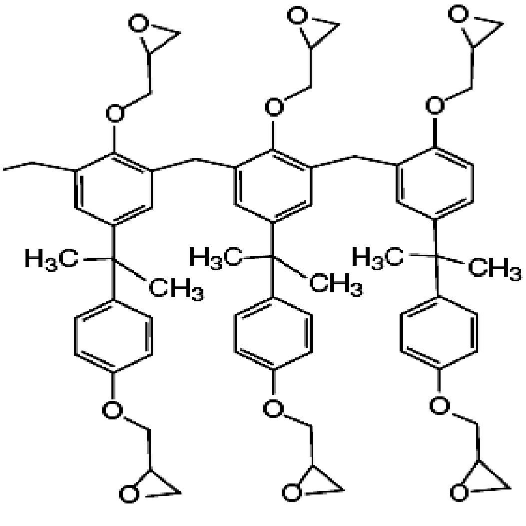

Figure 10: Chemical structure of SU8 epoxy photo resist [64].

PDMS is provided in an unreacted state, therefore the crosslinking and curing has to be performed directly before the use of the sample. Thus, the modulus of PDMS can be easily varied by changing the crosslinking density. In general, higher mechanical property values are expected, if the crosslinking density increases. The chemical structure of PDMS and the crosslinking reaction are shown in figure 11.

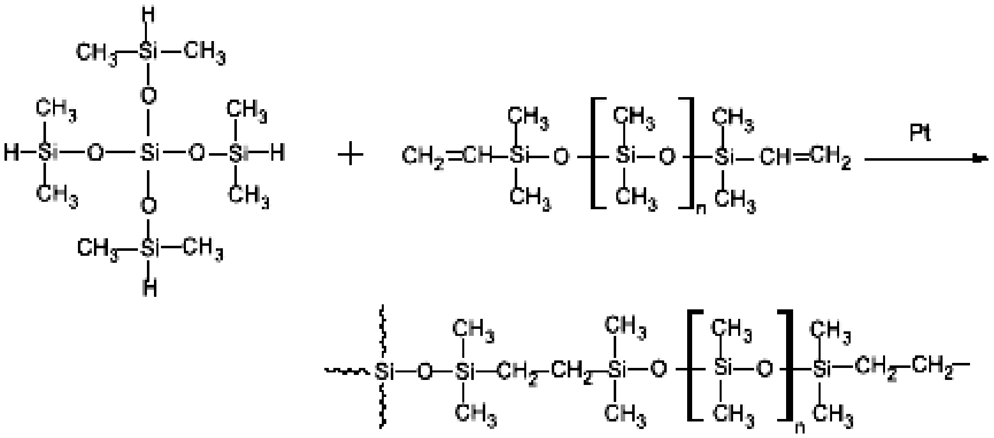

Figure 11: Crosslinking process of PDMS and chemical structure of the components [5].

In order to receive a set of PDMS samples with slightly different mechanical properties, the crosslinking densities as well as the curing processes of the samples were systematically varied. With the help of these PDMS samples the intention was to verify that nanoindentation experiments are capable of sensing such subtle differences in mechanical properties. The different curing temperatures used were 65 °C, 150 °C and 190 °C. The crosslinking states of the PDMS samples were changed through variation of the weight ratio of crosslinker to monomer. The selected ratios were ***1:2***, corresponding to a crosslinker portion of 33 wt% and a crosslinking density N_v (N_v = number of network chains per volume) of $1.14 \cdot 10^{27}$ 1/m^3. Further, the ratios ***1:3*** (25 wt%; $N_v = 8.59 \cdot 10^{26}$ 1/m^3), ***1:5*** (16 wt%; $N_v = 6.32 \cdot 10^{26}$ 1/m^3), ***1:7*** (12.5 wt%; $N_v = 5.27 \cdot 10^{26}$ 1/m^3), ***1:10*** (9 wt%; $N_v = 3.57 \cdot 10^{26}$ 1/m^3), ***1:20*** (5 wt%; $N_v = 2.11 \cdot 10^{26}$ 1/m^3), ***1:30*** (3 wt%; $N_v = 8.92 \cdot 10^{25}$ 1/m^3), and ***1:40*** (2.4 wt%; $N_v = 3.32 \cdot 10^{25}$ 1/m^3) were prepared.

Chapter 4

Surface detection in nanoindentation of soft polymers

Abstract

In this work we performed nanoindentation studies on polymers with different moduli in the range of several MPa up to several GPa. The focus was on the initial contact identification during indentation testing. Surface detection methods using quasi-static loading as well as methods employing the dynamic forces associated with the CSM technique were compared regarding their practicability and accuracy for testing of polymeric materials. For the most compliant material with a modulus of 1 MPa, where contact identification is most critical, we used load-displacement curves obtained from FEA analysis as a reference for evaluation of experimental techniques. The results show how crucial the precise surface detection is for achieving accurate indentation results, especially for compliant materials. Further we found that surface detection by means of dynamic testing provides mechanical property values of higher accuracy for all polymers used in this study. This was due to smaller errors in surface detection, thus avoiding a significant underestimation of the contact area.

4.1 Introduction

Over the past decade nanoindentation testing equipment and methods have continuously been improved to allow a fast and convenient determination of mechanical material properties such as modulus and hardness. This technique is now widely used to study the behavior of metallic and ceramic engineering materials. Nanoindentation offers the possibility to probe mechanical properties in confined volumes and with sub-µm and sub-µN resolution. For this reason it can also be beneficial for mechanical characterization of polymeric materials and biological tissues, which are of increasing importance for technological and medical purposes [1, 66].

Polymers are often used as wear- and scratch-resisting coatings, electrically insulating or optically functional films, and in medical applications. The use of polymeric material in reduced dimensions, however, requires adequate test methods which capture the time-dependent viscoelastic behavior of polymers and the small forces associated with mechanical testing of such materials. Several studies reported in the literature indicate that nanoindentation can be successfully applied to measure mechanical properties of polymers [2-8] and of biological materials [9-12], but there is still considerable uncertainty associated with the accuracy of these measurements.

The high compliance of polymers in comparison with metals or ceramics leads to very low forces between several nN and µN during the indentation experiment. [2, 4, 6]. For most commercially available nanoindentation instruments, the theoretical load resolution is better than 1 nN. Thus, they are theoretically capable of detecting the initial contact; in practice, however, the achievable load resolution is limited by external influences to no better than 100 nN [2], which leads to uncertainties in the surface position and erroneous results from indentation testing [20, 33, 67].

Setting the measured indentation depth and the contact area to zero by identifying the position of the sample surface is the basis of all indentation experiments. In many instruments a certain amount of pre-loading (~ 1 µN) is used for identifying the surface regardless of the stiffness of the specimen tested, which can cause a considerable indentation in softer materials. As a result the measured contact depth and area are in error [2-4, 12, 24]. As the contact area is in turn directly used for the calculation of the hardness and modulus values [12, 31], an incorrect surface detection leads to erroneous results. In general, it can be assumed that for softer materials the contact area will tend to be underestimated, which leads to an overestimation of modulus and hardness values. This is in agreement with experimental findings [2, 6], where nanoindentation results exceed those obtained from other techniques such as dynamic mechanical analysis (DMA).

Another typical feature of polymers is their viscoelasticity which results in time–dependent deformation behavior. Viscoelasticity leads to the formation of the typical "nose-shape" of the unloading curve, which complicates the conventional analysis of unloading data according to the Oliver & Pharr method [12, 31]. Several studies have been carried out on methods to account for the creep during nanoindentation [25-27] and on constitutive models for viscoelastic behavior [29, 30]. Recently the use of a dynamic indentation technique (Continuous Stiffness Measurement, CSM) has been proposed to facilitate the contact finding process as well as the treatment of viscoelasticity in indentation testing [2, 4, 6, 42]. In this method the tip is oscillated at very low amplitudes while it is displaced. Because of the fast tip oscillation, the retarded viscoelastic displacements should be suppressed and unrelaxed elastic responses should be obtained. Another advantage of the CSM technique is the possibility to determine the quantities of storage and loss modulus. Two applications of CSM are presented by Loubet et al. [7, 8] where natural rubber and LDPE were investigated and results compared favorably with literature data. In other studies, the results obtained from dynamic indentation were compared with results obtained from DMA and good agreement between both techniques has been found [4, 6]. Fischer-Cripps introduced an alternative to CSM, i.e. multiple-frequency dynamic indentation testing [42], where a random force signal is applied to the indenter including a certain frequency range. The measured response is then separated into single frequency components and gives the frequency dependence of the modulus.

Although viscoelasticity has to be taken into account when testing polymeric materials, the present paper will show that errors introduced by inaccurate surface detection are much bigger than the ones coming from viscoelastic effects and the most critical issue remains the detection of the initial point of contact between the tip and the specimen. In order to identify the most suitable parameter for contact identification, we performed indentation testing applying the most commonly used techniques for surface detection, as they are implemented in various commercially available indenter systems. The results obtained from methods of surface detection based on quasi-static loading parameters and methods employing dynamic loading parameters were compared and evaluated regarding their surface detection accuracy and subsequent errors in mechanical property values. Tests were performed on different polymers, which cover a wide range of stiffnesses.

4.2 Experimental methods

4.2.1 Surface detection using quasi-static loading

For indentation testing we used a Nano Indenter DCM® from MTS Nano Instruments (Oak Ridge, TN, USA) equipped with the CSM technique to perform dynamic indentation. Testing with quasi-static loading was performed on a TriboScope (Hysitron Inc., Minneapolis, MN, USA). For both instruments a Berkovich type diamond indenter tip was used. In order to establish a surface detection criterion that is adequate for polymeric materials, a PDMS sample with a tensile modulus of about 1 MPa was chosen. This is ~ 3 orders of magnitude below the moduli of the three other polymers used in section 3. The PDMS sample was 1 mm thick and the R_a (root mean square) roughness was 5 nm, as obtained from AFM measurements.

In the following we will describe the different methods of surface finding. The first possibility is the definition of a pre-set load value, at which the loading and unloading process starts and displacement values are set to zero. This procedure is commonly used in various kinds of mechanical instrumentations like tensile tester, but still it requires some beforehand knowledge about the properties of the specimen to choose a proper pre-load value. In order to see the effect of the pre-load on the load-displacement curves, we performed indentation tests in displacement-control mode with a displacement rate of 0.01 µm/s and an unloading rate of 20 µm/s. The pre-load values were 0.1 µN (the minimum value possible for this type of instrument), 0.25 µN, 0.5 µN and 1 µN. The load-displacement curves obtained for the different pre-load values are plotted in figure 12. It is interesting to note that when the pre-load value is reached and the loading/unloading cycle starts, the load is not set to zero, but remains equal to the pre-load value for zero displacement. This means that the pre-load is accounted for as part of the load on the surface, but the corresponding penetration into the surface is neglected, thus introducing an error in the calculation of the contact depth and area. The higher the pre-load value, the bigger the underestimation of the contact area and thus the overestimation of hardness and modulus values tend to be. The amount of overestimation will be discussed more quantitatively in the next section.

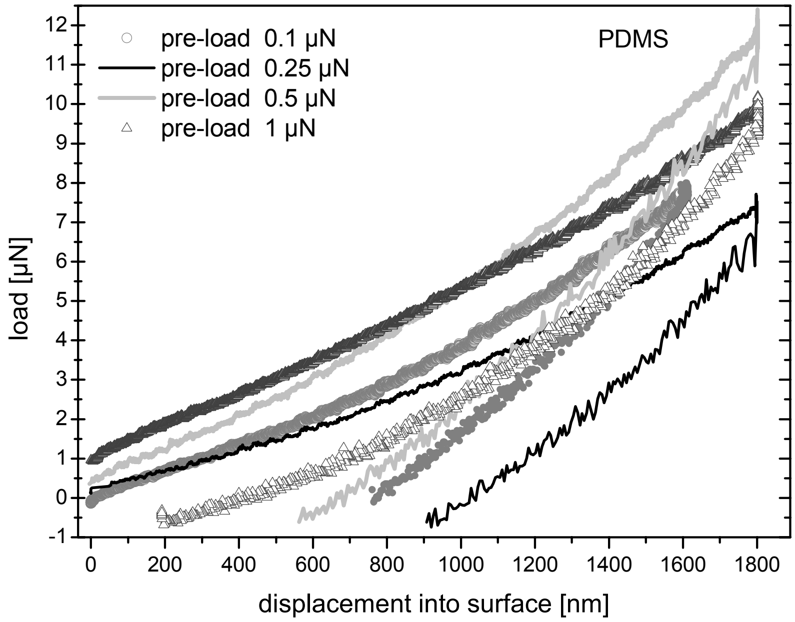

Figure 12: Load-displacement curves measured with different pre-load values on PDMS.

A second way of identifying contact formation between the tip and the sample is monitoring the slope of the load P vs. the displacement h, i.e. the slope of the secant $\Delta P / \Delta h$ in units of N/m. Note that for the application of this criterion in the MTS indenter, it has to be taken into account that the load required to displace the indenter consists of 2 parts. One is the force needed to deflect the support springs holding the indenter shaft and the other is the load necessary to let the tip penetrate into the sample. The first part is increasing linearly, since the springs are deformed in the linear regime only. Thus the slope of the load-displacement curve can be identified with the spring constant of the support springs (approximately 80 N/m for our instrument) and is constant while the tip is displacing in air and approaching the surface. This straight line can be seen in the left part of figure 13, where a complete indentation experiment is shown in terms of the load and displacement output of the system (both as measured originally). Any further increase in load, which leads to an increase in the slope of the curve, can be attributed to contact formation between the tip and the surface. In figure 13 the contact occurs at a displacement value of -3000 nm. However, the load increase occurring at the initial contact point is very little for PDMS, a penetration of 100 nm requires only about 0.5 µN of additional force, equal to a slope of 5 N/m. This is a quite small change compared to an average noise ratio of 15-20 N/m. Further, the minimum threshold value for the load vs. displacement slope (with respect to the constant support spring stiffness) recommended by the manufacturer for surface detection is 50 N/m and the pre-set “standard” value is 125 N/m, thus indicating a high probability for false or late surface detection when using the load vs. displacement slope.

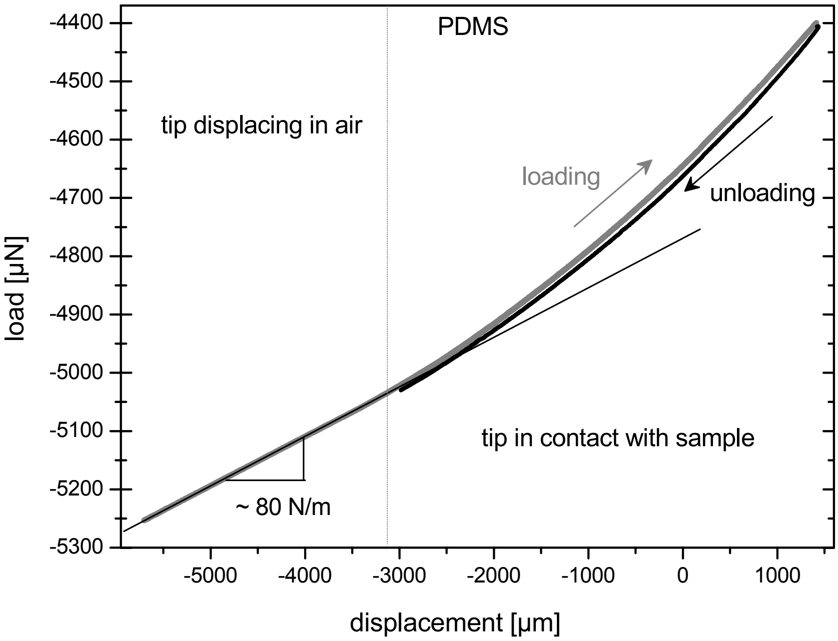

Figure 13: Raw load vs. raw displacement curve for PDMS. The surface approach as well as the loading (grey) and unloading (black) portions are shown.

In order to get an estimation of the errors associated with this method, we will consider figure 14, where a complete indentation test including the standard surface finding procedure is displayed. The raw displacement corresponds to the position of the tip with respect to the middle of its range of travel, thus illustrating the up (negative) and down (positive) movement of the tip during an indentation. In the first 200 s the pre-test procedure for surface finding is performed. This procedure is magnified in the insert in figure 14. During the pre-test the indenter is driven into the material three times assuming that the specimen surface is mounted at approximately zero raw displacement (points 1-3 in figure 14). Twice the tip reaches a raw displacement of 10 µm with a velocity of 100 µm/s, the third time the tip travels to 6 µm. After that, the indenter is withdrawn to the calculated surface position (corresponding to the least load vs. displacement slope threshold of 50 N/m in this case) for the measurement of the thermal drift assuming the tip to be “sitting on the specimen surface”. Then the indenter is withdrawn completely. At the beginning of the actual indent, the tip moves to a predefined position above the calculated surface position, the surface approach distance (point 4 in figure

14), holds for a few seconds and then starts the surface approach at a speed of 10 nm/s until the surface is detected. Once the surface has been identified through a certain threshold value for the load vs. displacement slope, the penetration depth and the load are set to zero. The sample is then loaded at a constant strain rate $\dot{\varepsilon} = 0.05 s^{-1}$, which is equivalent to a constant $\dot{P}/P$ [68]. When the desired displacement is reached, the load is held at its maximum value for 10 s and afterwards the indenter is withdrawn at a speed of 100 µm/s.

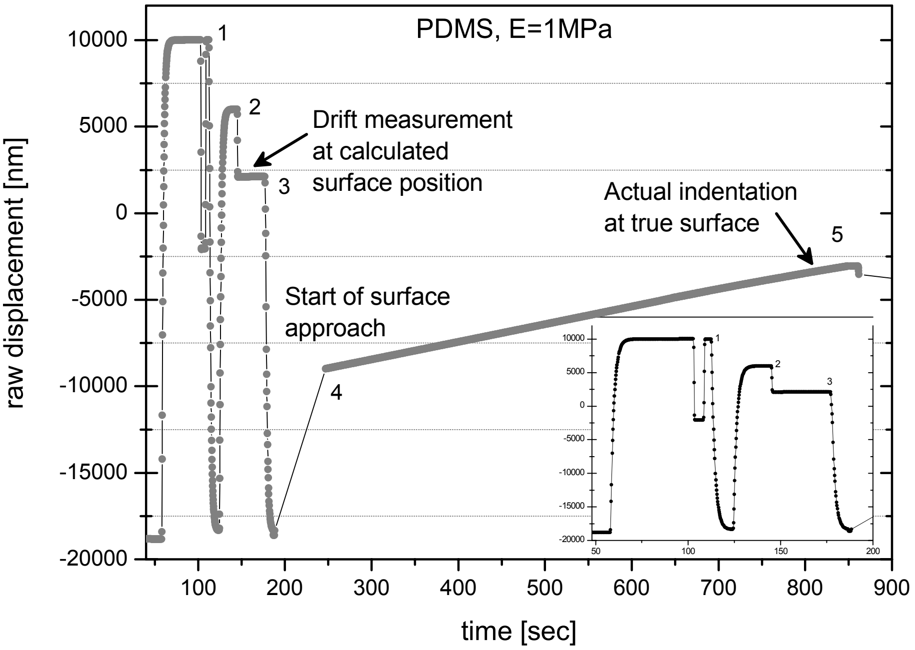

Figure 14: Test flow of an indentation test on PDMS. Zero raw displacement corresponds to the middle of the travel range of the tip. The insert shows the movement of the indenter tip during the pre-test surface finding segment.

It is clear from figure 14 that the surface position determined during the pre-test procedure differs substantially from the starting position of the actual indentation: The pre-test value is roughly 2100 nm (point 3 in figure 14), whereas the true surface lies at -3000 nm (point 5 in figure 14). In order to make clear the origin of the big difference between the two values, two things are important to note: First, the surface at point 3 has been identified using the load vs. displacement slope, whereas in point 5 the dynamic stiffness (discussed in the following section) was used. Second, the pre-test and the actual indentation were performed at the same spot of the sample, thus all influences of sample sloping or surface roughness have been canceled out This is possible because of the completely elastic behavior of PDMS (see figure 13), where no residual impressions can be found [4]. After careful examination of the indent locations with AFM and whitelight-profiliomety, we can ascertain that no permanent deformation existed. Therefore, the difference in surface positions in figure 14 can only be associated with the different contact detection criteria.

For this PDMS sample it can be stated that the surface detection with the help of the load vs. displacement slope occurred after more than 5 µm of penetration into the sample surface. For a 1 µm deep indentation this means that 80 % of the true penetration and about 95 % of the true contact area are not covered by the measurement and thus not considered in the calculation of hardness and modulus. Therefore the load vs. displacement slope is a very poor indicator of the initial contact formation and the need for a more accurate surface finding procedure is obvious.

4.2.2 Surface detection using dynamic loading and establishing an appropriate surface detection criterion

As it has been discussed in the previous section, contact identification based on quasi-static loading is very difficult and often erroneous for such soft materials. Therefore the suitability of quantities related to dynamic loading (CSM) is addressed in the following. The definition of a surface detection criterion requires that a measurement quantity exhibits a significant and immediate change upon contact formation. For the harmonic oscillation of the indenter tip in the CSM mode, the three quantities contact stiffness, harmonic load, and phase angle are monitored and compared to the (quasi-static) load vs. displacement slope used in the standard protocol of the MTS instrument. The contact stiffness F_0/z_0 (with F_0 and z_0 being the load and displacement amplitudes) is determined from the overall dynamic response, i.e. stiffness and damping of the whole system (instrument and the sample together) operated in the CSM mode and ranges from 5 to 70 N/m for the tip oscillating in air at different frequencies. The contribution of the specimen-tip contact has to be separated from the instrumental contributions according to [12, 62]. The harmonic force is the amplitude of the sinusoidal CSM force signal and the phase angle δ is the shift between force and displacement. All these quantities are accessible as output from the nanoindenter measurement and can be recorded continuously during an indentation test.

For comparison, several tests were performed on PDMS to a depth of 1 µm with excitation frequencies ranging from 30 to 210 Hz. The results are shown in figures 15 to 18. The load vs. displacement slope (figure 15) used in the standard procedure exhibited high noise and no clear trend upon contact. Only a very slight increase of ~5 N/m, significantly below the noise of approximately 15 N/m, could be seen in the range of 100 to 200 nm displacement, whereas the lowest threshold value for surface detection in the standard method is 50 N/m, which explains the late contact identification.

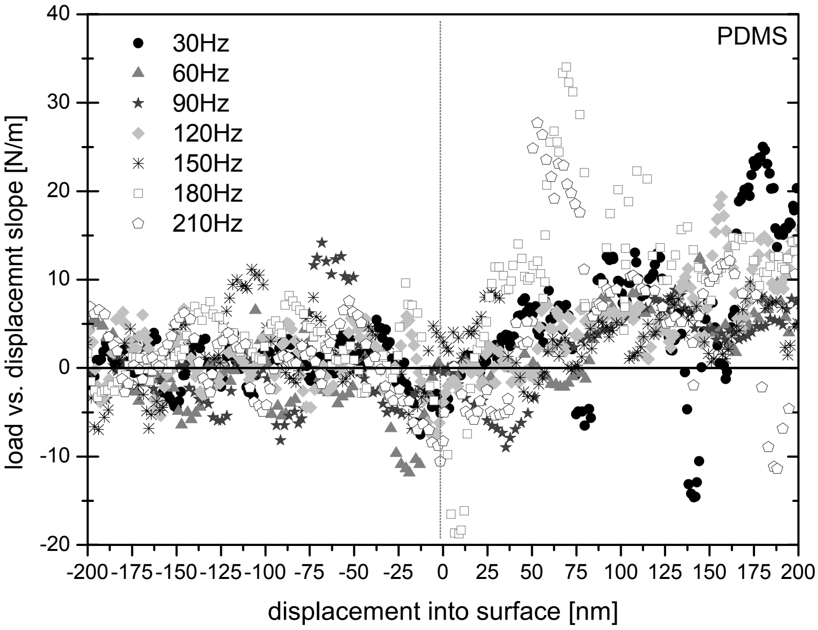

Figure 15: Load vs. displacement slope for various frequencies near the surface of a PDMS sample. The vertical line in the diagram indicates the position of the surface as determined from the dynamic method.

Similarly, the phase angle does not provide a suitable criterion for surface detection (figure 16). The values of the phase angle increased strongly with frequency, from 3-5 ° at 30 Hz up to 170 ° at 210 Hz. For frequencies below 120 Hz (shown in figure 16a) the phase angle increased upon contact, whereas for frequencies above 120 Hz the phase angle decreased (shown in figure 16b). This inversion was due to the resonance frequency of the instrument head, which lies around 150 Hz. In all cases, the changes upon contact are not very pronounced. For the harmonic load (figure 17) a clear bend was found close to the surface for all frequencies. But the resonance of the head again caused an inversion from increasing load for lower frequencies to decreasing load for higher ones. This complicates the applicability of this contact criterion.

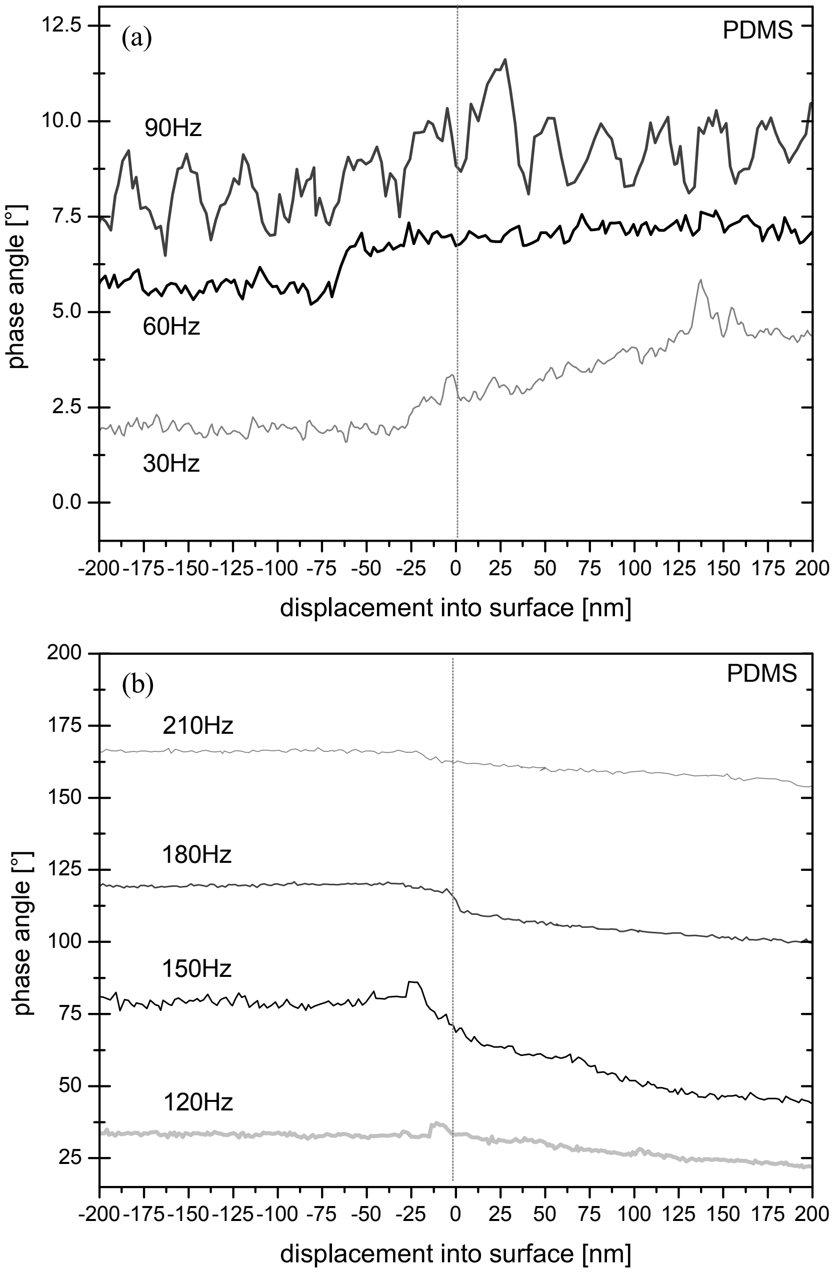

Figure 16: Phase angle vs. the displacement (a) for frequencies of 30, 60 and 90 Hz (b) for 120, 150, 180 and 210 Hz. Note the necessity of different ranges for the phase angle in the two diagrams.

The contact stiffness (figure 18) was identified as the most suitable contact parameter. Its value increased monotonically with an average slope of 10 N/m per 100 nm of depth. This behavior was independent of the testing frequency, which facilitated the definition of a surface detection criterion. Further, the contact stiffness exhibited the least signal to noise ratio of all quantities monitored. As the criterion for surface contact, a threshold value of 2 N/m for the contact stiffness was established in the testing protocol.

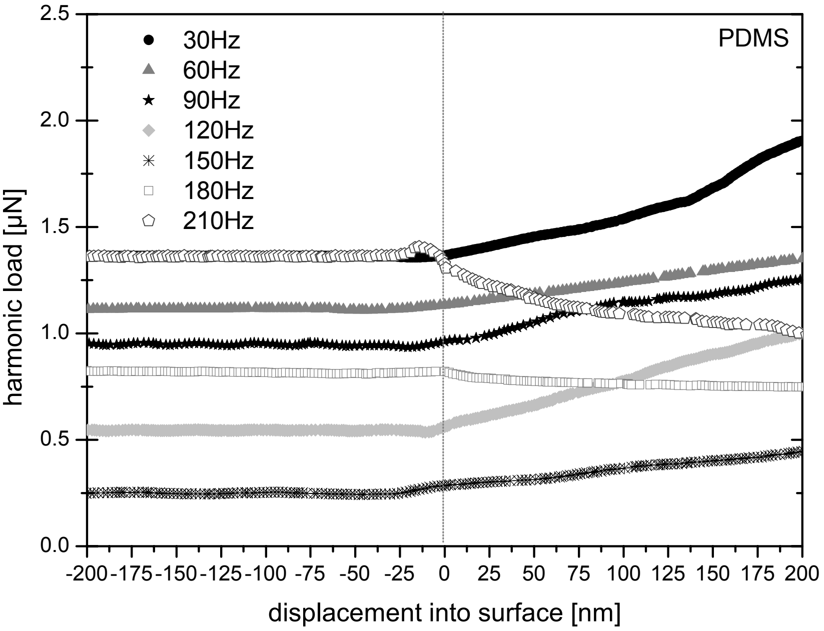

Figure 17: Harmonic load vs. displacement, which is the force needed to constantly excite the tip to an amplitude of 10 nm during the whole test. For frequencies below the resonance of the head, the load increases with increasing depth, for frequencies above, the load decreases.

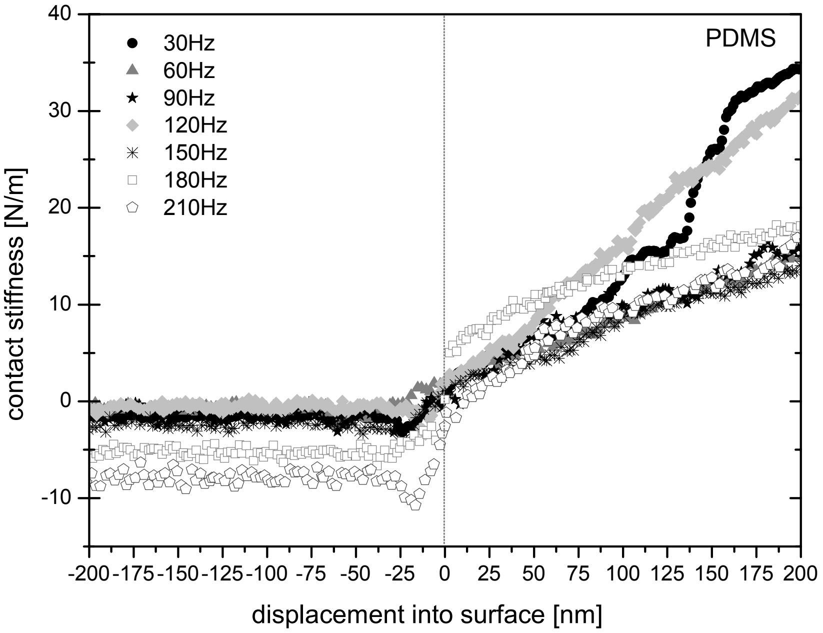

Figure 18: The contact stiffness plotted in the vicinity of the surface. Characteristic for this channel was the snap-to-contact phenomenon caused by attractive forces between the tip and the sample. The snap-to-contact appeared most clearly at 210 Hz.

4.2.3 Comparison of load-displacement curves and discussion

In order to evaluate the errors associated with the different methods of surface detection, we performed a finite element study of the indentation process in PDMS. For the FE-simulation we used the FE-code ABAQUS. The PDMS was model as a hyperelastic material using a Neo-Hooke strain energy potential [69]. The curve obtained from the FE-simulation can be seen as a reference load-displacement curve, with which the experimental curves can be compared. In figure 19 the simulated curve is plotted together with the curves measured dynamically as well as quasi-static with a least pre-load of 0.1 µN and a load vs. displacement threshold of 25 N/m (this is half of the recommended minimum threshold!).

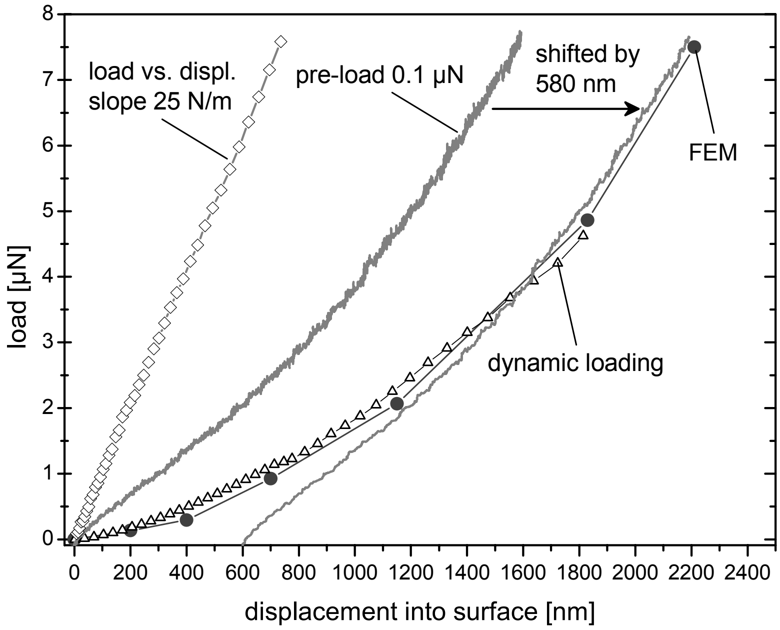

Figure 19: Load-displacement curves obtained with different techniques for surface detection. The FE curve is taken as a reference curve with known surface position corresponding to zero load and zero displacement.

As can be seen, the curve using the contact stiffness as contact parameter resembles the simulated curve quite well, whereas the curve using the pre-load is much steeper, almost twice the force is needed to reach the same penetration depth. This discrepancy can be attributed to the fact that the penetration of the tip due to the pre-load is not considered. The same holds for the curve measured with the load vs. displacement slope as contact indicator. Here the situation is even worse than for the pre-load method, because surface detection occurred much too late. The shape of the curves, i.e. the curvatures of the upper part, however, are comparable, thus the curves using quasi static loading can be shifted to higher displacements until the curve matches the FE curve. The displacement shift necessary to overlay simulated and experimental curve can be taken as an estimate of the surface detection accuracy of the method. For the pre-load method the displacement shift was 580 nm (shifted curve is also shown in figure 19) and for the dynamic method it was 30 nm. For the load vs. displacement slope curve the appropriate shift would exceed the limit of the FE curve, thus being more than 2 µm. The modulus values resulting from the load-displacement curves in figure 19 are 1 MPa for the FE (as determined from a tensile test and implemented in FEM), 1.1±0.02 MPa for the dynamic method (calculated using CSM data), 1.8±0.1 MPa and 3.3 ±0.3 MPa for the pre-loads of 0.1 µN and 1 µN (calculated from unloading data), and 4.7±0.05 MPa and 4.9±0.2 MPa for the load vs. displacement slope method, calculated using CSM and unloading data, respectively.

To conclude from these results, it is possible to detect the point of surface contact with an error of approximately 30 nm by using the contact stiffness measured in the CSM mode as a contact parameter. The error for the modulus calculation was reduced to about 10 %, taking the tensile test result as reference. Regarding the applicability of the load vs. displacement slope method the following estimation can be made: If the minimal load vs. displacement slope threshold, which can be detected reliably, is assumed to be twice the average noise ratio (30 N/m for our measurement setup), the depth at which surface detection occurs can be estimated from the relation $S = 2E_r a_c$ derived by Sneddon for a conical indenter [15]. Here the stiffness S is equal to the load vs. displacement slope threshold; E_r is the reduced modulus and a_c the radius of the contact circle. Taking the opening angle of the Berkovich equivalent cone, which is $\phi = 70.3°$, and substituting $a_c = h_c \tan\alpha$ (with h_c being the contact depth) into Sneddon´s equation, leads to the contact depth values at which surface detection occurs. These values can be seen as a measure for the absolute surface detection errors; the relative errors are dependent on the total indentation depth. For instance, if E_r is 1 MPa, the error would be around 5 µm, or 11 nm for E_r = 500 MPa, and 5 nm for E_r = 1 GPa. Although the contact depth values are slightly smaller than the total displacement values due to sink-in effects, the result extracted from figure 14 (5.2 µm) agrees well with the estimated 5.4 µm according to Sneddon's equation. Also for the other polymers used in section 3, the experimentally determined differences are consistent with the estimations according to Sneddon. Thus, the accuracy of contact identification through the dynamic contact stiffness is supported.

In order to stress the reason for the higher accuracy of dynamic stiffness method, the important numbers are summarized once again. The threshold value for the load vs. displacement slope is at least 50 N/m. The average noise ratio we observed in this study was around 15 N/m. The stiffness increase upon contact was 5 N/m. So the effect, which should be detected, is only 10 % or even less of the threshold value and only 30 % of the noise ratio, which obviously precludes surface detection. In contrast, for the dynamic method, the contact stiffness threshold is 2 N/m, whereas the noise ratio is half the threshold, approximately 1 N/m. In this case, the signal of 5 N/m is a multiple of noise and threshold, thus proper surface detection can take place.

Another important aspect associated with surface detection is test automation, which should be implemented into the testing procedure to ensure reproducibility of experiments. The intention behind this is to keep out the rate dependency of viscoelastic materials as a source of error. In order to ensure reproducibility of experiments the same loading history has to be ascertained for all tests. [2]. This can be seen as a clear advantage of instruments using a quasi-static loading at a constant rate, where the indenter velocity is constant and does not change when the surface is contacted. Thus, it is ensured that the influence of the loading history is minimized for viscoelastic samples. In contrast, the speed of the indenter tip changes after contact formation, if the loading is carried out at a constant deformation rate [68]. Since a considerable penetration of the surface at the point of surface detection exists, the switch between the rates appears within the material and will be included in the loading portion of the data. This change of rates within one loading cycle may affect the result, therefore an accurate and reproducible surface identification is needed in order to reduce errors associated with this intrinsic problem or at least to keep the error constant, which can only be achieved by automated surface detection.

4.3 Testing of three different polymers

4.3.1 Materials and methods

For indentation testing in this section we used the MTS Nano Indenter DCM® operated in the CSM mode with a frequency of 75 Hz, which is the standard operating frequency of the system. Again a diamond Berkovich tip was used for all tests. Here we compare measurements performed with surface finding through the load vs. displacement slope (hereafter referred to as standard method) to measurements with surface identification through the dynamic contact stiffness (dynamic method). The threshold for the contact stiffness was 2 N/m. For the standard method the tests were additionally carried out under a systematic variation of the instrument sensitivity by varying the threshold values. The lowest sensitivity was equivalent to a threshold value in the load vs. displacement slope of 125 N/m; the highest sensitivity was corresponding to a threshold value of 50 N/m, which is the minimum value recommended by the manufacturer [62]. Further, 75 N/m and 100 N/m were used. Since differences resulting from different surface detection methods should be emphasized, all other testing conditions (i.e. testing protocol, lab temperature, sample mounting etc.) were kept the same for all measurements.

The polymeric materials under investigation were an epoxy-based photo resist, SU8, and polyethylene samples of low density (LDPE) and of ultra-high molecular weight (UHMWPE) provided by Goodfellow. These materials were selected to cover a range of elastic moduli from several GPa down to several hundreds of MPa. Their elastic moduli are well characterized such that these materials can be used as reference material. The properties are provided by the manufacturers according to [64, 65]. The SU8 specimen was a spin-coated layer, approximately 5 µm thick, on a silicon substrate. The R_a roughness was 10 nm. LDPE and UHMWPE were delivered in form of 1 and 2 mm thick sheets and were in a semi-crystalline state. They were cut into rectangular pieces of ~ 1 cm^2 in size and mechanically polished down to 1 µm diamond paste to reduce the surface roughness. After polishing the R_a values were16 nm for LDPE and 30 nm for UHMWPE. The thickness of the polished samples was determined at 15 different locations across the sample to 0.952±0.001 mm for LDPE and 2.105±0.03 mm for UHMWPE.

4.3.2 Results

The load–displacement data measured for SU8 (figure 20a) were very smooth. The grey curve is the one measured with the dynamic method. In this curve the maximum load needed to reach a pre-set depth of 1000 nm was about 1 mN lower than in the standard method, therefore the loading curve is flatter, whereas the unloading curves are almost parallel for both methods. For the SU8 sample the influence of the different threshold values is negligible. Figure 20(b) shows the different contact criteria. For comparison, the curve corresponding to the dynamic method (open symbols) as well as the one obtained from the standard method

(125 N/m threshold, filled symbols) is displayed. All curves exhibited a significant change within a range of 5-10 nm upon contact. The difference between the two methods was almost negligible for the harmonic load and load vs. displacement slope. But for the phase angle and the contact stiffness, the curves were shifted by 5 nm. The effect of this little shift on the values of hardness and modulus can be seen in the graphs of figure 21.

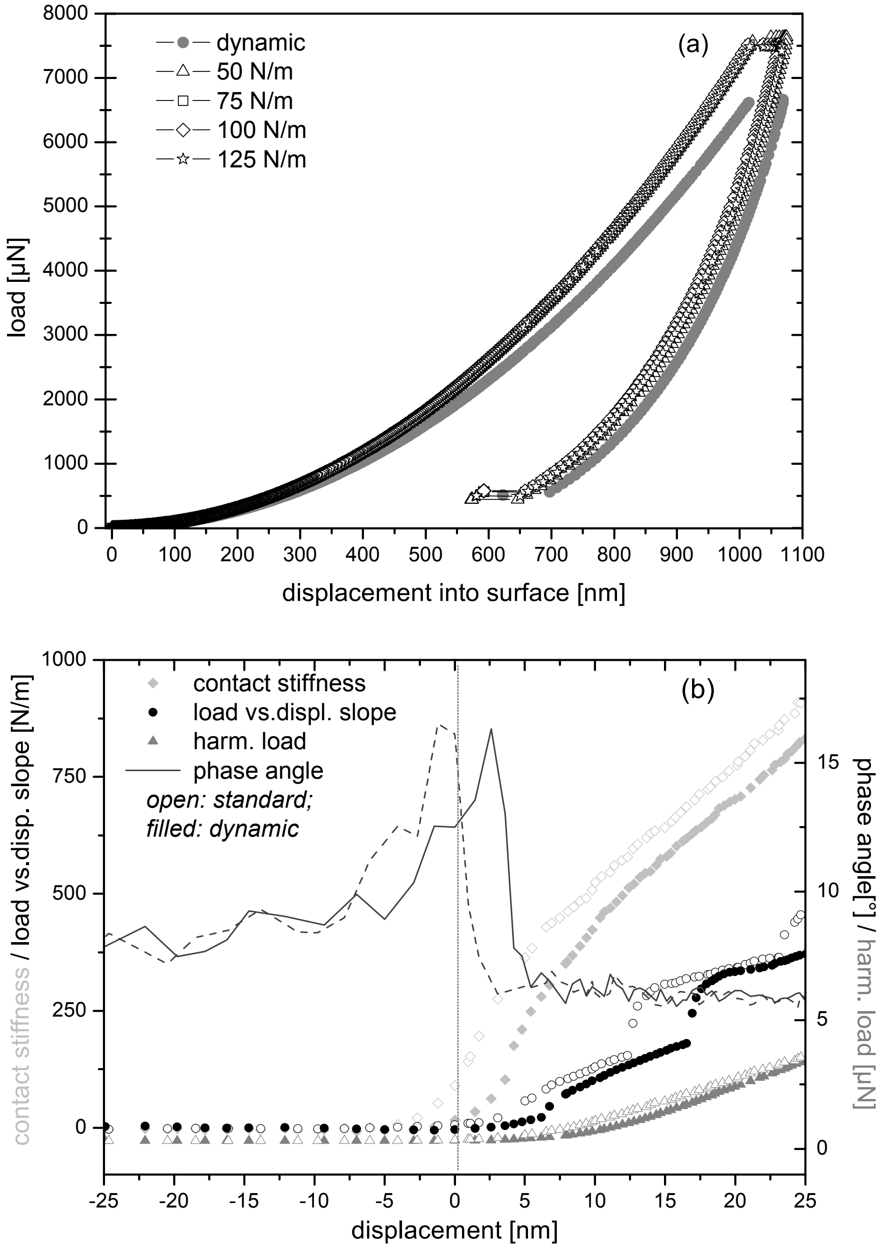

Figure 20: (a) Load-displacement data for SU8. The lower grey curve corresponds to the dynamic method; the upper curves to the standard method. (b) Comparison between standard and dynamic method. The accuracy of surface detection is 5 nm. The channels harmonic contact stiffness, load vs. displacement slope (left axis), phase angle and harmonic load (right axis) are displayed for the dynamic method (filled symbols) and the standard method with a threshold of 125 N/m (open symbols).

The elastic modulus is plotted in figure 21(a) as a function of the indentation depth. These data are obtained from the CSM technique and are the average of at least 15 indentations. The error bars given in the plots indicate the standard deviation. The curves went through a minimum between 20 and 80 nm and increased strongly for higher displacements. This behavior could be attributed to the influence of the Si substrate. The curves obtained with different sensitivities in the standard method were almost identical, whereas the data from the dynamic method lay approximately 200 – 300 MPa below the other values.

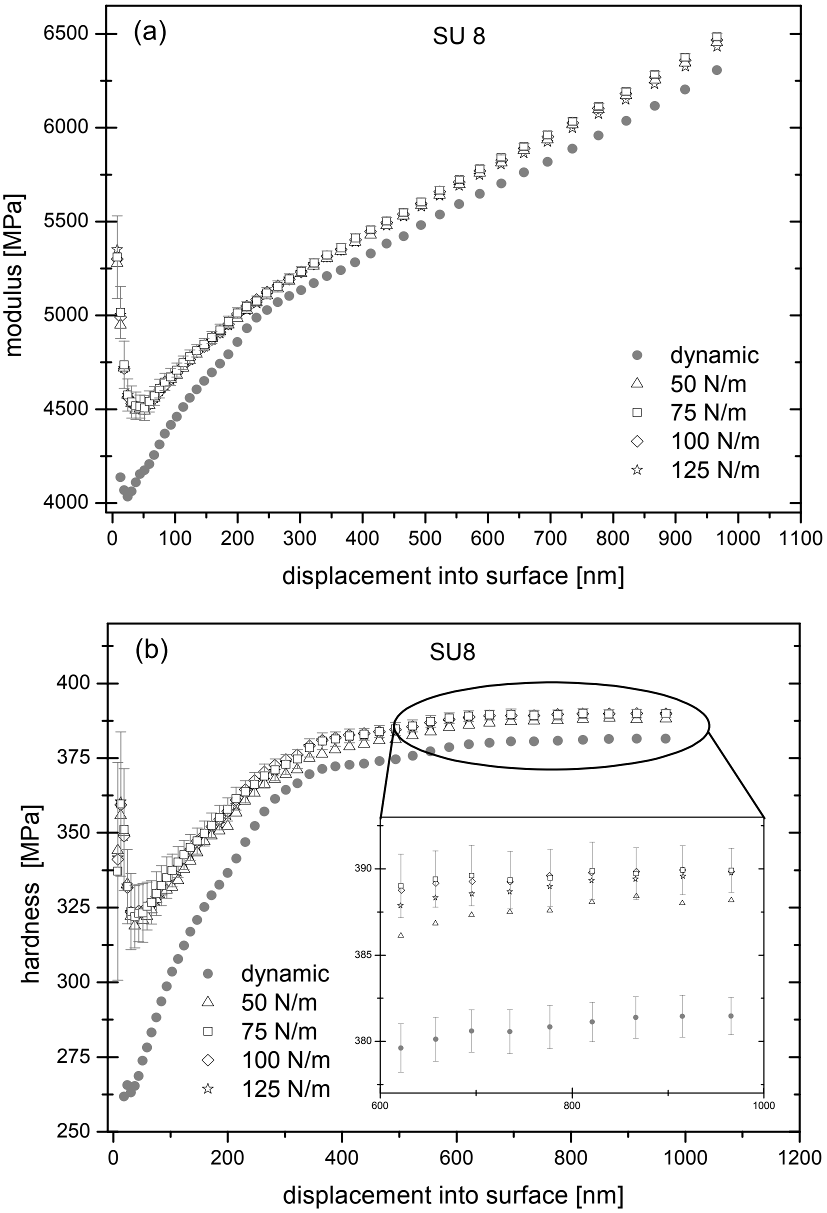

Figure 21: (a) Elastic modulus vs. displacement for SU8. The curves are the average of at least 15 individual indentations. The error bars (±20 MPa) indicate the standard deviation and are given only for the curve of 50 N/m threshold for the facility of inspection. (b) Hardness as a function of indentation depth. The inset compares the error bars, which are ±1.3 MPa and ±1.5 MPa for the dynamic and standard curves respectively.

In principle, the hardness vs. displacement curves (figure 21b) resembled the behavior of the moduli. The values of the dynamic method were again lower than the ones for the standard method. Above a depth of 300 nm, where the values reached a plateau, the distance between the curves was about 30 MPa, the hardness values being 360 MPa and 390 MPa. Note that these values are influenced by the substrate, thus are likely to be too high. In order to minimize the substrate effect, the average values given here were calculated for depths between 50 and 150 nm, thus not exceeding 10 % of the film thickness. Anyway, the difference between both methods is real, since both methods were performed under the same substrate influence. In this diagram, one set of error bars for the 50 N/m threshold curve is given as representative for all others.

For the polyethylene sample of ultra high molecular weight UHMWPE the load-displacement curves (figure 22a) scatter slightly more than for SU8. The maximum loads needed to reach a penetration of 1000 nm range from 1200 to 1300 µN for the different sensitivities, but no correlation between the sensitivity and the maximum load could be found. For the dynamic method the maximum load of 980 µN was significantly less than for the standard method. The contact stiffness again was a useful surface detection criterion (figure 22b).

For this material the difference of surface detection points were about 6 or 7 nm. The stiffness values rose to several hundreds of N/m within only 15 nm, which was a significant increase that could be measured easily. As a result of the scatter in the load-displacement data, the moduli and the hardnesses (figure 23) also showed a high scatter and large statistical error bars (standard deviation of 15 individual tests). No obvious correlation between the sensitivities and the average value of the two quantities was observed. In both graphs of figure 23 the curves coming from the dynamic method (filled symbols) were the only ones that reached a constant value after 300 nm, whereas the other curves decreased constantly.

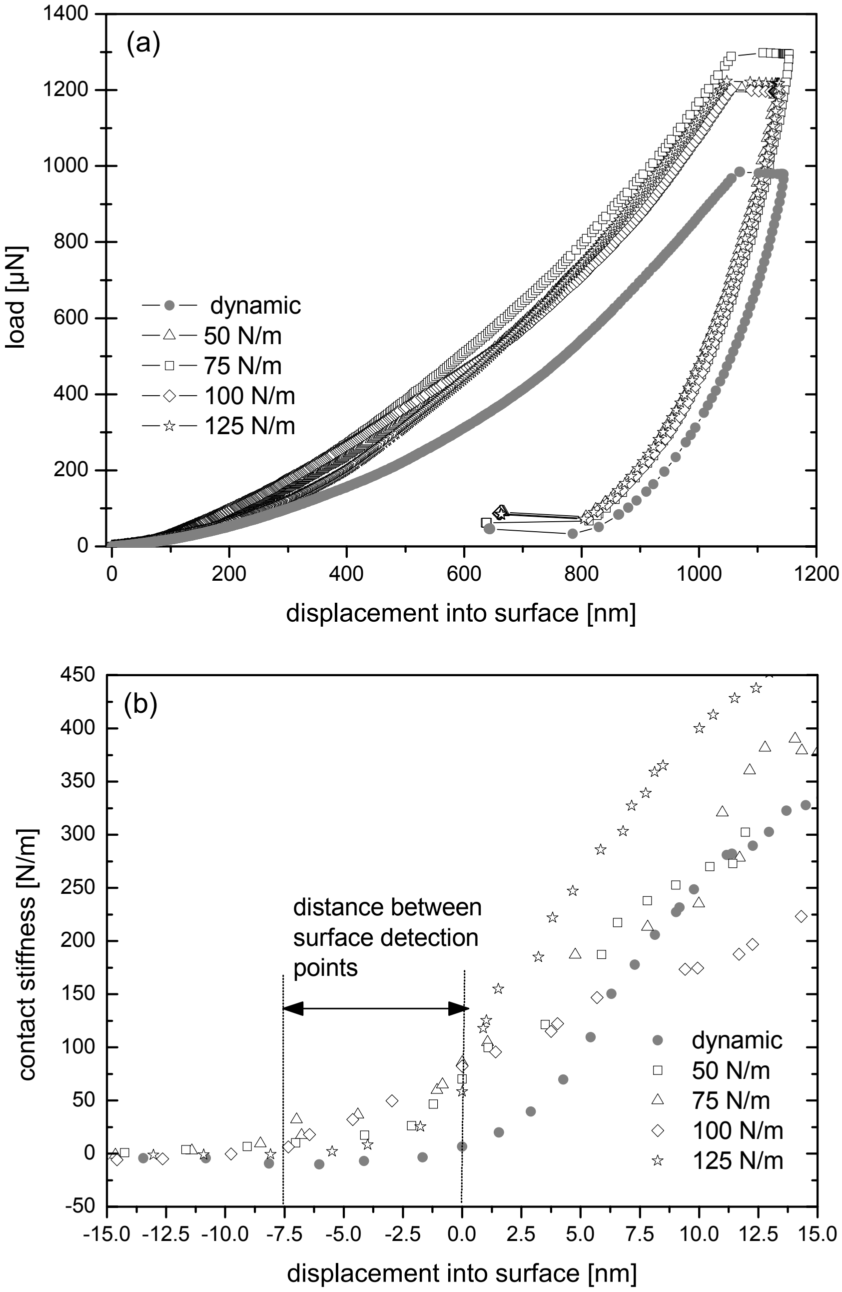

Figure 22: (a) Load-displacement data obtained for UHMWPE. The lower grey curve corresponds to the dynamic method; the other curves to the standard method. Since individual indentation data were plotted here, the load levels of the curves for different sensitivities showed scatter. (b) Contact stiffness of a UHMWPE sample 15 nm before and after the surface was contacted. The points where the harmonic contact stiffness increased above zero are separated by a distance of 5 to 7.5 nm, which was slightly more than for SU8.

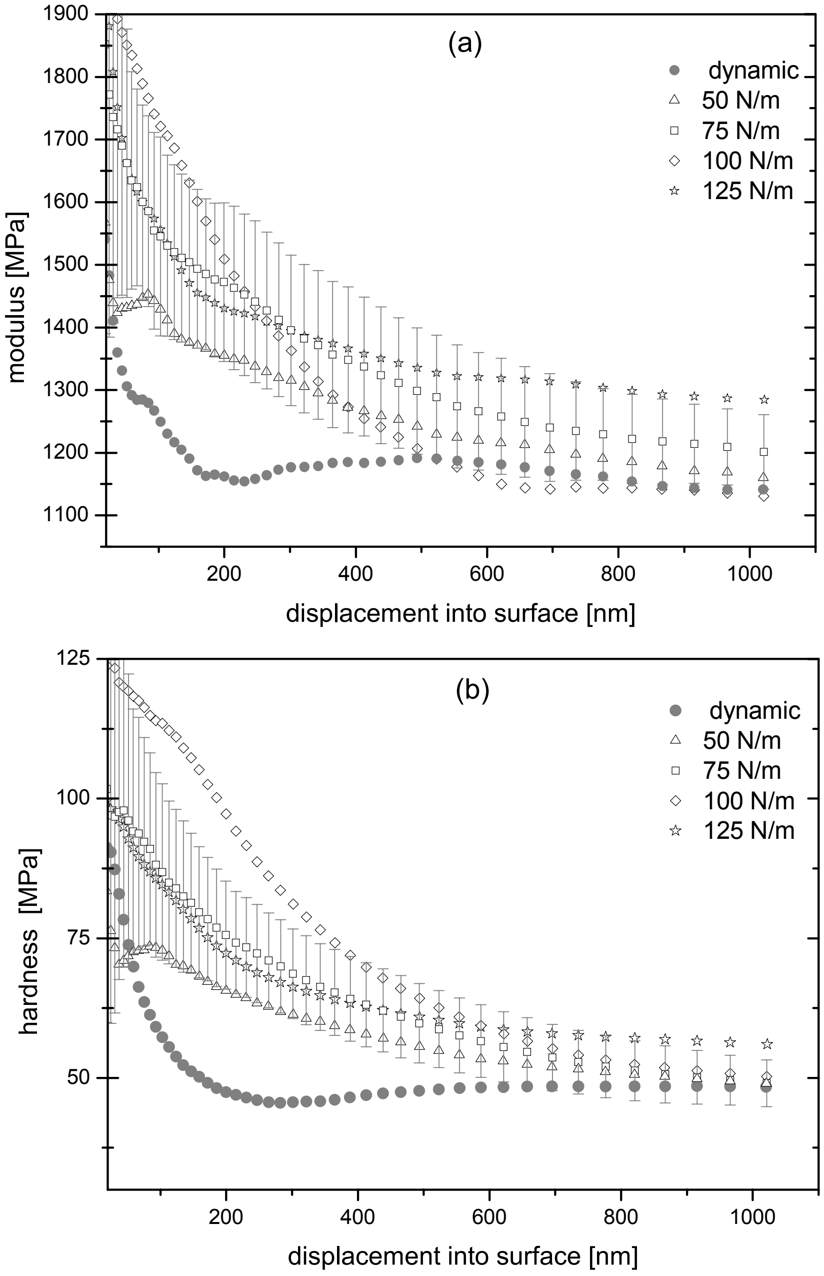

Figure 23: (a) Average moduli of UHMWPE as a function of displacement into surface. The amount of scatter in the data is quite high, which is also confirmed by the large error bars of ±150 MPa denoting one standard deviation of 15 measurements. (b) Average hardness of UHMWPE. The error bars are given for the 100 N/m threshold curve.

For LDPE with a modulus in the range of 100 and 300 MPa loads in the range of 600 to 650 µN for the standard method and about 500 µN for the dynamic method were necessary to reach the desired depth of 1000 nm (figure 24a). The contact stiffnesses (figure 24b) measured with different sensitivities coincided for all four values. The slope of the curves was approximately 15 to 20 N/m per nm displacement, which means that the contact stiffness rose to values above 100 N/m within 10 nm of surface penetration. The difference between the surface detection points for the two methods is 10 nm. Note that there was no influence of the sensitivity, although the effect should increase for materials with lower stiffnesses.

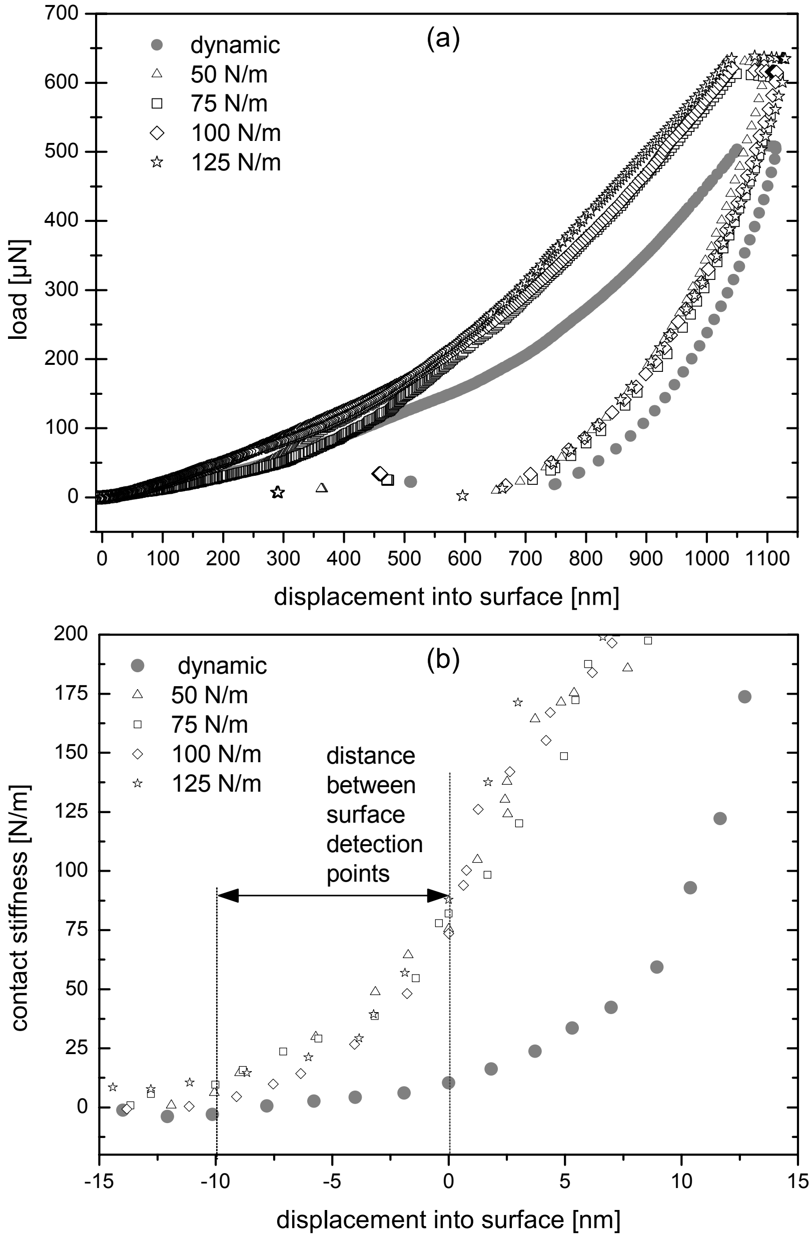

Figure 24: (a) Load-displacement curves obtained for LDPE. (b) The behavior of the contact stiffness in the vicinity of the surface of a LDPE sample was well distinguished for the two methods. In principle, the curves possessed the same shape, but the shift distance was 10 nm in this case, as marked by the two lines in the diagram.

Modulus and hardness as a function of the indentation depth are given in the figure 25. For the modulus the error bars were so big that all other curves lie within their range, although the difference between the plateau values at penetrations above 500 nm was 60 MPa. In the case of the hardness, the curves of the standard method did not reach a plateau but decreased until the maximum indentation depth of 1000 nm was reached. In contrast, the hardness determined with the dynamic method was constant between depths of 300 to 1000 nm. The smallest difference at 1000 nm was about 4 MPa, where the hardnesses were 27 MPa and 23 MPa for a threshold of 125 N/m and the dynamic method, respectively. Noticeable is that although the difference between the points of contact detection was no larger than 10 nm for LDPE, the results from the two method deviate about 10 to 15 %.

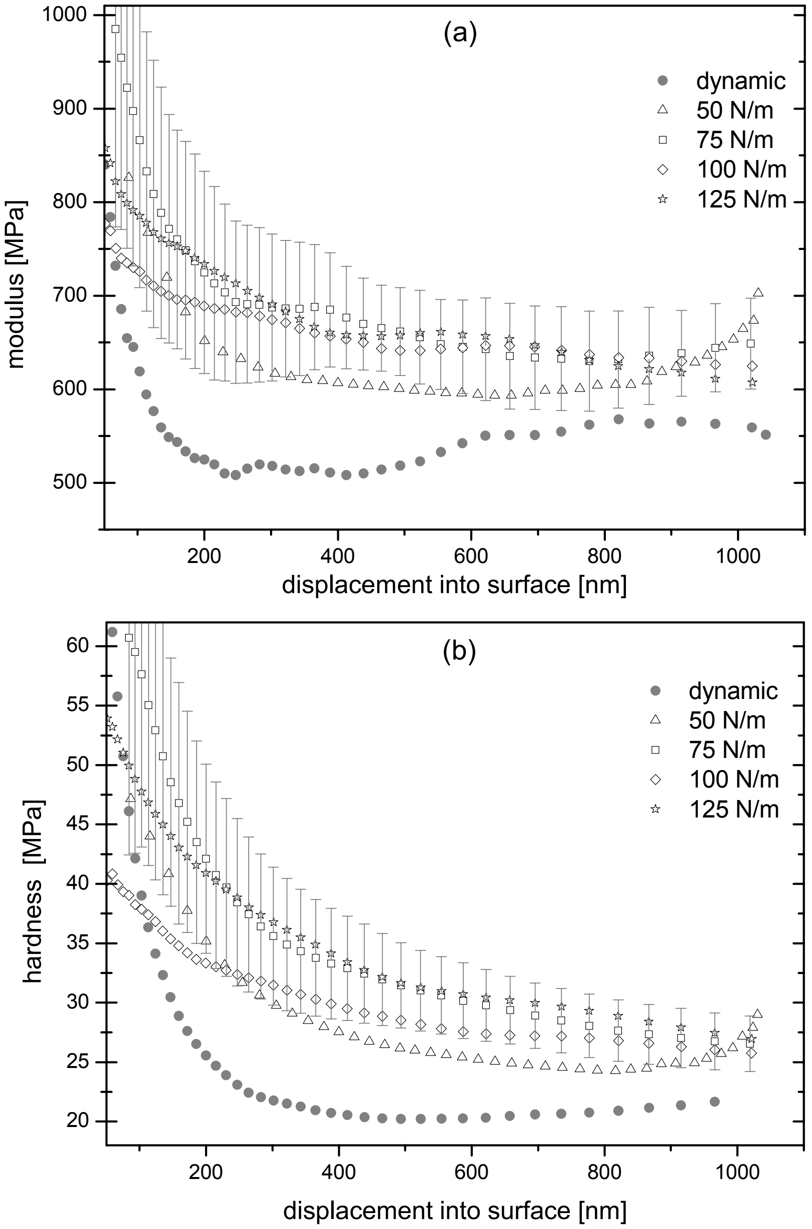

Figure 25: (a) Average modulus vs. displacement curves for LDPE. The error bars have a size of ±100 MPa and correspond to the 100 N/m threshold curve. (b) Average hardness values. The error bars (±10 MPa) are given again for the 100 N/m threshold curve. The range of the error bars of 40 MPa is equivalent to the difference in the average values of a 125 N/m threshold and the dynamic method.

4.3.3 Discussion

In the following the results that were obtained with the dynamic method are discussed and evaluated in order to point out both the advantage of the dynamic method as well as the uncertainties, which are still associated with this technique and which have to be addressed in the future work.

The measurements on different polymers reveal the difference between the dynamic method and the standard method in the load-displacement data. For all tests the maximum indentation depth was 1000 nm, and it is obvious that in all cases the load level of the dynamic method is lower than for the standard method. This can be explained by the more accurate surface detection in the dynamic method. The higher accuracy corresponds to less surface penetration due to earlier surface detection, which then reduces the force needed to reach the desired displacement.

In order to ensure that the differences in results are really surface detection related, we will consider, whether viscoelastic effects have to be taken into account for our measurements. It is known from [70] that the maximum load applied during an indentation cycle influences the unloading stiffness of polymeric materials, if they exhibit creep. It is found that for higher applied loads, the determined stiffness will be overestimated, because the "nose-formation" is more pronounced. Since we do get different maximum loads for different methods on one material, it seems to be reasonable to check, whether viscoelasticity effects influence the stiffness determination and hence the modulus and hardness results. Feng and Ngan [71] proposed a procedure to correct the unloading stiffness for creep effects, which occur during the unloading segment. Although the continuously recorded dynamic stiffness (not the unloading stiffness) was used for the calculations of the mechanical properties, this correction procedure was performed and results are compared to the dynamic stiffnesses. In Table 1 the originally measured unloading stiffnesses S_{unload} (averaged for 15 individual tests) determined with the Oliver & Pharr analysis are listed together with the dynamic stiffness values S_{CSM} at maximum load. Further the unloading stiffness values $S_{corrected}$ are given, which have been corrected for creep following the procedure of Feng and Ngan [71]. As can be seen from the values in Table 1, the creep correction does not change the unloading stiffnesses much. The differences between corrected and uncorrected unloading stiffness are only a fraction of the unloading stiffness standard deviation. Further, the dynamic stiffness values do not deviate significantly from the unloading stiffnesses (regardless whether they are corrected or not). This leads to the conclusion that creep effects are negligible. Thus, the differing hardness and modulus values are not caused by creep and must be due to the load differences, which originate from variation of the surface detection method.

Table 1: Comparison of stiffness values.

Material	Method	S_{unload} [N/m]	$S_{corrected}$ [N/m]	S_{CSM} [N/m]
SU8	dynamic	34163±800	33904	33876
SU8	50 N/m	34190±1200	33961	33979
SU8	125 N/m	34164±530	33935	34025
UHMWPE	dynamic	7477±630	7457	7460
UHMWPE	50 N/m	7344±470	7325	7335
UHMWPE	125 N/m	7476±480	7456	7592
LDPE	dynamic	3557±150	3554	3673
LDPE	50 N/m	3602±320	3598	3631
LDPE	125 N/m	3552±170	3548	3581

In quantitative terms the dynamic method yielded between 8 % and 17 % lower moduli and about 13 to 33 % lower hardness values, which can be seen from the summary of properties in Table 2. The surface detection difference was 5 nm for SU8, 7.5 nm for UHMWPE and 10 nm for LDPE, which is about 1 % of the total displacement into surface. The larger discrepancy for the hardness calculation is due to the direct proportionality $H \propto 1/A$ (with A being the contact area), whereas for the modulus $E \propto 1/\sqrt{A}$. It is interesting to see that such small differences in surface detection can lead to distinctly different results, thus underlining the importance of accurate surface detection, especially for soft materials.

The UHMWPE sample is supposed to have a modulus between 0.2 and 1.2 GPa. Our results are 1.14±0.07 GPa (dynamic method) and 1.34±0.1 GPa (standard method). The values for LDPE are 0.54±0.3 GPa for the dynamic method and 0.65±0.5 GPa (standard method); the values given by the manufacturer range between 0.1 to 0.3 GPa. This comparison does not comprise an agreement for all results; it is, however, consistent concerning the relative values, because for all materials the dynamic method delivers lower values than the standard method, which are closer to the reference values from the manufacturer. This was also expected as the standard method tends to underestimate the contact area, which leads to an overestimation of modulus and hardness.

Table 2: Comparison of moduli and hardness values of polymeric materials.

	modulus [GPa] [28; 29]	**dynamic method**	**standard method**
SU 8	4.4	4.43±0.23	4.82±0.45
UHMWPE	0.2 – 1.2	1.14±0.07	1.34±0.95
LDPE	0.1 - 0.3	0.54±0.32	0.65±0.05
	hardness [MPa]	**dynamic method**	**standard method**
SU 8	-	299±5	344±3
UHMWPE	-	47±4	60±6
LDPE	-	20±2	30±4

In order to understand the results for the PE samples, the actual indentation data have to be considered more closely. One issue concerning figures 23 and 25 is the decrease of properties with increasing penetration. Further the results of nanoindentation experiments are in the upper range or even significantly above (LDPE) the expected values. This enlargement of values was most probably caused by the mechanical polishing, which had to be performed prior to indentation testing to reduce the surface roughness. It is known that polymeric materials may undergo a densification processes or can crystallize when subjected to mechanical forces [32]. Mechanical polishing is a treatment that certainly can introduce large straining near the surface and thus may affect the mechanical properties. The polishing effect is expected to be most pronounced at shallow depths, which can explain the decrease in properties with increasing depth. For UHMWPE, where the indentation results are just at the upper limit of given range, the effects of polishing are not as big as for the more compliant LDPE, where the results are far beyond the range of 100 – 300 MPa. Another striking feature of the PE results is the large error bars displayed in the diagrams (figures 23 and 25). Various influences can cause such high standard deviations: insufficient polishing of the surface causing too high surface roughnesses, residue particles of the diamond paste that have been pressed into the surface during the polishing process or crystalline domains next to amorphous regions due to the semi-crystallinity of the PE samples. In the process of measuring an array of many indents, it is possible that the individual positions of indents are situated on locations that are strongly influenced by external factors, whereas other indents may be at locations with no influence. This brings about variations in the maximum loads and the resistance of the material to the penetration of the tip and thus a large amount of scatter in the individual results.

4.4 Conclusions

Our testing results have confirmed the importance of precise surface detection for the acquisition of reliable results in indentation testing. The accuracy of surface detection is strongly improved when using dynamic testing with the contact stiffness as contact criterion in comparison with quasi-static testing. For materials with moduli of several MPa the point of surface contact can be identified within 30 nm, compared to an uncertainty in the surface position of some hundreds of nm or even several µm for the techniques based on quasi-static surface identification. For the PDMS material used in this study this difference in surface position leads to deviations in the resulting modulus values by 400%. The investigation of three stiffer polymeric materials with known properties proves that even little inaccuracies in the range of several nm can lead to remarkable deviations in the modulus and hardness values. Other factors like surface roughness and viscoelasticity, which may have a significant influence on indentation results, have been excluded to cause the differences in results.

Chapter 5

Crosslinking and curing kinetics of PDMS studied by dynamic nanoindentation

Abstract

Polydimethylsiloxane (PDMS) networks are widely used in many different fields of applications, where the mechanical performance of these materials plays an important role. In order to get a better understanding of the mechanical behavior of PDMS-based materials we applied dynamic nanoindentation for the determination of storage modulus, loss modulus and hardness of PDMS samples of 8 different crosslinking densities. Furthermore, the influence of the curing time was investigated for 3 different crosslinking stages. The results of our investigation revealed that the elastic moduli of our samples cover a range of 2 orders of magnitude, and for one and the same PDMS the modulus may increase by a factor of 10 as a function of curing time. Complementary tensile tests were performed to validate the nanoindentation results and to determine the Poisson's ratios of 6 different PDMS samples. In contradiction to the general assumption, the measured Poisson's ratios deviate from 0.5, thus indicating a viscoelastic rather than ideal rubbery behavior.

5.1 Introduction

The first theoretical considerations of polymer elasticity and polymer networks arose in the 1930s [72]. Since then it has been attempted to improve the understanding of relations between the network structure and the resulting physical and mechanical properties of the polymer [73-76], which is of great importance for technological applications. For the experimental frameworks, which led to the development of network elasticity theories, poly-dimethylsiloxane (PDMS) and its derivatives have often been used as inorganic polymer model systems [78-81], since they allow easy tailoring of desired properties. The testing comprised swelling experiments, stress-relaxations [77, 78], uniaxial tensile and compression tests [8, 9] and the investigation of the elastic modulus as a function of temperature [81].

Nowadays, PDMS is a polymer widely used in medicine, engineering and everyday life and has even been suggested as a reference material for mechanical testing. It belongs to the group of silicones, which exhibit a unique combination of physical properties, like heat stability, resistance to the effects of weather, sunlight, moisture and many chemicals. Further, they are highly flexible, have a high permeability to gases and possess a low glass transition temperature T_g (about 200 K for PDMS) [82]. By modifying the chain structure of the polymer, its flexibility or rigidity can be tailored. Low surface energy, or surface tension, is another key feature of this material [83, 84].

PDMS is cured by an organometallic crosslinking reaction, e.g. [6, 85], which can be accelerated by exposure to heat [86]. Due to the multiple reaction sites on the base and the crosslinker oligomers, three-dimensional crosslinking occurs. In this type of reaction no waste products such as water are generated. Through a variation of the oligomer and/or crosslinker structures, other network architectures become possible in a controlled fashion [80]. In general, an increase of the ratio of curing agent to base leads to a more crosslinked and thus stiffer elastomer [35, 87-90]. This is consistent with the theory of rubber elasticity, where the elastic modulus is proportional to the number of network chains per volume, i.e. inversely proportional to the average chain segment length. In contrast, the tensile strength is dependent on the segment length distribution; the extensibility of a random network is determined by the shortest chain segments [80].

With all these different characteristics, polysiloxanes are used in a variety of applications, both medical and non-medical. The medical applications, based on the fact that PDMS is biocompatible [90, 91], include prostheses, artificial organs, artificial skin, and drug delivery systems [92], while the non-medical applications include high-performance elastomers, membranes, electrical insulators, adhesives and protective coatings, and release control agents for agricultural chemicals. As a fluid, PDMS oil is used for hydraulics, heat-transfer, and as dielectric fluids [93, 94].

The use of silicone rubbers based on PDMS in research is often motivated through the possibility of easily modifying the mechanical properties by varying the crosslinking density of the polymer networks. For instance, it is known that the attachment, adhesion and spreading of micro-organisms and cells on a polymer surface are influenced not only by chemical and surface properties of the polymer, but also by the substrate stiffness on which the cells sit, as has been shown by various studies on PDMS [87, 95-97] and other polymers [98, 99].

Several researchers also used the ability to tailor stiffness to apply mechanical testing methods (which were until then only used on stiffer and harder materials) on PDMS samples with varying crosslinking stages. Most work was done in the field of depth-sensing indentation (DSI) [7, 24, 33, 35, 90] with the main objectives being to determine the effects of adhesion on the measurements, to use adhesion contact mechanics models for data correction [24, 33, 34] and to compare their results with measurements from bulk testing methods [7, 35].

In the present study, we applied dynamic nanoindentation testing to PDMS samples of various crosslinking densities for the determination of storage modulus, loss modulus and hardness to deepen the understanding of the mechanical behavior of polysiloxanes. Furthermore, the influence of the curing time on PDMS of 3 different crosslinking stages has been investigated, since PDMS is known to be subjected to aging effects. These aging effects are due to incomplete crosslinking and lead to changing properties with time. Although these effects are known, their influence on the mechanical properties has never been studied. Therefore, a comprehensive study about the relationship of mechanical properties and changes in the polymer structure is long overdue.

5.2 Experimental

5.2.1 Instrumentation

For nanoindentation testing a Nano Indenter DCM from MTS Nano Instruments (Oak Ridge, TN, USA) was used. The continuous stiffness measurement (CSM) technique [12, 31] was applied to determine the storage and loss moduli as well as the hardness as a function of indentation depth. All indentation tests were carried out at a constant deformation rate of $5 \times 10^{-5}\ s^{-1}$ [68] and a frequency of 75 Hz to a maximum penetration depth of 2000 nm. The basic equations of determining the dynamic properties storage and loss modulus from indentation testing using CSM are taken from [62] and will be given in the following.

A sinusoidal force signal with an angular frequency ω and amplitude F_0 is applied to the system according to

$$F(t) = F_0 \cdot e^{i\omega t} \tag{11}$$

The resulting displacement z(t) with the displacement amplitude z_0 has the same frequency as F(t), but lags behind by a phase angle δ:

$$z(t) = z_0 \cdot e^{i\omega t + \delta} \tag{12}$$

The differential equation of motion for a harmonic oscillation can be applied to the overall behavior the whole system:

$$F(t) = m\ddot{z} + D\dot{z} + Kz \tag{13}$$

Here m is the mass, D is the effective damping, K is the effective stiffness and z represents the displacement and its derivatives with respect to time. In order to separate the contributions from the instrumentation setup and those from the sample-tip contact according to the model in figure 9 (see page 36), the effective stiffness K can be written as:

$$K = K_s + (\frac{1}{S} + \frac{1}{K_f})^{-1} \tag{14}$$

with K_s being the support spring stiffness, K_f the load frame stiffness and S the contact stiffness. The effective damping D can be written as:

$$D = D_i + D_s \tag{15}$$

Here D_i is the damping of the capacitive gage in the head and D_s is the damping of the contact. By substituting equations (14) and (15) into equation (13) and applying it to its particular solution (11), the following relationships can be obtained for the contact stiffness:

$$S = \left(\frac{1}{\frac{F_0}{z_0} \cdot \cos\delta - (K_s - m\omega^2)} - \frac{1}{K_f} \right)^{-1} \tag{16}$$

and for the contact damping:

$$D_s \cdot \omega = \frac{F_0}{z_0} \cdot \sin\delta - D_i \cdot \omega \tag{17}$$

The storage E’ and loss modulus E’’ are related to the quantities given in equations (16) and (17) as follows:

$$E' = S \cdot \frac{\sqrt{\pi}}{2\sqrt{A}} \tag{18}$$

$$E'' = D_s\omega \cdot \frac{\sqrt{\pi}}{2\sqrt{A}} \tag{19}$$

Here, A is the contact area. The storage modulus is associated with the elastically stored fraction of the deformation energy, the loss modulus with the energy dissipated during the indentation cycle. The ratio E''/E' is defined as tan δ, where δ is the phase angle between force and displacement. During indentation the angular frequency was set and the force and displacement amplitudes F_0 and z_0 were measured continuously along with the phase angle δ. For acquiring the load frame compliance, the dynamic behavior of the instrumentation and the area function of the tip, the calibration procedures according to Oliver and Pharr [12, 31] were performed.

Tensile testing was conducted with a Nano Bionix (MTS Nano Instruments, Oak Ridge, TN, USA). PDMS stripes of approximate size 0.5x0.5x10 mm were cut and decorated with a pattern for the determination of Poisson's ratio with the help of a video system. The principle of the procedure is illustrated in figure 26. For comparability of results, the tensile specimens were cut from the same PDMS piece that was used for indentation testing. The tensile strain rate was 5×10^{-5} s^{-1}, equivalent to the indentation deformation rate [68]. The specimens were strained up to a maximum of 20 %.

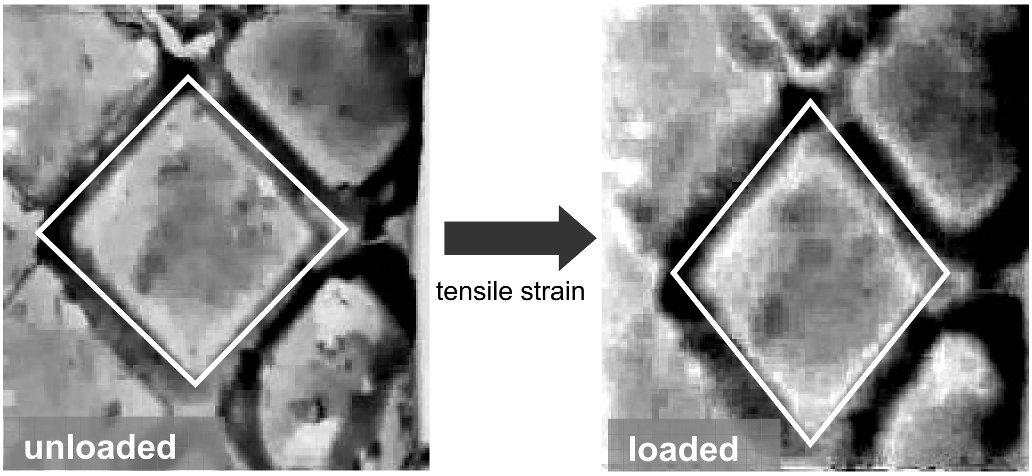

Figure 26: Principle of Poisson's ratio determination. The sample is loaded with a tensile strain in vertical direction. The strain in vertical and horizontal directions is calculated from the shape differences between the loaded and unloaded state.

5.2.2 Materials

PDMS (Sylgard 184, Dow Corning) was provided in an unreacted state. The crosslinking (see figure 11 on page 39) and curing was performed immediately before the use of the sample. In order to allow a systematic investigation, the crosslinking densities and the curing process of the samples were varied. For changing the crosslinking states of the samples, the following eight weight ratios of crosslinker to pre-polymer were selected: 1:2, corresponding to a crosslinker portion of 33 wt%, 1:3 (25 wt%), 1:5 (16 wt%), 1:7 (12.5 wt%), 1:10 (9 wt%), 1:20 (5 wt%), 1:30 (3 wt%), and 1:40 (2.4 wt%).

The curing process was divided into two steps: first, all samples were pre-cured at 65 °C for 12 h, as recommended by the manufacturer. For determining the effect of crosslinking density, the samples were cured at 190 °C for 48 h in a second step. Three compositions, 1:2, 1:10 and 1:30, were used to investigate the properties as a function of curing time. For this purpose PDMS discs with a diameter of several cm, which had only been pre-cured at 65 °C for 12 h were put into an oven at 150 °C under vacuum; after discrete periods of curing time, little pieces were cut from the big discs and measured with the nanoindenter within 12 h to avoid aging at room temperature.

5.3 Results

5.3.1 Variation of crosslinking density

The data obtained for the specimens with different crosslinking densities are displayed in figure 27. The contact stiffnesses (see figure 27a) increase nearly linearly with penetration depth and the slopes increase with the amount of crosslinker. The same trend can be observed for the load-displacement data in figure 27(b). The maximum load values needed to reach a maximum penetration depth of 1000 nm range from roughly 2 µN for PDMS 1:40 up to about 28 µN for PDMS 1:2.

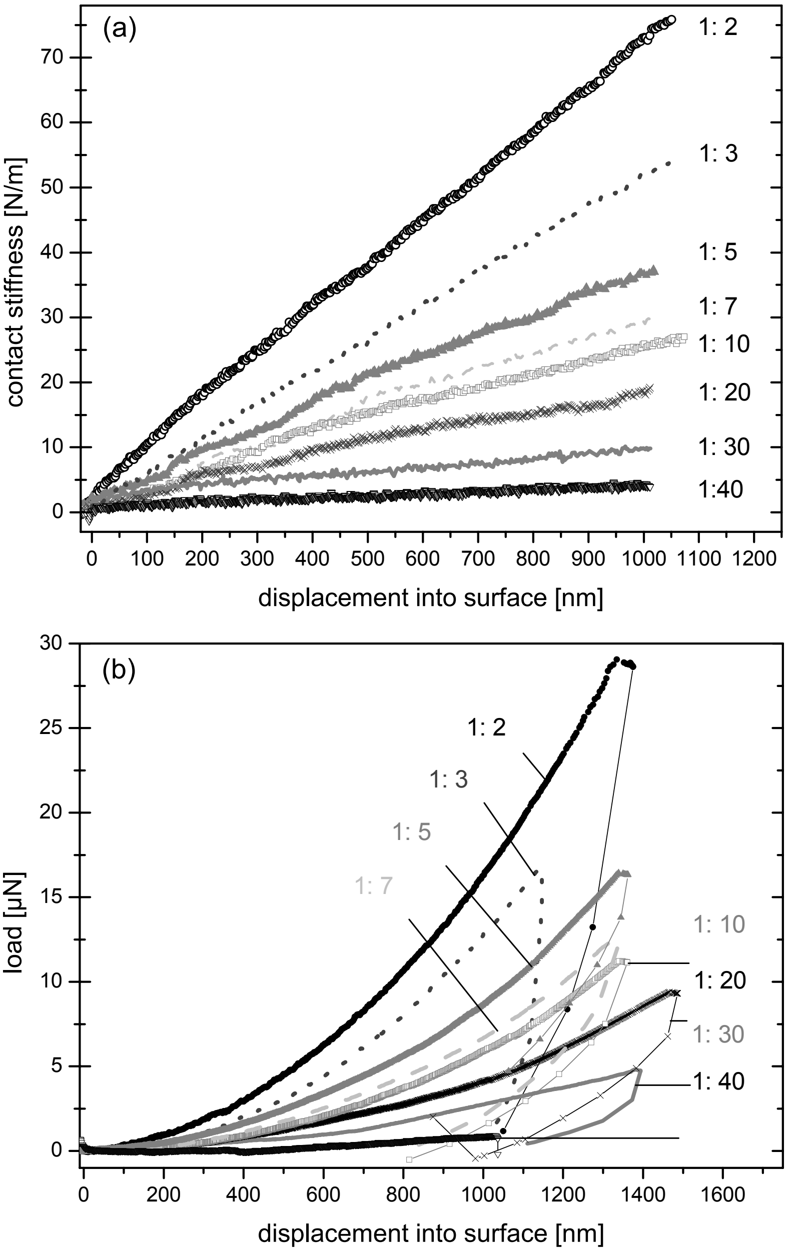

Figure 27: (a) Contact stiffness vs. displacement and (b) load-displacement curves for eight differently crosslinked PDMS specimens.

In figure 28 the storage and the loss moduli are plotted as functions of the displacement. These curves are the average calculated from at least 15 individual indentations on each specimen. For both storage and loss modulus the curves show a high amount of noise during the initial portion and become smooth after approximately 300 nm of penetration. After this depth is reached the values can be considered as constant. It is obvious that a higher crosslinking state corresponds to a higher storage and loss modulus. The indentation hardness values (figure 29) can again be correlated with crosslinking density. The values lie between 0.05 MPa for the softest PDMS 1:40 and 0.9 MPa for the stiffest PDMS 1:2.

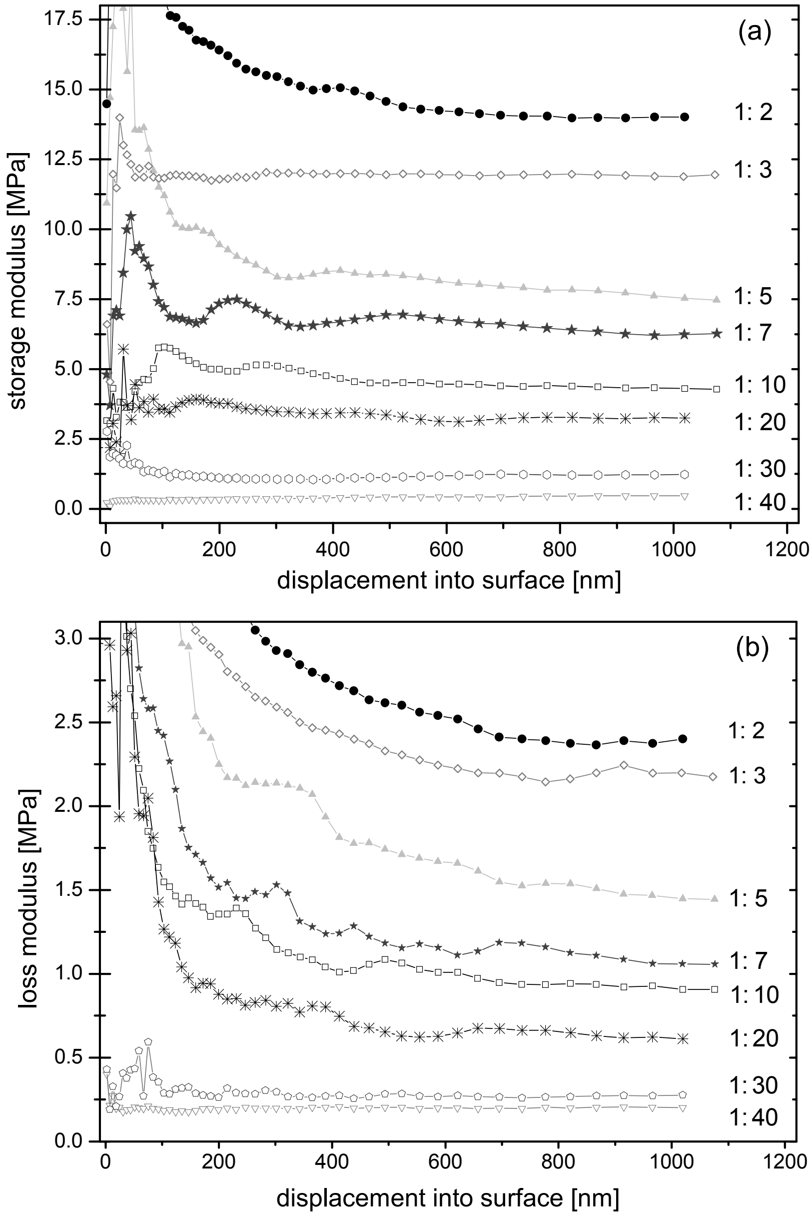

Figure 28: (a) Storage moduli of various PDMS samples as a function of penetration depth. For penetrations higher than 300 nm the curves run into a plateau and can be considered as constant. (b) Loss moduli plotted vs. the indentation depth. The loss modulus increased with higher crosslinking.

Poisson's ratios were determined according to the principle in figure 26 from 12 individual tensile tests for each composition. The values are summarized in Table 3 together with the standard deviations. For 6 out of 8 compositions the values are given after curing at 190 °C for 48 h. Additionally, the values after pre-curing are given for the 3 PDMS compositions that were also used in the following section, where the influence of curing time is investigated. As can be seen from Table 3, the Poisson's ratio depends on both the amount of crosslinking agent in the material and on the curing state of the sample. For materials with increasing crosslinking densities, Poisson's ratios deviate from 0.5 more and more.

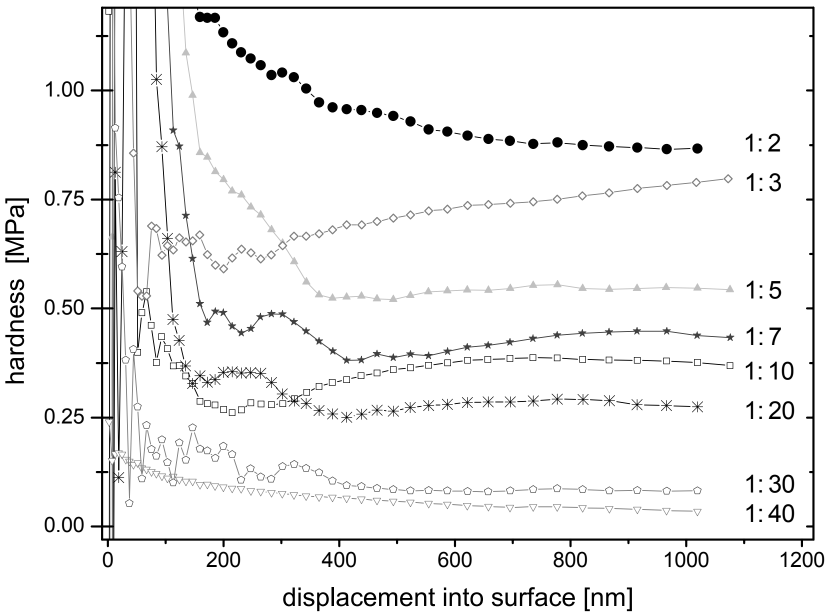

Figure 29: Hardness as a function of displacement. The hardness values derived from indentation testing are equal to the mean pressure under the indenter tip.

Table 3: Summary of Poisson's ratios determined according to figure 26.

Composition	weight%(crosslinker)	fully cured at 150 °C	after 12 h at 65 °C
1:2	33	0.386 ± 0.027	0.423 ± 0.020
1:3	25	0.408 ± 0.028	---
1:5	16	0.421 ± 0.015	---
1:10	9	0.430 ± 0.018	0.443 ± 0.026
1:30	3.2	0.452 ± 0.025	0.472 ± 0.013
1:40	2.4	0.469 ± 0.017	---

5.3.2 Curing of PDMS

Although PDMS is known to be subjected to aging effects, the influence of curing time on the mechanical properties has never been investigated. Three of the materials above, i.e. PDMS 1:2, PDMS 1:10 and PDMS 1:30 have been used to investigate the development of the mechanical properties, storage and loss modulus as well as hardness, as a function of curing time. The process of crosslinking can be characterized by the maximum load values in the load-displacement curves (figure 30a). For the 1:2 specimens the load required to reach a penetration depth of 2000 nm were 8 μN after curing at 65 °C and went up to 108 μN after curing at 150 °C for 217 h. The contact stiffnesses in figure 30()b show the same trend until the end of the reaction after approximately 100 h. The curves for 123 h and 217 h coincided.

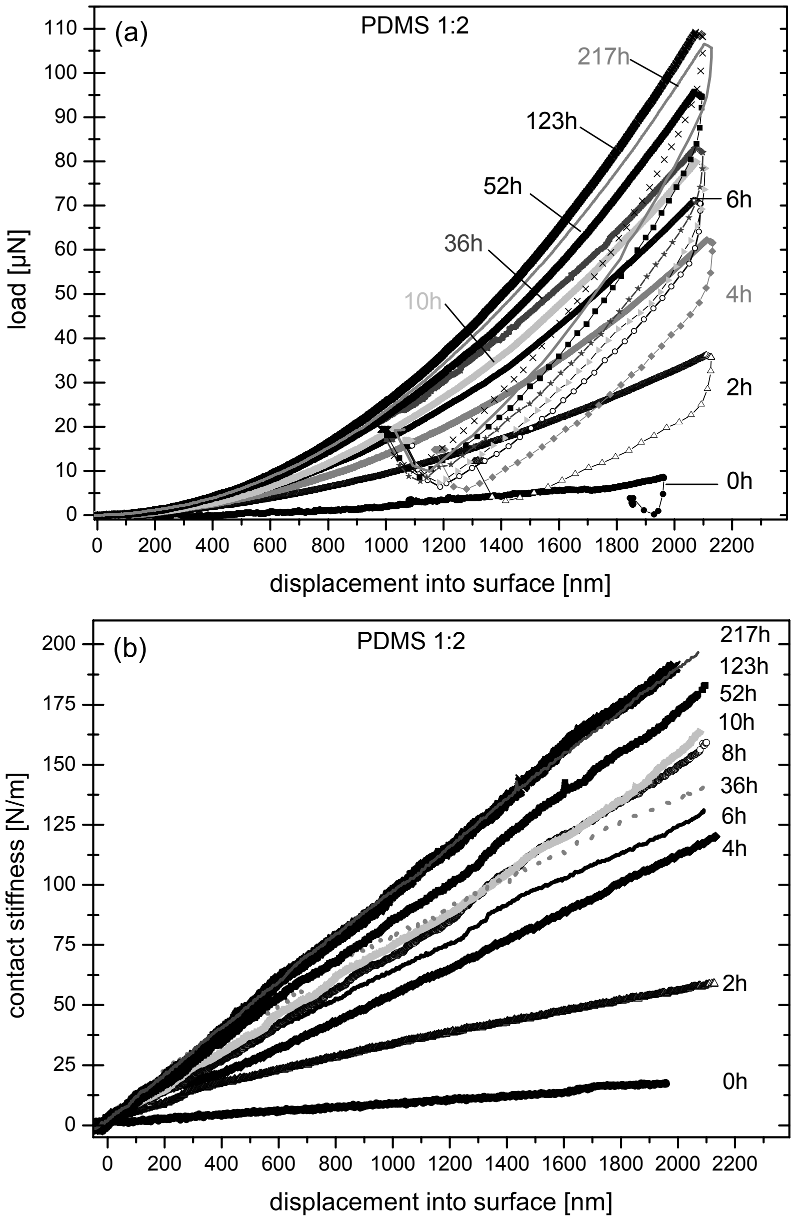

Figure 30: (a) Load-displacement curves of PDMS 1:2 after discrete steps of curing at 150 °C. (b) Corresponding contact stiffnesses obtained from CSM. The curves plotted here are data from individual tests representative for the different specimens.

Also for the two more compliant samples the crosslinking process is mirrored in the load and contact stiffness values (data not shown here). In the case of PDMS 1:10, the load values at the maximum penetration of 2000 nm doubled from 19.5 µN after pre-curing to 41 µN after complete reaction. The contact stiffnesses were 21 N/m and 65 N/m, respectively. The forces needed to drive the indenter 2000 nm into PDMS 1:30 ranged between 5.8 µN (pre-cured) and 8.5 µN (fully cured). The associated stiffness values were 6 N/m and 10 N/m.

The storage and loss moduli of PDMS 1:2 in figure 31 were calculated from the CSM data in figure 30 according to equations (18) and (19), and are the averages of 15 tests. The properties increased continuously with longer curing times. The strongest increase in properties by a factor of 6 was observed in the first 10 h, between 10 and 100 h the values still increased slowly and after that saturation was reached.

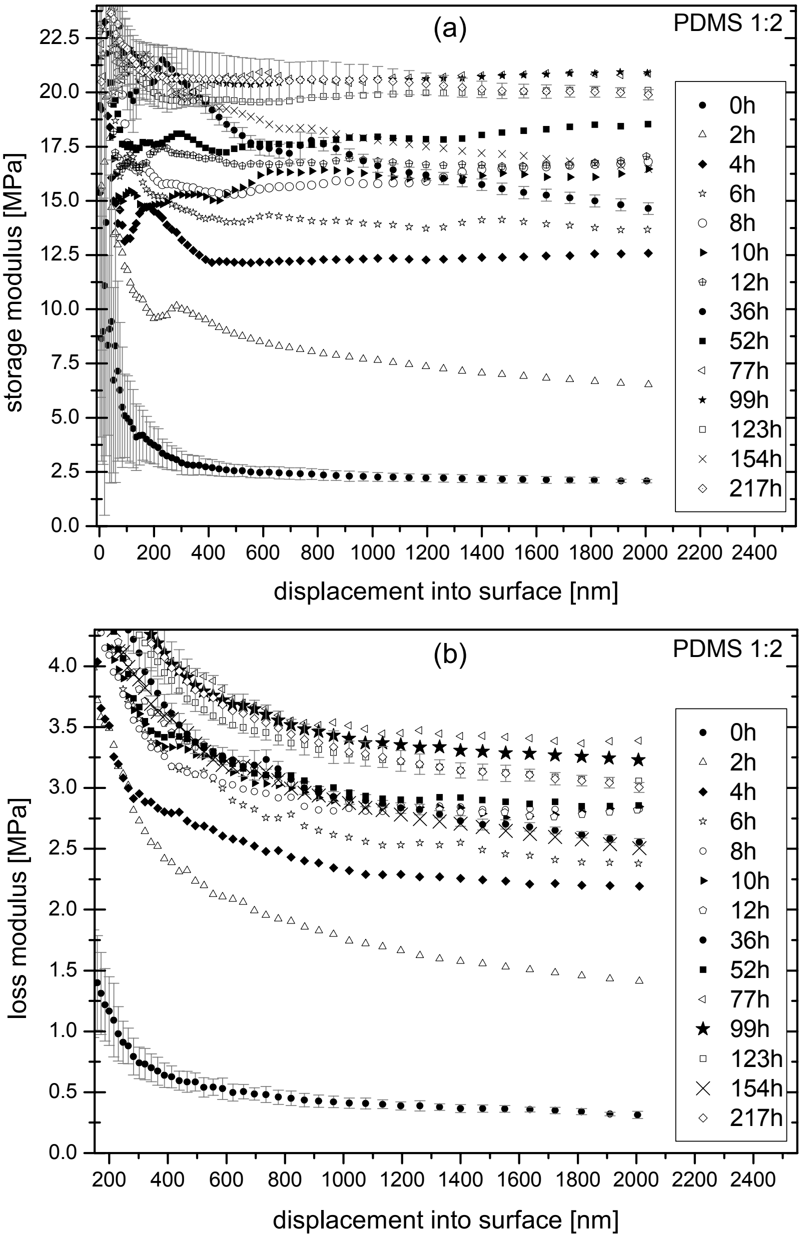

Figure 31: (a) Storage moduli as a function of penetration depth for PDMS 1:2 after curing at 150 °C. (b) Loss modulus values calculated from CSM data according to equation (19). These curves represent the averages of at least 15 individual tests. The error bars denote the standard deviation.

Similar behavior was also found for the hardness values, which are plotted in figure 32. Noticeable about these curves is that the scatter was quite large in the beginning, i.e. the first 300 nm of the indentation, as can be seen from the error bars in figure 32, which denote the standard deviation of 15 tests. For penetrations larger than 400 nm, the values did not change any more and a plateau region was reached. Also the size of the error bars decreased significantly for the plateau region.

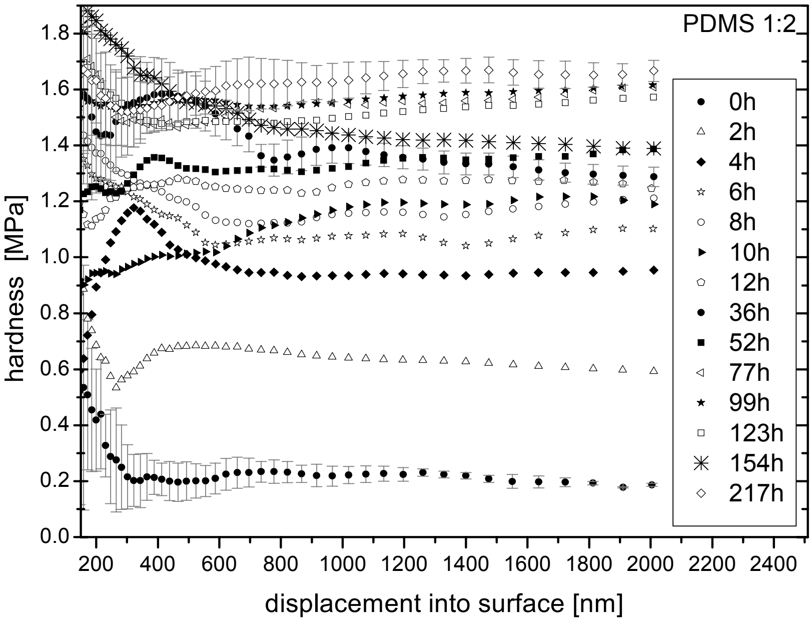

Figure 32: Hardness values vs. displacement for various curing times of PDMS 1:2.

The overall behavior of PDMS 1:2 during the crosslinking reaction is summarized in figure 33(a), where the storage and loss modulus as well as the hardness values are plotted as functions of curing time. The same kind of overview plot is given for PDMS 1:10 in figure 33(b). Here the values increased by a factor of ~ 2 within 10 h of curing at 150 °C. The storage modulus ranges from 2.5±0.1 MPa to 5.0±0.3 MPa, the loss modulus from 0.57±0.05 MPa to 1.44±0.04 MPa. The hardness values lie between 0.37±0.02 MPa and 0.59±0.01 MPa. The CSM data for PDMS 1:10 are not shown, but the curves resemble the behavior of the curves in figures 30 and 31.

For the softest of the three materials, PDMS 1:30, the contact stiffness curves after curing for 0, 4, 10, 24, 51, and 96 h are given in figure 34(a). For the possibility of comparing and validating the indentation results, the same specimens were tested in tension. In figure 34(b) the stress-strain curves of these tensile tests are displayed. For both methods the curves rose with curing time, the completion of the crosslinking was reached after approximately 30 h. This can be concluded from the data after 24 h of curing, which were well below the curves for 51 h and 96 h.

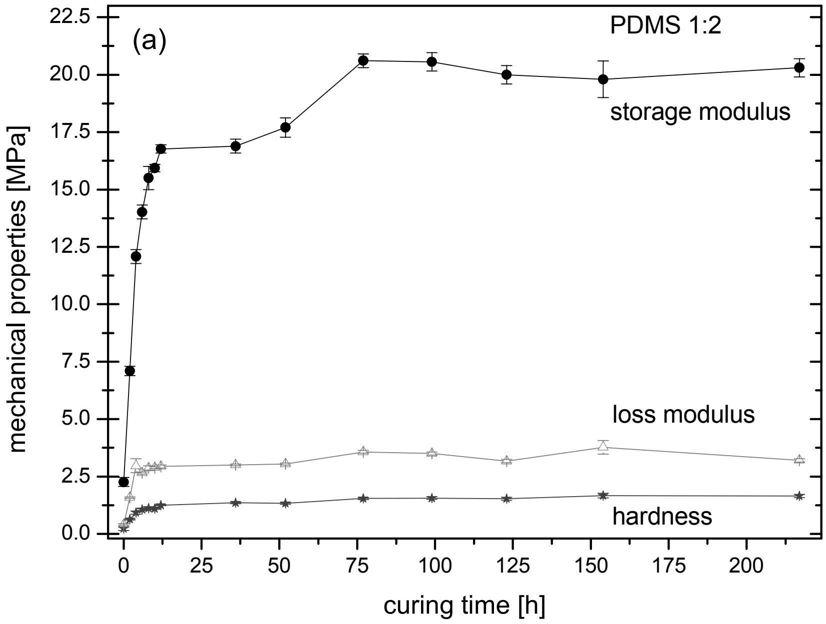

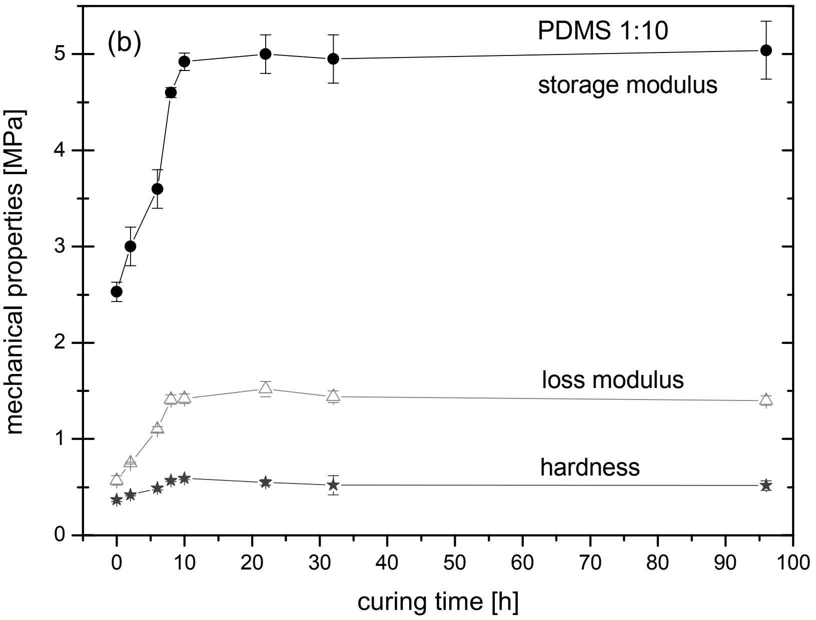

Figure 33: (a) Mechanical properties of PDMS 1:2 as a function of curing time at a curing temperature of 150 °C. The crosslinking reaction took approximately 100 h to complete. (b) Development of mechanical properties of PDMS 1:10 with cuing time. After 15 h the values reach a plateau, thus the sample is fully crosslinked.

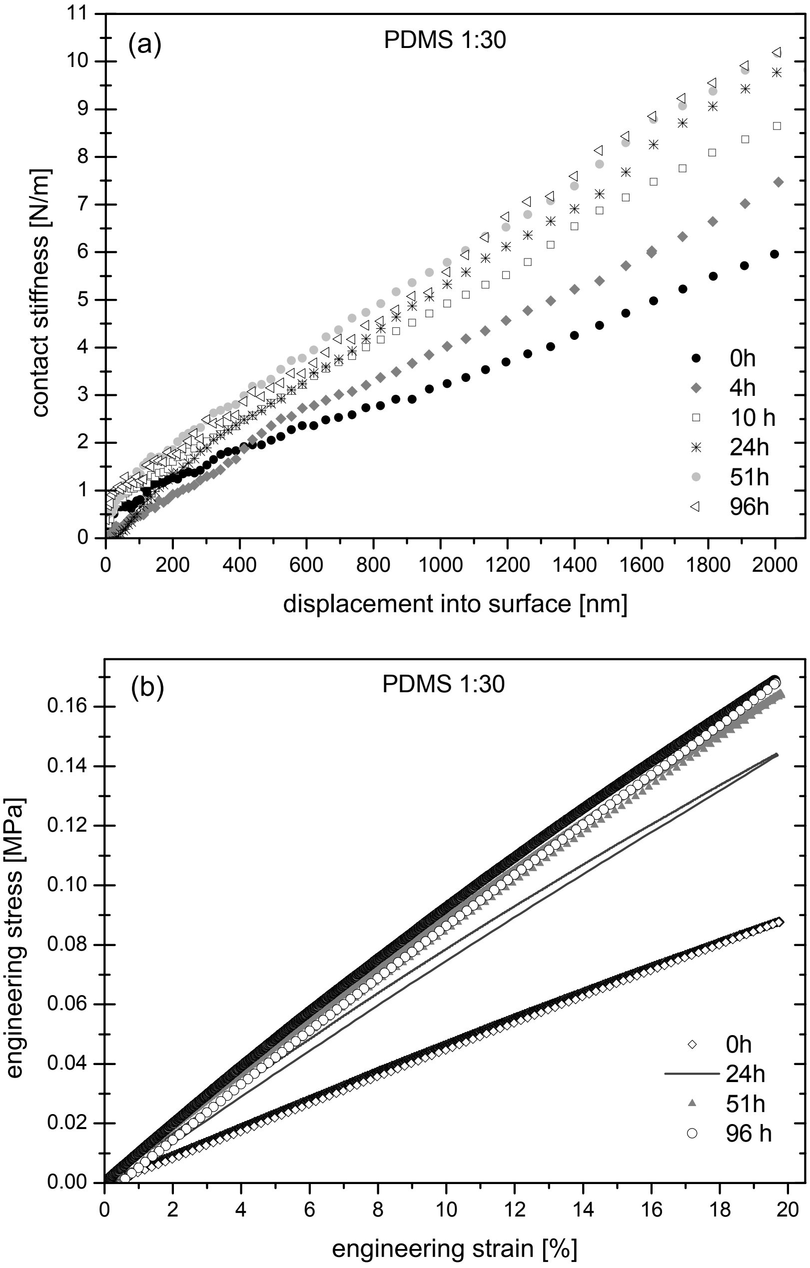

Figure 34: (a) Contact stiffness vs. displacement. Even slight changes in the stiffness of PDMS 1:30, which are only a few N/m can be sensed. (b) Average stress-strain curves for 4 different curing times.

After the pre-curing step at 65 °C the storage modulus was 0.51±0.02 MPa, the loss modulus 0.23±0.01 MPa, and the hardness was 0.085±0.007 MPa. In the fully cured state the properties were determined as follows: storage modulus 0.85±0.1 MPa, loss modulus 0.38±0.03 MPa, and hardness 0.11±0.03 MPa. The values are shown in figure 35 together with the results for intermediate curing times. The moduli obtained from the tensile testing are listed in Table 4 along with the storage moduli from indentation testing.

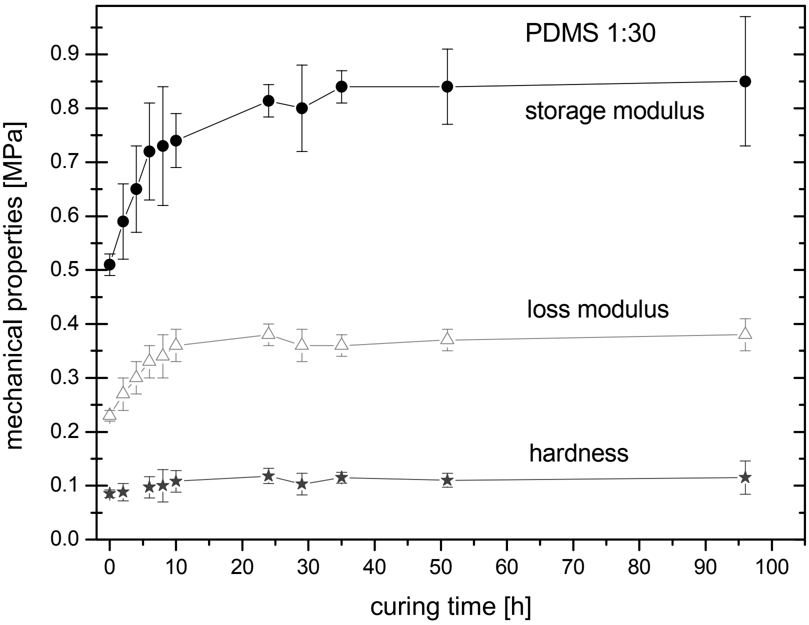

Figure 35: Overview of the mechanical properties of PDMS 1:30 as a function of curing time at 150 °C. The fully crosslinked state was reached after ~ 30 h.

Table 4: Comparison of results from tensile and indentation testing for PDMS 1:30.

Curing time (150 °C)	Young's modulus [MPa]	Storage modulus [MPa]	deviation [%]
0 h	0.43 ± 0.02	0.51 ± 0.02	18
24 h	0.8 ± 0.01	0.81 ± 0.03	1.25
51 h	0.86 ± 0.01	0.84 ± 0.07	2.34
96 h	0.855 ± 0.01	0.85 ± 0.09	0.6

5.4 Discussion

5.4.1 Variation of crosslinking density

The results of PDMS specimens with different crosslinking densities are given as an overview in figure 36, where the abscissa has been expressed in weight % of crosslinker. It can be seen that the values increase with rising crosslinking density, as is expected from the molecular theory of rubber elasticity [72-76]. The higher the amount of crosslinker in the material, the shorter are the chain segments between two crosslinking molecules, resulting in less chain flexibility and thus higher moduli [78]. For randomly crosslinked networks, however, this trend of increasing mechanical strength may reverse. Since they can exhibit a very broad distribution of chain segment lengths, chain rupture of the shorter chains may occur under deformation and cause softening of the material [80, 100]. Obviously, this effect could not be observed for our specimens, although PDMS 1:2 contains 33 wt % of crosslinker and is strongly crosslinked.

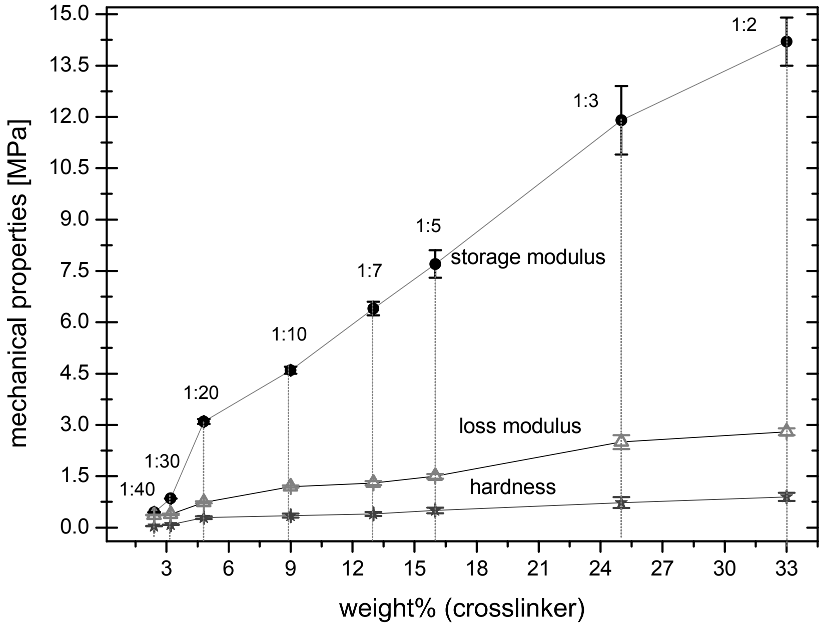

Figure 36: Mechanical properties plotted vs. the weight percentage of crosslinker. With increasing crosslinking density in the PDMS the storage modulus increased by a factor of 30 for the softest 1:40 and the stiffest 1:2, the loss modulus increased 10 times, the hardness value were 20x higher.

Further, our data are consistent with findings of other researchers [35, 87-90], who found increasing moduli for more highly crosslinked PDMS, regardless of the PDMS type and the varying test methods like tensile tests [87], DMA [88], buckling [89] and compression testing [35]. In one study only [90], conducted by means of nanoindentation and tensile testing, a decrease in modulus values as well as in ultimate tensile strengths was found for amounts of crosslinker higher than 21 %. This finding is partly consistent with results of Mark and Sullivan [80], who also found decreasing elongations at break and decreasing tensile strength with increasing crosslinking densities, yet, the moduli increased. Therefore, the results of Mata et al. [90] appear questionable. Only 5 indentations per sample were performed and no error margins are given. In contrast, the calculation of average values in our study comprised at least 15 indentations and showed good reproducibility.

Comparison of modulus values from the literature, which have been reported for PDMS 1:10 of the Sylgard 184 type, gives good agreement with our values. Literature data [7, 24, 33-35, 87-90] range from 1.8 MPa up to 3 MPa, we obtained 2.7±0.1 MPa; for the loss modulus a value between 0.4 and 0.6 MPa [7] can be compared to 0.57±0.05 MPa. Also values for less crosslinked PDMS are available, for 1:20 the literature value is 0.5 to 0.9 MPa [35, 87, 101], for 1:30 0.4 to 0.5 MPa are given, where our values are 0.63±0.08 MPa and 0.51±0.02 MPa, respectively. However, when considering the absolute values that are given in the literature, the comparability of results has to be checked carefully, because the curing procedures, i.e. time as well as temperature, used in various studies differ substantially, thus results might not at all be comparable. Therefore it might be better to give a certain range of values for comparable treatments, as it has been done in this section.

Regarding the variation of properties with crosslinking density (figure 36), the increase of the storage modulus is most significant. The modulus of PDMS 1:2 is 30 times higher than for PDMS 1:40. This large increase is probably due to the fact that the PDMS of the Sylgard 184 type contains silica filler particles [82]. According to Aranguren and co-workers, the PDMS chains are bonded to the silica filler particles [100], thus the filler particles function as crosslinking sites, which contribute to the stiffness of the system. Hence, during curing, the crosslinking density of the network/filler system increases much faster than it would through the crosslinking of PDMS chains alone. This effect should be even more pronounced if the initial concentration of crosslinking agent is high, which explains the 30-fold higher modulus of PDMS 1:2 compared to PDMS 1:40.

The increases in the hardness (20 times) and the loss modulus (a factor of 10) are also remarkable. Regarding the increase of the loss modulus, this result is counterintuitive, since the stiffer samples with much higher crosslinking densities should be closer to an ideal network. But some explanation might be found in [102], where the effects of dangling chains are studied and a decrease of the tan δ (and thus the loss modulus) with increasing content of dangling chains is found. Here [102] this was attributed to reduced chain segment rotations due to interactions with neighboring chains. For lower temperatures even crystallization of dangling chains becomes possible. For our samples it can be assumed that the dangling chains in the softer samples are longer and thus experience a stronger hindrance for chain segment rotation than do the presumably shorter dangling chains in the stiffer samples. This is a possible reason why the higher crosslinked samples can dissipate more energy than the weaker crosslinked ones, as indicated by the higher loss modulus.

The fact that the loss modulus rises with increasing crosslinking density, but not as strongly as the storage modulus, further leads to the conclusion that there is a viscous contribution in the deformation behavior of PDMS. This is also supported by the tan δ values determined from dynamic indentations, which decreased from 0.48 ± 0.02 for PDMS 1:40 to 0.17 ± 0.001 for PDMS 1:2. This is an important finding because PDMS-based materials are often referred to as silicone rubbers and ideally elastic behavior with a Poisson's ratio of 0.5 is assumed [35, 75, 92, 97]. This assumption of Poisson's ratio cannot be supported by the results obtained in this study. To our knowledge, the Poisson's ratio of PDMS has not been measured before. Therefore the Poisson's ratios of the differently crosslinked samples were determined based on micrograph analysis, which were taken during tensile testing. The results for all samples are significantly below 0.5, thus indicating viscoelastic rather than ideal rubber-like behavior as well. An interesting finding is the dependence of the Poisson's ratio on the crosslinking density. The higher the crosslinking density, the smaller is the Poisson's ratio. This can again be attributed to the high stiffness and reduced flexibility of the chains / molecules in the strong crosslinked samples, which makes it more difficult for them to move away from the original position; this effect results in less strain in the direction perpendicular to the tensile axis.

For the complementary tensile tests, the exact same specimens were used to avoid influences of different treatments or small compositional changes. Results from both methods are compared in figure 37. The modulus values differ at most by about 8 %, which is most probably attributed to experimental uncertainties. Although results from other studies indicate an effect of adhesive forces on nanoindentation results [24, 33], our results do not indicate a systematic error in the nanoindentation testing, because the indentation results diverge to higher as well as to lower values compared to tensile results. Thus, adhesion effects seem to be of limited influence for our measurements, and it can be concluded that these effects play a role only for shallow indentations (below 1 μm), where the contact area increase due to adhesive forces is a significant portion of the overall contact area.

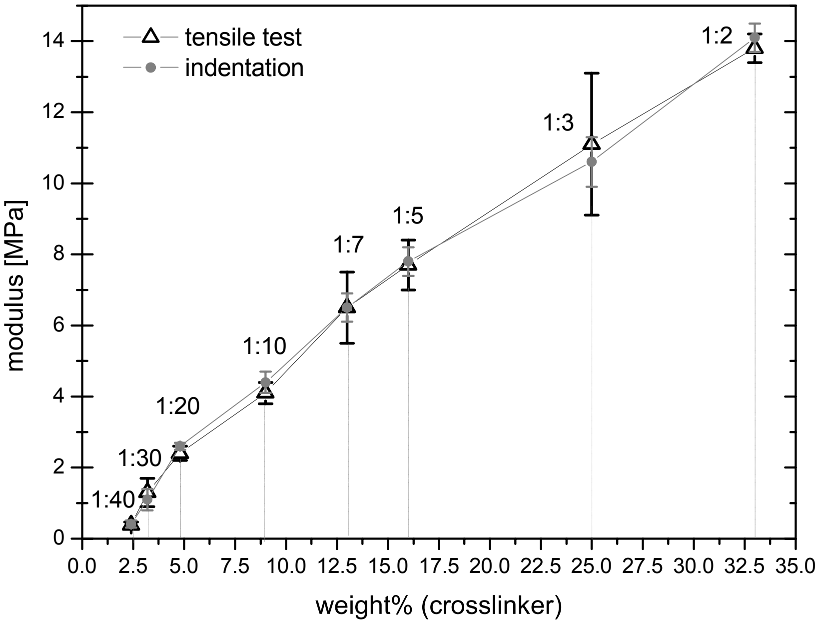

Figure 37: Comparison of results from tensile testing and indentation.

5.4.2 Curing of PDMS

The mechanical properties of PDMS with 3 different crosslinking stages were monitored as a function of curing time. After the pre-curing step the samples were tested for the first time and further curing at elevated temperature of 150 °C resulted in a significant increase in storage modulus, loss modulus and hardness; in contrast, the Poisson's ratio (see Table 3) and tan δ, as a measure of viscous losses in the system, decreased when the crosslinking reaction proceeded. These results are in agreement with other investigations [103-105], where the rheology of a crosslinking reaction was followed with DMA for an entire crosslinking reaction (from the liquid state through the gel formation to fully cured state). It can also be seen from those studies that the storage modulus increased more significantly in comparison with the loss modulus, thus leading to a decrease in tan δ. This is not only true for PDMS [104], but also for other polymers, e.g. epoxy and polyurethane [105].

The results of the tensile tests on PDMS 1:30 also validate the nanoindentation results for materials with a modulus below 1 MPa (Table 4). The deviations of the two techniques are not more than ~ 2 %. Only the softest material (after pre-curing) yielded a large difference of 18 %, yet the results are in comparable range of results from other investigators [35].

Another result is that the crosslinking reaction during the curing process slows down. Within the first couple of hours a fast rise in mechanical properties is observed, where limited crosslinking sites allow fast diffusion of crosslinker molecules. As the crosslinking becomes stronger, the viscosity of the system increases [106], thus the diffusion of unreacted molecules is increasingly hindered. Therefore the values increase only a little further and finally reach a plateau region. Similar observations have been made by Hild and co-workers for the tensile modulus of polystyrene networks [107]. It is interesting to see that the time required to complete crosslinking is shortest for PDMS 1:10 with a medium quantity of crosslinker, where only 15 h are necessary. For PDMS 1:30 the reaction terminates after ~ 30 h and PDMS 1:2 takes almost 100 h (figures 33 and 34). This short curing time for 1:10 is probably due to the optimized ratio of pre-polymer and crosslinking agent, since this is the ratio recommended by the manufacturer.

These results are of importance and relevance for researchers working with PDMS. So far, aging effects of PDMS have never been investigated in a systematic way. The only hint for a time scale is given by Dow Corning, who state that PDMS 1:10 has reached its fully cured state after 2 weeks when kept at room temperature [82]. Since PDMS is often used for purposes that are influenced by the stiffness, as e.g. a substrate material for cell experiments [96], it is important to take into account the curing of the PDMS and also to be aware of substantial differences in mechanical properties after storing PDMS. In order to estimate the effect of curing at room temperature, a PDMS 1:10 sample was kept at 25 °C and measured after one month and after six months. These tests revealed that the mechanical properties reach about 75 % of the plateau values in figure 33(b) if PDMS is stored/cured at room temperature for one month and do not change for longer curing /storage times.

Considering the effect of varying testing frequencies on the behavior of PDMS, springs and dashpots are often used to describe the elastic and viscous contributions to the overall behavior. Polymeric materials are usually described with the three-element standard model which consists of a Kelvin-Voigt element and a spring in series. It is assumed that the unrelaxed modulus measured at fast deformation or high frequencies, is larger than the relaxed modulus obtained for slow deformation or low frequencies. For the PDMS samples used in this study, storage and loss modulus are plotted vs. the frequency in figure 38. For both quantities an increase in the values is obtained, which has also been found by others [7, 103, 105]. In contrast, the hardness values are not affected by the changing frequency and remain constant. The modulus values are listed in Table 5, where the values at frequencies of 5 Hz, 75 Hz (used for all other measurements) and 200 Hz are given for all 3 compositions.

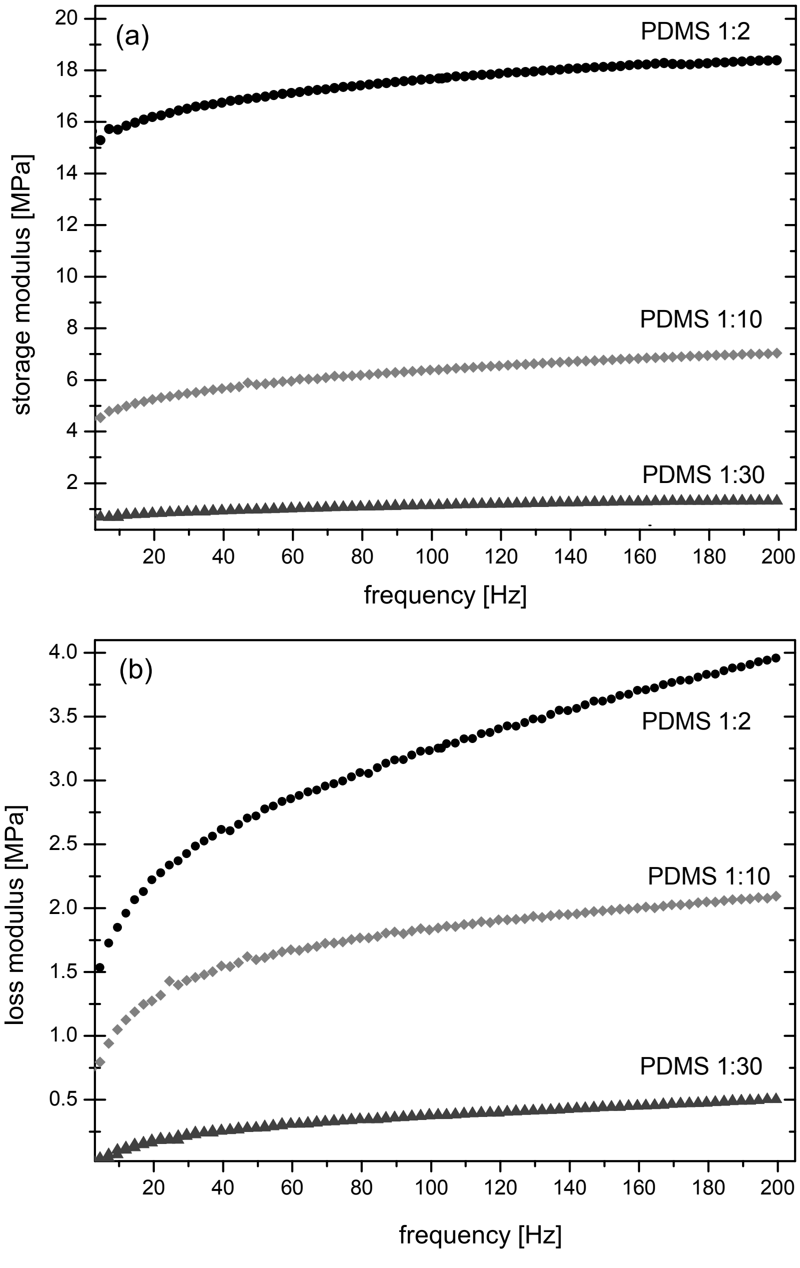

Figure 38: The viscoelastic properties storage (a) and loss modulus (b) for PDMS 1:2, 1:10, and 1:30 as a function of frequency. The tip oscillation frequency has been varied between 1 and 200 Hz.

Another factor that possibly influenced the indentation results is the amplitude of the tip oscillation, the harmonic displacement. The literature data [5, 7] regarding the influence of this parameter are contradictory. In one study no significant differences for a variation of the harmonic displacement was found [7], whereas higher values for greater harmonic displacements were observed in the other [5]. In the present study the harmonic displacement was always kept constant at 10 nm to avoid an influence and to ensure comparability of results. Anyway, we believe that the tip oscillation (independent of the amplitude) affects the contact formation as well as contact stabilization for displacements between 0 and approximately 300 nm and thus the results obtained at these shallow depths. This can be seen in figures 29 and 30, 33. Constant values were only measured for penetrations above ~ 300 nm, whereas higher values were obtained smaller penetrations. Note that this increase and the associated high scatter were not due to surface roughness because the roughness determined from AFM-measurements was in the range of 3 nm. Yet, our results are consistent with measurements of other researchers [108, 109], who also found this effect. One possible explanation for the increase in properties with decreasing indentation depth can be found in [48], where the increase is attributed to surface stress, against which the indentation load is working to deform the surface. This surface stress leads to a large increase in the hardness values for shallow indentation depths. Interestingly, the same researchers found that this effect was considerably more pronounced for a silicone elastomer than for other polymeric materials.

Table 5: Influence of testing frequency on results.

Composition	**1:2**		**1:10**		**1:30**	
Modulus [MPa]	***storage***	***loss***	***storage***	***loss***	***storage***	***loss***
5 Hz	15.1	1.49	4.54	0.73	0.61	0.04
75 Hz	17.4	2.99	6.13	1.4	1.08	0.33
200 Hz	18.3	3.96	6.98	2.03	1.37	0.49

5.5 Conclusions

The dependence of the mechanical properties of PDMS on the crosslinking density and on the curing time was investigated by means of nanoindentation. Tensile testing was performed to compare and also complement the indentation results in order to improve the understanding of the mechanical behavior of PDMS-based materials. The following conclusions can be drawn:

- The indentation technique has proven to be a suitable method for testing very soft and compliant polymeric materials. It was possible to determine storage and loss moduli as well as indentation hardness values reliably; the deviations with respect to tensile testing were only several %. Even subtle changes in mechanical properties that occurred in modulus ranges below 1 MPa were measured reproducibly.

- The results obtained for differently crosslinked samples showed that, through variation of the crosslinking density, the mechanical properties of this PDMS material can be varied from well below 1 MPa up to almost 20 MPa. This offers a useful and simple tool for studying phenomena depending on material stiffness, e.g. [96] as well as the possibility to tailor the properties as desired for specific applications.

- Further, we have indications that PDMS is a viscoelastic rather than a rubbery material, because the loss values and also Poisson's ratios clearly depended on the crosslinking state of the material. Regarding the influence of curing time on the mechanical properties, it has clearly been demonstrated that PDMS properties undergo significant changes as the crosslinking process proceeds during curing, which has never been investigated in a systematic form before.

Chapter 6

In-situ indentation testing of elastomers

Abstract

The development of the contact area is crucial in indentation testing, yet only very limited knowledge exists on the true contact size for soft and compliant materials; the applicability of the Oliver & Pharr procedure in this case is not proven up to now. In this investigation the contact evolution and the deformation behavior of Polydimethylsiloxane (PDMS) was studied during indentation with Berkovich and cube corner tips in-situ inside a SEM and by optical observation. Since detailed information on the true contact area and on the amount of sink-in or piling-up can be acquired from finite element analysis, simulations on the indentation process have been performed in order to verify and complement the in-situ testing. Comparison of results revealed that the simulations provide a good estimate of the true contact size, thus it can be concluded that the average deviations of the contact areas calculated according the standard Oliver & Pharr procedure from the real contact size were found to amount to ~ 10 %.

6.1 Introduction

Mechanical testing by means of nanoindentation is now widely used for many different kinds of materials ranging from metals or ceramics to composite materials and thin films. Also testing of polymeric and biological materials attracts increasing interest. This is due to the fact that this technique allows probing of mechanical properties of small volume samples, which are usually not accessible with other methods. However, nanoindentation is not readily applicable and especially for soft materials like polymers and biological samples some open questions remain.

Indentation theory is based on contact mechanics, where analytical solutions can be derived only for simple geometries, which are often not representative of true experimental conditions. The early work of Hertz [13] and Boussinesq [14] was extended and modified later for different geometric conditions. Sneddon [14] considered a punch of arbitrary profile in contact with an elastic half space and derived a relation between load and penetration, as well as for the pressure distribution beneath the indenter and the shape of the deformed surface. These equations of Sneddon now form the basis of the well known Oliver and Pharr method [12, 31], which is commonly used for evaluating instrumented indentation data. Although this method is generally accepted to provide accurate and reliable values of mechanical properties, it has to be kept in mind that it is derived for purely elastic material. But for materials with a more complex behavior like strain-hardening or viscoelasticity, additional information is necessary to fully understand the indentation process.

Two approaches are possible to achieve a more comprehensive understanding of the indentation process: numerical simulations [39, 43, 45-48, 51, 52] and in-situ techniques [110-120]. The aim of simulations is to access quantities which are not measurable by experimental techniques, such as deformations under the indenter. For instance, Larsson et al. [46] presented a detailed finite element (FE) analysis of Berkovich indentation for elastic and elastic-plastic materials. Bucaille and coworkers [47, 48] used a broader spectrum of material behavior for FE-simulations of indentation and scratch testing. Through a variation of the rheological factor, i.e. the ratio of elastic and plastic contributions in the overall deformation, the transition from elastically to plastically dominated deformation is covered in their work. These studies addressed the determination of stress/strain fields under the indenter and the contact evolution (inside the contact area as well as along the contact periphery) and how these are influenced by the material behavior. Determination of the contact area from simulations [45, 51, 52] is important, since the contact area is crucial for the calculation of mechanical properties from indentation data. Simulation offers the possibility to vary the indentation conditions in a systematic and controlled way, such that the influences e.g. of surface roughness [39], indenter geometry [43], or sink-in and pile-up effects [45] on the contact area and hence the results can be studied.

Experimentally, the contact area in the presence of sink-in or pile-up effects can be determined by optical observation of the contact, which is only possible for transparent samples. This technique is widely used in tribological studies [110, 111], but also finds application in indentation testing. In most cases a transparent sample or substrate is used [111, 112]. In contrast, Miyajima presented some work that used a transparent indenter [113]. This allows testing of non-transparent media as well, which makes it a useful tool for investigating indentation contact formation and retraction.

Another technique is in-situ testing in a SEM [115-117]. This technique provides in the first place qualitative information on the contact area, but enables mechanistic insight. Moser et al. demonstrated that displacement pop-ins in the load-displacement data are associated with the activation of shear bands in metallic glasses [115, 116]. Further interesting results on the deformation behavior and cracking modes during scratching were obtained through in-situ SEM scratch testing [117]. Also, several in-situ TEM studies have been performed in order to get a deeper insight in the deformation mechanisms at smaller scales, e.g. dislocation behavior in martensitic steels [118], in silicon [119], and cracking in polyethylene [120].

A drawback of electron-optical methods is the sensitivity of polymeric materials to influences of the electron beam [121-132]. In polymeric materials irradiation changes their chemical structure. Chain scission occurs and free radicals form. This can lead to polymer decomposition or additional crosslinking, depending on the intensity of the beam [123, 127]. Several studies investigated the influences of radiation on PDMS [127-131], which is of particular interest for the present paper. In the work of Russell and co-workers [127] indications for chain scission and even fragment removal during irradiation with electron beams (15- 30 kV acceleration voltage) have been found. Under the influence of higher energy electron (~ MeV) or γ-radiation, PDMS tends to be further crosslinked [128-131].

In the present paper, the indentation process of very soft elastomeric materials is investigated with the help of in-situ indentation testing (SEM and optical) and finite element simulations. The aim was to provide insight in contact formation and deformation behavior during indentation of soft elastomeric materials. The results will be discussed with respect to the applicability of common contact descriptions to polymers.

6.2 Experimental methods

6.2.1 Sample material

PDMS of the Sylgard 184 type (Dow Corning Corp.) was used for this study. For specimen preparation the liquid mixtures of 1:10 and 1:30 weight ratios of crosslinking agent to pre-polymer were poured onto a silicon wafer and cured in a vacuum furnace at 150°C. The curing temperature was maintained until the crosslinking reaction was completed [133]. The fully cured state was intended to ensure constant mechanical properties, at least within the time period of testing.

The specimens were sputter-coated with a thin (approximately 10 nm thick) Au-Pd layer in order to avoid charging effects during investigation in the SEM. For the observation of the true polymer surface small areas were shielded during sputter-coating. Subsequent indentations were performed on these uncoated areas. The charging of the sample could be reduced to a reasonable amount by the surrounding Au-Pd layer.

6.2.2 Instrumentation

For the indentation tests a Nano Indenter DCM from MTS Nano Instruments (Oak Ridge, TN, USA) was used. Testing was carried out in the continuous stiffness measurement (CSM) mode with a frequency of 75 Hz using diamond Berkovich and cube corner tips. Contact area and contact depth were determined according to the Oliver & Pharr procedure [12, 31]. For a more detailed investigation of the sample surfaces at the indent locations, AFM imaging was conducted on a DME Dual Scope system.

In-situ indentation tests were performed inside a Zeiss DSM 962 SEM operated at acceleration voltages between 5 and 15 kV and a working distance of ~12 mm. The chamber was equipped with a home-built indenter which allows observation of the indentation process at various angles, depending on the indenter tip in use [117]. Also for this study, diamond cube corner and Berkovich tips were chosen. Unfortunately, the load resolution of the system was not sufficient for these soft materials, therefore no quantitative load-displacement curves could be recorded during indentation.

A custom-built adapter in combination with a Nano Bionix system (MTS Nano Instruments, Oak Ridge, TN, USA) was used for the optical in-situ observations. The projected contact area during Berkovich indentation was imaged directly through the transparent specimen perpendicular to the test surface. The maximum possible magnification of the CCD/video-system was 420 x. The images were analyzed with the software Sigma Scan Pro 5.5.

6.2.3 Simulations

Comparative 3D finite element analysis (FEA) was performed with the commercial code ABAQUS Version 6.61 [69]. Making use of the three-fold symmetry of the pyramidal indenter tips (cube corner and Berkovich), the FE model was reduced to one third of the actual problem for convenience. Thus the modeled geometry incorporates the contact between one face of the tip and the specimen. Expecting more than 5% strain, a hyperelastic constitutive model was chosen to represent the mechanical behavior of PDMS. ABAQUS provides a tool to select the material model which best fits the experimental test data [134]. Uniaxial tensile and compression tests were conducted on the same PDMS specimens that have also been used for the indentation experiments. Based on the obtained stress-strain relations, the material evaluation process determined the parameters of numerous hyperelastic material models. The Neo-Hooke strain energy potential [135] was identified as the most adequate description. It is defined by two coefficients, C_{10} and D_1 which are defined as:

$$C_{10} = \mu_0 / 2 \tag{21}$$

$$D_1 = 2 / K_0 \tag{22}$$

Here, μ_0 is the initial shear modulus and K_0 is the initial compression modulus. For the two differently crosslinked PDMS 1:10 and 1:30 the coefficients were determined to $D_1 = 0.662$ and 0.0922 and $C_{10} = 0.255$ and 1.123, respectively. Assuming isotropy for the 3D randomly crosslinked PDMS network, these values correspond to Young's moduli of approximately

4 MPa for PDMS 1:10 and 0.6 MPa for PDMS 1:30, if Poisson's ratios are taken to be 0.42 and 0.45 according to [133].

To optimize discretisation, extensive studies concerning the mesh density, the element type and contact formulation were carried out. While the geometric order of the elements showed no significant influence on the results (thus 8-node linear elements were chosen for efficiency), mesh density did matter. The result of the mesh convergence study is a strongly biased mesh (denser at the indenter tip) with an overall of 23275 elements, while the indenter face is represented by an analytically rigid plane. Tangential frictionless contact behavior was assumed and finite sliding was enabled to allow any possible relative movement of the surfaces. Having the same results when calculating contact with a rigid body, the computationally less expensive node-to-surface contact formulation was preferred to the surface-to-surface alternative and the Lagrange method was chosen to avoid penetration.

6.3 Results

6.3.1 In-situ SEM indentation

During the in-situ indentation experiments inside the SEM the deformation behavior was monitored by the recording of movies. In the following section the results will be presented by showing individual frames from these movies. In figure 39(a) to (c) a typical loading and unloading (d to f) cycle on a fully coated PDMS 1:10 specimen using a cube corner tip is shown. The square cracks occurred during sample mounting and preexisted before the test. During loading to a depth of 15 µm, the tip penetrated into the material with hardly any deformation visible in the vicinity. Therefore the contact contour is close to a straight line. On unloading two different types of cracks became visible in the metal layer. The first type of cracks formed along the edges of the tip, where a stress concentration occurred. The others were concentric circular cracks that formed along the faces of the tip. Further, it is interesting to see that the metal layer delaminated in the area around the cracks. This can be seen from figure 39(e) where the PDMS adhered to one edge of the tip and was pulled out of the surface above the Au-Pd layer. No residual impression was formed during the test.

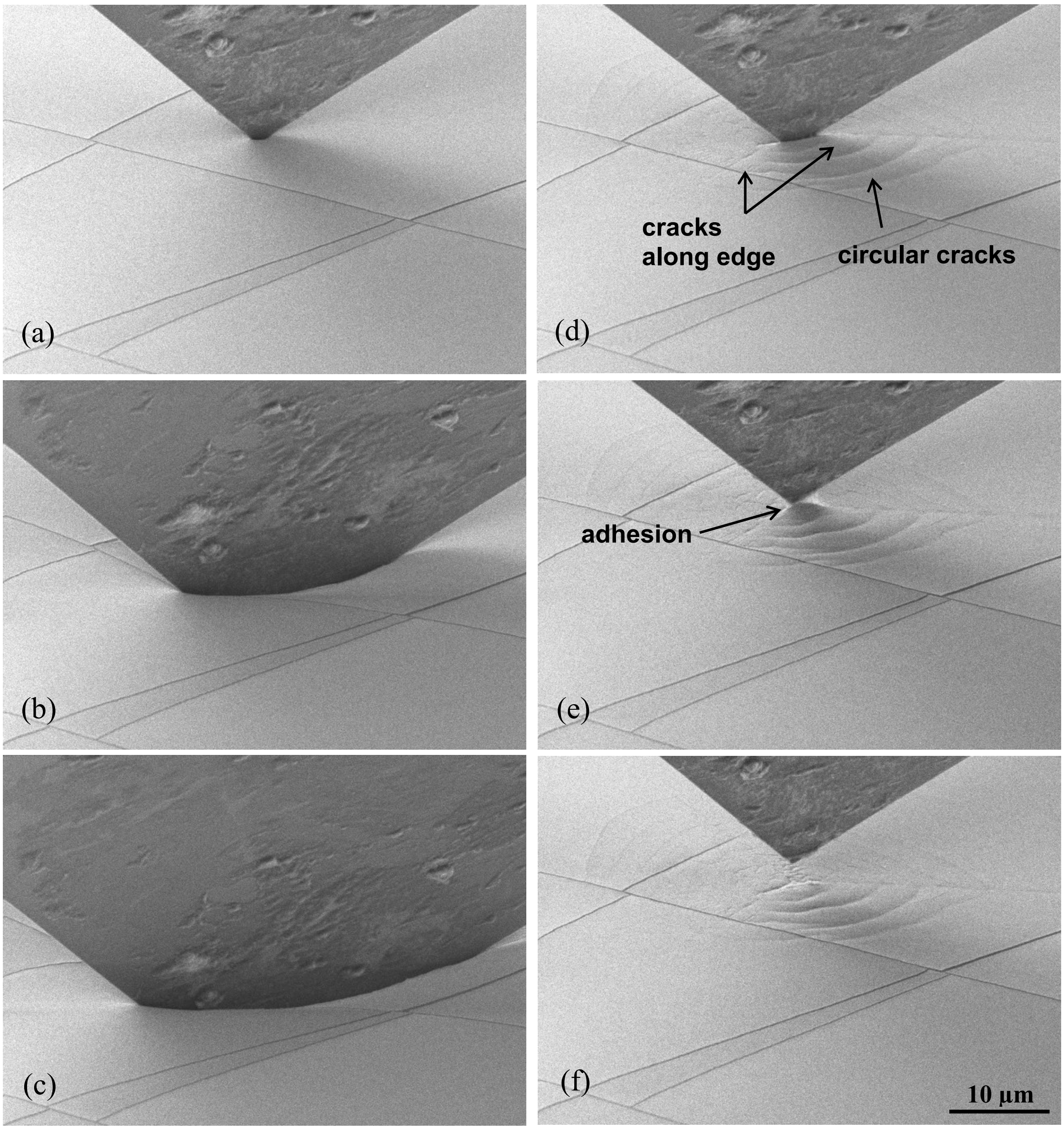

Figure 39: 15 µm indentation of a coated PDMS specimen with a cube corner tip. (a) and (b) loading; (c) fully loaded; (d) unloading; (e) detachment with contact along one edge of the tip; (f) fully unloaded with cracks in the coating.

Figure 40 shows a similar experiment for an uncoated surface of PDMS 1:10. Again, a cube corner tip was used and the maximum penetration was 15 µm. During loading a clear sink-in effect was visible indicated by the bowed contact contour. The shape of the impression was more conical; seeming like the center of the faces did not come into contact. This is proven by the dirt particle on the left side of the tip, which remained visible even though it came below the original surface position (circle in figures 40a and c). During unloading (figure 40d to f) adhesion between the tip and the PDMS occurred at the rear face and caused the steep groove-like impression with hillocks one each side.

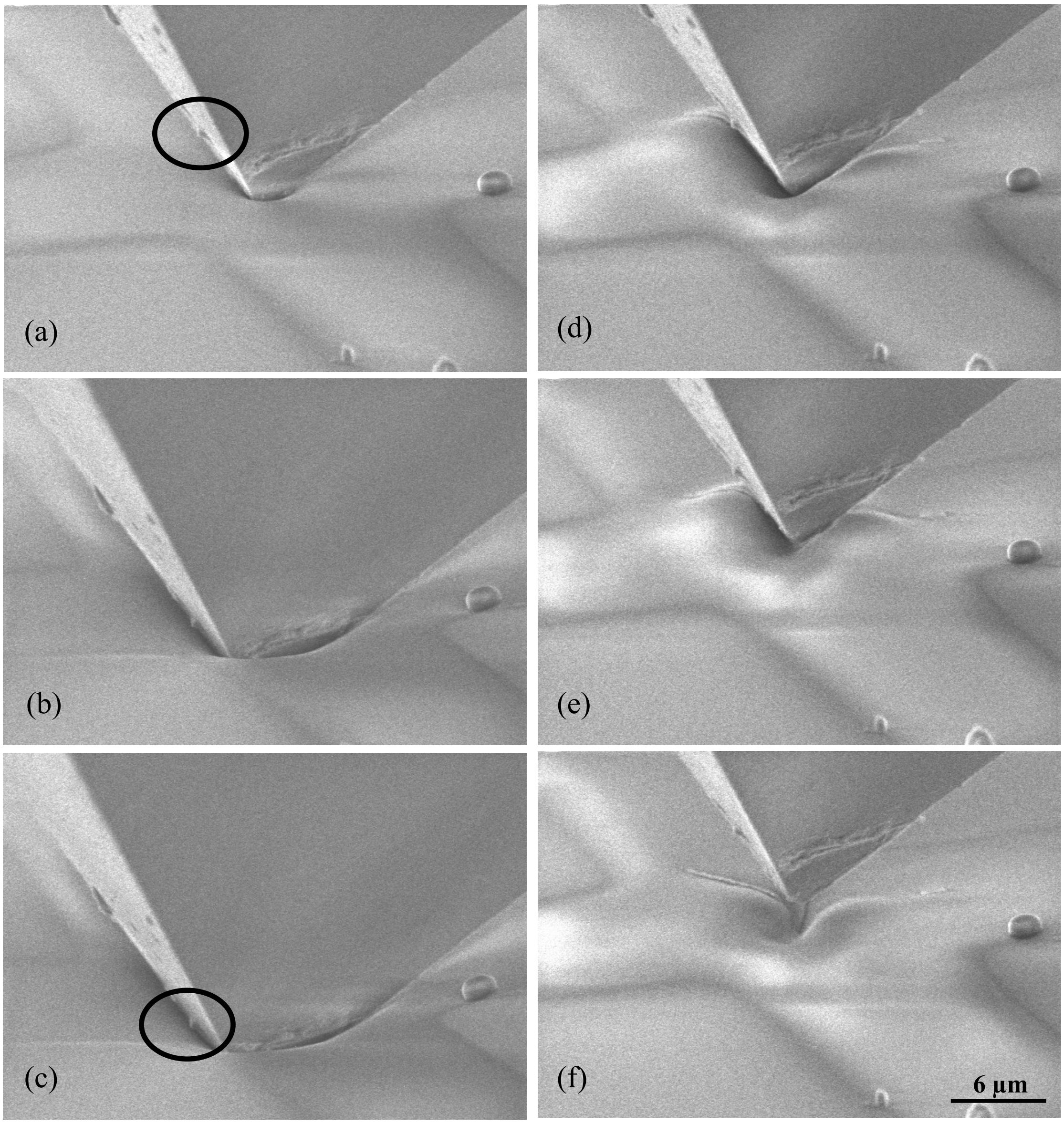

Figure 40: 15 µm indentation on an uncoated PDMS specimen with a cube corner tip. (a) – (c) loading; (d) unloading with the tip apex still in contact; (e) detachment with tip-sample contact only at the indenter faces; (f) fully unloaded with a permanent impression.

A Berkovich tip was used for the 5 µm deep indentations on PDMS 1:10 in figure 41. The micrographs in (a) to (c) show the test on the uncoated and (d) to (f) on the coated specimen. Due to the large faces of the non-conductive Berkovich tip, the charging was more pronounced than for the cube corner tip. Direct comparison of (a) and (d) suggests that no sink-in effect occurred in the coated sample, whereas the dark area along the contact edge (a) denotes a gap between tip and surface. No significant residual impressions were created.

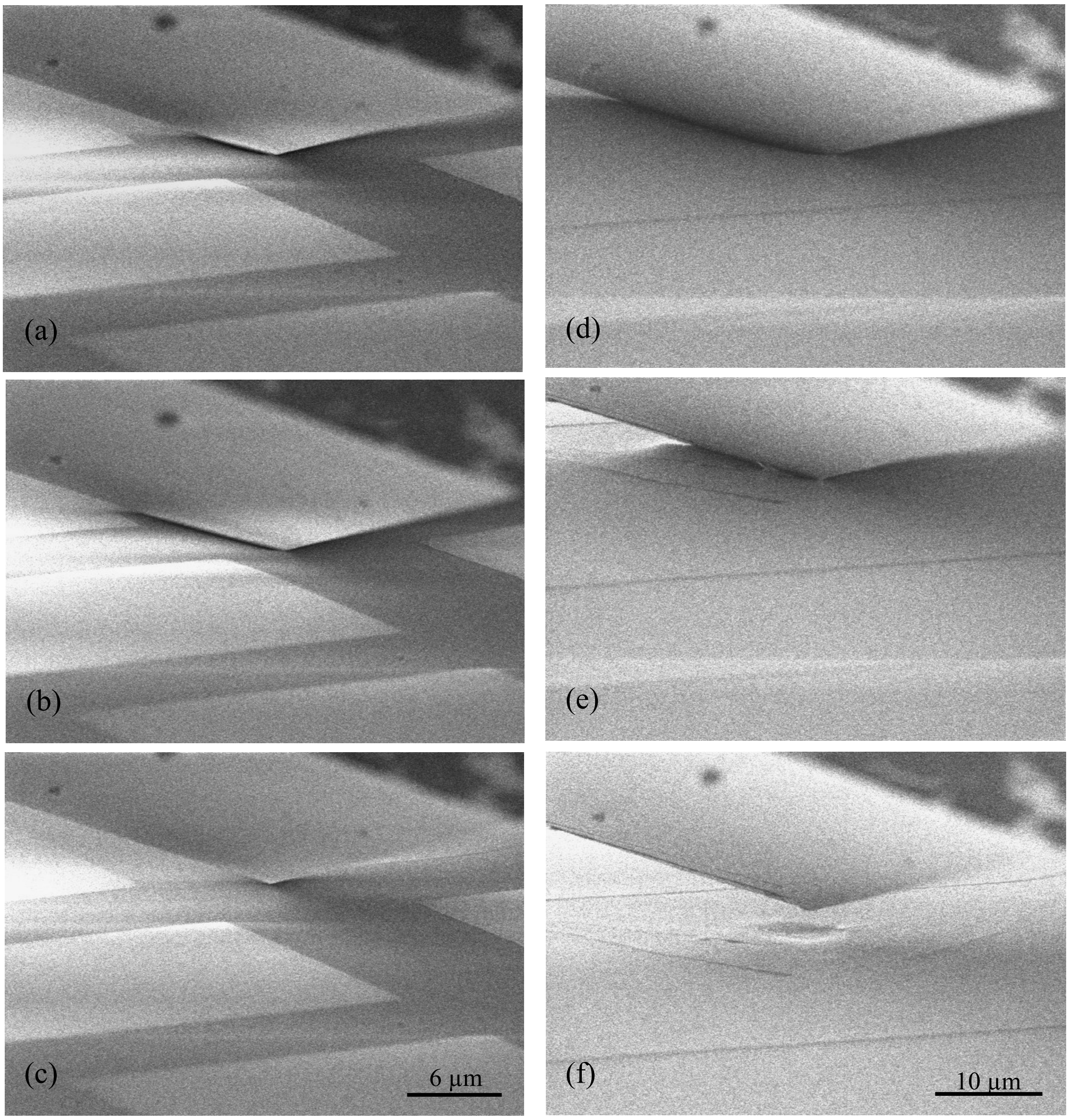

Figure 41: Testing with a Berkovich tip on an uncoated (left, a – c) and a coated specimen (right, d – f). Direct comparison reveals that the uncoated sample shows a stronger sink-in effect than the coated one.

Figure 42 summarizes the observations of a series of tests on uncoated PDMS 1:10 with the cube corner tip, where two parameters were varied: the indentation depth, ranging from 5 up to 20 µm and the loading rate, between 9 and 200 nm/s. In all tests permanent deformation took place. The size of the residual impressions increased slightly with indentation depth and decreased with loading rate. For higher penetrations and lower loading rates the shape of the impressions approached the pyramidal tip shape, in extreme cases cracks formed in PDMS.

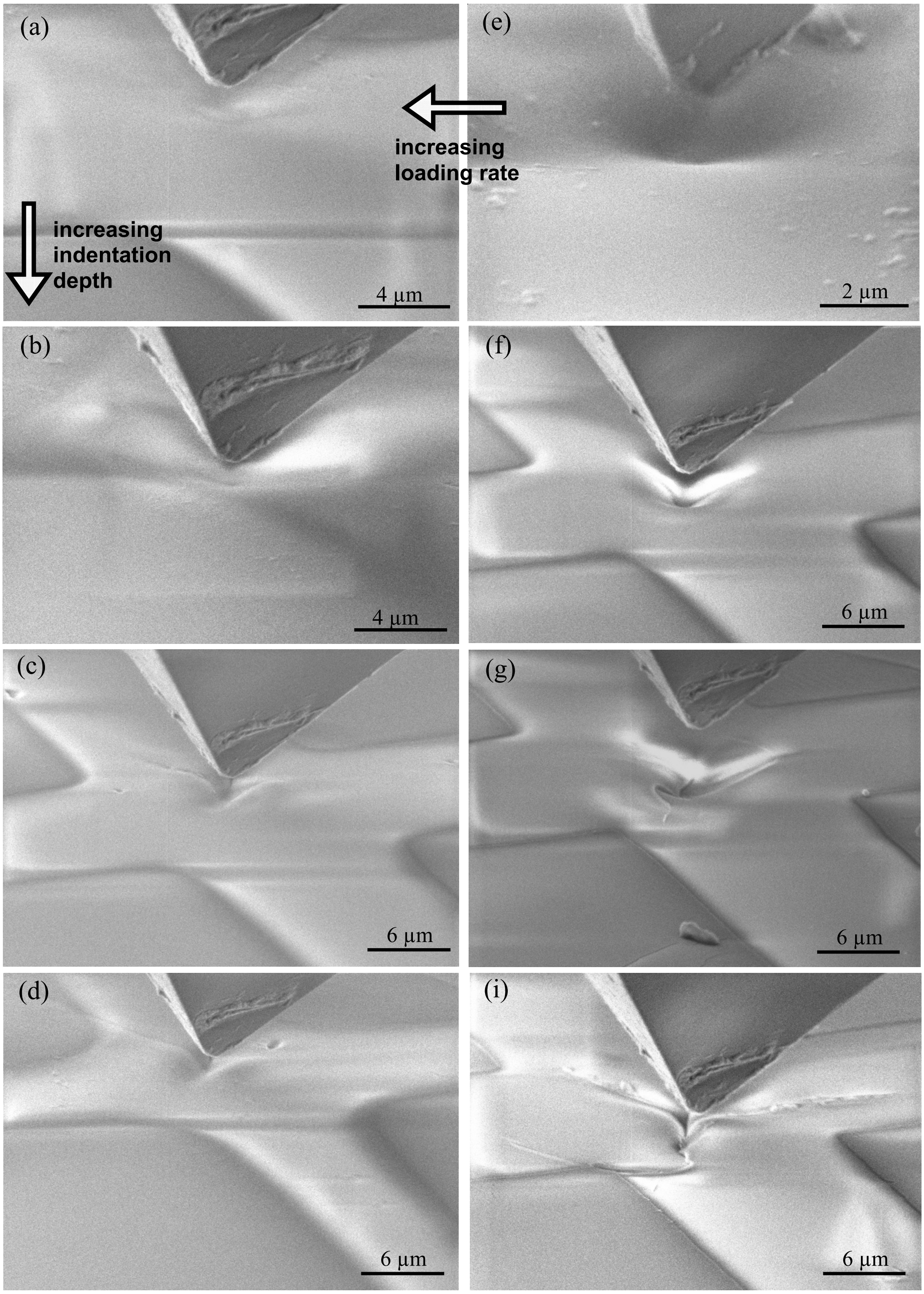

Figure 42: Residual impressions on PDMS after testing with different loading rates and to various depths. The left column (a – d) was performed at 200 nm/s, the right column (e – i) at 9 nm/s. The rows correspond to indentation depths of 5 µm (a and e); 10 µm (b and f); 15 µm (c and g); 20 µm (d and i).

For a more detailed characterization AFM imaging was performed. The images in figure 43 represent tests to 5 and 10 µm at loading times of 100 and 600 s. The increase in size with lower rates and higher penetrations is again confirmed by the profiles. All profiles correspond roughly to the position given in figure 43(a).

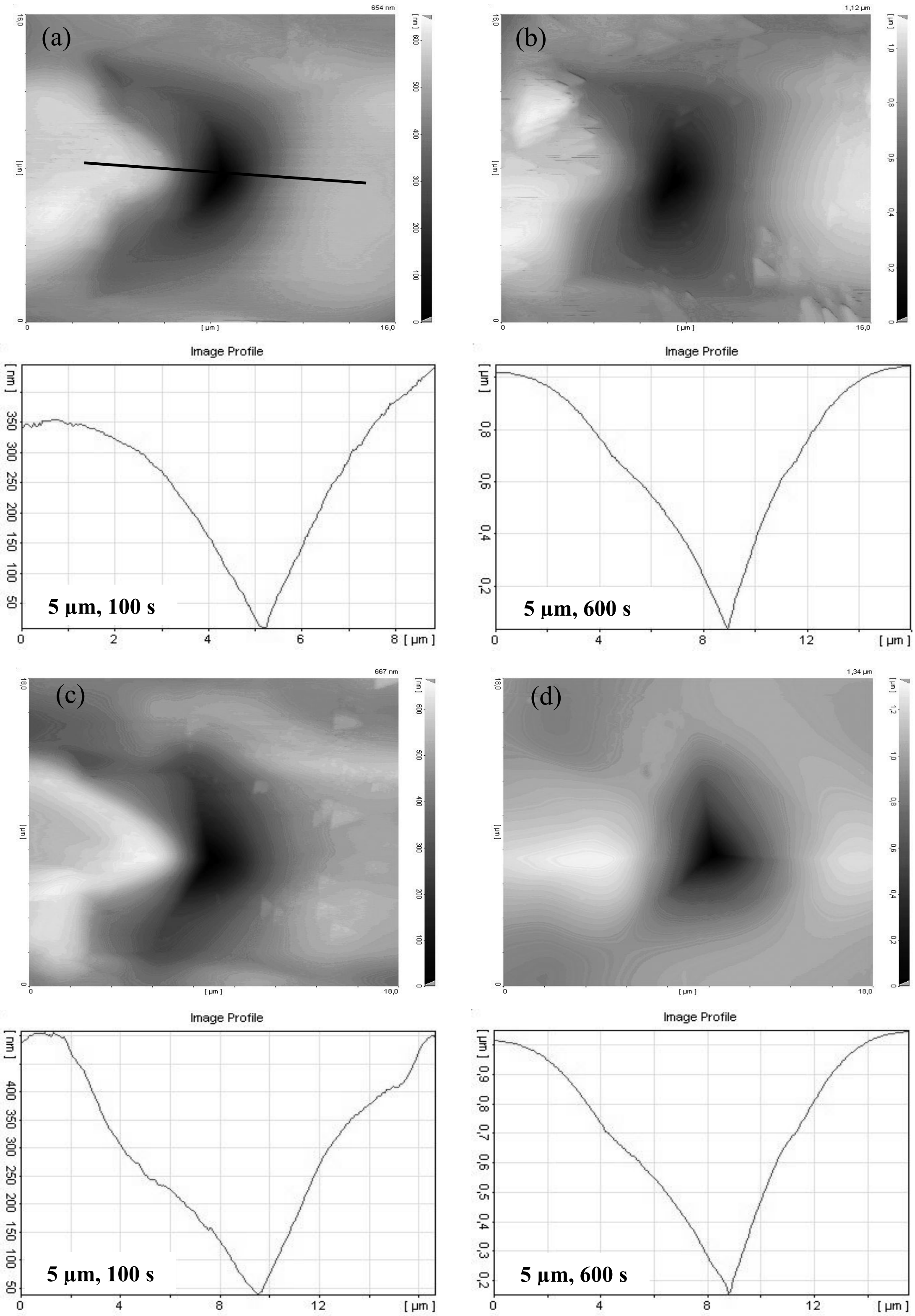

Figure 43: AFM images and surface profiles of permanent impressions after in-situ testing. As can be seen, the residual indent size is more dependent on the loading time than on the penetration depth.

6.3.2 Simulation

The load-displacement data is used to check the quality of the material model in order to describe the behavior of PDMS accurately. In figure 44 the experimentally determined load-displacement curves are plotted together with the data obtained from the simulations. The data sets show good agreement. The experimental curves are the average of 10 individual indentations; the standard deviations are denoted by error bars. Note that in most cases, the error bars for the standard indentation tests were smaller than the symbol sizes.

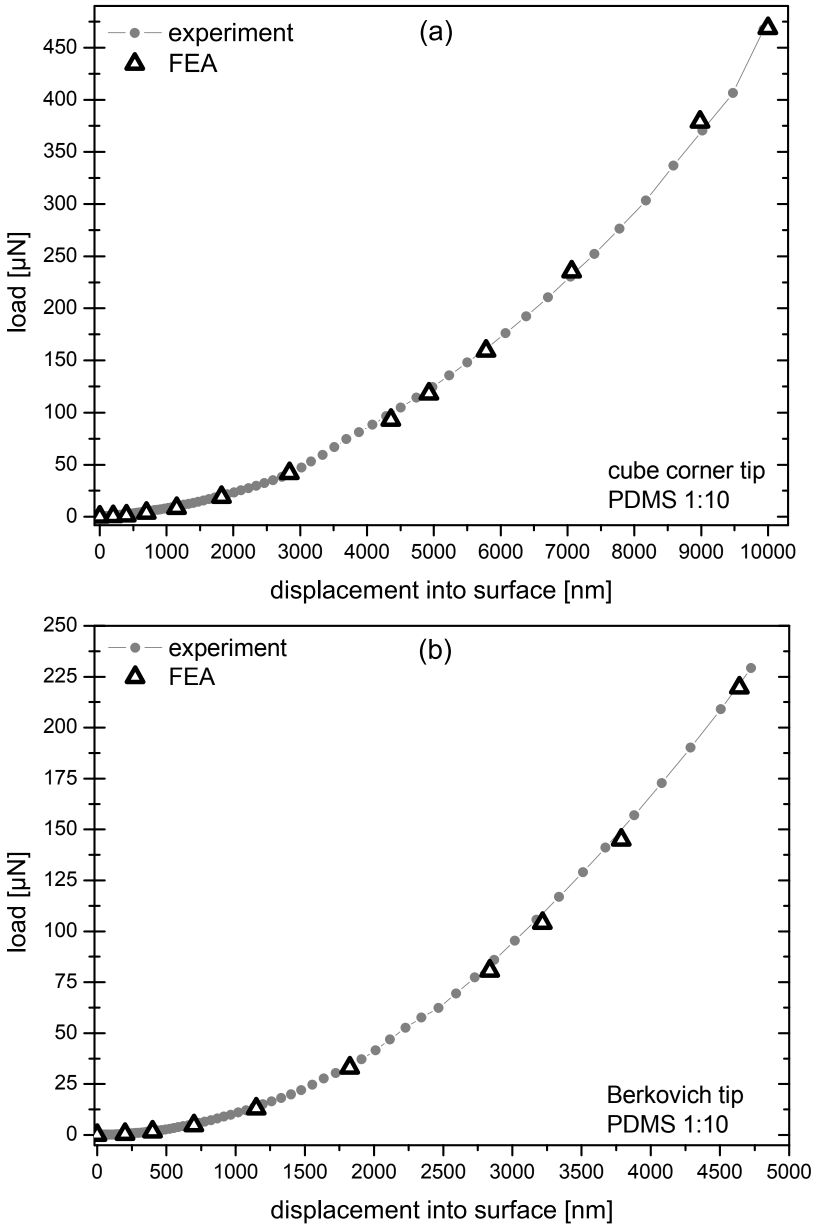

Figure 44: Experimental load-displacement curves for PDMS 1:10 in comparison with simulated curves (a) for the cube corner tip; (b) for the Berkovich tip.

The experimental values of the contact area result from the Oliver & Pharr calibration and analysis procedure according to [12, 31]. To illustrate the results, figure 45(a) shows an optical micrograph of the projection of a contact between PDMS and a cube corner tip. The white lines correspond to the connection between the contact boundaries along two tip edges, also shown as white lines in figure 45(b) and (c). These lines can be associated with the upper limit of the contact area in the absence of sink-in. In figure 45(b) the simulation results for the contact between one side of the pyramidal tip and the surface (corresponding to 1/3 of the problem) is given. The curved contact contour in this picture illustrates the difference between the contact depth along the tip edges (white line) and the face centers (black line). A white line denoting the upper limit of the contact area is also drawn in figure 45(c), where a frame of an in-situ test with a cube corner is shown. Thus, the FEA results and the in-situ testing results can be compared through this upper area limit, although the true area of contact cannot be determined from the in-situ tests, since the contact shape along the face of the tip is not visible.

This comparison is seen in figures 46 to 48 for different tip geometries and materials. The projected contact areas and the corresponding contact depth values are plotted as a function of penetration depth. The solid grey lines indicate the limits of the contact as shown by the black and white lines in figure 45(a). The star symbols represent the area determined from the in-situ testing (white line in figure 45b). Thus, the upper grey lines and the star symbols are to be compared and give reasonable agreement between in-situ tests and FEA. Further, the experimental results according to Oliver & Pharr [12, 31] are marked by grey dots and the true contact areas obtained from the simulations by black triangles. The error bars denote one standard deviation of 10 tests. Yet, for the experimental results the error bars were approximately the symbol size in figures 46 to 48, thus they are not visible.

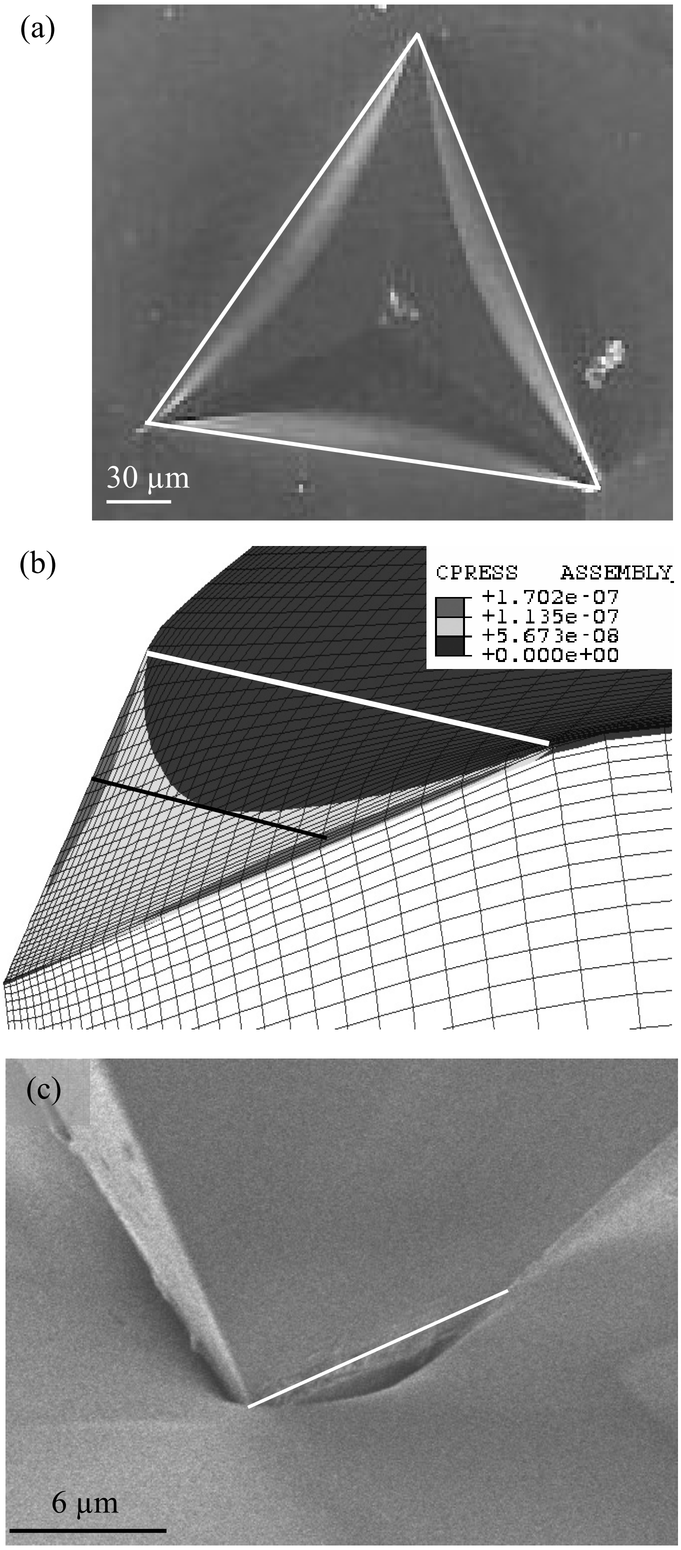

Figure 45: (a) Optical micrograph of the contact perpendicular to the surface. The contour is bowed due to sink-in effects. The white triangle indicates the connection between the contact edges at the tip edges and can be seen as the upper limit of the contact area. (b) The contact of one side of the indenter tip as obtained from FEA. The white line represents the upper, the black line the lower limit of the contact area. (c) The upper limit of the contact area for in-situ testing with a Cube corner tip is again indicated by the white line. All areas denoted by white lines should theoretically be the same.

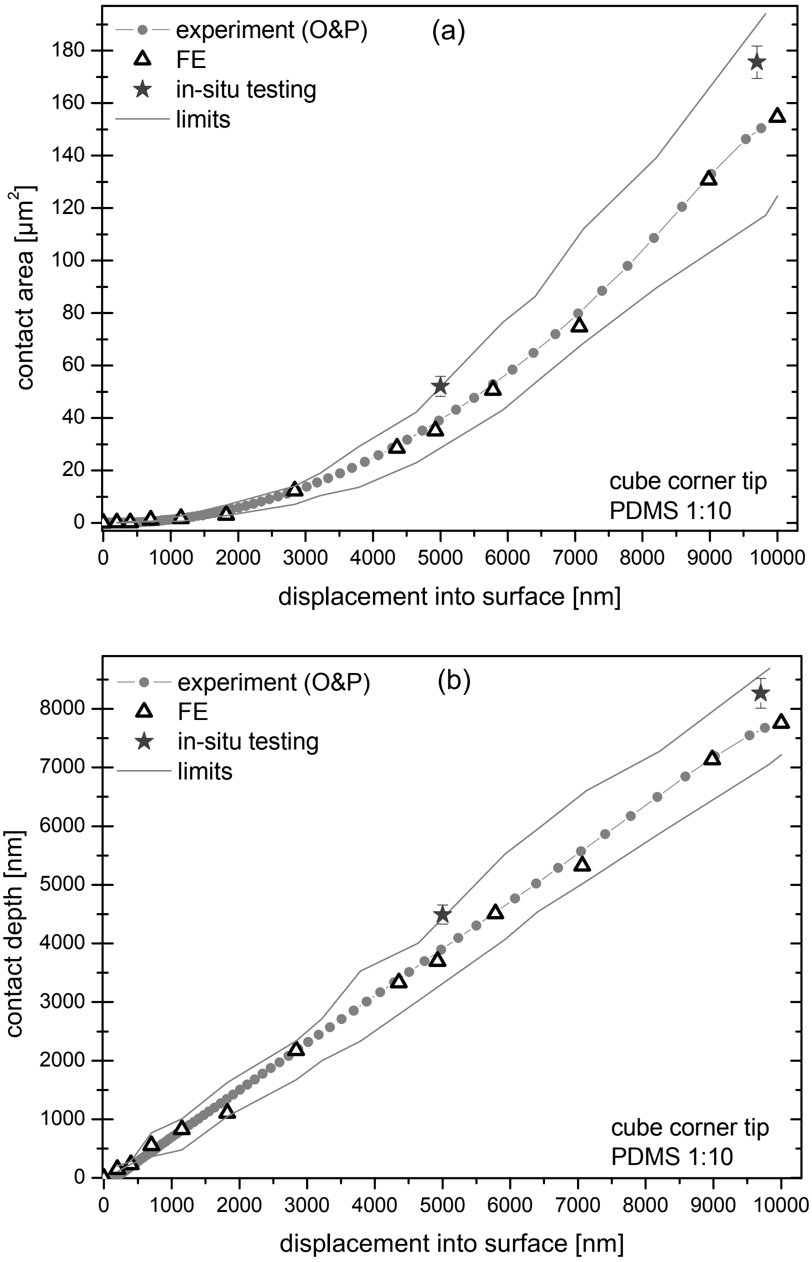

Figure 46: Comparison of results from standard ex-situ and in-situ testing with simulation results for PDMS 1:10. The tip was a cube corner. (a) Contact area; (b) Contact depth.

Figure 46 shows the results for uncoated PDMS 1:10 indented with a cube corner tip. PDMS 1:10 tested with a Berkovich tip is seen in figure 47 and the softer PDMS 1:30 tested with a cube corner tip in figure 48. For the Berkovich tip (figure 47) the maximum penetration was 5 µm with the contact area being 308±2 μm^2 and the contact depth being 3.52±0.08 µm. In this case the results from in-situ testing and FEM are again in reasonable agreement, but the true FEA derived contact area was slightly smaller than calculated from the Oliver & Pharr method. For the cube corner the contact area at the maximum penetration of 10 µm was 150±1 µm^2, the contact depth 7.67±0.18 µm. The match of results for the softer PDMS 1:30 was also quite good. The contact area and depth at 10 µm penetration were 159±2 µm^2 and 7.82±0.11 µm, respectively.

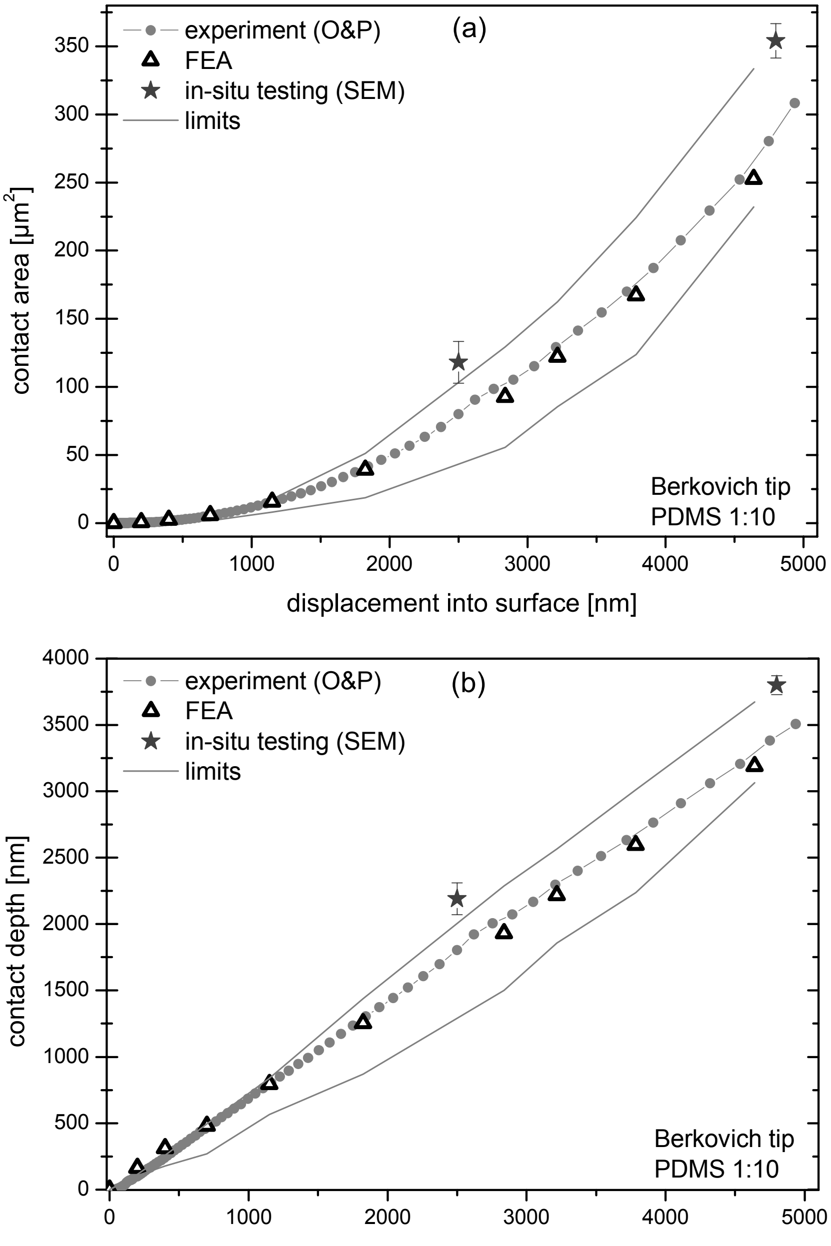

Figure 47: Results from ex-situ and in-situ testing in comparison with simulation. The tests were performed on PDMS 1:10 using a Berkovich tip. (a) Contact area; (b) Contact depth.

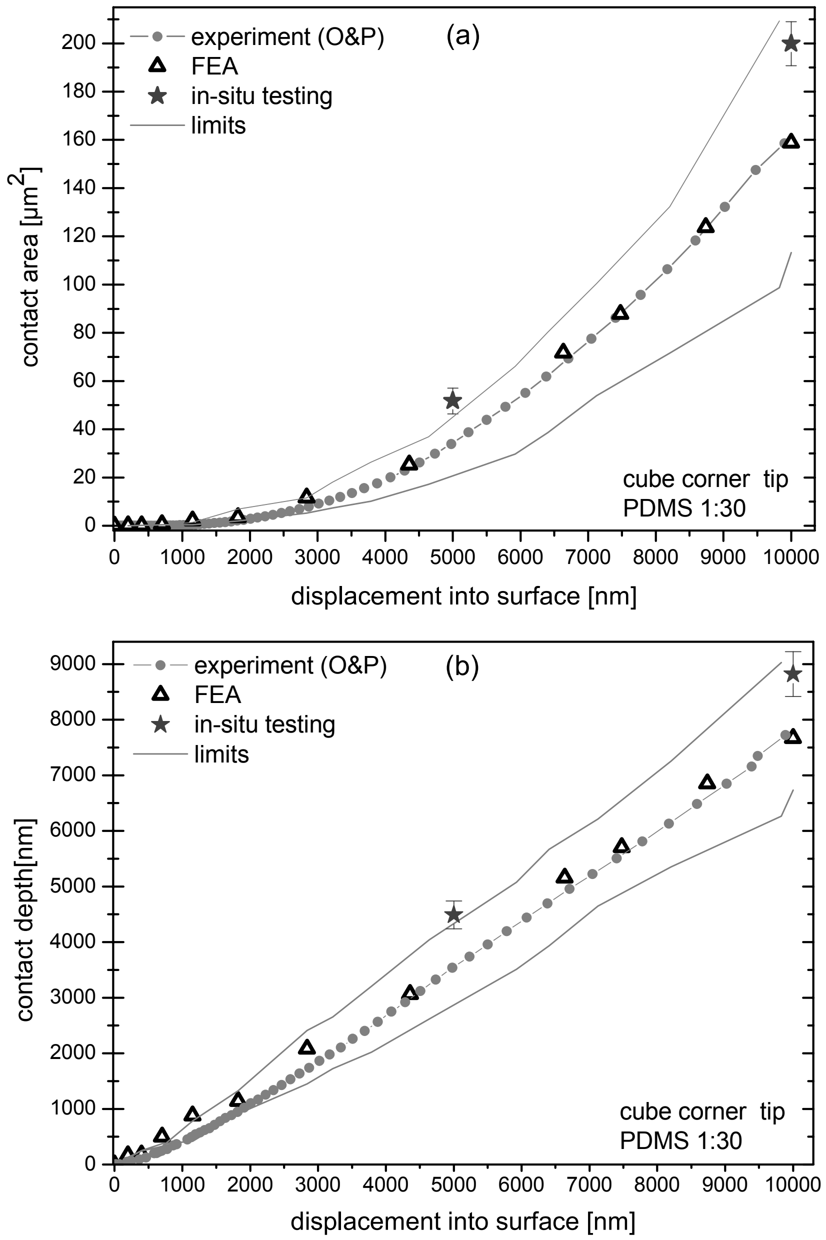

Figure 48: Comparison results from different techniques for the more compliant PDMS 1:30 tested with a cube corner tip. (a) Contact area; (b) Contact depth.

6.3.3 Optical in-situ indentation

The results of the optical observation of the indentation tests with a Berkovich tip are given in figures 49 and 50. The micrographs were taken at penetration depths of 2, 2.5, 4, and 5 µm. In order to compare them to the results from in-situ SEM testing, the area determined was again the upper limit (see white triangle in figure 45a). For comparison, the values obtained from in-situ testing (optical and SEM) are plotted together with the FEA results in figure 50. As the graph shows, all three methods gave approximately the same values.

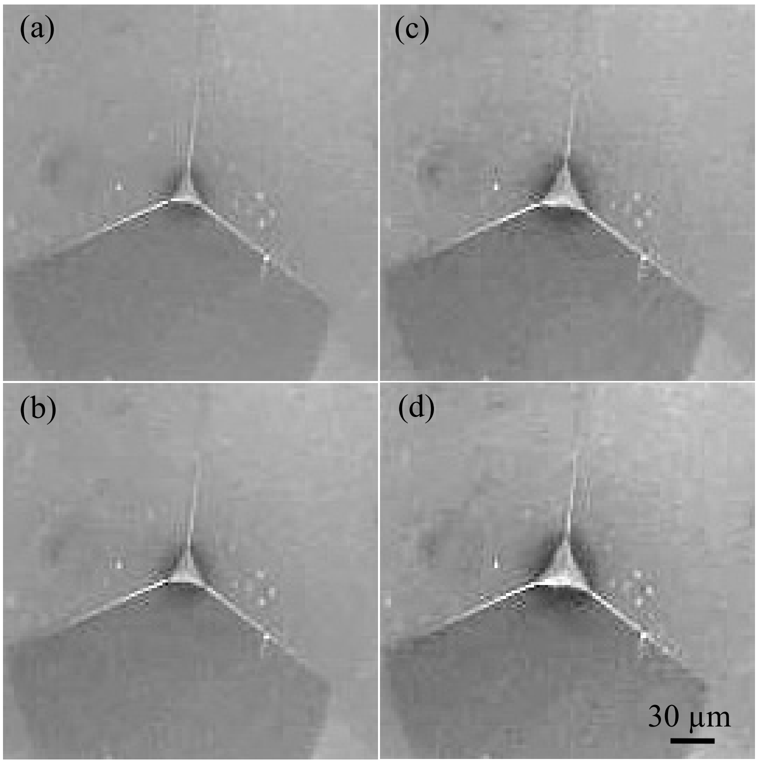

Figure 49: In-situ micrographs taken during indentation of PDMS with a Berkovich tip. (a) 2000nm penetration (b) 2500nm (c) 4000nm (d) 5000nm. These micrographs are used to determine the projected area of contact in order to be able to compare the results to those from testing inside the SEM. From this a possible influence of the electron beam on the deformation behavior can be estimated.

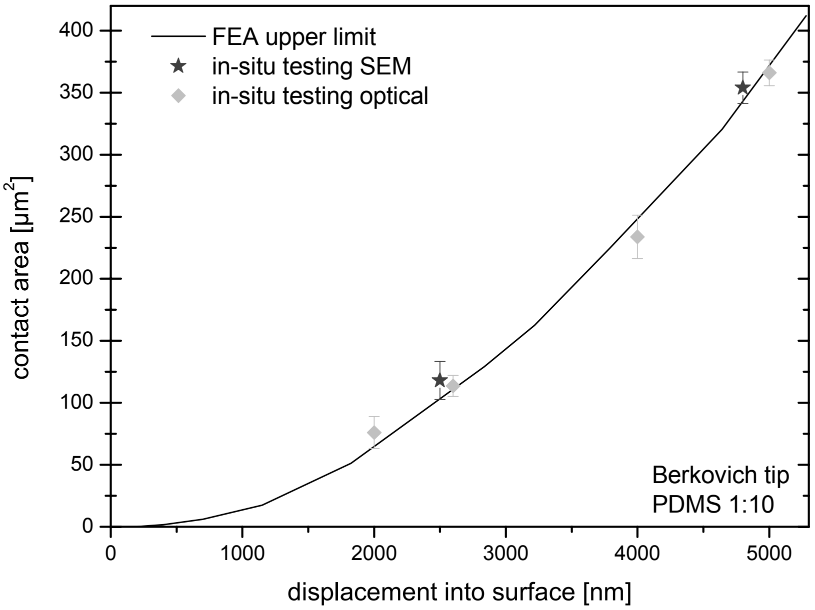

Figure 50: Comparison of results from FEA (grey line as in figure 9a), in-situ testing in the SEM (dark grey) and optical in-situ tests (light grey as obtained from the micrographs in figure 47). The error bars denote one standard deviation.

6.4 Discussion

In the first paragraph some issues regarding the observation of PDMS inside a SEM will be addressed. In the subsequent section the results from different methods of contact area determination will be compared and discussed.

6.4.1 In-situ indentation in the SEM

When investigating PDMS inside a SEM, it has to be taken into account that PDMS is a non-conductive polymeric material. The imaging of polymeric materials is difficult due to several reasons. Charging effects can occur; they exhibit a low contrast and are prone to interactions with the electron-beam or are even damaged through the irradiation at higher acceleration voltages [127-131]. In the course of our investigations two major factors turned out to determine the deformation behavior of the specimens, either the coating of the specimen or the interactions with the electron beam, if the samples were uncoated.

6.4.1.1 Influence of the Au-Pd coating

How the indentation testing was affected by the thickness of the conductive Au-Pd layer can be seen in figure 51. The three micrographs show significant differences for samples with a 10 nm thick coating, a 1 nm thick coating, and an uncoated sample. In the case of the thicker metal layer cracking and delaminating of the layer occurred because of the comparatively high stiffness and therefore a small deformability of the Au-Pd layer. In contrast, the thin 1 nm layer seemed to adhere and deform well. Here an extreme sink-in happened with a presumably very small contact between the sample and the tip.

The deformation behavior of hard films on soft substrates was investigated with finite element simulations by Laursen and Simo [45]. They found that hard film-soft substrate systems generally tend to show a sink-in behavior and that the deformation occurred predominantly in the substrate. Assuming that the amount of sink-in is determined by the ratio of film stiffness to substrate stiffness [45] and that the stiffness of the gold film increased with increasing thickness, our observations can be understood. Further, they showed that for a constant film thickness increasing the penetration depth led to reduced sink-in, which explains the very close contact between tip and surface in the case of the 10 nm thick coated sample.

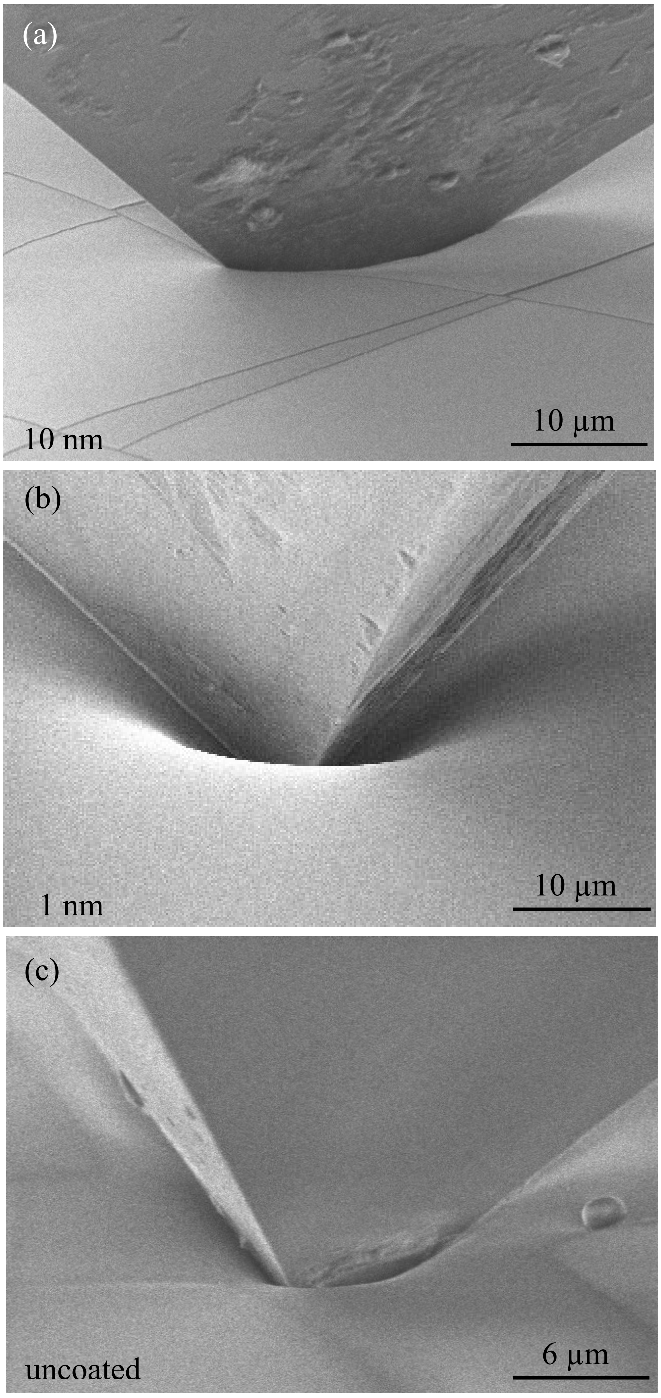

Figure 51: Deformation state at a penetration of ~ 8 µm for differently coated specimens. (a) Coating thickness 10 nm Au-Pd; (b) coating thickness 1 nm; (c) uncoated.

For the uncoated PDMS in figure 51(c) the situation was quite different again, because here the very high flexibility or rubber-like deformation of PDMS alone led to a steep, yet conically shaped indentation. Thus, it can be argued that due to the high stiffness differences of PDMS and Au-Pd the deformation of the coated specimens did not display the true PDMS behavior. Therefore, the specimens were coated partially so that the indentations could be performed on uncoated spots. This ensured the observation the real PDMS deformation behavior and the determination of the contact size between PDMS and the tip.

6.4.1.2 Electron-beam irradiation effects

From a mechanical point of view the free PDMS surface was necessary for the indentation testing. Yet, the effects of subjecting PDMS directly to the electron beam have to be considered. The consequences of the electron irradiation during imaging were obvious immediately after the indentations. The scanned area was clearly distinguishable from the non-irradiated area. It could be identified through its considerably lower position compared to the original, i.e. non irradiated surface. This is proven by the AFM image and the corresponding surface profile in figure 52. In the AFM image in figure 52(a) the irradiated area was darker, thus deeper than the surrounding. The direction of the electron beam was from the upper right corner towards the lower left corner. Therefore the V-shape in the lower left part of the image is due to the electron shade of the tip. The position of the profile in figure 52(b) is marked by the black line on the right. The step height at this location was approximately 140 nm. The fact that the irradiated area was below the original surface, leads to the conclusion that the radiation has caused a volume reduction of the PDMS, which was permanent. This can be associated either with the evaporation of volatile low molecular PDMS fragments [127] or with a density increase due to crosslinking [130]. For both phenomena, evidence has been found in different studies [127-131]. In our case, it can not be finally decided, which of the processes took place. The voltages between 5 and 15 kV used for the tests are relatively low compared to the voltage values reported in [128-131], which caused PDMS to further crosslink. In contrast, they matched quite well the voltages at which the evaporation of PDMS fragments occurred [127]. Therefore, fragment removal seems to be more likely. During the tests, however, the chamber vacuum was stable, thus contradicting a significant degradation and degassing of the sample. This is further supported by the fact that fully cured PDMS samples were used for the study, which should contain only a limited amount of volatile fragments. The fraction of unreacted, potentially volatile particles in the PDMS was determined by the specimen weight loss after swelling/extraction experiments and was around 7 wt%. Considering these arguments, further crosslinking appears more reasonable. Thus, it is hard to decide what happened during the irradiation of PDMS. Most probable seems that both, fragment removal and crosslinking occurred in parallel.

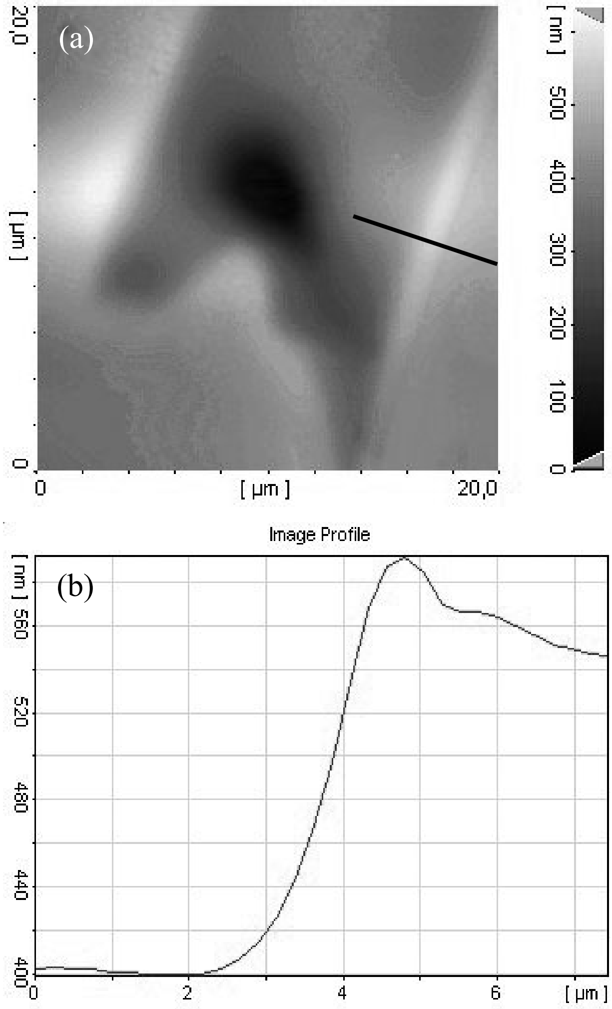

Figure 52: (a) AFM image of residual impression after testing in the SEM. The indent location is visible in the middle. The darker area was the scanning area of the electron beam. In the lower part the electron shade of the tip can be seen. (b) Profile across the step at the boundary between irradiated and non irradiated PDMS surface. The difference is approximately 140nm.

Another interesting finding concerning the beam-specimen interaction is that permanent deformation in the PDMS could only be achieved where PDMS was exposed to the electron beam. This finding is related to the AFM images in figure 53. In figures 53(a) to (d) the permanent impression which formed after the in-situ indentation test with the cube corner and the Berkovich tip are shown. Even a crack emerged during the Berkovich indentation. This is surprising when considering figures 53(e) and (f), where no sign of plasticity or permanent deformation could be found after a 20 µm deep indentation with a cube corner tip. This points out the strong influence of the electron beam on PDMS once again.

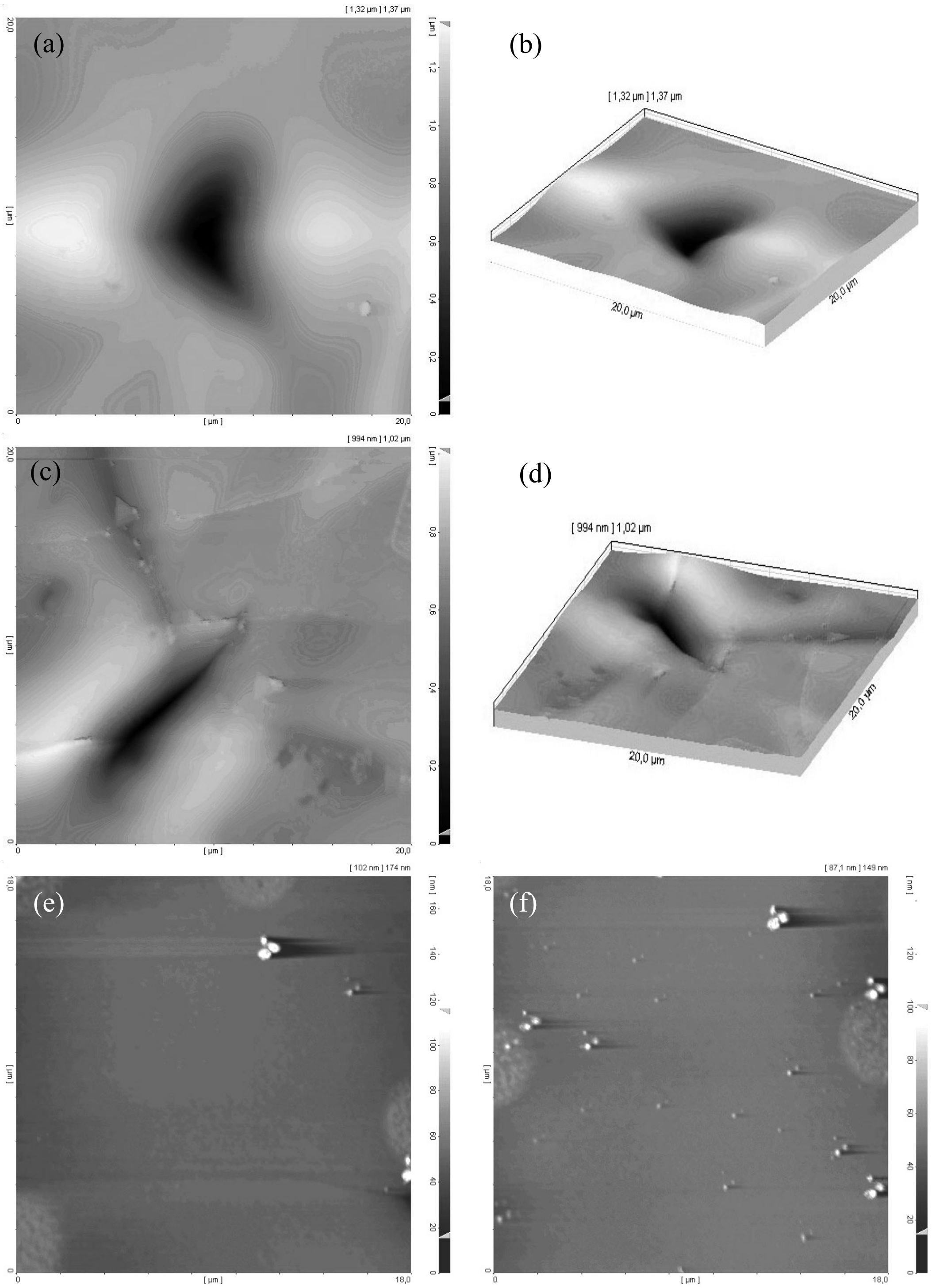

Figure 53: AFM images of indent locations. (a) After an in-situ test with a cube corner and (c) after an in-situ test with a Berkovich tip; (b) and (d) 3D images, respectively. Location before (e) and after (f) an ex-situ test with a cube corner tip has been performed.

Under atmospheric conditions PDMS behaved truly rubber-like and the recovery of indentations was 100 %, whereas permanent impressions were created, when PDMS was exposed to the electron radiation. The reason for the permanent deformation under the electron beam seemed to be associated with the sample heating, since it is known that PDMS undergoes a hardening process and becomes increasingly brittle [82] when it is kept at elevated temperatures above 200 °C. This embrittlement with prolonged temperature exposure also explains the results displayed in figure 43. Here a residual impression was found for 5 µm (figure 43a and b) as well as for 10 µm deep indentations (figures 43c and d). A comparison of the depth of the residual impressions after these experiments reveals that they were almost independent of maximum penetration depth, but approximately the same for the same time of testing. In figures 43(a) and (c) the loading segment took 100 s (the total cycle duration was 160 s); the indent depth is roughly 450 nm in both cases, corresponding to 92 % and 95 % recovery. Accordingly, in figures 43(b) and (d) the load segment duration was 600 s. This resulted in an indent depth of 1100 nm, which was ~ 80 % recovery for the 5 µm test and 90 % for the 10 µm test. Relatively speaking, an increase in the maximum penetration of 100 % led to no change in the residual impression depth; whereas a six-fold increase in loading time increased the indent depth by almost a factor of 3. This clearly indicates that the beam exposure time is the decisive factor for the size of the permanent impression, whereas the indentation depth itself plays a minor role.

6.4.1.3 Surface profiles

In order to get a deeper insight in the deformation mechanism associated with the creation of the residual indent and the recovery mechanism, a comparison between the surface profiles of a residual impression (measured after testing with AFM) and profiles during loading (extracted from simulations) is given in figure 54 for a cube corner. Further this graph contains the comparison between the profiles along the edge and the face center of the tip. The first conclusion from figure 54 is that the recovery for a pyramidal tip happened in a similar way than it is assumed for conical tips [136]. For conical impressions, a significant recovery of the depth is expected, which is accompanied by an increase in the inclined angle with respect to the opening angle of the cone. Further, a slight reduction in the indent diameter is found. These features of elastic recovery are found in figure 54, when considering the slopes of the solid and the dotted lines. Noticeable is further that the deformation as well as the recovery are different for the material deformed by the face than for the material deformed by the edge of the tip. In the loaded state the material adapted the straight shape of the tip in the regions of contact; therefore the slope along the face is higher than along the edge. In the recovered state, however, the difference of slopes is much smaller for the edge areas, indicating less recovery and hence more plastic deformation in the area of the edge compared to the face areas. This can be understood, as the edges induced a stress concentration and thus caused a higher amount of plastic deformation.

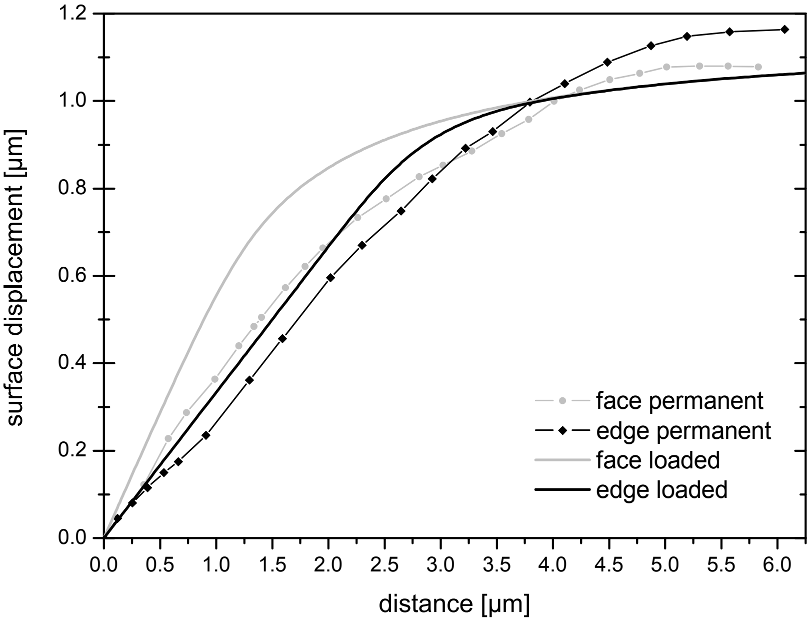

Figure 54: Comparison of surface profiles in the loaded state at ~ 1 µm and of a permanent impression of 1.1 µm depth for PDMS 1:10 and a cube corner tip. The surface displacements are given along the tip edges and in the center of the tip face in order to show the effects of the tip edges.

6.4.2 Contact area determination

In the view of the strong interactions between PDMS and the electron beam the validity of in-situ SEM results may be in doubt. It appears questionable whether the contact area determination using the SEM micrographs delivers reliable results. In order to clarify whether the deformation behavior of PDMS is actually influenced by the electron irradiation, we performed the second type of in-situ indentation tests, which are based on light microscopic contact observation. With this setup, the PDMS specimens were tested in their original unaffected state.

Qualitatively, there was no obvious difference in the way PDMS deformed when indented under the electron beam or under atmospheric conditions. This is supported by figure 45, where all three techniques applied in this study are contrasted with each other. The similarity is obvious, most strikingly in the considerable amount of sink-in. Quantitative evidence is given in figure 50. Here the results of the three different techniques are plotted together for the Berkovich tip. The range of experimental error for in-situ measurements is indicated by the error bars, which denote the standard deviation of 10 individual measurements. In order to maintain the comparability of the values, the upper limit of the contact area indicated by the triangle in figure 45(a) was calculated for figure 50, since this area is available from FEA (figure 45b), in-situ SEM (figure 45c) and in-situ-testing using light microscopy. First, figure 50 reveals that the simulations gave the same results for the contact area as the in-situ testing methods did. This consistence of simulation and experiments points out the adequacy of the chosen material model. The deformation of PDMS could be represented satisfactorily by the Neo-Hookeian strain energy potential. Second, it is noticeable that the results of the two in-situ methods also matched well, which leads to the conclusion that the SEM micrographs allow a quantitative calculation of the upper contact area limit and the deformation is not altered significantly by the effects of the electron beam. Regarding the two in-situ testing techniques, it is worth mentionable that both techniques are highly complementary because they offer completely different perspectives for the contact observation, and still they deliver the same results for the contact area.

We can now reconsider figures 46 to 48, where experimental results after Oliver & Pharr are compared to the simulations and the in-situ SEM results. In all cases, the results agree in a reasonable way. In figures 46 and 47 the differences between cube corner and Berkovich indentation can be seen for PDMS 1:10. An important finding is that the FEA gave a contact area about 8 % smaller than the Oliver & Pharr method did in the case of the Berkovich tip and an about 5 % smaller value for the cube corner tip. This implies that the Oliver & Pharr method underestimates the sink-in effect compared to the FE modeling and hence slightly overestimates the contact area. This result contradicts the common assumption, e.g. [33, 34], that the Oliver & Pharr analysis underestimates the contact area for soft polymeric (or biological) materials. Our results indicate that the Oliver & Pharr method provides a too high, yet acceptable estimate of the contact area for penetrations of a few μm.

Regarding the influence of crosslinking density and thus the stiffness of the specimen material on the contact evolution figures 46 and 48 should be compared, which show the results for PDMS 1:10 and PDMS 1:30. For the more compliant PDMS 1:30 the experimental determined as well as the simulated contact area and depth values were 5 % higher than for the stiffer PDMS 1:10. From the experimental data of the two PDMS types, the relative load increase was by a factor of 5.8, whereas the relative stiffness increase was 6 times. Thus it can be concluded that the relative increase in load, which is necessary to drive the tip to a certain penetration is roughly the same as the relative increase in the contact stiffness. According to the Oliver & Pharr calculations the contact depth h_c is the difference between the total displacement into the surface and the displacement of the original surface h_s. The surface displacement is determined by the ratio of load to contact stiffness. Thus, the relatively stronger increase in contact stiffness compared to the load leads to a larger contact depth and area respectively.

In order get a more quantitative evaluation of the amount of sink-in, several attempts have been presented in the literature, e.g. by Choi et al. [137] and by McElhaney et al. [138]. Choi et al. [137] used the ratio of contact depth to total displacement as a measure for sink-in. In this case no sink-in corresponds to a ratio of unity, the smaller the ratio, the stronger is the sink-in. The ratios h_c/h_{tot} obtained in this study were the following: For PDMS 1:10 and a cube corner h_c/h_{tot} was 0.79 ± 0.01, for the Berkovich it was 0.72 ± 0.03, and for PDMS 1:30 and the cube corner tip 0.78 ± 0.005 was obtained. In [138] another ratio is proposed as a measure for the sinking-in or piling-up of materials, which is the ratio of the contact area to the triangle area in figure 45(a). This ratio is expected to be smaller than 1, if sink-in occurs and for piling-up materials it is greater than 1. The values calculated for PDMS 1:10 and cube corner were 0.75 ± 0.04, for the Berkovich 0.74 ± 0.02 and for the cube corner and PDMS 1:30 0.74 ± 0.03. These measures of sink-in suggest that the sink-in for the Berkovich was a slightly more pronounced than for the cube corner. The results indicate that, despite the scatter, the ratio h_c/h can provide a useful estimate of how strong the tendency for sinking-in or piling-up in a certain case might be.

6.5 Conclusions

We have applied in-situ indentation testing inside a SEM in combination with finite element simulations to investigate the indentation process in soft elastomeric materials. The aim was to study the deformation and sink-in behavior and the evolution of the contact area during indentation. From this study the following conclusions can be drawn:

- For the coated samples the layer thickness of the Au-Pd coating determined the deformation behavior. The true deformation behavior of the PDMS specimens could only be monitored if the PDMS surface was uncoated.

- Under the direct influence of the electron beam, permanent impressions were created, whereas no residual indents could be found for indentations under atmospheric conditions. However, an influence of the electron beam on the contact area evolution could be excluded with the help of in-situ indentation based on light microscopy.

- The finite element results for the upper limits of the contact area could be confirmed by the values obtained from in-situ testing inside the SEM as well as from in-situ testing using light microscopy; therefore the FE values for the projected area can be considered as a reliable measure for the real contact size.

- Since the contact area determination after Oliver & Pharr delivered approximately the same values as the simulations, the results of this study indicate that the standard Oliver & Pharr method gives an acceptable estimate of the contact area during indentation of soft elastomeric materials.

Chapter 7

Contact area determination in indentation testing of elastomers

Abstract

For the evaluation of mechanical properties by means of nanoindentation information on the contact area is crucial. However, the contact area is not directly accessible in experiments and is usually calculated according to the Oliver & Pharr procedure. When applied to polymers this procedure turned out to be unsatisfying. For polymeric materials the contact size during indentation can be influenced significantly by various effects like viscoelasticity or adhesion. In this study complementary indentation testing, in-situ indentation and Finite Element Analysis (FEA) were performed. Through the combination of these techniques several individual error sources in the conventional contact area determination have been identified and quantified for two different Polydimethylsiloxane (PDMS) compositions. For shallow penetration depths contact areas after Oliver & Pharr were 40 % smaller than the in-situ testing results, for larger penetrations the contact size was overestimated by ~6 %. The deviations of the resulting mechanical properties were around 10 %. Viscoelastic effects could be captured if dynamic indentation testing was carried out. For reducing adhesive effects, pyramidal tips seem to be favorable compared to conical tips.

7.1 Introduction

Depth-sensing indentation techniques have nowadays become very popular for mechanically characterizing different kinds of materials across size scales from bulk material down to individual grains in metal specimens. In order to establish nanoindentation as a reliable means of mechanical testing, many efforts were made to get a better knowledge of the mechanics and deformation mechanisms involved in the indentation process, since this is inevitable for a successful analysis of indentation data. In this respect, simulations of the indentation process, e.g. with finite element (FE) methods [39, 43-52, 60, 139-142] or atomistic simulations [53-59], have proven to be a very useful tool to help in understanding the mechanics of indentation. Simulations allow the researchers to investigate issues quite easily, which cannot be directly accessed experimentally or require complicated and time-consuming experimental work. Further, it is possible to vary certain parameters in a systematic way and analyze their influences on the indentation process. Taking all these advantages, it is not surprising that simulating the indentation process provided a lot of insight in different aspects of indentation testing [12], e.g. for evaluating different constitutive material models [48, 60], understanding effects of the tip geometry [43, 139] or improving thin film testing [45, 50, 139, 140].

One of the most important purposes of simulating the indentation process is the accurate determination of the contact area between the specimen and the indenter [45, 46, 49, 51, 52, 141]. During a standard indentation test it is not possible to measure the contact area directly; the contact area and depth are usually obtained from the tip shape function calibration and the measured penetration of the tip according the relations derived by Sneddon [15] and Oliver and Pharr [12]. In many cases the contact areas calculated by this procedure are not accurate, thus significant errors are introduced in the indentation results. Also some basic assumptions in the load displacement data analysis can be checked by FE-simulations e.g. whether a constant contact area regime exists during the initial unloading stage or not. In the work of Laursen and Simo [45] no constant contact area regime was found, whereas Li and co-worker observed a constant contact area for several different materials except amorphous carbon. A detailed study of Berkovich indentation was presented by Larson et al. [46], who found a reasonable agreement between numerical results and theoretical assumptions on contact area determination from unloading data. Another very interesting result of their study is the examination of the contact shape, which was almost triangular for elastic-plastic materials and hyperbolic for purely elastic behavior.

Although the investigation of the contact formation with finite element methods is a very helpful tool, it still has to be noted that the results from simulations can also be misleading. A common approach to the simulation of pyramidal indentation is to use a cone with an equivalent area-depth relation [45, 49-52, 141]. This procedure is justified with the argument that it facilitates the simulations substantially [44] and that only a few elements in the vicinity of the edges experience different stress states [50, 139], which does not influence the overall results [141]. In order to verify these assumptions, several comparative studies have been carried out [2, 3, 10, 13]. The load displacement data obtained from the different geometries deviate by several percent [44, 60], for elastic materials the deviation are a little higher than for elastic-plastic materials. In consequence, also the contact areas are somewhat different [60]. Thus, it can be concluded that the equivalent cones deliver similar, but not identical results. Therefore results obtained from conical tips must be carefully compared to results from 3D- pyramidal results.

Regarding polymer indentation a lot of experimental work was presented in recent years, but not many finite element studies on the specific issues related to indentation of polymeric materials can be found [25, 39, 142-146]. The studies in this field are mainly a combination of theoretical and simulation work introducing new constitutive models, e.g. for biological tissues [142], glassy elastic-plastic polymers [39] or viscoelastic-plastic polymeric materials [143, 144]. In the work of Larsson and Carlsson [144] a reasonable agreement of simulation results and spherical as well as punch indentation experiments was found for viscoelastic materials. Especially in the case of punch testing, the interpretation of viscoelastic load-displacement data is relatively easy, since the contact area remains constant throughout the entire experiment [144]. The situation is much more complex, if conical or pyramidal tips, e.g. Berkovich tips are used for testing of viscoelastic materials. Here the contact area determination according to the Oliver & Pharr method is found not to be valid [25].

For modeling the behavior of rubber-like materials in FEA, the theoretical framework reaches back to the 1930s, when Kuhn [147] and Guth and Mark [148] presented the first statistical treatments of the network structure of rubber-like materials. These first approaches to describe the elasticity of polymer networks were pursued and advanced by the work of Treloar, who presented one of the first strain energy functions in 1943 [149, 150], which is today known as the Neo-Hookeian form [137]. Ever since many extensions on [149, 150] and also alternative forms describing the strain energy during deformation of rubber-like network structures have been elaborated [151-155]. In order to evaluate the numerous different forms of strain energy potentials comparative studies on the various forms presented in [150-154] have been conducted [146, 156, 157]. These studies agree in their conclusion that none of the models can be considered as the best one in any case and that the proper model has to be chosen for each combination of material and loading condition individually. In the work of Jerrams et al. [149] the focus was on a comparison of strain energy functions derived on the basis of strain tensor invariants I_i (i=1-3) [150, 154] and functions derived using the principal stretches λ_i (i=1-3) [153]. They found that the potentials using the principal stretches delivered a better description for the behavior of nitrile rubbers than the potentials using the strain tensor invariants. In the study conducted by Raos [157] it was shown that the experimental data used for the determination of the material constants in the strain energy potentials strongly influence the results of the fitting and hence of the FEA. Further he proved that the early models [150, 152] provide a very poor representation in the tensile regime and are only reliable in the compressive regime.

For this study, finite element modeling of the indentation process in elastomeric materials was performed to determine the contact area quantitatively. As an experimental approach to a quantitative measurement of the true contact area, an in-situ indentation testing method is presented. Through the combination of experimental and simulation techniques it was possible to quantify the effects of adhesion, sink-in behavior and viscoelasticity on the contact area and hence on the resulting mechanical properties.

7.2 Experimental

For this study PDMS (Sylgard 184, Dow Corning Corp., Midland, MI, USA) was selected as a model system for elastomeric behavior. Its optical transparency offers the possibility to perform in-situ indentation tests. Two different PDMS compositions (weight ratios of crosslinking agent to pre-polymer 1:10 and 1:30) were prepared for this investigation in order to study the influence of changing crosslinking density on the indentation behavior. PDMS sheets of ~1 mm thickness were obtained from pouring the liquid, uncured PDMS onto a silicon wafer and curing it in a vacuum furnace at 150 °C until the crosslinking reaction was completed [133]. For testing rectangular pieces of PDMS were cut from the sheets.

Uniaxial tensile and compression testing was conducted on a Nano Bionix (MTS Nano Instruments, Oak Ridge, TN, USA). For compression testing, cylindrical pieces of PDMS were strained between two aluminum plates to a maximum load of 450 mN. A custom-built sample holder for the Nano Bionix system was designed to allow light-microscopic in-situ observation of the contact during an indentation test. This system offers the same load and displacement resolution as the commercial MTS nanoindenter XP. The magnification of the CCD/video-microscope was 1000 x. With this setup, the evolution of the contact area could be monitored through the transparent specimen perpendicular to the test surface, thus the projected contact area could be deduced directly from the micrographs. For the determination of the contact area the images were analyzed with the software Sigma Scan Pro 5.5.

Standard indentation testing was performed on a Nano Indenter DCM (MTS Nano Instruments) in the CSM mode (continuous stiffness measurement) with a frequency of 75 Hz. Loading was carried out under constant strain rate conditions, where $\dot{P}/P = 0.05s^{-1}$ [68]. The indenters were diamond Berkovich and cube corner tips with curvature radii below 20 nm. The calibration and analysis procedure according to Oliver and Pharr [12] was applied for the determination of the tip area function. These calibrations were used to calculate the contact area from the experimental data.

7.3 Simulations

The commercial FE-code ABAQUS Version 6.61 (ABAQUS Inc., Providence, RI, USA) [69] was used for the performance of comparative 3D finite element simulations of the indentation process in PDMS. The indenter geometries under investigation were the three-sided pyramidal tips of the Berkovich (face opening angle $\alpha = 65.3°$) and cube corner ($\alpha = 35.3°$) type and the Berkovich equivalent cone (half-opening angle $\phi = 70.3°$). For the pyramidal tips modeling of one third of the actual problem, incorporating the contact between one face of the tip and the specimen is sufficient because of the three-fold symmetry of these geometries.

Detailed studies concerning the influences of the mesh density, the element type and contact formulation on the resulting load-displacement data have been carried out, before the final discretisation was defined. For the geometric order of the elements no significant influence on the results was found. Therefore 8-node linear elements were selected for efficiency. Since the mesh density did have an influence on the results, a mesh convergence study was performed.

The convergence of results is shown in figure 55 for the cone and the Berkovich model. Finally a strongly biased mesh was created, which becomes continuously denser towards the center. The overall number of elements was 23275, which corresponded to 40 elements along the edge in figure 55. The indenter tip was represented by an analytically rigid body (a plane for the pyramidal tip face or a cone). Tangential frictionless contact behavior was assumed and finite sliding was enabled to allow relative movement of the surfaces. The computationally less expensive node-to-surface contact formulation was preferred to the surface-to-surface alternative, since the same results were expected for the calculation of a contact with a rigid body. In order to avoid any penetration the Lagrange method was chosen.

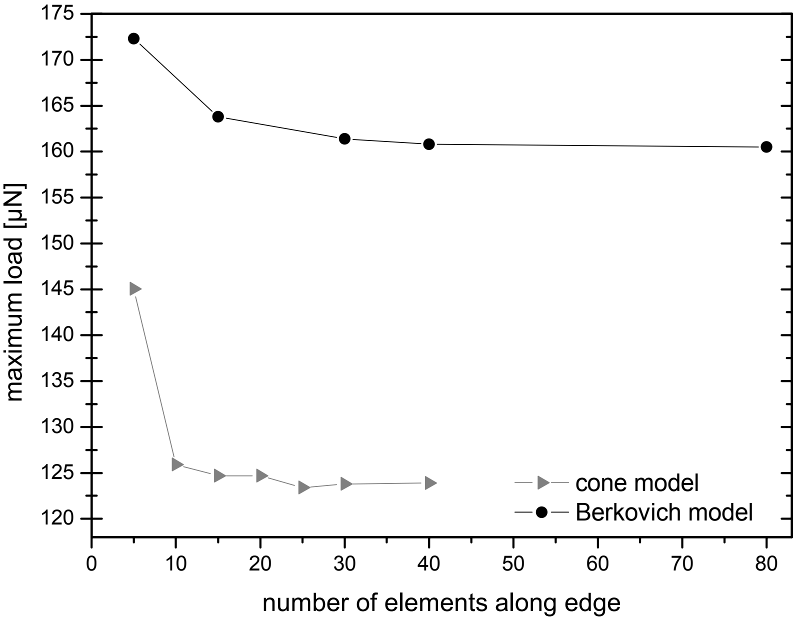

Figure 55: Maximum load values at an indentation depth of 10 µm for PDMS 1:30 as a function of mesh density. The results for the Berkovich and the cone model are shown.

7.3.1 Constitutive material model

For representing the material behavior of elastomeric materials, a hyperelastic constitutive material model has to be selected, which incorporates large deformation analysis. Hyperelasticity [69, 134] is described by strain energy potentials $U = f(I_1, I_2, I_3)$, which give the stored deformation energy of a deformed rubbery network system U as a function of the strain tensor invariants I_i (i = 1-3). Several different strain energy potential formulations are implemented in the ABAQUS package. In order to help deciding which of the various strain energy potentials is the one most suitable for a specific material or purpose, ABAQUS provides a tool for evaluating the different models on the basis of experimental data from the material of interest [42]. Through this evaluation tool the experimental data are fitted automatically; at the same time the relevant material constants are determined and the expected numerical stability of the individual fits/models is checked.

In order to choose an appropriate strain energy potential for PDMS, uniaxial tensile and compression tests were conducted. The resulting stress-strain plot for PDMS 1:30 is given in figure 56. To correct the data measured in compression for friction and barreling, Hicsasmaz and Rizvi [158] proposed to multiply the apparent modulus with a shape factor to obtain the true modulus value. For our specimens the average shape factors lay in the range of 0.22 and 0.25 [159]. Applying this correction to the compression data delivered a similar modulus value as the one obtained from tensile tests. The equivalent slope of both branches in figure 56 is indicated by the grey line.

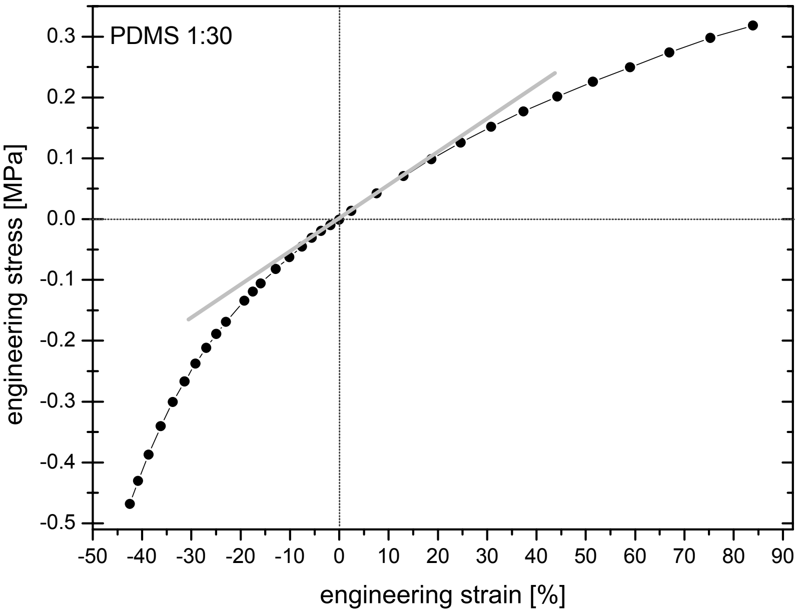

Figure 56: Tensile and compressive stress-strain curve for PDMS 1:30.

In addition to the recording of stress-strain data, the Poisson's ratios of the two PDMS samples were determined from the tensile tests according to [133]. Poisson's ratios are needed in the fitting to ensure a reliable description of the volumetric deformation behavior [134], which cannot be deduced from uniaxial data alone. Since only one mode of deformation is covered by the experimental data, it is recommendable not to determine more than two parameters from this data. Following these guidelines for the evaluation process [69], two possible strain energy potentials have been chosen. The first one was the Marlow model [134], which is given by:

$$U = U_{dev}(\bar{I}_1) + U_{vol}(J_{el}) \tag{23}$$

Here U_{dev} and U_{vol} are the deviatoric and the volumetric portions of the strain energy U, $\bar{I}_1$ is the first invariant of the deviatoric strain tensor and J_{el} is the elastic volume ratio. The second form was the Neo-Hooke strain energy potential [135]:

$$U = C_{10}(\bar{I}_1 - 3) + \frac{1}{D_1}(J_{el} - 1)^2 \tag{24}$$

The material properties initial shear modulus μ_0 and initial compression modulus K_0 are related to the two coefficients C_{10} and D_1 in the following way:

$$\mu_0 = 2C_{10} \tag{21}$$

$$K_0 = \frac{2}{D_1} \tag{22}$$

The first invariant of the strain tensor I_1 is defined as:

$$I_1 = \lambda_1^2 + \lambda_2^2 + \lambda_2^2 \tag{25}$$

with λ_i being the principal stretches, i.e. the ratio of actual length l to initial length l_0.

The fitting results are shown in figure 57 together with the experimental data. In general, it can be seen that the Marlow potential represented the tensile regime very well, but the fits were quite poor for the compressive part. In turn, when using the Neo-Hooke potential the tensile data could not be fitted well. Since it has been shown in various studies that the material constants are significantly influenced by the selection of the experimental data used in the fitting procedure [134, 146], not only the tensile and compression data together were fitted, but also the tensile and the compressive data individually. The results of these fits are also plotted in figure 57.

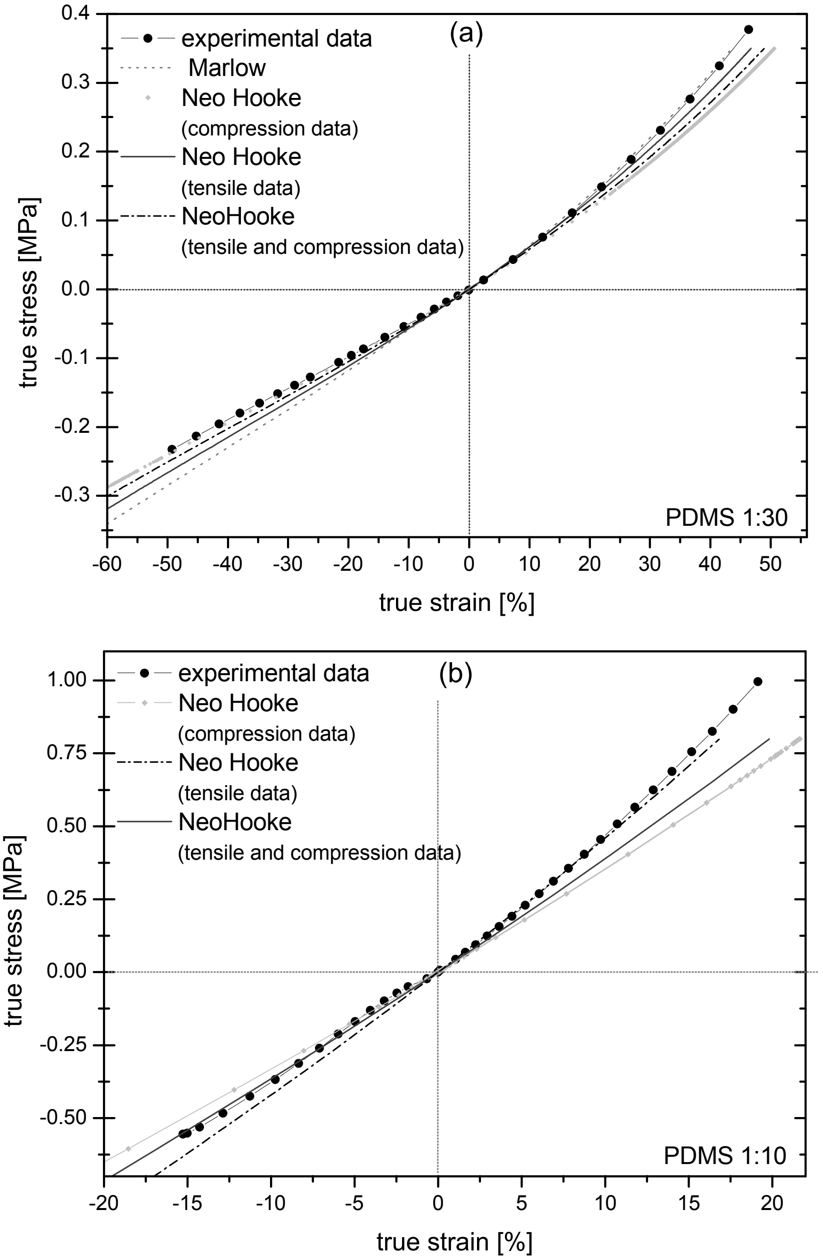

Figure 57: Comparison of ABAQUS fitting results with true stress-strain curves obtained from experiments for (a) PDMS 1:30 and (b) PDMS 1:10.

This finding is in agreement with other investigations, where the Neo-Hooke potential was found to be favorable for modeling compression [146, 157]. For PDMS 1:10 the coefficients were derived from tensile and compression data; for PDMS 1:30 only the compressive data were used in the fit. The coefficients and material properties are summarized in Table 6.

Table 6: Summary of Neo-Hooke material constants.

	Modulus [MPa]	Poisson's ratio	C_{10}	D_1
PDMS 1:10	4.3±0.2	0.43±0.02	0.662	0.255
PDMS 1:30	0.66±0.05	0.46±0.02	0.0922	1.123

7.3.2 Results

The finite element results for the indentation of PDMS 1:30 with a cube corner tip are plotted in figure 58 together with the experimental data. The load-displacement curves in figure 58(a) possessed a very similar shape and also the force values match quite closely. The maximum load at a penetration depth of 10 µm was 66 µN in the FEA and 64 µN in the experiment. For smaller penetrations below 3 µm the load values in the FEA tended to be slightly smaller. The contact area is given in figure 58(b). Here the results from FEA were a little higher for the small displacements, but again in reasonable agreement with the experimental results for bigger displacements. The contact areas at maximum displacement were 162 µm^2 and 168 µm^2 for FEA and experiment, respectively.

Figure 59 contains the results for the stiffer PDMS 1:10 indented with a Berkovich tip. The load-displacement curves (figure 59a) were almost identical with maximum load values of 1080 µN (FEA) and 1075 µN (experiment) at 10 µm penetration. However, a clear deviation between the FE results and the experimentally determined contact areas was obtained (figure 59b). The contact area determined after Oliver & Pharr is larger than the contact in the FEA. At a depth of 3 µm the FE result was 119 µm^2 and after Oliver & Pharr 128 µm^2 were obtained, at ~6.4 µm approximately 480 µm^2 (FEA) and 540 µm^2 (O & P), and at maximum depth the contact areas were 1230 µm^2 (FEA) and 1330 µm^2 (O & P). The results for PDMS 1:30/Berkovich and PDMS 1:10/cube corner are not shown explicitly here, but the results resembled the trends in figures 58 and 59. In any case the load-displacement data were in good agreement with the experiments, for the cube corner tip the contact areas calculated in the FE-simulations were slightly smaller than the experimental values, for the Berkovich tip this deviation was more pronounced.

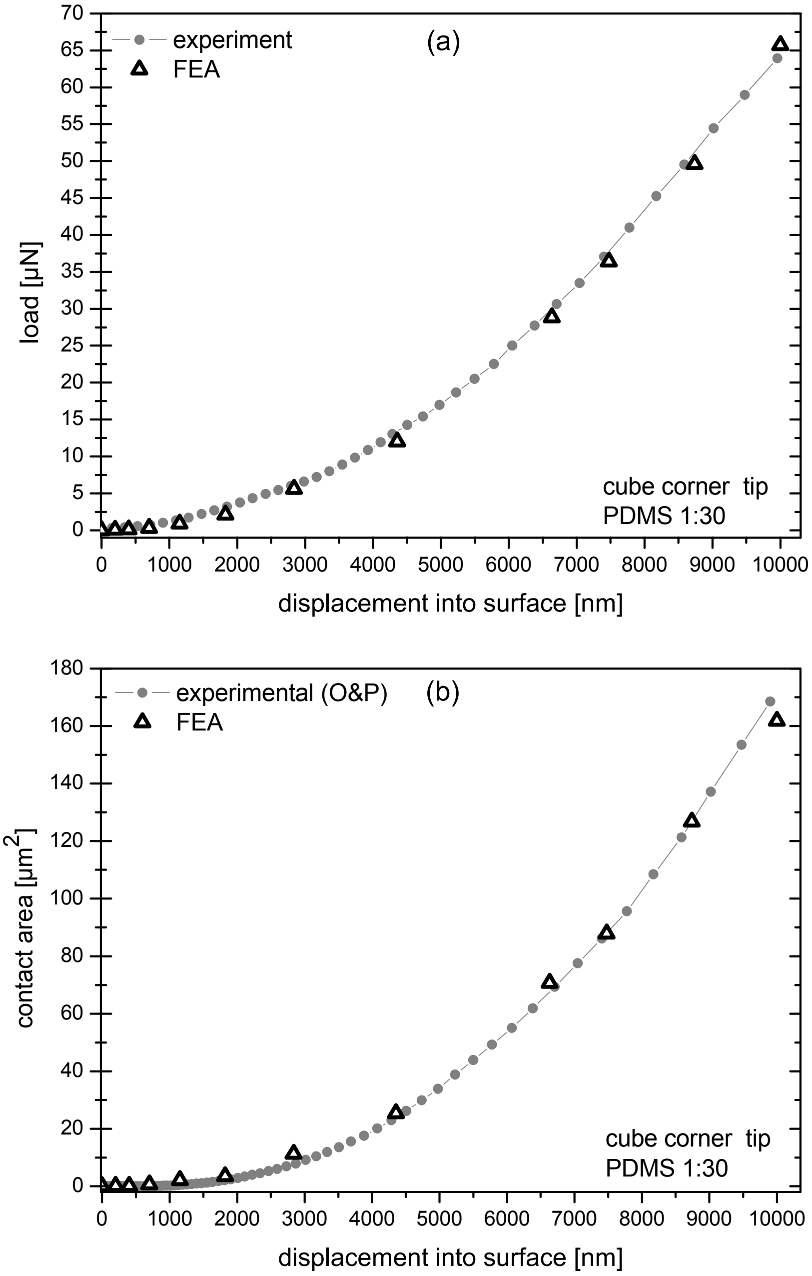

Figure 58: FEA results for cube corner indentation on PDMS 1:30 in comparison with experimental data. (a) Load-displacement data; (b) Contact area as a function of displacement.

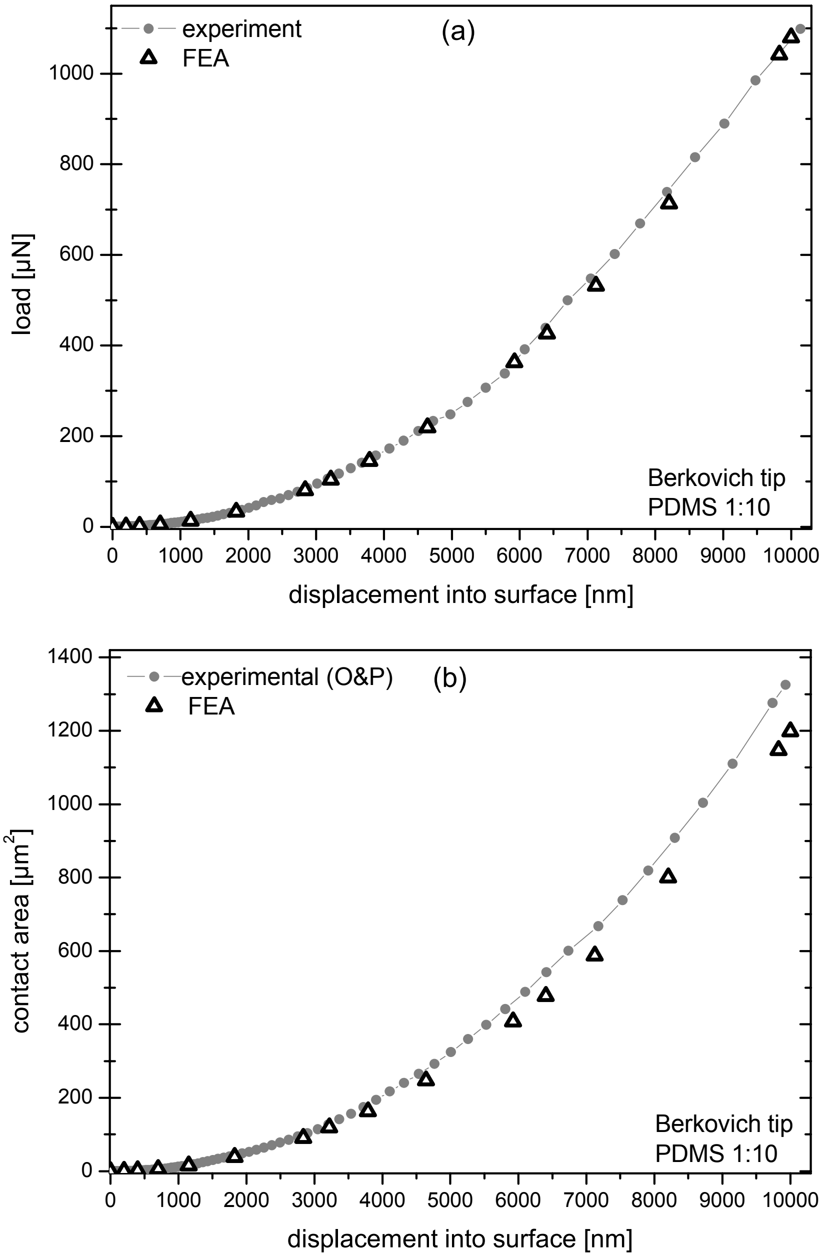

Figure 59: Comparison of experimental data and FE results for PDMS 1:10 tested with a Berkovich tip. (a) Load-displacement curves (b) Contact areas. For higher penetration depths the experimentally determined contact area is larger than the area obtained from the FE simulations.

The deformation field and the contact area can be visualized from the simulation, which is done in figure 60. The displacement field under a Berkovich tip can be seen in figure 60(a). This image represents the material volume, which is deformed during the indentation. This deformation reaches quite far in comparison to the actual area of contact between the tip and the surface, as can be seen in figure 60(b). Characteristic for the shape of the contact is the bowed-in contour of the contact, which is a consequence of the sink-in behavior of PDMS.

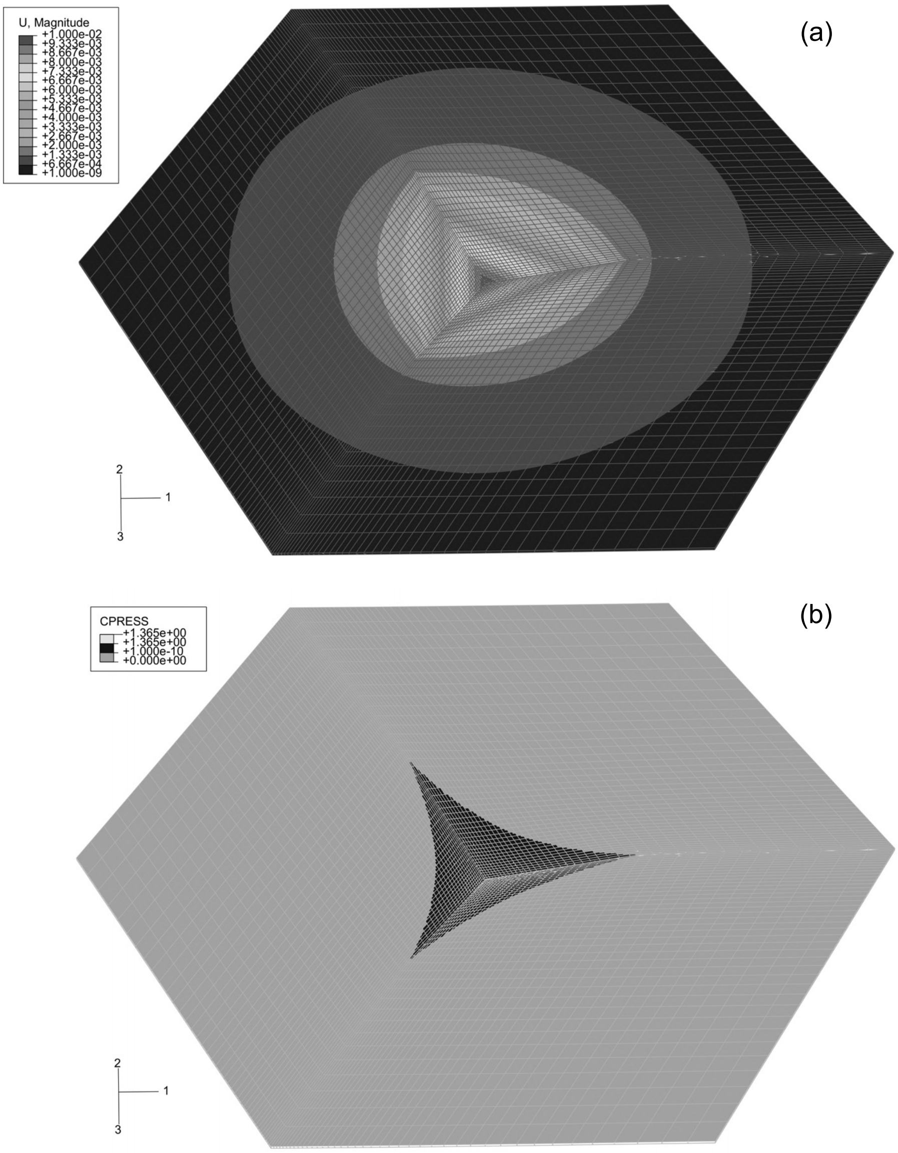

Figure 60: (a) Simulated deformation field under a Berkovich tip, illustrating the deformed material. (b) Area of contact for Berkovich tip. Notable is the wide-spread deformation compared to the actual contact size with the bowed-in contour.

7.3.3 Discussion

The comparison of experimental data with results obtained from FE calculations revealed a significant deviation between the contact area values, although the load-displacement data from FE calculations gave a reasonable representation of the experimentally measured curves. In the following possible reasons for this disagreement, e.g. the material model or the sink-in behavior will be discussed.

7.3.3.1 Sensitivity of material model

In order to understand the origin of these deviations we will first check the sensitivity of the Neo-Hooke material model for uncertainties in the experimental data, which are used in the material evaluation and fitting process. It has been pointed out in literature that the experimental data must be selected carefully, since small deviations of individual data points can already influence the fitting results [69, 157].

For this purpose a parameter study was performed, where the modulus values and Poisson's ratios of PDMS 1:30 were varied systematically; two smaller values and two larger values were chosen for each quantity. The resulting load-displacement curves are given in figure 61 (for simplicity only selected curves are shown), where the curves for 75 %, 100 % and 125 % of the measured modulus and Poisson's ratios of 0.4, 0.45, and 0.49 are plotted. Figure 61 shows that the forces needed to reach a certain penetration increased with increasing modulus values and vice versa. For the influence of the Poisson's ratio can be said that the larger the Poisson's ratio was, the higher the forces became. Thus it has to be noted that certain combinations of moduli and Poisson's ratios can lead to very similar load-displacement curves, although the individual values differ noticeably. In figure 61 an example for such combinations are E=100 %, ν=0.49 and E=125 %, ν=0.45. The measured load-displacement curve of PDMS 1:30 was also matched closely by E=110 % and ν=0.40, E=110 % and ν=0.425 as well as E=125 % and ν=0.40. These results point out clearly, how important it is to use accurate experimental data for the fitting procedure in order to obtain reasonable material constants from the fitting process. For the determination of the Neo-Hooke coefficients in this work, both modulus and Poisson's ratio have been measured experimentally to ensure a suitable description of PDMS by the Neo-Hooke material model. Further it was found that the variation of the contact area with material constants is much less than the variation of the load. For changing modulus values the contact area change was below 1 %, for changing Poisson's ratios the difference was below 3 %. Thus, uncertainties in the material constants cannot cause the contact area deviation of experiment and simulations.

The sensitivity of material constants can be advantageous in case that the material properties are not known or cannot be determined experimentally. In practice, the Poisson's ratio is often difficult to measure and a value around 0.3 is taken for simplicity. In this case the fitting tool can be helpful in obtaining a more accurate value for Poisson's ratio. Through an iterative process of fitting and comparison with experimental data, the simulated curve can be approximated to the experimental curve. The Poisson's ratio in the fit, which matches the experimental data best, can then be taken as the most accurate estimate of the Poisson's ratio.

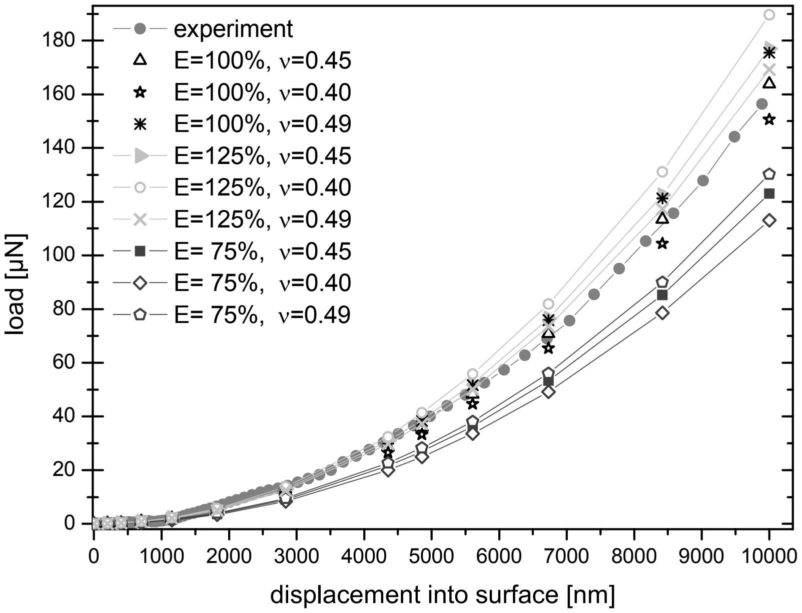

Figure 61: Load-displacement curves for studying the material model sensitivity. The variation was accomplished through slight changes in the modulus and/or Poisson's ratio of PDMS 1.30.

7.3.3.2 Equivalency of Berkovich and cone

For understanding the deviations between experiment and simulations it is instructive to consider results obtained from the 3D Berkovich model and results obtained from the equivalent cone model. This comparison is shown in figure 62. From the load-displacement data in figure 62(a) it was obvious that the cone model did not give the same results as the Berkovich model. The load at a penetration of 10 µm for the cone was 18 % below the load of the Berkovich. The differences in the contact area (figure 62b) were about 30 %; where the contact area from the cone was larger than for the Berkovich. In other investigations similar results for elastic materials were obtained. Shim and co-workers [60] also found lower loads for elastic indentations in fused silica. For elastic-plastic materials the deviations between cone and Berkovich were smaller but still noticeable [43, 44, 60]. Thus, the results of this study clearly show that the equivalency of Berkovich and cone model is not valid for elastomeric materials like PDMS.

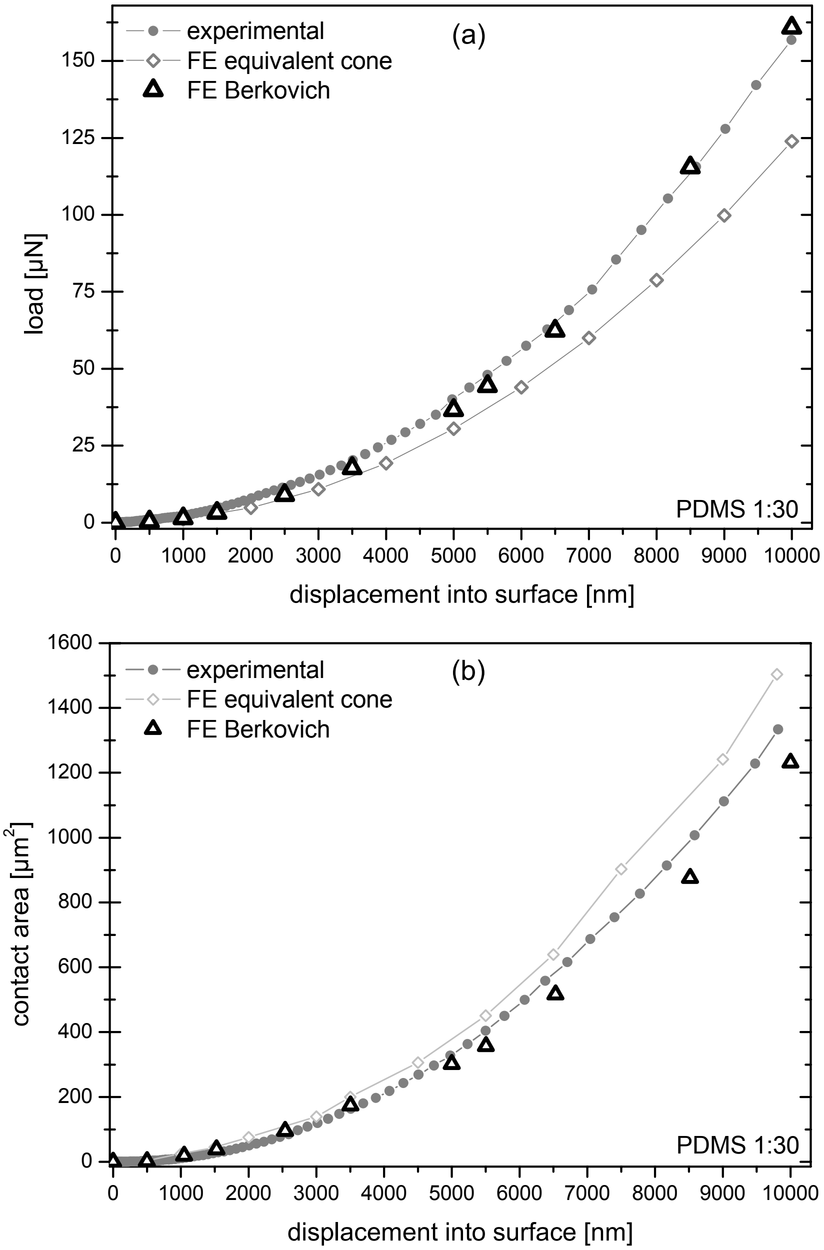

Figure 62: (a) Results for the 3D Berkovich model and the equivalent cone model. Both models delivered significantly different results for (a) the load-displacement data, and (b) the contact area values.

Following the arguments of Shim et al. [60] the increases in load must be attributed to edge effects. It was often assumed in literature that only a small number of elements come in contact with the edges and that the contribution of these elements did not affect the overall results [49, 141]. This might be true for elastic-plastic materials, where the stress concentrations at the edges lead to stress relaxation through plastic flow. For elastic materials, however, this argument is not correct. Considering the deformations under the pyramidal tips or the material displacements in the surrounding of the actual impression it becomes clear that the edges of the pyramidal tip did not only increase the load needed for driving the tip into the material. They also changed the complete deformation behavior under and around the tip, especially for the case of materials which exhibit a sink-in behavior. The contour of the contact for Berkovich indentation possessed a hyperbolic shape as has been derived by Larson et al. [46]. The deformation field of the Berkovich in figure 60(a) reveals that only the far field deformation is symmetric, in the direct vicinity the pyramidal form of the tip is adapted, thus the edge effects were obvious.

7.3.3.3 Sink-in behavior

The surface profiles are used to get a more quantitative picture about the effects of the edges and the sink-in behavior. In figure 63(a) the surface profiles of the Berkovich tip along the edge and along the face center are plotted together with the profile of the equivalent cone for comparison. Along the face a significant amount of sink-in occurred, whereas the profile along the edge showed much less sink-in. The difference in contact depth is denoted by the horizontal lines and amounts to 3 µm roughly. For the cone the profile is somewhat steeper, i.e. the distance between sample surface and tip is smaller, which indicates a less pronounced sink-in. Quantification for the amount of sink-in can be given through the ratio of contact depth h_c and penetration depth h [137]. The lower this ratio, the more pronounced the sink-in effect. The sink-in parameters h_c/h were calculated for the different profiles in figure 63 and are summarized in Table 7.

Table 7: Summary of sink-in parameters.

	edge	face	Berkovich FEM	Berkovich O & P	cone
PDMS 1:30	0.84	0.55	0.75	0.79±0.03	0.83
PDMS 1:10	0.81	0.54	0.73	0.77±0.01	---

From these values several conclusions can be drawn. First, the sink-in for the Berkovich is clearly higher than for the cone. This explains the disagreement between the 3D Berkovich model and the cone model and hence the non-validity of the Berkovich/cone equivalency. Second, the experimental data calculated according to Oliver & Pharr predicted less sink-in than obtained from the simulations. Less sink-in results in a larger contact area, thus the deviations between the experimental results and simulations become understandable. Third, the sink-in in the vicinity of the edges is reduced, whereas it is enhanced in the center of the Berkovich face. Figure 63(b) illustrates the influence of the crosslinking density on the sink-in behavior. The sink-in for the stiffer PDMS 1:10 seems to be slightly stronger, but the differences is only very small. For the cube corner, there is no noticeable difference between PDMS 1:10 and 1:30. Obviously, the difference in modulus due to a change in crosslinking density did not influence the sink-in behavior markedly.

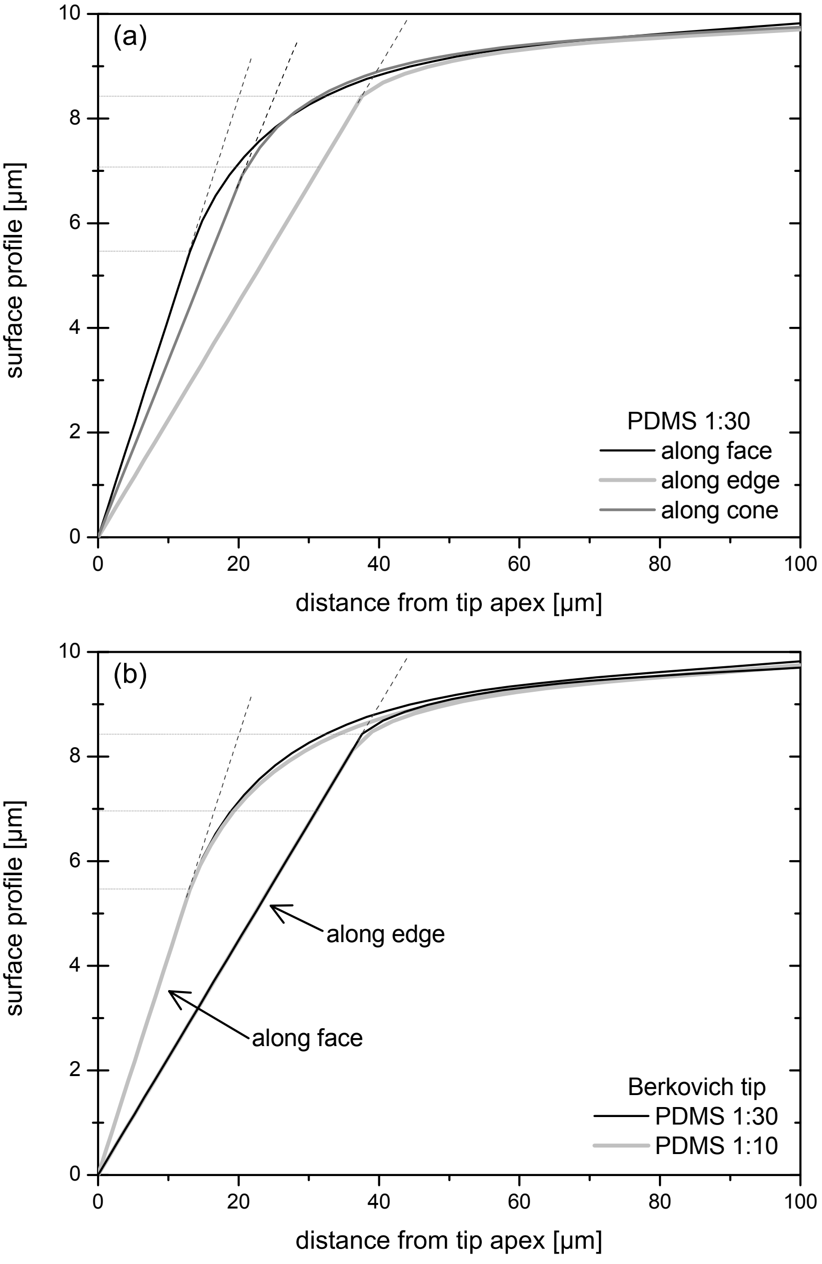

Figure 63: (a) Surface profiles from FEA under maximum load. (a) Comparison of Berkovich and cone indentation. For the Berkovich the profiles along the edge and along the face are given to illustrate the edge effects. (b) Profiles for PDMS 1:10 (grey) and PDMS 1:30 (black).

7.4 In-situ indentation testing

The purpose of the in-situ indentation testing was to examine the contact evolution on a material, which exhibits elastomeric behavior. For this optically transparent material the real projected area could be measured directly from the light-microscopic videos. These truly measured contact areas will be compared to experimental and simulation results. Further, this setup was used for a series of tests with different strain rates [68] in order to study the influence of viscoelasticity on the contact evolution during testing.

7.4.1 Influence of strain rate

In figure 64 several micrographs of indents with a Berkovich tip on PDMS 1:30 are given. On the left side (a to c) the contact evolution during loading for a strain rate of 0.1s^{-1} can be seen; on the right side (d to f) a lower strain rate of 0.01 s^{-1} was used. In (c) and (f) fringes were visible along the contact contour, which proved that there was no contact in these areas. Direct comparison of the micrographs revealed a change in the contact area with strain rate. It was found that the contact area decreased for higher strain rates, which is most obvious in (a) and (d) for a penetration depth of 2 µm. The corresponding load-displacement curves and resulting contact areas are plotted in figure 65. For the lowest strain rate of 0.01 s^{-1} the maximum load at 10 µm penetration was 138 µN and at 2.0 s^{-1} the load increased up to 180 µN. This increase in load for faster loading is consistent with the theory of viscoelastic solids. As the load was directly used for the calculation of the contact depth, the increase in load caused a decrease in contact depth and hence in contact area [12, 25]. This decrease can be seen in figure 65(b), were the contact areas for the different strain rates are plotted as a function of displacement. For comparative reasons the contact areas at maximum displacement are listed in Table 8 together with the areas determined from the micrographs.

Table 8: Contact area values for testing at different strain rates.

Strain rate	[s^{-1}]	0.01	0.05	0.1	0.5	2
Contact area (O & P)	[µm^2]	1435±12	1364±15	1316±6	1229±14	1153±10
Contact area (in-situ)	[µm^2]	1348±16	1286±19	1238±15	1198±29	1112±41
deviation	[%]	6.4	6.0	6.3	2.6	3.7

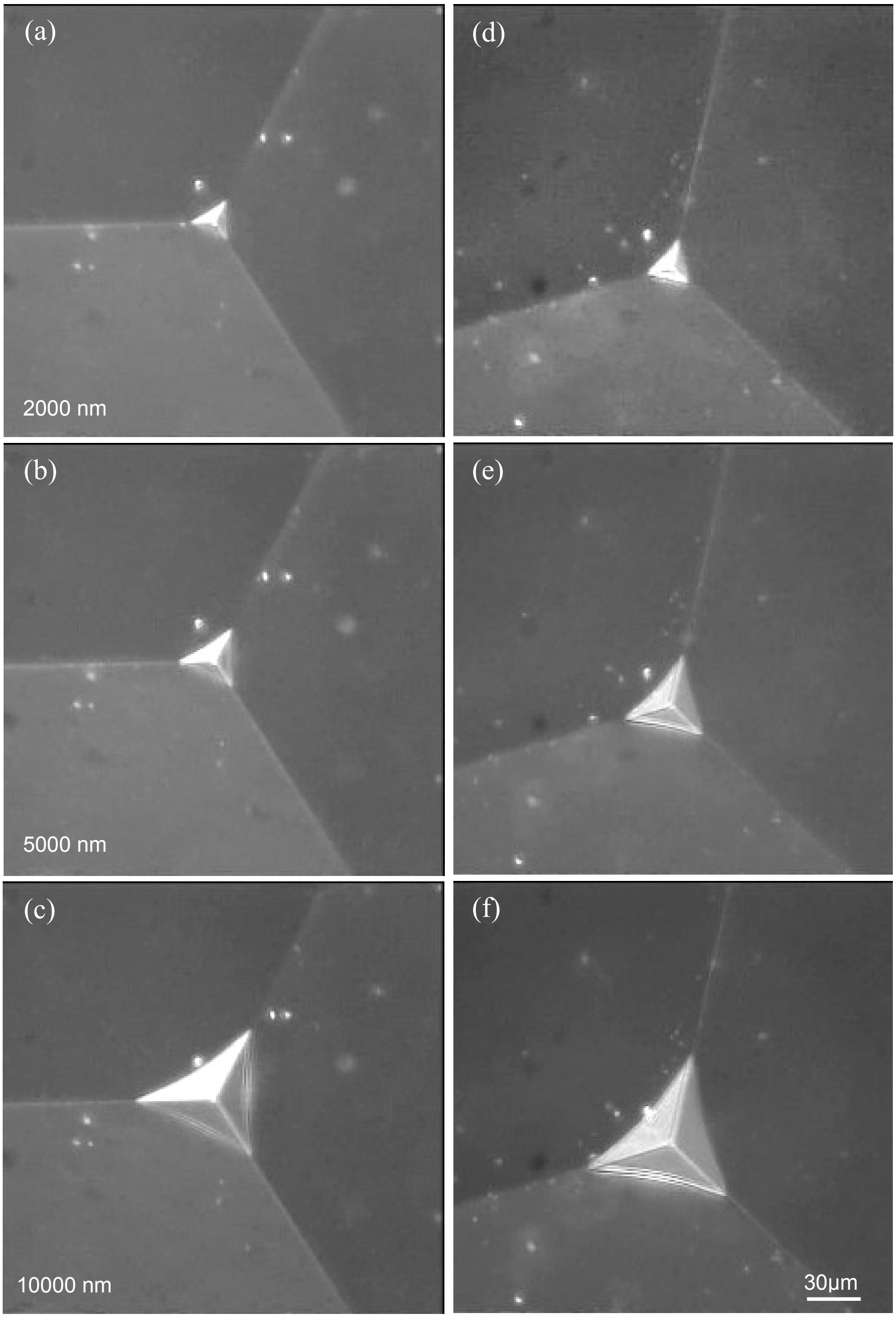

Figure 64: Optical micrographs of the contact during Berkovich indentation on PDMS 1:10. (a - c) Test at a strain rate of $0.1s^{-1}$ and (d - f) $0.01s^{-1}$. Note the fringes in (b), (c), (e), and (f).

For all strain rates the true contact area was several percent smaller than the area obtained from the experiments. This deviation is again due to the pronounced sink-in effect of the PDMS, for which the Oliver & Pharr method did not account. Yet, the relative decrease in contact area with increasing strain rate was consistent. In both cases the contact area at the highest strain rate was about 80 % of the area obtained at the lowest strain rate. Thus, it can be concluded that it is possible to capture viscoelastic effects and the rate dependency of polymeric materials with nanoindentation testing in the CSM mode. At this point, it has to be insisted once again on the fact, that all experiments were carried out in the CSM mode and no unloading data were used. This is an important finding, because work presented in literature shows that the determination of unloading stiffness and contact area from unloading data is not always possible for viscoelastic materials [25].

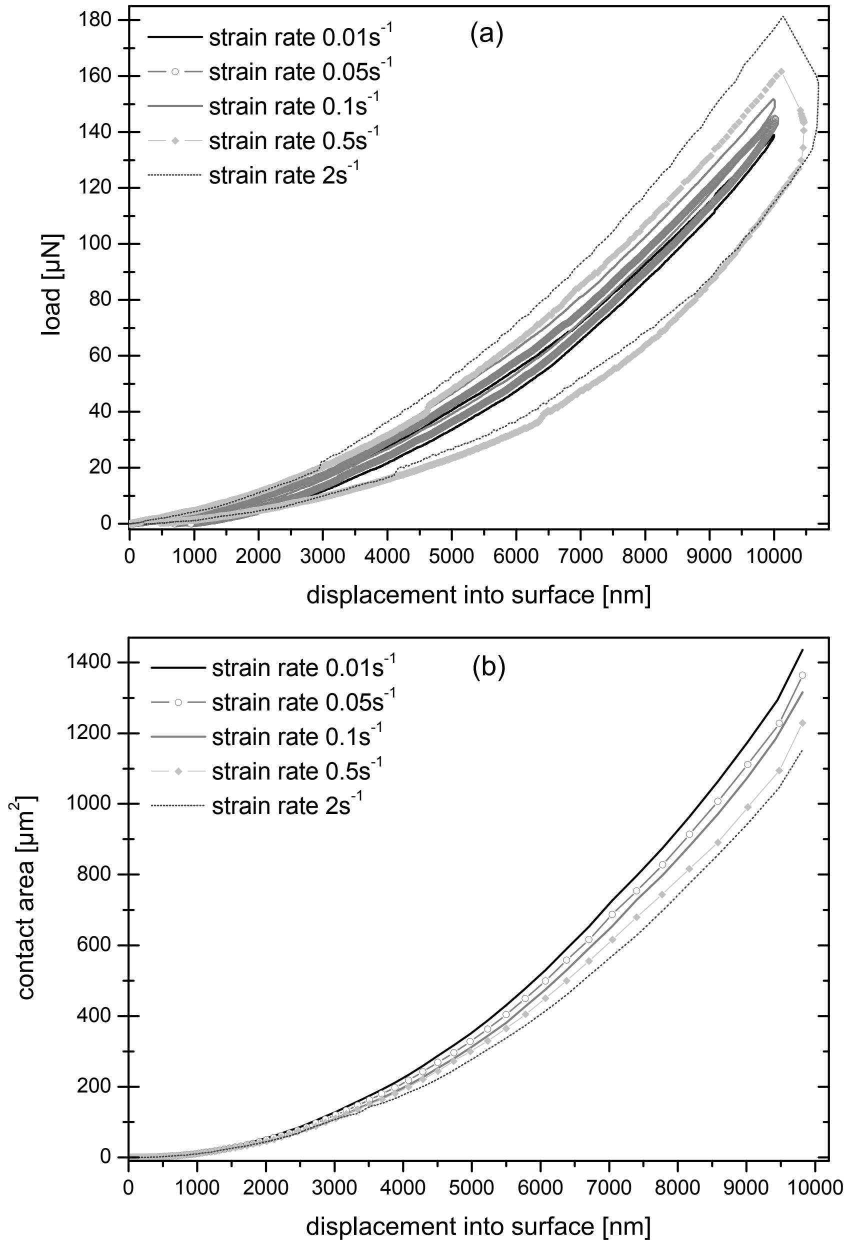

Figure 65: Results for testing at different strain rates. (a) For increasing strain rates the load increased. (b) As a consequence of the load changes the contact area decreased in accordance with the in-situ tests.

Regarding the load-displacement data in figure 65(a) another valuable observation can be made. The shape of the curves did not only provide information on the mechanics, but also revealed some information on the relaxation time spectra of the material tested. For the 3 lower strain rates, the curves exhibit a quite similar shape and a relatively small hysteresis of ~10 %. For the two highest strain rates, the shape of the unloading portion changed significantly. The hysteresis increased to 20 % at 0.5 s^{-1} and 30 % at 2.0 s^{-1}.

Obviously, the loading segment of the slower test was long enough for relaxation processes within the sample to mostly complete, whereas nose formation and larger hysteresis for the faster tests indicated creep and relaxation processes also during the unloading segment. The duration of the loading segment in an indentation test with small hysteresis can thus be taken as an estimate for the duration of relaxation processes within the material of interest. This can also be beneficial for the determination of mechanical properties from unloading data, since the minimum hold period at maximum penetration, which is required to let creep in the sample decay, can be found out from considering the load displacement data.

7.4.2 Comparison of experiment and simulation

In the following the results from the different techniques will be discussed with regard to their complementary information. From the in-situ tests the real projected area could be measured including all possible influences like adhesion etc. The simulations are based on results from tensile tests and incorporate the elastomeric deformation behavior of the material. Thus, comparison of results from these techniques with experimental data allows the separation of different sources of error and further the quantification of their individual contribution to the erroneous contact areas obtained from the Oliver & Pharr procedure.

The contact area values obtained from experiments, in-situ testing and simulations are plotted together in figure 66. The relative deviations of the experimental values after Oliver & Pharr from the in-situ testing results are also given in the plots of figure 66. For shallower depths below 1 µm the deviations were around 40 % and diminished to approximately 5 % for penetrations of several µm. The simulation results matched the experimental data quite well for displacements smaller than 3 µm, for higher displacements the increase in contact area was less, thus FEA and in-situ testing gave the same results.

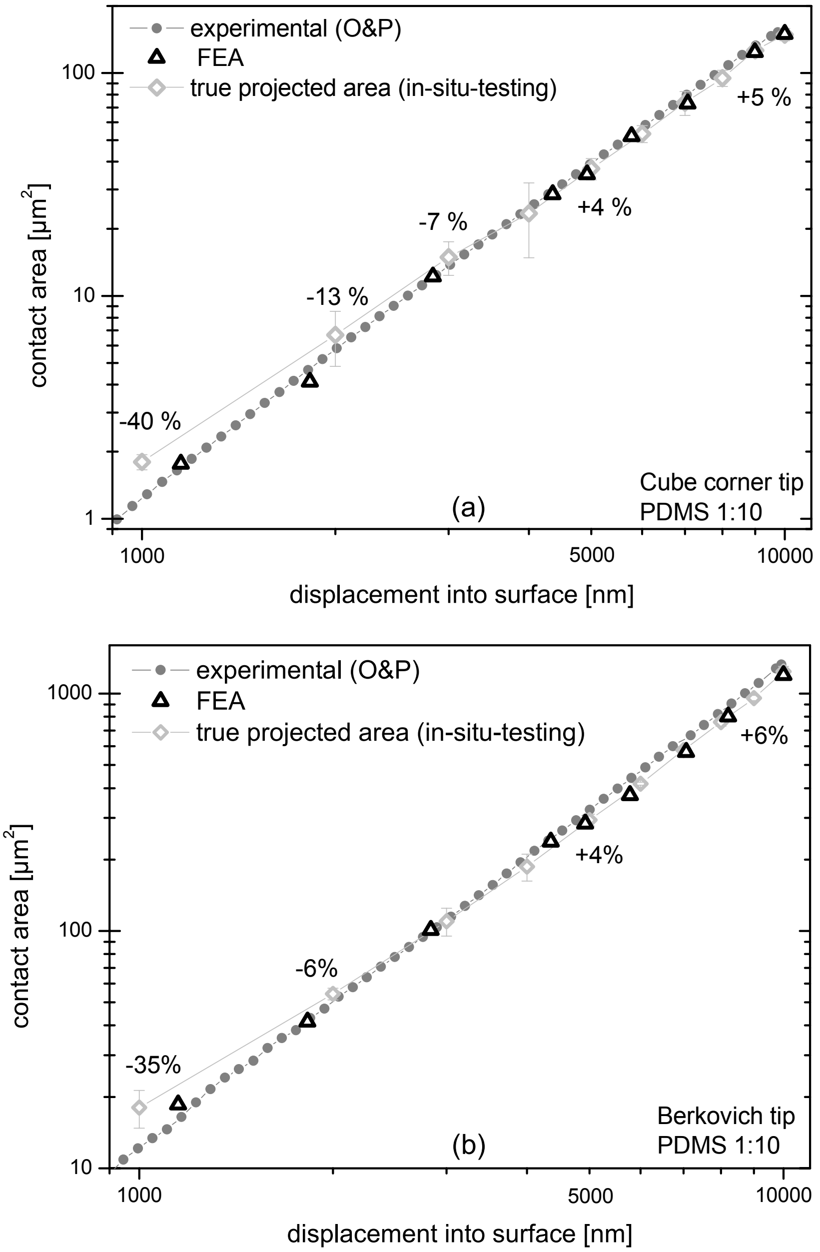

Figure 66: Comparison of contact area values from standard experiments (O & P = after Oliver & Pharr), in-situ indentation and simulations. (a) Cube corner and (b) Berkovich tip.

From these comparisons several important factors for the evolution of the contact during testing can be deduced. For very compliant materials like PDMS, surface detection plays a critical role and false surface detection can lead to erroneous calculations of the contact area. For the experiments in this study, this source of error can obviously be excluded, since the agreement between experiment and simulation for small depths confirms the accuracy of the measurements. For higher depths, experiment and simulation results deviated. As has been discussed in section 3, this could be attributed to the underestimation of the sink-in effect in the Oliver & Pharr calculations. This pronounced sink-in behavior was not only found in the FEA but also during the in-situ observation of the contact. This, in turn, proved the correct selection of the constitutive material model, which led to FE contact area results in agreement with the true contact areas observed in the in-situ tests.

Another important factor for the contact area determination for soft materials is adhesion. Due to attractive forces between the specimen and the tip the contact area can be enlarged [37]. The contribution of adhesion to the total contact area can be estimated from the comparison of the true contact areas from in-situ testing, which covered adhesive effects, and FEA, where adhesive forces have not been considered. For larger penetrations the results agreed well, thus it can be concluded that the adhesive contribution can be neglected. The formation of fringes during the in-situ tests and the strong sink-in effect further support this conclusion. However, the situation is quite different for shallow penetration depths, where the areas from in-situ testing are by 40% larger than from FEA. This difference must be related to adhesive effects.

Decisive for the amount of contact area increase due to adhesion are the range of attractive forces and the distance between the sample surface and the tip. As a rough estimate, it can be said that the additional contact area will be the region, where the distance between the tip and the surface is smaller than the range of the adhesive forces. From the snap-to-contact in the experimental load-displacement data, 20 nm were found to be a reasonable estimate for the range of adhesive forces between diamond and PDMS. Thus, the surface area separated less than 20 nm from the tip surface would be the additional contact area as a consequence of adhesion. This additional area closer than 20 nm can roughly be estimated from the surface profiles displayed in figure 60. Relative increases of 38 % and 30 % are obtained for the Berkovich and the cube corner, respectively, if the penetration depths are below 1 µm. For higher penetrations, the total contact area increased, therefore the relative portion of the additional area decreased to about 3 % for the Berkovich and to ~5% for the cube corner. Again the importance of the tip edges for the indentation process has to be underlined. As can be seen for the cone surface profile qualitatively, the sink-in is smaller; hence the additional area due to adhesive forces would be significantly larger for a cone compared to a pyramidal tip. As a consequence, the data from cone indentation would need to be corrected for adhesion, e.g. following [34-37], whereas the data measured with pyramidal tips can be used as measured.

In figure 67 the influence of the contact area on the resulting hardness and modulus is shown. For the grey curves the contact areas from in-situ testing have been used for the calculations instead of the experimental values after Oliver & Pharr.

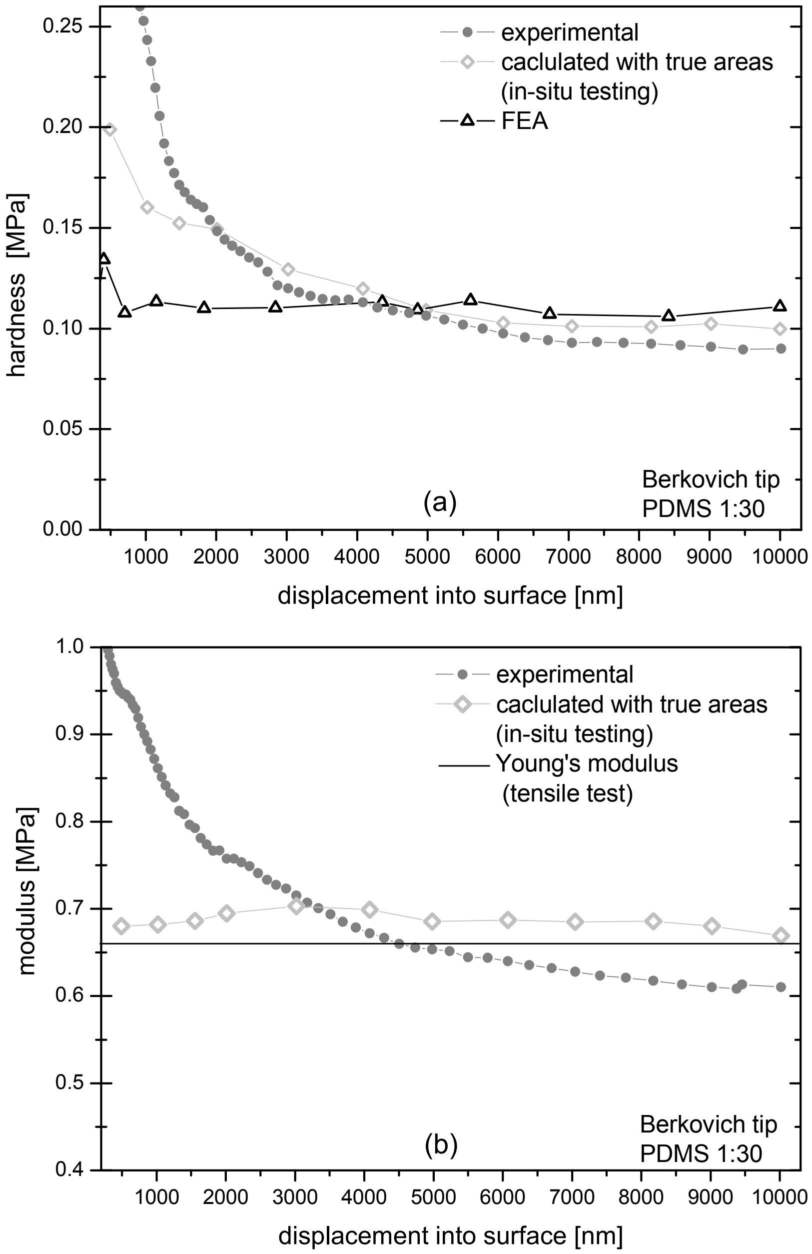

Figure 67: (a) Comparison of hardness values calculated with the contact areas from figure 12 (squares) and the contact areas from FEA (triangles). (b) Modulus calculated using the contact area values from figure 12. Using the true contact areas led to constant properties independent of penetration depth. The black line indicates the result obtained from the tensile tests performed for the fitting procedure.

The hardness and modulus are slightly increased compared to the experimentally determined values, because the contact areas are smaller. Yet, using the true areas for the calculation, constant properties throughout the displacement range are obtained, as it would be expected for a homogeneous and isotropic material. The hardness can be calculated from the FE results, since only contact area and load are necessary, which are both direct output variables from the simulations. The modulus cannot be accessed, because the stiffness is not available without additional calculations. However, regarding the good agreement between the load-displacement data and the contact area values, similar results as for the calculations using the in-situ results could be assumed. According to these results the modulus could be determined with a deviation of 7 % and the hardness was measured with approximately 10 % deviation with respect to in-situ testing.

7.5 Conclusions

In this study the indentation process for an elastomeric material was modeled using finite element simulations. Complementary, in-situ tests were performed for the determination of the true projected area. Comparison of simulations, in-situ testing results and experimental data led to the following conclusions:

- The PDMS behavior could successfully be described with a hyperelastic constitutive model based on the Neo-Hooke strain energy potential.

- The results for the 3D Berkovich model and the equivalent cone model deviated considerably, thus the equivalency of cone and Berkovich is not valid for elastomeric materials like PDMS. The deviations are attributed to the influence of the tip edges on the deformation field under the tip.

- The sink-in effect is more pronounced than predicted by Oliver & Pharr, therefore the experimentally determined contact areas are overestimated at higher penetrations.

- Adhesive effects significantly increase the contact area for shallow penetrations. Reasonable values for the contact areas with deviations around 5 % can be obtained above 2 µm. Data obtained from penetration depths below 1 µm should be corrected for adhesion.

- Viscoelasticity and time-dependent phenomena of polymeric materials can be captured, if dynamic indentation testing in the CSM-mode is used.

8 Summary and outlook

The focus of the work presented in this thesis was the improvement of nanoindentation methodologies in order to make nanoindentation a reliable technique for the mechanical characterization of soft and compliant materials, either polymeric or biological materials. The most complicated feature herein is the high compliance of these kinds of materials and the associated measurement of the very small forces during the testing. For biological materials also the limited amount of specimen material available and tissue hydration can be challenging issues. Anyway, the mechanical characterization of these kinds of materials is of great importance for medical and clinical applications as well as for fundamental research, thus the development of adequate testing methods is necessary. Nanoindentation is a well established technique for the characterization of engineering materials, not only for bulk but also for small volume samples. Therefore it is a promising technique that possesses the technical capabilities to overcome the difficulties associated with testing of soft materials.

As a first result of this study it was observed that the original testing protocols implemented in the nanoindenter software were not suitable for testing materials with elastic moduli below the GPa-regime and that the results could deviate by more than 400% from results obtained by tensile testing. These enormous errors were caused by failing surface detection, which leads to erroneous contact area measurements and hence wrong mechanical properties. To address this problem, the testing protocol was modified and improved through the definition of a new surface detection criterion, which reduced the error in surface identification from initially more than 1µm down to values in the range of 20-30 nm. The higher accuracy of the new criterion has been proven for various polymeric materials with elastic moduli ranging from several GPa down to 1 MPa. The nanoindentation method with the modified surface detection criterion delivered consistent and reproducible results for all polymeric materials tested and was capable of sensing very small modifications in mechanical properties of polymers. In order to achieve a verification of the mechanical properties determined by nanoindentation, comparative tensile tests on the same set of polymers were carried out. The biggest deviation in the modulus values that was obtained from this comparison was no larger than ~ 8%. This proved the big improvement of surface detection accuracy once again.

In order to identify the origin of the small, but still existing errors in the nanoindentation results, further investigations focused on different ways to quantify the contact area. False surface detection is not the only issue that can lead to erroneous contact areas. Especially for soft materials several other factors are known to affect the contact area, yet automated experimental techniques cannot always account for them. In this respect, particularly the material deformation behavior, adhesion and viscoelastic effects need to be considered.

In order to access these issues experimentally, in-situ testing is a helpful a tool, since this allows the visualization of the scenes /properties of interest. For investigating the contact and its evolution during an indentation two different in-situ techniques were applied. The first technique was testing inside a SEM, which delivers a side view of the contact and thus valuable information on the deformation mechanism of the specimen material. Also a semi-quantitative determination of the contact size is possible. In the second in-situ setup light-microscopic contact observation through a transparent sample and perpendicular to the surface was used. Form this method the projected contact area, which is necessary for the evaluation of indentation data, is directly accessible. Thus, the two in-situ techniques are highly complementary. For comparative reasons and in order to gain a deeper insight in the deformation processes during indentation, finite element simulations were performed. With the help of simulations a parameter study (variation of the elastic modulus and Poisson's ratio) could be used for investigating the effects of changing parameters on the indentation data. Further, the true contact area and the amount of sink-in have been calculated.

The combination of the results from in-situ experiments and from simulations can be summarized as follows: The deformation mechanisms of elastomeric materials can clearly be distinguished from the behavior of elastic-plastic materials like metals or ceramics. Since the common analysis procedure for indentation data, e.g. the Oliver & Pharr method, is based on elastic-plastic material behavior, the mechanical properties measured by indentation deviate from those determined by other techniques. The different deformation behavior of elastomers gives rise to errors in the contact area determination. These errors are most significant for shallow indentations, where the contribution of adhesive forces is not taken into account; therefore the true contact areas are about 30 to 40% larger than calculated by the Oliver & Pharr method. For larger penetrations the deviations are below 10%, but in this case the true contact areas tend to be larger due to a pronounced sinking-in.

The work presented in this thesis focused on indentation methodologies for investigating very soft, highly elastic polymers. It has been shown that the mechanical properties of such materials can be obtained from indentation testing with reasonable accuracy. The limitations of current indentation equipment/techniques become obvious for shallow indentation testing below 1µm and for materials with moduli below 0.5 MPa. Under these conditions, the technical limits of current indentation systems are reached and indentation testing can not be considered as reliable. Thus, further technical improvements are necessary for indentation of softer materials. Additionally, more robust set-ups, which allow indentation testing under liquids, are needed for the characterization of biological specimens, because the hydration state influences strongly the properties of biological materials. Two obvious requirements in this direction are the construction of closed indentation systems on one hand, which can be used in connection with liquids or under vacuum. One the other hand a less stiff tip support would be beneficial, since this would increase the load resolution and facilitate surface detection.

Another interesting issue in terms of a possible application of this technique to biological specimens is to clarify the influence of constraining effects on the mechanical behavior, since biological materials are often composite materials. This could be studied on a polymeric model system again and results could be transferred to biological systems. For this purpose a similar approach as to thin film testing would be needed in order to deconvolute the contributions of the individual composite components. The only difference would be to constrain the components in 3 dimensions instead of constraining them in 1 dimension (thin film approach). Such an investigation should contribute a lot to the understanding and interpretation of data obtained from biological samples, which is of great importance for many different medical and scientific purposes.

9 Deutsche Kurzfassung

9.1 Motivation und Literaturübersicht

Die Methode der Nanoindentation hat sich in den vergangenen beiden Jahrzehnten stark entwickelt. Technische Neuerungen ermöglichen heute einen breiten Einsatz dieser Methode für die mechanische Charakterisierung unterschiedlichster Materialien. Ein wesentliches Merkmal der Nanoindentation ist die sehr hohe Kraft- und Wegauflösung, die moderne Geräte besitzen. Dadurch eröffnet sich ein breites Feld von Einsatzmöglichkeiten im Vergleich zur konventionellen Härteprüfung oder Zug/Druckversuchen und Biegetests. Besonders Interesse ruft diese Technik im Polymer-Bereich [2-8] sowie in der Bio- und Medizintechnik [9-11] hervor. Hier handelt es sich oft um weiche und nur in sehr geringen Mengen verfügbaren Substanzen, deren Eigenschaften mit Hilfe von Nanoindentation untersucht werden sollen. Leider kann die Nanoindentation bislang nur für steifere Werkstoffe als zuverlässig angesehen werden, da bei weicheren Materialien verschiedene Effekte auftreten, die die Ergebnisse aus Indentationsversuchen stark beeinflussen können. Im Folgenden sollen diese Effekte, die dadurch entstehenden Probleme und mögliche Lösungsansätze anhand eines kurzen Literaturüberblicks näher erläutert werden.

Um Nanoindentation erfolgreich für die Charakterisierung von Materialien anwenden zu können, deren E-Moduli im MPa-Bereich oder darunter liegen, ist vor allem die Kraftmessung eine große Herausforderung. Die Maximalkräfte, die typischerweise beim Indentieren von polymeren Materialien auftreten, sind einige Hundert µN. Die Kräfte bei der Kontaktbildung zwischen Spitze und Probenoberfläche liegen meist im nN-Bereich [2, 4, 6]. Diese geringen Kräfte müssen genau gemessen werden, um die Position der Probenoberfläche zu ermitteln. Die genaue Bestimmung der Oberflächenposition ist wichtig, da an der Probenoberfläche die Nullposition der Kraft- und Wegmessung festgelegt werden. Die meisten kommerziellen Geräte bieten zwar theoretisch eine ausreichend Kraftauflösung, in der Praxis jedoch können Kräfte meist nur mit einer Genauigkeit von etwa 50-100 nN gemessen werden [2, 16]. Dies ist bedingt durch externe Störungen wie z.B. Temperaturschwankungen. Durch Fehler bei der Detektion der Probenoberflächen ergeben sich Folgefehler bei der Berechnung der Kontaktfläche [23, 24] und somit der mechanischen Kennwerte [12, 31].

Die Kontaktfläche A_c wird direkt für die Berechnung der mechanischen Kenngrößen benötigt. Eine möglichst genaue Bestimmung der Kontaktfläche ist daher von entscheidender Bedeutung. Im Experiment kann sie jedoch nicht direkt gemessen werden, sondern wird indirekt berechnet, meist nach der Oliver & Pharr Methode [12, 31]. Zunächst erfolgt die Kalibrierung der Spitzengeometrie, bei der eine Flächenfunktion A(h) bestimmt wird. A ist dabei die Querschnittsfläche der Pyramide und h der senkrechte Abstand von der Spitze des pyramidalen Indenters. Anhand dieser Flächenfunktion kann dann für jede Eindringtiefe h die Kontaktfläche A_c berechnet werden. Allerdings muss hierbei beachtet werden, dass als Standardmaterial für die Kalibrierung Quarzglas verwendet wird, was um Größenordnungen steifer ist als Polymere und ein kompliziertes mechanisches Verhalten aufweist. Daher stellt sich die Frage, in wie weit die aus dieser Methode gewonnen Flächenfunktion für Messungen an polymeren Proben übertragbar ist [2, 4, 6, 23]. Trotz intensiver Bemühungen [2, 4] ist es bisher nicht gelungen, ein Polymer als Standard zu etablieren.

Im Falle von weichen Materialien treten weitere Effekte auf, die bei der Bestimmung der Kontaktfläche berücksichtigt und ggf. mit in die Berechnung einbezogen werden müssen. Als erstes ist dabei Adhäsion zu nennen. Durch attraktive Wechselwirkungskräfte zwischen Spitze und Probe kann sich die Kontaktfläche vergrößern, was vor allem bei geringen Eindringtiefen eine Rolle spielt. Verschiedene Gruppen haben sich mit diesen Adhäsions-Effekten beschäftigt und diverse Ansätze vorgestellt, wie man der Adhäsion bei der Kontaktflächenermittlung Rechnung tragen kann [33-36]. Gemein ist all diesen Ansätzen, dass sie auf der Johnson-Kendall-Roberts (JKR) Theorie beruhen [37], die adhäsive Kräfte in ein kontaktmechanisches Model einbindet.

Ein weiteres polymertypisches Phänomen ist Viskoelastizität. Viskoelastizität bezeichnet das Auftreten eines zeitabhängigen Deformationsverhaltens. Die elastischen Eigenschaften sind also dehnraten- bzw. frequenzabhängig. Auf molekularer Ebene lässt sich dieses Phänomen mit der makromolekuraren Natur der Polymere erklären. Die Kettenmoleküle benötigen eine gewisse Zeit, um der aufgebrachten Deformation folgen zu können. Daher erhält man für Polymere meist einen Anstieg des E-Moduls mit steigender Deformationsgeschwindigkeit. Um diese Effekte phänomenologisch zu erfassen und zu beschreiben, benutzt man häufig Federn bzw. Dämpfer und deren klassische Kombinationen [38] in Serie (Maxwell-Element) und in Reihe (Kelvin-Voigt-Element). Um das Indentationsverhalten von verschiedenen Polymermaterialien zu modellieren, wurden in der Literatur viele mögliche Kombinationen aus Federn und Dämpfern vorgestellt [26, 29]. Es wurden sogar quadratische Elemente verwendet, um viskos-elastisch-plastisches Verhalten zu beschreiben. Während eines

Indentationstest führt das verzögerte Auftreten von Deformation beim Entlasten zur Ausbildung einer sogenannten „Nase“, d.h. zu überhöhten oder im Extremfall negativen Steigungen der Last-Eindringtiefe-Kurven [27]. Für die Auswertung wird aber gerade diese Steigung der Entlastungskurve benötigt, da sie die elastische Rückfederung des Materials widerspiegelt und somit die Berechnung des E-Moduls ermöglicht [25, 27]. Dieses Verfahren ist bei Auftreten der „Nase“ stark fehlerbehaftet. Es wird daher üblicherweise ein ausreichend langes Haltesegment unter Maximallast eingefügt, um alle viskosen Effekte abklingen zu lassen. Entlastet wird so rasch wie möglich, so dass nur spontane, jedoch keine verzögerten Prozesse ablaufen können [22-24]. Eine andere Möglichkeit, viskose Effekte zu umgehen, bietet die Continuous Stiffness Measurement (CSM) Methode, bei der mit oszillierender Spitze dynamisch gemessen wird. Mit dieser Methode konnten für verschiedene Proben Speicher- und Verlustmoduli gemessen werden, die gut mit Literaturwerten übereinstimmen [2, 4, 6-8, 23].

Simulationen des Indentationsprozesses [39-60] stellen eine hilfreiche und sinnvolle Ergänzung zu experimentellen Arbeiten dar, da sie die Möglichkeit bieten, experimentell nicht zugängliche oder nur mit großem Aufwand messbare Parameter zu untersuchen. So wird die Finite Elemente Methode (FEM) häufig eingesetzt, um Kontaktflächen für verschiedene Materialien zu bestimmen [40, 45, 51, 52] oder Spannungsfelder zu berechnen, die sich unter der Indenterspitze ausbilden [46-48]. Ein großes Potential besteht auch deshalb, da bei Simulationen einzelne Parameter systematisch variiert werden können und somit deren Einfluss optimal untersucht werden kann, wie z.B. die Oberflächenrauhigkeit der Probe [39], die Indentergeometrie [43, 44] oder das sink-in oder pile-up-Verhalten unterschiedlicher Materialien [45-48].

Im Rahmen dieser Arbeit wurden Nanoindentationsexperimente an verschiedenen Polymeren durchgeführt. Um ein besseres Verständnis des Indendationsprozesses bei Polymeren zu erlangen und den Einfluss von Viskoelastizität sowie Adhäsion auf die Bestimmung der Kontaktfläche zu beurteilen, wurden in-situ-Versuche durchgeführt, ergänzt von Finite Elemente Simulationen. Die Erkenntnisse aus diesen Arbeiten konnten soweit umgesetzt werden, dass die Charakterisierung von Materialien mit E-Moduli unter 1 MPa nun möglich ist.

9.2 Ergebnisse und Diskussion

In diesem Abschnitt sollen die wesentlichen Ergebnisse und Erkenntnisse der Arbeit zusammengefasst werden. Dem Aufbau der Dissertation entsprechend werden die Arbeiten zu den unterschiedlichen Themengebieten im Folgenden in einzelnen Kapiteln dargestellt.

9.2.1 Oberflächenfindung bei weichen Polymeren

Im Ablauf eines Indentationstests stellt die Bestimmung der Position der Probenoberfläche den entscheidenden Schritt für das Gelingen des Tests dar. An der Probenoberfläche beginnt die eigentliche Indentation, an dieser Stelle werden die Nullpunkte der Kraft- und Wegmessung gesetzt. Eine falsche Oberflächenposition führt konsequenterweise zu Fehlern in allen zur Auswertung notwendigen Messgrößen. Im Fall von weichen, z.B. polymeren Materialien ist die Erkennung der Oberfläche problematisch, da die Kräfte sehr gering sind, oft kaum größer als das durch externe Vibrationen bedingte Rauschen. Daher wird die Oberfläche meist erst nach einem gewissen Eindringen der Spitze in das Material, also „zu spät“ detektiert. Dies bedingt die Aufnahme von zu hohen Kräften und zu geringen Kontaktflächen, folglich ergeben sich zu hohe E-Modul- und Härtewerte. Durch die in diesem Kapitel vorgestellten Arbeiten konnte gezeigt werden, dass die E-Moduli und Härtewerte für PDMS um 400 % von dem aus Zugversuchen bestimmten Wert abwichen, wenn mit der bestehenden Oberflächenfindungsmethode gemessen wurde. Dies entsprach einem Fehler von 5 µm in der Oberflächenposition, wobei eine maximale Eindringtiefe von 1 µm programmiert war und erreicht werden sollte. Diese enorme Abweichung macht deutlich, dass die Oberflächenfindung die weitaus größte Fehlerquelle darstellte und deshalb zunächst ein für die Oberflächendetektion bei weichen Materialien geeignetes Kriterium gefunden werden musste.

In kommerziellen Geräten können zwei Strategien zur Oberflächenerkennung unterschieden werden. Bei der einfacheren Methode wird lediglich eine Vorlast definiert, bei deren Erreichen die Kontaktbildung angenommen wird. Unabhängig von den Eigenschaften des Probenmaterials sind Vorlasten im Bereich einiger µN üblich. Die andere Methode benötigt einen rückgekoppelten Steuerkreis, der dynamische Messungen mit oszillierender Spitze ermöglicht. Hierbei wird die Steigung der quasi-statischen Last-Weg-Kurve gemessen und für die Oberflächenerkennung wiederum ein Schwellwert festgelegt. Mit beiden Methoden wurden Messungen an PDMS (E-Modul ca. 1 MPa) durchgeführt und die erhaltenen Last-

Eindringtiefekurven wurden mit den Ergebnissen von Finite Elemente Simulation verglichen. Dieser Vergleich ergab, dass beide Methoden unzulänglich sind, um die Oberfläche mit ausreichender Genauigkeit zu detektieren. Daher wurden verschiedene Messgrößen als mögliche, alternative Kriterien ausgewählt, die in Zusammenhang mit der Spitzenoszillation stehen. Dies waren die Kraftamplitude, der Phasenwinkel und die dynamische Kontaktsteifigkeit. Diese dynamischen Messgrößen scheinen eher geeignet, da sie ein wesentlich geringeres Signal-Rausch-Verhältnis zeigen als die quasi-statischen Größen. Die Eignung dieser Messgrößen für die Oberflächendetektion wurde durch eine Testreihe an PDMS überprüft, die ergab, dass mit der dynamischen Kontaktsteifigkeit die größte Genauigkeit erzielt werden konnte. Als neues Oberflächenfindungs-Kriterium wurde ein Schwellwert von 2 N/m für die dynamische Kontaktsteifigkeit festgelegt. Durch Anwendung dieses Kriteriums konnte die Oberfläche bis auf eine Genauigkeit von etwa 30 nm detektiert werden.

Die verbesserte Methode wurde nun vergleichend mit der ursprünglichen Methode zur Charakterisierung verschiedener polymerer Materialien mit bekannten Eigenschaften angewendet. Diese Materialien wurden so gewählt, dass sie einen möglichst breiten E-Modul Bereich (von ca. 300 MPa bis ca.4,5 GPa) abdecken. Für alle untersuchten Polymere ergaben sich auf Basis der Oberflächenfindung über die dynamische Kontaktsteifigkeit kleinere Härte- und E-Modul-Werte. Diese wiesen eine geringere Abweichung von den erwarteten Werten, d.h. den von den Herstellerfirmen angegebenen Werten auf. Somit war bestätigt, dass die Genauigkeit der Indentationsergebnisse durch die verbesserte Oberflächendetektion erhöht werden konnte.

9.2.2 Untersuchung der Vernetzungskinetik von PDMS

PDMS ist ein Material, dass sich durch seine hohe Beständigkeit gegenüber Chemikalien, Witterungseinflüssen und Temperaturschwankungen, durch optische Transparenz sowie durch einen sehr hohen elektrischen Widerstand auszeichnet, weshalb es verstärkt als Isolier- und Beschichtungsmaterial verwendet wird. Durch seine Biokompatibilität wird es auch häufig für biomedizinische Anwendungen z.B. als Werkstoff für Gewebeimplantate eingesetzt. Trotz dieser breit gefächerten technologischen Anwendungen sind die mechanischen Eigenschaften von PDMS nur wenig untersucht. Im Besonderen ist bekannt, dass PDMS altert. Dies ist bedingt durch eine unvollständige Vernetzung bei der Herstellung und den weiter fortschreitenden Vernetzungsprozess im Laufe der Zeit. Dieses Phänomen führt zu deutlichen

Änderungen in den Eigenschaften und im Verhalten des Materials. Dies ist bisher nicht quantitativ untersucht worden. Um diese Lücke zu schließen, wurde eine systematische Untersuchung der mechanischen Eigenschaften von PDMS-Proben durchgeführt, die zum einen unter-schiedliche Vernetzungsgrade aufwiesen; zum anderen wurde die Entwicklung der mechanischen Kenngrößen als Funktion der Auslagerungsdauer und Auslagerungstemperatur gemessen.

Als Methoden zur mechanischen Charakterisierung kam neben Nanoindentation auch Mikrozugprüfung zum Einsatz. Dies bot zum einen eine Möglichkeit, die durch Nanoindentation erhaltenen Ergebnisse durch unabhängige Messungen zu verifizieren; zum anderen wurden anhand der Zugversuche die Querkontraktionszahlen der Proben bestimmt. Dafür wurde auf die Probenoberfläche eine rautenförmige Markierung aufgebracht und diese während des Versuchs gefilmt. Daraus konnten die Dehnungen sowohl in Zugrichtung als auch quer dazu bestimmt und so die Poissonzahl errechnet werden. Durch dynamische Nanoindentation wurden neben der Härte die viskoelastischen Größen Speicher- und Verlustmodul bestimmt.

Im Rahmen dieser Studie wurden Proben mit 8 verschiedenen Vernetzungsgraden untersucht, die folgende Zusammensetzung (Gewichtsverhältnis Vernetzer zu Oligomeren) hatten: 1:2, entsprechend 33 Gew % Vernetzer, 1:3 (25 Gew %), 1:5 (16 Gew %), 1:7 (12.5 Gew %), 1:10 (9 Gew %), 1:20 (5 Gew %), 1:30 (3 Gew %), und 1:40 (2,4 Gew %). Zur Messung der Eigenschaften als Funktion der Auslagerungsdauer wurden die Zusammensetzungen 1:2, 1:10 und 1:30 verwendet. Die Messungen ergaben, dass die E-Moduli dieser Proben einen Bereich von fast 2 Größenordungen abdecken und durch Variation des Vernetzungsgrades E-Moduli zwischen ~0.3 MPa und ~20 MPa erhalten werden können. Des Weiteren wurde festgestellt, dass sich durch Auslagerung der E-Modul einer Probe um ein Vielfaches erhöht. Bei PDMS 1:2 wurde so im vollständig vernetzten Zustand das 10-fache des Ausgangswertes erreicht. Die gemessenen Poissonzahlen lagen im Bereich zwischen 0,39 und 0,48, und waren damit deutlich niedriger als 0,5, was für elastomere Materialien erwartet wird. Ferner konnte eine klare Abhängigkeit der Querkontraktion von der Vernetzungsdichte festgestellt werden. Je stärker vernetzt das PDMS, desto geringer war die Querkontraktion. Der Vergleich zwischen den Ergebnissen der Zugversuche und den Indentationsergebnissen ergab eine gute Übereinstimmung der Resultate, die maximale Abweichung betrug 8 %.

9.2.3 In-situ Indentation von Elastomeren

Die Bestimmung der Kontaktfläche stellt eine der wesentlichen Herausforderungen bei der Durchführung von Nanoindentationsmessungen dar. Üblicherweise wird für die Bestimmung der Kontaktfläche die von Oliver und Pharr entwickelte Methode [12, 31] angewendet. Diese Methode wurde ursprünglich für Materialien entwickelt, die ein elastisch-plastisches Verformungsverhalten zeigen, also für Metalle oder Keramiken. Für weichere, hochelastische Materialien muss folglich genau überprüft werden, in wie weit die der Oliver & Pharr Methode zugrunde liegenden Annahmen bezüglich des Deformationsverhaltens übertragbar sind. Bisher gibt es hauptsächlich theoretische Studien darüber, wie sich Elastomere unter einer Indenterspitze verhalten und wie das Material verformt wird. Die Kenntnis der Verformung während eines Indentationstests stellt allerdings einen wichtigen Schritt zum Verständnis des Indentationsprozesses dar und ist unabdingbar für eine korrekte Bestimmung der Kontaktfläche. Experimentell ist die Beobachtung des tatsächlichen Verformungsverhaltens durch In-situ Indentationsexperimente möglich.

Für die Durchführung von In-situ Indentationsexperimenten in einem Rasterelektronenmikroskop (REM) wurde wiederum PDMS als elastomeres Material herangezogen. Da PDMS elektrisch isolierend ist, wurden die Proben für die Untersuchungen mit einer sehr dünnen Au-Pd-Schicht überzogen, um eine leitfähige Oberfläche zu erhalten und Aufladungseffekte unter dem Elektronenstrahl zu vermeiden. Während des Beschichtungsvorganges waren kleine Bereiche der Probe abgedeckt, so dass diese ohne Beschichtung blieben. Diese unbeschichteten Bereiche wurden benutzt, um die Eindrücke auf diesen freien Oberflächen setzen zu können. Wie sich in Vorversuchen mit vollständig beschichteten Proben gezeigt hatte, wird das Deformationsverhalten durch die Schichtdicke des Au-Pd bestimmt, was natürlich unerwünscht ist. Durch die teilweise beschichteten Proben konnte dieses Problem jedoch gelöst werden und die Deformation von PDMS konnte beobachtet werden. Aus Beobachtungen konnte geschlossen werden, das PDMS ein deutlich ausgeprägtes Einsink-Verhalten zeigt und dass sich durch die Einwirkung des Elektronenstrahls eine permanente Deformation ergibt. Je länger die Bestrahlung mit dem Elektronenstrahl andauerte, desto größer waren die bleibenden Eindrücke. Es konnte aber mittels AFM-Messungen bestätigt werden, dass unter atmosphärischen Bedingungen keine bleibenden Eindrücke entstehen. Des Weiteren konnte ausgeschlossen werden, dass der Elektronenstrahl das Verformungsverhalten beeinträchtigt.

Zur Ermittlung der Kontaktfläche wurde der Indentationsprozess mittels der Finite Elemente (FE) Methode simuliert. Um die Simulationsergebnisse mit den In-situ Experimenten abzugleichen, wurde jeweils die maximale Indenterquerschnittsfläche bestimmt, die durch den Kontakt an den Kanten des Indenters festgelegt wird. Diese Fläche kann sowohl aus den In-situ Experimenten berechnet werden als auch aus der Simulation. Der Vergleich der Ergebnisse aus beiden Methoden ergab eine gute Übereinstimmung. Dies lässt darauf schließen, dass sich aus der Simulation auch verlässliche Werte für die tatsächliche Kontaktfläche ergeben. Als wichtiges Ergebnis dieser Arbeiten zeigt sich, dass die aus der FE-Simulation erhaltenen Werte für die Kontaktfläche im Vergleich zu den mit der Oliver & Pharr Methode bestimmten Kontaktflächen um ca. 8 % kleiner waren. Dies war ein überraschendes Resultat, da oftmals davon ausgegangen wird, dass sich aus der Oliver & Pharr Methode zu kleine Werte für die Kontaktfläche ergeben.

9.2.1 Kontaktflächenbestimmung bei Elastomeren

Der Schwerpunkt dieses Kapitel lag auf einer quantitativen Bestimmung der Kontaktfläche während der Indentation von weichen, elastomeren Materialien. Mit Hilfe von Finite Elemente Simulationen (ABAQUS Version 6.6, ABAQUS Inc., Providence, RI, USA) wurde die Kontaktausbildung sowie das Verformungsverhalten von PDMS untersucht. Zunächst waren ausführliche Vorabreiten erforderlich, um die Verlässlichkeit der Simulationsergebnisse zu gewährleisten. So wurden mehrere Materialmodelle verglichen, die zur Beschreibung von hyperelstischem, d.h. elastomerem Materialverhalten in ABAQUS benützt werden können. Des Weiteren wurde untersucht, wie die Vernetzungsdichte und die Ordnung der Elementansatzfunktion die Ergebnisse beeinflussen. Die Erkenntnisse aus diesen Arbeiten führten zu einer Vernetzung mit linearen Elementen, die im Kontaktbereich graduell feiner wurde. Als Materialgesetz wurde ein hyperelastisches Modell der Neo-Hooke'schen Form ausgewählt.

Dieses FE- Modell wurde nun verwendet, um die Indentation mit verschiedenen Spitzengeometrien (Cube corner, Berkovich und flächengleicher Kegel) zu simulieren. Für die pyramidalen Spitzen ergaben die Simulationen Kraft-Eindringkurven, die sehr gut mit den experimentell gemessenen Daten übereinstimmten. Im Gegensatz dazu wurden für die Kegelgeometrie deutlich geringere Kräfte erhalten. Laut Theorie sollten die Berkovich-Spitze und ein Kegel mit gleichem Verhältnis von Höhe zu Querschnittsfläche (flächengleich) die selben Ergebnisse liefern [15]. Daher ist es in der Praxis üblich, für Simulationen die Kegelgeometrie zu verwenden anstatt der pyramidalen Geometrie. Wie sich anhand unserer Ergebnisse zeigte, ist dieses Vorgehen jedoch nicht immer gerechtfertigt. Vor allem bei rein elastischen Materialien treten Unterschiede zwischen Berkovich und Kegel auf. Dies ist zurückzuführen auf die Kanten der pyramidalen Spitze, die den Verformungszustand der Probe wesentlich beeinträchtigen. Eine Folge der Kanten ist z.B: das starke Einsinken des Materials um die Spitze. Aus den Simulationsergebnissen zeigte sich, dass das Einsinken bei der Berkovich-Spitze deutlich ausgeprägter ist als beim Kegel. Folglich stimmten auch die Kontaktflächen der beiden Spitzengeometrien nicht überein, beim Kegel ergaben sich höhere Werte. Des Weiteren konnte durch das Einsinkverhalten auch die Diskrepanz zwischen den experimentell ermittelten und den aus der Simulation erhaltenen Kontaktflächen erklärt werden. In der Oliver & Pharr Methode für die Berechnung der Kontaktfläche wird das Einsinken ebenfalls unterschätzt, daher sind die Kontaktflächen zu groß.

Um die projizierte Kontaktfläche experimentell zugänglich zu machen, wurde ein spezieller Messaufbau für die Durchführung von In-situ Versuchen entwickelt. Mit diesem Messaufbau kann der Kontakt zwischen Spitze und Probe während des gesamten Eindruckversuches lichtmikroskopisch beobachtet werden. Dabei wird senkrecht zur Probenoberfläche durch die transparente Probe hindurch beobachtet. Dies ermöglichte erstmals die genaue experimentelle Bestimmung der Kontaktfläche und eine quantitative Untersuchung von Adhäsions- und Viskoelastizitäts-Effekten. Viskoelastizität bedeutet ein zeitlich verzögertes Auftreten der Probendeformation gegenüber dem Eindringen der Spitze. Die resultierende Kontaktfläche ist folglich kleiner als die durch die Flächenfunktion berechnete Kontaktfläche. Je schneller die Belastung erfolgt, desto größer sollte die Differenz zwischen wahrer und berechneter Kontaktfläche werden. Dies konnte durch die in-situ-Versuche bestätigt werden. Eine Erhöhung der Belastungsrate um das 200-fache führte zu einer Verkleinerung der Kontaktfläche um ca. 20 %. Aus den Standard-Indentationsmessungen ergab sich qualitativ die selbe Veränderung der Kontaktfläche mit der Belastungsrate. Die absoluten Werte waren im Vergleich zu den In-situ Messungen etwas zu hoch. Diese Abweichungen lagen wie zuvor im Einsink-Verhalten begründet, das sich bereits in den Simulationen zeigte und nun durch die In-situ Ergebnisse bestätigt werden konnte. Trotz dieser Abweichungen konnte mit diesen Ergebnissen bestätigt werden, dass die Messung und Quantifizierung von Viskoelastizität mittels Nanoindentation prinzipiell möglich ist.

Durch Vergleich der Ergebnisse aus Simulationen und in-situ Versuchen konnte der Einfluss von Adhäsion auf die Kontaktfläche bestimmt werden. Im Bereich kleiner Eindringtiefen lagen die In-situ Ergebnisse beträchtlich höher als die FE-Ergebnisse. Bei Eindringtiefen von einigen µm stimmten die Resultate aus beiden Methoden sehr gut überein. Des Weiteren ergaben sich bei kleinen Eindringtiefen aus den Simulationen und aus den Experimenten (Oliver & Pharr) ähnliche Werte für die Kontaktfläche. Da Adhäsion lediglich bei den In-situ Versuchen erfasst wurde, jedoch bei FEM sowie bei der Oliver & Pharr Methode unberücksichtigt blieb, konnte die höhere Kontaktfläche in den In-situ Versuchen auf die Wirkung von adhäsiven Kräften zurückgeführt werden. Die Erhöhung durch Adhäsion betrug etwa 30 bis 40 %. Als Faustregel konnte abgeleitet werden, dass die erhöhte Kontaktfläche berücksichtigt werden muss, wenn Daten bei Eindringtiefen unter 2 µm gemessen wurden, oberhalb dieser Tiefe kann der Einfluss von Adhäsion vernachlässigt werden.

10 References

[1] K. Herrmann, P. Strobel, and A. Stibler: Neues Härtemessverfahren für sehr weiche Elastomere, Materialprüfung 44 (2003) 83–86

[2] M.R. VanLandingham, J.S. Villarrubia, W.F. Guthrie, and G.F. Meyers: Nanoindentation of Polymers: An Overview, Proceedings of 220th American Chemical Society National Meeting, Macromolecular Symposia, Washington D.C., (2001) 15-43

[3] S.A. Hayes, A.A. Goruppa, and F.R. Jones: Dynamic nanoindentation as a tool for the examination of polymeric materials, J. Mater. Res. 19 (2004) 3298-3306

[4] G.M. Odegard, T.S. Gates, and H.M. Herring: Characterization of Viscoelastic Properties of Polymeric Materials through Nanoindentation, Exp. Mech. 45 (2005) 130–136

[5] Z. Li, J.C.M. Brokken-Zijp, and G. deWith: Determination of elastic moduli of silicone rubber coatings and films using depth-sensing indentation, Polymer 45 (2004) 5403-5406

[6] C.C. White, M.R. VanLandingham, P.L. Drzal, N-K. Chang, and S-H. Chang: Viscoelastic Characterization of Polymers Using Instrumented Indentation. II. Dynamic Testing, J. Polym. Sci. B: Polym. Phys. 43 (2005) 1812–1824

[7] J-L. Loubet, B.N. Lucas, and W.C. Oliver: Some Measurements of Viscoelastic Properties with the Help of Nanoindentation, NIST Special Publication 896, Proceedings of International Workshop on Instrumented Indentation, San Diego, Ca, USA (1995) 31–34

[8] J-L. Loubet, W.C. Oliver, and B.N. Lucas: Measurement of the loss tangent of low-density polyethylene with a nanoindetation technique, J. Mater. Res. 15 (2000) 1195–1198

[9] T. Jamsa, J.-Y. Rho, Z. Fan, C.A. Mackkay, S.C. Marks Jr., and J. Tuukkanen: Mechanical properties in long bones of rat osteoporotic mutations, J. Biomech. 35 (2002) 161-165

[10] J. L. Cuy, A. B. Mann, K. J. Livi, and M. F. Teaford: Nanoindentation mapping of the mechanical properties of human molar tooth enamel, Archs. Oral Biol. 47 (2002) 281-291

[11] M.E. Dickinson and A.B. Mann: Nanomechanics and chemistry of caries-like lesions in dental enamel, Mechanical Properties of Bioinspired and Biological Materials Symposium, Mater. Res. Soc., Warrendale, PA, USA (2005) 59-64

[12] W.C. Oliver and G.M. Pharr: An improved technique for determining hardness and elastic modulus using load and displacement sensing indentation experiments, J. Mater. Res. 7 (1992) 1564-1583

[13] H. Hertz: Über die Berührung fester elastischer Körper, J. für die reine und angew. Mathematik 92 (1881) 156-171

[14] J. Boussinesq: Application des Potentials à l'Étude de l'Équilibre et du Mouvement des Solides Élastiques, Gauthier-Villard, Paris (1885).

[15] I.A. Sneddon: The relation between load and penetration in the axissymmetric Boussinesq problem for a punch of arbitrary profile, Int. J. Eng. Sci. 3 (1965) 47-57

[16] A.C. Fischer-Cripps: Nanoindentation, Springer-Verlag, New York, (2002) ch. 9, 142

[17] A.C. Fischer-Cripps: Nanoindentation, Springer-Verlag, New York, (2002) ch. 7, 100

[18] H. Bei, E.P. George, J.L. Hay, and G.M. Pharr: Influence of Tip Geometry on Elastic Deformation during Nanoindentation, Phys. Rev. Lett. 95 (2005) 45501-1 – 45501-4

[19] W.W. Gerberich, J.C. Nelson, E.T. Lilleodden, P. Anderson, and J.T. Wyrobek: Indentation induced dislocation nucleation: the initial yield point, Acta Mater. 44 (1996) 3585-3598

[20] E.J. Berger, S. Tripathy, K. Vemaganti, Y.M. Kolambkar, H.X. You, and K. Courtney: An atomic force indentation study of biomaterial properties, Proceedings of World Tribology Congress III, Washington, D.C., USA (2005) 63244

[21] H. Wang and Y. Fan: The compressive strength, tensile strength, flexural strength and micro-hardness of Plat-II Castable Ceramics, J. West China Univ. Med. Sci. 28 (1997) 349-352

[22] K.Y. Lee and D.J. Mooney: Hydrogels for tissue engineering, Chem. Rev. 101 (2001) 1869-1879

[23] E.T. Lilleoden, P. Ciccolella, B.M. Clemens, and W.D. Nix: Nanoindentation studies of polymeric materials: methods and applications, unpublished

[24] Y. Cao, D. Yang, and W. Soboyejoy: Nanoindentation method for determining the initial contact and adhesion characteristics of soft Polydimethylsiloxane, J. Mater. Res. 20 (2005) 2004–2011

[25] Y.T. Cheng and C.M. Cheng: Relationship between initial unloading slope, contact depth, and mechanical properties for conical indentation in linear viscoelastic solids, J. Mater. Res. 20 (2005) 1046-1053

[26] S. Yang, Y-W. Zhang, and K. Zeng: Analysis of nanoindentation creep for polymeric materials, J. Appl. Phys. 95 (2004) 3655-3666

[27] B. Tang and A.H.W. Ngan: Accurate measurement of tip-sample contact size during nanoindentation of viscoelastic materials, J. Mater. Res. 18 (2003) 1141–1148

[28] M. Mareanukroh, R.K. Eby, R.J. Scavuzzo, G.R. Hamedand, and J. Preuschen: Use of Atomic Force Microscope as a Nanoindenter to Characterize Elastomers, Rubber Chem. Technol. 73 (2000) 912-925

[29] A.C. Fischer-Cripps.: A simple phenomenological approach to nanoindentation creep, Mater. Sci. Eng. A 385 (2004) 74–82

[30] M.L. Oyen and R.F. Cook: Load-displacement behaviour during sharp indentation of viscous-elastic-plastic materials, J. Mater. Res. 18 (2003) 139–150

[31] W.C. Oliver and G.M. Pharr: Measurement of hardness and elastic modulus by instrumented indentation: Advances in understanding and refinements to methodology, J. Mater. Res. 19 (2004) 3–20

[32] J.C. Grunlan, X. Xia, D. Rowenhorst, and W.W. Gerberich: Preparation and evaluation of tungsten tips relative to diamond for nanoindentation of soft materials, Rev. Sci. Instrum. 72 (2001) 2804-2810

[33] D.M. Ebenstein and K.J. Wahl: A comparision of JKR-based methods to analyze quasi static and dynamic indentation force curves, J. Colloid Interface Sci. 298 (2006) 652-662

[34] S. Gupta, F. Carillo, C. Li, L. Pruitt, and C. Puttlitz: Adhesive forces significantly affect elastic modulus determination of soft polymeric materials in nanoindentation, Mater. Lett. 61 (2007) 448-451

[35] F. Carrillo, S. Gupta, M. Balooch, S. Marshall, G. Marshall, L. Pruitt, and C. Puttlitz: Nanoindentation of polydimethylsiloxane elastomers: Effect of crosslinking, work of adhesion, and fluid environment on elastic modulus, J. Mater. Res. 20 (2005) 2820–2830

[36] F. Yang: Effect of adhesion energy on the contact stiffness in nanoindentation, J. Mater. Res. 21 (2006) 2683–2688

[37] K. L. Johnson, K. Kendall, and A. D. Roberts: Surface energy and the contact of elastic solids, Proc. R. Soc. Lond., Ser. A 324 (1971) 301-313

[38] H.G. Elias: Makromoleküle Band 1, Hütig&Wepf Basel, 5. Auflage (1990) 940

[39] S. Gupta, F. Carillo, M. Balooch, L. Pruitt, and C. Puttlitz: Simulated soft tissue indentation: A finite element study, J. Mater. Res. 20 (2005) 1979-1994

[40] A.C. Fischer-Cripps: Nanoindentation, Springer-Verlag, New York, (2002) ch. 2, 25

[41] H.G. Elias: Makromoleküle Band 1, Hütig&Wepf Basel, 5. Auflage (1990) 946

[42] A.C. Fischer-Cripps: Multiple-frequency dynamic nanoindentation testing, J. Mater. Res. 19 (2004) 2981–2988

[43] M. Li, W.-M. Chen, N.-G.Liang, and L.-D. Wang: A numerical study of indentation using indenters of different geometry, J. Mater. Res. 19 (2004) 73-78

[44] S. Swaddiwudhipong, J. Hua, K.K. Tho, and Z.S. Liu: Equivalency of Berkovich and conical load-indentation curves, Modelling Simul. Mater. Sci. Eng. 14 (2006) 71-82

[45] T.A. Laursen and J.C. Simo: A study of the mechanics of microindentation using finite elements, J. Mater. Res. 7 (1992) 618-626

[46] P.-L. Larsson, A.E. Giannakopoulos, E. Söderlund, D.J. Rowcliffe, and R. Vestergaard: Analysis of Berkovich Indentation, Int. J. Solids Structures 33 (1996) 221-248

[47] J.-L- Bucaille and E. Felder: Finite-element analysis of deformation during indentation and scratch tests on elastic-perfectly plastic materials, Phil. Mag. 82 (2002) 2003-2012

[48] J.-L- Bucaille, E. Felder, and G. Hochstetter: Mechanical analysis of the scratch test on elastic and perfectly plastic materials with the three- dimensional finite element modeling, Wear 249 (2001) 422-432

[49] M. Lichinchi, C. Lenardi, J. Hauptand, and R. Vitali: Simulation of Berkovich nanoindentation experiments on thin films using finite element method, Thin Solid Films 312 (1998) 240-248

[50] Y. Sun, T. Bell, and S. Zheng: Finite element analysis of the critical ratio of coating thickness to indentation depth for coating property measurements by nanoindentation, Thin Solid Films 258 (1995) 198-204

[51] K. Li, T.W. Wu, and J.C.M. Li: Contact area evolution during an indentation process, J. Mater. Res. 12 (1997) 2064-2071

[52] K.-D. Bouzakis and N. Michailidis: Indenter surface area and hardness determination by means of a FEM-supported simulation of nanoindentation, Thin Solid Films 494 (2006) 155-160

[53] S.D. Chen and F.J. Ke: MD simulation of the effect of the contact area and tip radius on nanoindentation, Science in China Series G- Physics Astronomy 47 (2004) 101-112

[54] R. Komanduri, N. Chandrasekaran, and L.M. Raff: MD simulation of indentation and scratching of single crystal aluminum, Wear 240 (2000) 113-143

[55] H. Jang and D. Farkas: Interaction of lattice dislocations with a grain boundary during nanoindentation simulation, Mater. Lett. 61 (2007) 868-871

[56] S.-R. Jian, T.-H. Fang, D.-S. Chuu, and L.-W. Ji: Atomistic modeling of dislocation activity in nanoindented GaAs, Appl. Surf. Sci. 253 (2006) 833–840

[57] A. Hasnaoui, P.M. Derlet, and H. Van Swygenhoven: Interaction between dislocations and grain boundaries under an indenter – a molecular dynamics simulation, Acta Mater. 52 (2004) 2251–2258

[58] G. Päzold, A. Linke, T. Hapke, and D.W Heermann: Computer simulation of nanoindentation into polymer films, Z. Phys. B 104 (1997) 523–521

[59] K. Yashiro, A. Furuta, and Y. Tomita: Nanoindentation on crystal/amorphous polyethylene: Molecular dynamics study, Comp. Mater. Sci. 38 (2006) 136–143

[60] S. Shim, W.C. Oliver, and G. M. Pharr: A critical examination of the Berkovich vs. conical indentation based on 3D finite element calculations, Mater. Res. Soc. Symp. Proc. 841 (2005) R9.5.1-R9.5.6

[61] Nano Instruments Innovation Center, MTS Systems Corporation: Nanoindenter SA2, Customer Care Kit (2004)

[62] Nano Instruments Innovation Center, MTS Systems Corporation: Nanoindenter XP, Testworks 4 Software for Nanoindentation, Operating Instructions (2004)

[63] N. Zhang, J. Xie, M. Guers, and V.K. Varadan: Chemical bonding of multiwalled carbon nanotubes to SU-8 via ultrasonic irradiation, Smart Mater. Struct. 12 (2003) 260–263

[64] http://www.geocities.com/guerinlj/

[65] http://www.goodfellow.com

[66] N. Barbakadze, S. Enders, S. Gorb, and E. Arzt: Local mechanical properties of the head articulation cuticle in the beetle Pachnoda marginata, J. Exp. Bio. 209 (2006) 722-730

[67] C.A. Tweedie and K.J. van Vliet: On the indentation recovery and fleeting hardness of polymers. J. Mat. Res. 21, (2006) 3029-3036

[68] B.N. Lucas, W.C. Oliver, G.M. Pharr, and J-L. Loubet: Time dependent deformation during indentation testing. Thin Films: Stresses and Mechanical Properties VI. Symposium Pittsburgh, PA, USA (1997) 233-238

[69] ABAQUS Analysis User’s manual 6.6, ABAQUS Inc., Providence, RI, USA (2006)

[70] A.H.W. Ngan and B. Tang: Viscoelastic effects during unloading in depth-sensing indentation, J. Mater. Res. 17 (2002) 2604-2610

[71] G. Feng and A.H.W. Ngan: Effects of creep and thermal drift on modulus measurement using depth-sensing indentation, J. Mater. Res. 17 (2002) 660-668

[72] L.R.G. Treloar: Physics of Rubber-like Materials, Nature 167 (1957) 452-427

[73] A.V. Tobolsky: The Mechanical Properties of Polymers, Scientific American 197 (1957) 121-134

[74] A.V. Tobolsky, D.W. Carlson, and N. Indictor: Rubber Elasticity and Chain Configuration, J. Polym. Sci. 54 (1961) 175-192

[75] P.J. Flory: Theory of elasticity of polymer networks. The effect of local constraints on junctions, J. Chem. Phys. 66 (1977) 5720-5729

[76] L.R.G. Treloar: Rubber elasticity, Contemporary Physics 12 (1971) 33-56

[77] D.H. Johnson, J.R. McLoughlin, and A.V. Tobolsky: Chemorheology of some specially prepared silicone rubbers, J. Phys. Chem. 58 (1954) 1073-1075

[78] L.H. Sperling, S.L. Cooper, and A.V. Tobolsky: Elastomeric and Mechanical Properties of poly-m-carboranylenesiloxane, J. Appl. Polym. Sci. 10 (1966) 1725-1735

[79] B. Erman, W. Wagner, and P.J. Flory: Elastic Modulus and Degree of Crosslinking of Poly(ethyl acrylate) Networks, Macromolecules 13 (1980) 1554-1558

[80] J.E. Mark and J.L. Sullivan: Model networks of end-linked polydimethylsioxane chains. I. Comparison between experimental and theoretical values of the elastic modulus and the equilibrium degree of swelling, J. Chem. Phys. 66 (1977) 1006-1011

[81] M. Narkis and A.V. Tobolsky: Characterization of Poly(Dimethylsiloxane)-Polycorbonate Block Copolymers, Journal of Marcomolecular Science B4 (1970) 877-887

[82] Dow Corning Corporation: Information about high technology silicone materials, Sylgard 184 silicone elastomer data sheet (2001)

[83] H. Hillborg, M. Sandelin, and U.W. Gedde: Hydrophobic recovery of Polydimethylsiloxane after exposure to partial discharges as a function of crosslink density, Polymer 42 (2001) 7349-7362

[84] Y. Berdichevsky, J. Khandurina, A. Guttman, and Y.-H. Ho: UV/ozone modification of Poly(dimethylsiloxane) microfluidic channels, Sensors and Actuators B 97 (2004) 402-408

[85] R.T. Johnson Jr., R.M. Biefeld, and J.A. Sayre: High-Temperature Electrical Conductivity and Thermal Decomposition of Sylgard 184 and Mixtures Containing Hollow Microspherical Fillers, Polym. Eng. and Sci. 24 (1984) 435-441

[86] D.J. Campbell, K.J. Beckmann, C.E. Calderon, P.W. Doolan, R.H. Moore, A.B. Ellis, and G.C. Lisensky: Replication and Compression of Bulk Surface Structures with Polydimethylsiloxane Elastomer, J. Chem. Educ. Vol.76, (1999) 537-541

[87] J.N. Lee, X. Jiang, D.W. Ryan, and G.M. Whitesides: Compatibility of Mammalian Cells on Surfaces of Poly(dimethylsioxane), Langmuir 20 (2004) 11684-11691

[88] G. Bar, L. Delineau, R. Brandsch, and M. Bruch: Importance of indentation depth in tapping-mode atomic force microscopy study of compliant materials, Appl. Phys. Lett. 75 (1999) 4198-4200

[89] E.A. Wilder, S. Guo, S. Lin-Gibson, M.J. Fasolka, and C.M. Stafford: Measuring the Modulus of Soft Polymer Networks via a Buckling-Based Metrology, Macromolecules 39 (2006) 4138-4143

[90] A. Mata, A.J. Fleischman, and S. Roy: Characterization of Polydimethylsiloxane properties for Biomedical Micro/Nanosystems, Biomedical Devices 7 (2005) 281-293

[91] M.C. Belanger and Y. Marois: Hemocompatibility, biocompatibility, inflammatory and in vivo studies of primary reference materials low-density polyethylene and polydimethylsiloxane: A review, J. Biomed. Mater. Res. 58 (2001) 467-477

[92] Z. Gao, J. Schulze Nahrup, J.E. Mark, and A. Sakr: Poly(Dimethylsiloxane) Coatings for Controlled Drug Release. III. Drug Release Profiles and Swelling Properties of the Free-Standing Films, J. Appl. Polym. Sci. 96 (2005) 494–501

[93] R.G. Jones: Silicon-Containing Polymers - The Science and Technology of Their Synthesis and Applications, edited by: R.G. Jones; W. Ando, and J. Chojnowski, 1st edition, Springer Netherlands (2000)

[94] J.M. Zeigler: Silicon-Based Polymer Science : A Comprehensive Resource, edited by J.M. Zeigler and F.W. Fearon, The American Chemical Society, Washington DC (1990)

[95] N.Q. Balaban, U.S. Schwarz, D. Riveline, P. Goichberg, G. Tzur, I. Sabanay, D. Mahalu, S. Safran, A. Bershadsky, L. Addadi, and B. Geiger: Force and focal adhesion assembly: a close relationship studied using elastic micropatterned substrates, Nature Cell Biology 3 (2001) 466-472

[96] E. de Souza and R. Kemkemmer: unpublished results

[97] R.L. Taylor, C.M. Liauw, and C. Maryan: The effect of resin/crosslinker ratio on the mechanical properties and fungal deterioration of a maxillofacial silicone elastomer, J. Mater. Sci.: Materials in medicine 14 (2003) 497-502

[98] M.T. Thompson, M.C. Berg, I.S. Tobias, M.F. Rubner, and K.J. Van Vliet: Tuning compliance of polyelectrolyte multilayers to modulate cell adhesion, Biomaterials 26 (2005) 6836-6845

[99] D.E. Discher, P. Janmey, and Y.-L. Wang: Tissue cells feel and respond to the stiffness of their substrate, Science 310 (2005) 1139-1143

[100] M.I. Aranguren, E. Mora, C.W. Macosko, and J. Saam: Rheological and mechanical properties of filled rubber: Silica-Silicone, Rubber Chem. Technol. 67 (1994) 820-833

[101] Y.Y. Lim and M.M. Chaudhri: Experimental investigations of the normal loading of elastic spherical and conical indenters on to elastic flats, Phil. Mag. 83 (2003) 3427-3462

[102] A.L. Andrady, M.A. Liorente, and J.E. Mark: Effects of dangling chains on some dynamic mechanical properties of model poly(dimethylsiloxane) networks, Polymer Bulletin 28 (1992) 103-108

[103] F. Chambon and H.H. Winter: Linear Viscoelasticity at the Gel point of a Crosslinking PDMS with Imbalanced Stoichiometry, J. Rheol. 31 (1987) 683-697

[104] F. Chambon and H.H. Winter: Stopping of Crosslinking Reaction in a PDMS Polymer at the Gel Point, Polymer Bulletin 13 (1985) 499-503

[105] L. Matejka: Rheology of epoxy networks near the gel point, Polymer Bulletin 26 (1991) 109-116

[106] A.T. Guertin: Diffusion controlled termination in free radical polymerization, Polymer Lett. 1 (1963) 477-481

[107] G. Hild, R. Okasha, and P. Rempp: Free radical crosslinking copolymerization in the post gel state, 3: Swelling and mechanical properties of polystyrene networks, Macromolecular Chemistry 186 (1985) 407-422

[108] T.-Y. Zhang and W.-H. Xu: Surface effects in nanoindentation, J. Mater. Res. 17 (2002) 1715-1720

[109] D.C.C. Lam and A.C.M. Chong: Indentation model and strain gradient plasticity law for glassy polymers, J. Mater. Res. 14 (1999) 3784-3788

[110] I. Nitta: Measurements of real contact areas using PET films, Wear 181-183 (1995) 844-849

[111] A. Ovcharenko, G. Halperin, G. Verberne, and I. Etsion: In situ investigation of the contact area in elastic-plastic spherical contact during loading-unloading, Tribol. Lett. 25 (2007) 153-1660

[112] D. J. Morris and R.F. Cook: In-situ Cube Corner Indentation of Soda-Lime Glass and Fused Silica, Journal of the American Ceramic Society 87 (2004) 1494-1501

[113] T. Miyajima and M. Sakai: Optical indentation microscopy- a new family of instrumented indentation testing, Phil. Mag. 86 (2006) 5729-5737

[114] S. Ruffell, J.E. Bradby, J.S. Williams, and O.L. Warren: An in-situ electrical measurement technique via conducting diamond tip for nanoindentation in silicon, J. Mater. Res. 22 (2007) 578-586

[115] B. Moser, J. Kuebler, H. Meinhard, W. Muster, and J. Michler: Observation of Instabilities during Plastic Deformation by in-situ SEM Indentation Experiments, Adv. Eng. Mat. 7 (2005) 388-392

[116] B. Moser, J.F. Löffler, and J. Michler: Discrete deformation in amorphous metals: an in situ SEM indentation study, Phil. Mag. 86 (2006) 5715-5728

[117] J. Michler, R. Rabe, J.-L. Bucaille, B. Moser, P. Schwaller, and J.-M. Breguet: Investigation of wear mechanisms through in situ observation during microscratching inside the scanning electron microscope, Wear 259 (2005) 18-26

[118] T. Ohmura, A. Minor, K. Tsuzaki, and J.W. Morris, Jr.: Indentation induced deformation behavior in martensitic steel observed through in-situ nanoindentation in a transmission electron microscopy, Materials Science Forum 503-504 (2006) 239-244

[119] A.M. Minor, E.T. Lilleodden, M. Jin, E.A. Stach, D.C. Chrzan, and J.W. Morris: Room temperature dislocation plasticity in silicon, Phil. Mag. 85 (2005) 232-330

[120] J. Zhou, K. Komvopulos, and A.M. Minor: Nanoscale plastic deformation and fracture of polymers studied by in-situ nanoindentation in a transmission electron microscope, Appl. Phys. Lett. 88 (2006) 181908-1-3

[121] A. Oshima and M. Washio: Radiation-induced phenomena in ethylene-co-tetraflouroethylene polymer: Temperature and LET effects, NIM B 208 (2003) 380-384

[122] Z.G. Song, C.K. Ong, and H. Gong: Secondary and backscattered electron yields of polymer surface under electron beam irradiation, Appl. Surf. Sci. 119 (1997) 169-175

[123] S.C.J. Loo, C.P. Ooi, and Y.C.F. Boey: Influence of electron-beam radiation on the hydrolytic degradation behaviour of poly(lactide-co-gycolide) (PLGA), Biomaterials 26 (2005) 3809-3817

[124] L.F. Drummy, J. Yang, and D. C. Martin: Low-voltage electron microscopy of polymer and organic molecular thin films, Ultramicroscopy 99 (2004) 247-256

[125] A. Safrany and L. Wojnarovits: Electron-beam induced crosslinking in poly(N-isopropylacrylamid) aqueous solutions, Radiation Physics and Chemistry 69 (2004) 289-293

[126] A.J. Lovinger, F.J. Padden, and D.D. Davis: Morphology and electron-irradiation behavior of Poly(dimethysilylene), Polymer 32 (1991) 3086-3090

[127] M.T. Russell, L.S.C. Pingree, M. C. Hersam, and T.J. Marks: Microscale Features and Surface Chemical Functionality Patterned by Electron Beam Lithography: A Novel Route to Poly(dimethylsiloxane), Langmuir 22 (2006) 6712-6718

[128] R. S. Maxwell, S.C. Chinn, D. Solyom, and R. Cohenour: Radiation-induced Cross-linking in a Silica-Filled Silicone Elastomer as Investigated by Multiple Quantum ^{1}H NMR, Macromolecules 38 (2005) 7026- 7032

[129] D.A. Bradley, K.Z. Dalhan, and S.C. Roy: Measurement of the viscosity of irradiated silicone using a differential viscometer, Applied Radiation and Isotopes 53 (2000) 921-928

[130] L.N. Pankratova, I.I. Dubovik, A.Y. Rabikina, and L.T. Bugaenko: Radiation-Induced Structural Transformations of Siloxane Diblock Copolymers, High Energy Chemistry 37 (2003) 423-425

[131] Y.C. Zhu, X.H. Zhang, J.L. Qiao, and G.S. Wei: A study on radiation crosslinking of polydimethylsiloxane (PDMS) rubber latex, Chinese J. Polym. Sci. 22 (2004) 147-154

[132] M.R. Stevens, Q. Chen, U. Weierstall, and J.C.H. Spence: Transmission Electron Diffraction at 200eV and Damage Thresholds below the Carbon K Edge, Micrscopy and Microanalysis 6 (2000) 368-379

[133] J. Deuschle, E. de Souza, S. Enders, and E. Arzt: Crosslinking and curing kinetics of PDMS studied by dynamic nanoindentation, to be published

[134] ABAQUS Theory manual, ABAQUS Inc., Providence, RI, USA (2006)

[135] L.R.G. Treloar: The Physics of Rubber Elasticity, 3rd ed. (1975) Clarendon Press, Oxford

[136] N.A. Stilwell and D. Tabor: Elastic recovery of conical indentations, Proc. Phys. Soc. 78 (1961) 169-179

[137] Y. Choi, H.-S. Lee, and D. Kwon: Analysis of sharp-tip indentation curve for contact area determination taking into account pile-up and sink-in effects, J. Mater. Res. 19 (2004) 3307-3315

[138] K.W. McElhaney, J.J. Vlassak, and W.D. Nix: Determination of indenter tip geometry and indentation contact area for depth-sensing indentation experiments, J. Mater. Res. 13 (1998) 1300-1306

[139] N. Yu, A.A. Polycarpou, and T.F. Corny: Tip-radius effect in finite element modeling of sub-50nm-shallow nanoindentation, Thin Solid Films 450 (2004) 295-303

[140] H.F. Wang and H. Bangert: Three-dimensional finite element simulation of Vickers indentation on coated systems, Mater. Sci. Eng. A 163 (1993) 42-50

[141] A. Bolshakov, W.C. Oliver, and G.M. Pharr: Influences of the stress on the measurement of mechanical properties using nanoindentation: Part II. Finite element simulations, J. Mater. Res. 11 (1996) 760-768

[142] S. Swaddiwudhipong, L.H. Poh, J. Hua, Z.S. Liu, and K.K. Tho: Modeling nano-indentation test of glassy polymers using finite elements with strain gradient plasticity, Mater. Sci. Eng. A 404 (2005) 179-187

[143] L. Anand and N.M. Ames: On modeling the micro-indentation response of an amorphous polymer, International Journal of Plasticity 22 (2006) 1123–1170

[144] P.-L. Larsson and S. Carlsson: On Microindentation of Viscoelastic Polymers, Polymer Testing 17 (1998) 49-75

[145] A.E. Giannakopoulos and A. Triantafyllou: Spherical indentation of incompressible rubber-like materials, J. Mech. Phys. Solids 55 (2007) 1196–1211

[146] S.J. Jerrams, M. Kaya, and K.F. Soon: The effects of strain rate and hardness on the material constants of nitrile rubbers, Materials and Design 19 (1998) 157-167

[147] W. Kuhn: Über die Gestalt fadenförmiger Moleküle in Lösungen, Kolloid-Zeitschrift 68 (1934) 2-15

[148] E. Guth and H. Mark: Die Elastizität des Kautschuks und ihr Zusammenhang mit dem Strukturmodell, Naturwissenschaften 25 (1937) 353-359

[149] L.R.G. Treloar.: The elasticity of a network of longchain molecules I, Transactions of the Faraday Society 39(1943) 36-41

[150] L.R.G. Treloar.: The elasticity of a network of longchain molecules II, Transactions of the Faraday Society 39(1943) 241-246

[151] M. Mooney: A theory of Large Elastic Deformation, J. Appl. Phys. 11 (1940) 582-592

[152] R.S. Rivlin: Large Elastic Deformations of Isotropic Materials IV: Further Developments of the General Theory, Phil. Trans. A 241 (1948) 379-397

[153] R.W. Ogden: Large Deformation Isotropic Elasticity: On the Correlation of Theory and Experiment for Incompressible Rubberlike Solids, Proc. R. Soc. Lond. A 326 (1972) 565-584

[154] O.H. Yeoh: Characterization of elastic properties of carbon-black-filler rubber vulcanizates**,** Rubber Chem. and Technol. 63 (1990) 792-805

[155] E.M. Arruda and M.C. Boyce: A three-dimensional constitutive model for the large stretch behavior of rubberelastic materials, J. Mech. Phys. Solids 41 (1993) 389-412

[156] L. Valenta and L. Molnar: Vergleich des Neo-Hooke'schen und des Mooney-Rivlin'schen Materialmodels in der FEM-Berechnung, Periodica Polytech. Mech. Eng. 45 (2001) 95-101

[157] P. Raos: Modelling of elastic behaviour of rubber and its application in FEA, Plastics Rubber and Composites Processing and Applications 19 (1993) 293-303

[158] Z. Hicsasmaz and S.S.H. Rizvi: Effect of size and shape on modulus of deformability, LWT 38 (2005) 431-435

[159] R. Brown: Physical Testing of Rubber, Springer, New York USA, 4th editon (2006), ch. 6, 151

11 Appendices

Appendix A: Additional information to chapter 4

The materials SU 8, polyethylene of low density (LDPE) and PE of ultra high molecular weight (UHMWPE) were selected for use in chapter 4, because their mechanical properties are well known and thus offer a good possibility to compare our results to results from completely independent measurements. In the following, the material properties specified by the manufacturers are summarized.

Table A1: Properties of SU8 [64]

Young's modulus E	4.4 GPa
Poisson's coefficient	0.22
Viscosity	
40% SU8-60% solvent :	0.06 Pa.s
60% SU8-40% solvent :	1.5 Pa.s
70% SU8-30% solvent :	15 Pa.s
Coefficient of thermal expansion	50 ppm/K
Thermal conductivity:	0.2 W/m K
Glass temperature Tg:	200 deg C
Degradation Temperature	~380 deg C
Refractive index n	1.8 at 100 GHz
	1.7 at 1.6 THz
Absorption coefficient	2 /cm at 100 GHz
	40 /cm at 1.6 THZ
Relative dielectric constant	3 at 10 MHz

Table A2: Properties of UHMWPE [65]

Mechanische Eigenschaften	
E-modul im Zugversuch (GPa)	0,2-1,2
Härte - Rockwell	R50-70
Kerbschlagzähigkeit nach Izod (J m^{-1})	>1000
Poisson - Verhältnis	0,46
Reibungskoeffizient	0,1-0,2
Reißdehnung (%)	500
Zugfestigkeit (MPa)	20-40
Physikalische Eigenschaften	
Dichte (g cm^{-3})	0,94
Entzündbarkeit	HB
Mindestsauerstoffgehalt (%)	17
Strahlungswiderstand	befriedigend
Wasserabsorption - über 24 Stunden (%)	<0,01
Widerstand gegen ultraviolettes Licht	schlecht
Thermische Eigenschaften	
Hitzebiegungstemperatur - 0,45 MPa (C)	69
Hitzebiegungstemperatur - 1,8 MPa (C)	42
Linearer Wärmeausdehnungskoeffizient (x10^{-6} K^{-1})	130-200
Max. Dauergebrauchstemperatur (C)	55-95
Spezifische Wärme (J K^{-1} kg^{-1})	1900
Wärmeleitfähigkeit (W m^{-1} K^{-1})	0,42-0,51 bei 23C

Table A3: Properties of LDPE [65]

Mechanische Eigenschaften	
E-modul im Zugversuch (GPa)	0,1-0,3
Härte - Rockwell	D41-46 - Shore
Kerbschlagzähigkeit nach Izod (J m^{-1})	>1000
Reißdehnung (%)	400
Zugfestigkeit (MPa)	5-25
Physikalische Eigenschaften	
Brechungsindex	1,51
Dichte (g cm^{-3})	0,92
Entzündbarkeit	HB
Mindestsauerstoffgehalt (%)	17
Strahlungswiderstand	befriedigend
Wasserabsorption - über 24 Stunden (%)	<0,015
Widerstand gegen ultraviolettes Licht	schlecht
Thermische Eigenschaften	
Hitzebiegungstemperatur - 0,45 MPa (C)	50
Hitzebiegungstemperatur - 1,8 MPa (C)	35
Linearer Wärmeausdehnungskoeffizient ($x10^{-6}$ K^{-1})	100-200
Max. Dauergebrauchstemperatur (C)	50-90
Min. Dauergebrauchstemperatur (C)	-60
Spezifische Wärme (J K^{-1} kg^{-1})	1900-2300
Wärmeleitfähigkeit (W m^{-1} K^{-1})	0,33 bei 23C

Appendix B: Additional information to chapter 5

The following table lists the formulas, parameters, and constants, which typically have been used for the indentation tests and data analysis.

```
Method Name : C:\Program Files\MTS Systems\TestWorks\Methods\DCM\Julia methods\DCM CSM
Specific Frequency Berkovich, viscoandelastic.msm
Owner : MTS
Channels
        Modulus
                Internal Name : Modulus
                Units : MPa
                Formula : IF (Isvalid(DisplacementIntoSurface) AND (CurrentIndex() <
EndOfLoadingMarker), (1.0-pow( PoissonsRatio, 2.0))*pow ( (1/ReducedModulus-(1-
pow(IndenterTipPoissonsRatio, 2.0) )/TipModulus()), -1.0), InvalidDouble())
        Contact Area
                Internal Name : ContactArea
                Units : nm^2
                Formula : TipArea(ContactDepth,_TipName)
        Loss Tangent
                Internal Name : LossTangent
                Units :
                Formula : LossModulus/StorageModulus
        Time
                Internal Name : _Time
                Units : s
                Formula :
        Displacement Value
                Internal Name : DisplacementValue
                Units :
                Formula : _Displacement/OneNanoMeter
        Transfer Function
                Internal Name : TransferFunction
                Units : N/m
                Formula : _HarmonicLoad/_HarmonicDisplacement
        Harmonic Contact Stiffness
                Internal Name : Stiffness
                Units : N/m
                Formula : 1/(1/(_HarmonicStiffness)-1/ (
_HarmonicFrame+HarmonicFrameCorrection))
        Contact Depth
                Internal Name : ContactDepth
                Units : nm
                Formula : if (Isvalid(DisplacementIntoSurface) AND CurrentIndex() <
UnloadStiffnessMarker , DisplacementIntoSurface-Epsilon*LoadOnSample/DynamicContactStiffness,
InvalidDouble())
        Raw Load
                Internal Name : _Load
                Units : mN
                Formula :
        Hardness
                Internal Name : Hardness
                Units : MPa
                Formula : if ((DisplacementIntoSurface>0.0) AND (CurrentIndex() <
EndOfLoadingMarker), LoadOnSample/ContactArea, InvalidDouble())
        Segment Number
                Internal Name : SegmentIndex
```

```
                Units :
                Formula : IF(CurrentIndex() eq 0, 0, SegmentIndex)
        X Position
                Internal Name : _XPosition
                Units : um
                Formula :
        Dynamic Contact Stiffness
                Internal Name : DynamicContactStiffness
                Units : N/m
                Formula : 1/(1/(TransferFunction*cos(_PhaseAngle)-
DynamicSystemStiffness+mOmega2)-1/ ( _HarmonicFrame+HarmonicFrameCorrection))
        Y Position
                Internal Name : _YPosition
                Units : um
                Formula :
        Frame Stiffness
                Internal Name : _Frame
                Units : N/m
                Formula :
        Harmonic Load
                Internal Name : _HarmonicLoad
                Units : uN
                Formula :
        Segment Type
                Internal Name : SegmentType
                Units :
                Formula : IF(CurrentIndex() eq 0, 0, SegmentType)
        Reduced Modulus
                Internal Name : ReducedModulus
                Units : GPa
                Formula : if ((DisplacementIntoSurface>0.0) AND (CurrentIndex() <
EndOfLoadingMarker),Stiffness*Sqrt(Pi())/(2*Beta*sqrt(ContactArea)),InvalidDouble())
        Raw Displacement
                Internal Name : _Displacement
                Units : nm
                Formula :
        Load Over Stiffness Squared
                Internal Name : LoadVStiff2
                Units : 1/GPa
                Formula : LoadOnSample/(DynamicContactStiffness*DynamicContactStiffness)
        Load vs Displ Slope
                Internal Name : _ContactStiffness
                Units : N/m
                Formula :
        Harmonic Damping
                Internal Name : _HarmonicDamping
                Units : N/m
                Formula :
        Harmonic Frame Stiffness
                Internal Name : _HarmonicFrame
                Units : N/m
                Formula :
        Support Spring Stiffness
                Internal Name : _Column
                Units : N/m
                Formula :
        Storage Modulus
                Internal Name : StorageModulus
                Units : MPa
                Formula : if ((DisplacementIntoSurface>0.0) AND
(CurrentIndex()<=EndOfLoadingMarker),
DynamicContactStiffness*Sqrt(Pi())/(2*Beta*sqrt(ContactArea)),InvalidDouble())
```

```
        Harmonic Frequency
                Internal Name : _HarmonicFrequency
                Units : Hz
                Formula :
        Harmonic Displacement
                Internal Name : _HarmonicDisplacement
                Units : nm
                Formula :
        Dynamic System Damping
                Internal Name : DynamicSystemDamping
                Units : (N/m)/s
                Formula : D4*pow(DisplacementValue*pow(10,-
6),4)+D3*pow(DisplacementValue*pow(10,-6),3)+D2*pow(DisplacementValue*pow(10,-
6),2)+D1*DisplacementValue*pow(10,-6)+D0
        Load On Sample
                Internal Name : LoadOnSample
                Units : uN
                Formula : _Load-_Load[SurfaceMarker] -(_Displacement-
_Displacement[SurfaceMarker])*DynamicSystemStiffness[SurfaceMarker]
        Harmonic Stiffness
                Internal Name : _HarmonicStiffness
                Units : N/m
                Formula :
        m Omega 2
                Internal Name : mOmega2
                Units :
                Formula :
MassValue*pow(2*PI()*_HarmonicFrequency/OneRadianPerSecond,2)*OneNewtonPerMeter
        Harmonic System Damping
                Internal Name : _HarmonicSystemDamping
                Units : N/m
                Formula :
        Dynamic System Stiffness
                Internal Name : DynamicSystemStiffness
                Units : N/m
                Formula : K0+K1*DisplacementValue*pow(10,-6)
        CSM Status
                Internal Name : _CSM
                Units :
                Formula :
        Phase Angle
                Internal Name : _PhaseAngle
                Units : deg
                Formula :
        Loss Modulus
                Internal Name : LossModulus
                Units : MPa
                Formula : if ((DisplacementIntoSurface>0.0) AND
(CurrentIndex()<=EndOfLoadingMarker),
DynamicContactDamping*Sqrt(Pi())/(2*Beta*sqrt(ContactArea)),InvalidDouble())
        Displacement Into Surface
                Internal Name : DisplacementIntoSurface
                Units : nm
                Formula : _Displacement - _Displacement[SurfaceMarker]  -DriftCorrection*(_Time -
_Time[SurfaceMarker]) - ((_Load-_Load[SurfaceMarker] )/( _Frame+FrameStiffnessCorrection))
        Dynamic Contact Damping
                Internal Name : DynamicContactDamping
                Units : N/m
                Formula : TransferFunction*Sin(_PhaseAngle)-
DynamicSystemDamping*2*PI()*_HarmonicFrequency
        Harmonic System Stiffness
                Internal Name : _HarmonicSystemStiffness
```

```
        Units : N/m
        Formula :
Inputs
    Batch Inputs
        Allowable Drift Rate
            Internal Name : _AllowableDriftRate
            Default Value : 5.000  nm/s
        Approach Distance To Store
            Internal Name : _ApproachDistanceToSave
            Default Value : 2000.000  nm
        Beta
            Internal Name : Beta
            Default Value : 1.034
        D0
            Internal Name : D0
            Default Value : 0.0112955  (N/m)/s
        D1
            Internal Name : D1
            Default Value : 0.0709439  (N/m)/s
        D2
            Internal Name : D2
            Default Value : 44.7969917  (N/m)/s
        D3
            Internal Name : D3
            Default Value : 561.2104797  (N/m)/s
        D4
            Internal Name : D4
            Default Value : 0.9432997  (N/m)/s
        Delta X For Finding Surface
            Internal Name : _DeltaXForFindingSurface
            Default Value : 0.000  um
        Delta Y For Finding Surface
            Internal Name : _DeltaYForFindingSurface
            Default Value : 0.000  um
        End Unloading
            Internal Name : EndUnloading
            Default Value : 0.000  um
        Frequency Surface Find
            Internal Name : FrequencySurfaceFind
            Default Value : 150.000  Hz
        Harmonic Displacement Surface Find
            Internal Name : HarmonicDisplacementSurfaceFind
            Default Value : 100.000  nm
        Hold Higher Position Time
            Internal Name : HoldHigherPositionTime
            Default Value : 10.000  s
        Hold Lower Position Time
            Internal Name : HoldLowerPositionTime
            Default Value : 15.000  s
        K0
            Internal Name : K0
            Default Value : 80.9044783  N/m
        K1
            Internal Name : K1
            Default Value : -54.0931070  N/m
        Mass Value
            Internal Name : MassValue
            Default Value : 0.0000886
        Max Approach Points
            Internal Name : MaxApproachPoints
            Default Value : 5000
        Max Hardware Load
```

Internal Name : MaxHardwareLoad
Default Value : 15.000 mN
Max Loading Time
Internal Name : MaxLoadingTime
Default Value : 10000.000 s
Maximum Calculation Depth
Internal Name : Max_Modulus_Depth
Default Value : 800 nm
Maximum Calculation Percentage
Internal Name : MaximumCalculationPercentage
Default Value : 90 %
Measure Drift Rate Flag
Internal Name : MeasureDriftRateFlag
Default Value : 1
Minimum Calculation Depth
Internal Name : Min_Modulus_Depth
Default Value : 200 nm
Minimum Calculation Percentage
Internal Name : MinimumCalculationPercentage
Default Value : 30 %
NilVelocity
Internal Name : NilVelocity
Default Value : 0.000 nm/s
One Nano Meter
Internal Name : OneNanoMeter
Default Value : 1.000 nm
One Newton Per Meter
Internal Name : OneNewtonPerMeter
Default Value : 1.000 N/m
OneRadianPerSecond
Internal Name : OneRadianPerSecond
Default Value : 1.000 rad/s
Part Number and Version
Internal Name : PartNumberandVersion
Default Value : see description field
Perform Drift Correction
Internal Name : PerformDriftCorrection
Default Value : 1
Phase Corr Coef 1
Internal Name : PhaseCorrCoef1
Default Value : 0.11630
Phase Corr Coef 2
Internal Name : PhaseCorrCoef2
Default Value : -0.39882
Phase Corr Coef 3
Internal Name : PhaseCorrCoef3
Default Value : -20.73801
Phase Corr Coef 4
Internal Name : PhaseCorrCoef4
Default Value : 1.00000
Phase Corr Coef 5
Internal Name : PhaseCorrCoef5
Default Value : 1.33279
Position For Surface Find
Internal Name : PositionForSurfaceFind
Default Value : 7.000 um
Sample Frequency
Internal Name : SampleFrequency
Default Value : 75.000 Hz
Stiffness Limit Surface Find
Internal Name : StiffnessLimitSurfaceFind
Default Value : 5.000 N/m

- Stiffness Peak Hold Time
  - Internal Name : StiffnessPeakHoldTime
  - Default Value : 10.000 s
- Strain Rate Target
  - Internal Name : StrainRate
  - Default Value : 0.050 1/s
- Surface Approach Distance
  - Internal Name : _SurfaceApproachDistance
  - Default Value : 2000.000 nm
- Surface Approach Sensitivity
  - Internal Name : _SurfaceApproachSensitivity
  - Default Value : **** %
- Surface Approach Velocity
  - Internal Name : _SurfaceApproachVelocity
  - Default Value : 10.000 nm/s
- Surface Detection Method
  - Internal Name : _SurfaceDetectionMethod
  - Default Value : method 1
- Surface Find Flag
  - Internal Name : _SurfaceFind
  - Default Value : 0
- Surface Find Rate
  - Internal Name : SurfaceFindRate
  - Default Value : 0.050 mN/s
- Surface Stiffness
  - Internal Name : SurfaceStiffness
  - Default Value : 10.000 N/m
- X Test Position
  - Internal Name : _XLocation
  - Default Value : **** um
- Y Test Position
  - Internal Name : _YLocation
  - Default Value : **** um

Internal Use

- Analyst Program Name
  - Internal Name : AnalystProgramName
  - Default Value : AnalystDriver.xls
- Blank String
  - Internal Name : BlankString
  - Default Value :
- Computational Method
  - Internal Name : _ComputationalMethod
  - Default Value :
- Number of Tests in this Sample
  - Internal Name : _MaxSpecimens
  - Default Value : 10.000
- Surface Displacement
  - Internal Name : _SurfaceDisplacement
  - Default Value : 100.000 mm
- Test Aborted
  - Internal Name : _Abort
  - Default Value : 0.000
- Use Computational Method Flag
  - Internal Name : _UseCompMethod
  - Default Value : ****

Limits

- High Displacement Position
  - Internal Name : HighDisplacementPosition
  - Default Value : -20.000 um
- Maximum Displacement
  - Internal Name : MaximumDisplacement
  - Default Value : 0.025 mm

```
            Minimum Displacement
                        Internal Name : MinimumDisplacement
                        Default Value : -0.025  mm
      Load Segment Inputs
            Depth Limit
                        Internal Name : DepthLimit
                        Default Value : 1000.000  nm
      Hold Segment Inputs
            Drift Determination Time
                        Internal Name : DriftDeterminationTime
                        Default Value : 20.000  s
            Hold For Start Position
                        Internal Name : HoldForStartPosition
                        Default Value : 25.000  s
            Peak Hold Time
                        Internal Name : PeakHoldTime
                        Default Value : 10.000  s
      Unload Segment Inputs
            Percent To Unload
                        Internal Name : PercentToUnload
                        Default Value : 90.000  %
      XY Table Inputs
            X Y Table Speed
                        Internal Name : XYTableSpeed
                        Default Value : 1.000  mm/s
      Data Acquistion Inputs
            Data Acquisition Rate
                        Internal Name : DataRate
                        Default Value : 20.000  Hz
            Drift Determination Acquisition Rate
                        Internal Name : DriftDeterminationAcquisitionRate
                        Default Value : 0.500  Hz
            Outer Loop Rate
                        Internal Name : _OuterLoopRate
                        Default Value : 40.000  Hz
      Oliver & Pharr Constants
            Epsilon
                        Internal Name : Epsilon
                        Default Value : 0.750
            Frame Stiffness Correction
                        Internal Name : FrameStiffnessCorrection
                        Default Value : 0  N/m
            Harmonic Displacement Target
                        Internal Name : HarmonicDisplacement
                        Default Value : 10.000  nm
            Harmonic Frame Stiffness Correction
                        Internal Name : HarmonicFrameCorrection
                        Default Value : 0  N/m
            Indenter Tip Poissons Ratio
                        Internal Name : IndenterTipPoissonsRatio
                        Default Value : 0.070
            Number Of Bins
                        Internal Name : NumberOfBins
                        Default Value : 100
            Poisson's Ratio
                        Internal Name : PoissonsRatio
                        Default Value : 0.400
            Script Name
                        Internal Name : ScriptName
                        Default Value :
ShiftLoadSegScript.xls,Visualsfcsmscript.xls,qualifycsmscript.xls,HandMCSMscript.xls
      Method Inputs
```

```
            Method Type
                Internal Name : MethodType
                Default Value : Indent
        Temp Inputs
            Number Of Period Controlled
                Internal Name : NumberOfPeriodControlled
                Default Value : 5
        Constants
            Analyst Directory
                Internal Name : AnalystDirectory
                Default Value : c:\program files\mts systems\analyst
        Segment Types
            Hold Segment Type
                Internal Name : Hold
                Default Value : 300
            Load Segment Type
                Internal Name : Load
                Default Value : 0
            Thermal Drift Hold Segment
                Internal Name : ThermalDriftHold
                Default Value : 400
            Unload From Peak Segment Type
                Internal Name : UnloadFromPeak
                Default Value : 600
            Unload Segment Type
                Internal Name : Unload
                Default Value : 500
    Formulas
        Batch Formulas
            Approach Loading Rate
                Internal Name : ApproachLoadingRate
                Units : uN/s
                Formula : _SurfaceApproachVelocity*_Column
            Approach Position
                Internal Name : ApproachPosition
                Units : nm
                Formula : _SurfaceDisplacement-_SurfaceApproachDistance
            Assign Surface Displacement
                Internal Name : AssignSurfaceDisplacement
                Units :
                Formula : _SurfaceDisplacement=_Displacement
            Batch Name
                Internal Name : _BatchName
                Units :
                Formula : concat(CurrentDate("yyyy-MM-dd")," Batch #")
            contactstiffness_1
                Internal Name : contactstiffness
                Units : N/m
                Formula : ChannelIndex (DynamicContactStiffness, 0.000204,t)
            E Average Over Defined Range
                Internal Name : E_Over_Depth_Range
                Units : MPa
                Formula : AverageValue (Modulus,MinCalcMarker, MaxCalcMarker)
            H Average Over Defined Range
                Internal Name : HAverageOverDefinedRange
                Units : MPa
                Formula : AverageValue (Hardness,MinCalcMarker, MaxCalcMarker)
            Index Max Calc Modulus
                Internal Name : IndexMaxCalcModulus
                Units :
```

```
                        Formula : ChannelIndex(LoadOnSample,LoadOnSample[EndOfLoadingMarker]*MaximumCalculationPercentage)
                Index Min Calc Modulus
                        Internal Name : IndexMinCalcModulus
                        Units :
                        Formula : ChannelIndex(LoadOnSample,LoadOnSample[EndOfLoadingMarker]*MinimumCalculationPercentage)
                Loss Modulus
                        Internal Name : AverageLossModulus
                        Units : MPa
                        Formula : AverageValue (LossModulus, MinCalcMarker, MaxCalcMarker)
                Loss Tangent
                        Internal Name : AverageLossTangent
                        Units :
                        Formula : AverageValue (LossTangent, MinCalcMarker, MaxCalcMarker)
                Max Calc Depth Setting
                        Internal Name : MaxCalcDepthSetting
                        Units :
                        Formula : Max_Modulus_Depth=DisplacementIntoSurface[IndexMaxCalcModulus]
                Max Calc Marker
                        Internal Name : MaxCalcMarker
                        Units :
                        Formula : ChannelIndex(DisplacementIntoSurface, Max_Modulus_Depth, SurfaceMarker)
                Min Calc Depth Setting
                        Internal Name : MinCalcDepthSetting
                        Units :
                        Formula : Min_Modulus_Depth=DisplacementIntoSurface[IndexMinCalcModulus]
                Min Calc Marker
                        Internal Name : MinCalcMarker
                        Units :
                        Formula : ChannelIndex (DisplacementIntoSurface, Min_Modulus_Depth, SurfaceMarker)
                Phase Angle Correction
                        Internal Name : PhaseAngleCorrection
                        Units :
                        Formula : -(PhaseCorrCoef1*pow(_HarmonicFrequency,PhaseCorrCoef4)+PhaseCorrCoef2+PhaseCorrCoef3/pow(_HarmonicFrequency,PhaseCorrCoef5))
                Point Number To Store
                        Internal Name : PointNumberToStore
                        Units :
                        Formula : Floor(_ApproachDistanceToSave*DataRate/_SurfaceApproachVelocity)
                Prescribed Loading Rate
                        Internal Name : LoadingRateForStrain
                        Units : uN/s
                        Formula : LoadOnSample*StrainRate + _SurfaceApproachVelocity * _Column
                Reset Surface Displacement
                        Internal Name : ResetSurfaceDisplacement
                        Units :
                        Formula : _SurfaceDisplacement=_Displacement[SurfaceMarker]
                Start Drift Marker
                        Internal Name : DriftDeterminationMarker
                        Units :
                        Formula : CurrentIndex()
                Start Hold Marker
                        Internal Name : StartHoldMarker
```

Units :
Formula : CurrentIndex()
Storage Modulus
Internal Name : AverageStorageModulus
Units : MPa
Formula : AverageValue (StorageModulus, MinCalcMarker, MaxCalcMarker)
Surface Stiffness Increase
Internal Name : SurfaceStiffnessIncrease
Units : N/m
Formula : 100*OneNewtonPerMeter*_SurfaceApproachSensitivity
Test File Name For Export
Internal Name : _ExportFileName
Units :
Formula : IF((NumberOfSpecimens (1)+1) GT 99, Concat("Test",IToA((NumberOfSpecimens (1)+1))), IF((NumberOfSpecimens (1)+1) GT 9, Concat("Test0",IToA((NumberOfSpecimens (1)+1))),Concat("Test00",IToA(NumberOfSpecimens (1)+1))))
Time Constant
Internal Name : TimeConstant
Units :
Formula : Floor((Log10(NumberOfPeriodControlled/_HarmonicFrequency))/0.35+14.5)
Unload Limit
Internal Name : UnloadLimit
Units : uN
Formula : LoadOnSample * (1.0-PercentToUnload)
Unload Rate
Internal Name : UnloadRate
Units : uN/s
Formula : IF (LoadOnSample*StrainRate>UnloadRate, LoadOnSample*StrainRate, UnloadRate)
Unload Stiffness Marker
Internal Name : UnloadStiffnessMarker
Units :
Formula : CurrentIndex()
X Precise Surface Find Position
Internal Name : XPreciseSurfaceFindPosition
Units : nm
Formula : _XLocation+_DeltaXForFindingSurface/2
X Surface Find Position
Internal Name : XSurfaceFindPosition
Units : um
Formula : _XLocation+_DeltaXForFindingSurface
Y Precise Surface Find Position
Internal Name : YPreciseSurfaceFindPosition
Units : nm
Formula : _YLocation+_DeltaYForFindingSurface/2
Y Surface Find Position
Internal Name : YSurfaceFindPosition
Units : nm
Formula : _YLocation+_DeltaYForFindingSurface
Hold Segment Formulas
Drift Correction
Internal Name : DriftCorrection
Units : nm/s
Formula : IF((MeasureDriftRateFlag<1) ,NilVelocity, PerformDriftCorrection*SlopeValue (_Displacement,_Time, DriftDeterminationMarker, EndDriftMarker))
Test Formulas
Test Status
Internal Name : TestStatus
Units :

```
                Formula : if (DriftDeterminationMarker >0 , 1,0)
Segment Markers
        Assign Surface Marker
                Internal Name : AssignSurfaceMarker
                Units :
                Formula : SurfaceMarker=CurrentIndex()
        End Drift Marker
                Internal Name : EndDriftMarker
                Units :
                Formula : CurrentIndex()
        End Of Loading Marker
                Internal Name : EndOfLoadingMarker
                Units :
                Formula : CurrentIndex()
        Surface Marker
                Internal Name : SurfaceMarker
                Units :
                Formula : ChannelIndex (DynamicContactStiffness,0.000356,t)
        t
                Internal Name : t
                Units :
                Formula : CurrentIndex()
Oliver & Pharr Calculations
        Area Coefficient 1
                Internal Name : AreaCoefficient1
                Units :
                Formula : TipParameter(1)
        Area Coefficient 10
                Internal Name : AreaCoefficient10
                Units :
                Formula : TipParameter(10)
        Area Coefficient 2
                Internal Name : AreaCoefficient2
                Units :
                Formula : TipParameter(2)
        Area Coefficient 3
                Internal Name : AreaCoefficient3
                Units :
                Formula : TipParameter(3)
        Area Coefficient 4
                Internal Name : AreaCoefficient4
                Units :
                Formula : TipParameter(4)
        Area Coefficient 5
                Internal Name : AreaCoefficient5
                Units :
                Formula : TipParameter(5)
        Area Coefficient 6
                Internal Name : AreaCoefficient6
                Units :
                Formula : TipParameter(6)
        Area Coefficient 7
                Internal Name : AreaCoefficient7
                Units :
                Formula : TipParameter(7)
        Area Coefficient 8
                Internal Name : AreaCoefficient8
                Units :
                Formula : TipParameter(8)
        Area Coefficient 9
                Internal Name : AreaCoefficient9
                Units :
```

```
                        Formula : TipParameter(9)
                Modulus From Unload : [ Disabled ]
                Tip Name
                        Internal Name : _TipName
                        Units :
                        Formula : TipName()
Configuration Objects
        Indenter Tip
                CurrentTipName : Berk2_1_9_06
                OriginalTipName : Berk2_1_9_06
        Units
                Category : SI
        Sample Report
                Report Template : %system%\MTS Nano Standard Sample Report.rtf
        Hardware Status
                Maximum Displacement Limit : [ Disabled ]
                Minimum Displacement Limit : [ Disabled ]
                Crosshead Stopped : [ Disabled ]
                Positive Device Overload : [ Disabled ]
                Hardware Communication Error : [ Disabled ]
                Negative Device Overload : [ Disabled ]
                Amp Fault : [ Disabled ]
                Lost Frame Communication : [ Disabled ]
                Emergency Stop : [ Disabled ]
                Z Stage Upper Limit : [ Disabled ]
                Lower Auxiliary Limit Active : [ Disabled ]
        Limit Detection
        Miscellaneous
                Method Access Level : 0
                Raw Data : Save Raw Data
                Automatically Save Every Test : Yes
                Master Flag : No
        Tag Limits
        Excel Output Configuration
Test Segments
```